ISSN 1811-1165 (Print)
ISSN 2413-2179 (Online)

EURASIAN PHYSICAL TECHNICAL JOURNAL

VOLUME 22, NO. 3(53), 2025

phtj.buketov.edu.kz

EURASIAN PHYSICAL TECHNICAL JOURNAL

p - ISSN 1811-1165
e - ISSN 2413-2179

Volume 22, No. 3(53), 2025

1st issue – June, 2004

Journal Founder:

NON-PROFIT LIMITED COMPANY «KARAGANDA NATIONAL RESEARCH UNIVERSITY NAMED AFTER ACADEMICIAN YE.A. BUKETOV»

https://phtj.buketov.edu.kz

www.facebook.com/groups/1103109540750967

Registration Certificate No.4382-Zh, November 7, 2003.

Re-registration Certificate No.KZ50VPY00027647, October 6, 2020 issued by Information Committee of the Ministry of Information and Public Development of the Republic of Kazakhstan

Contact information:

Editorial board of EAPhTJ
(Build. 2, room 216)
Karaganda Buketov University
Universitetskaya Str.28, Karaganda,
Kazakhstan, 100024
Subscription index: 75240

Tel: +7(7212) 77-04-03
Fax: +7(7212) 35-63-98
E-mail: ephtj@mail.ru,
ephtj2021@gmail.com

Signed to print 30.09.2025
Format 60x84 1/8. Offset paper.
Volume 21.63 p.sh. Circulation 300 copies.
Order No. 128.

Printed in the Publishing House of
Karaganda National Research University named after academician Ye.A. Buketov

Tel. +7 (7212) 35-63-16.
E-mail: izd_karu@buketov.edu.kz

Chief EDITOR

Sakipova S.E., Buketov Karaganda National Research University, Karaganda, Kazakhstan

EDITORIAL BOARD

Aringazin A.K., L.N. Gumilyov Eurasian National University, Astana, Kazakhstan

Dzhumanov S., Institute of Nuclear Physics, Uzbekistan Academy of Sciences, Tashkent, Uzbekistan

Hançerlioğullari A., Kastamonu Üniversitesi, Kastamonu, Turkey

Ibrayev N.Kh., Institute of Molecular Nanophotonics, Buketov Karaganda National Research University, Karaganda, Kazakhstan

Jakovics A., Institute of Numerical Modelling, University of Latvia, Riga, Latvia

Kucherenko M.G., Director of the Laser and Information Biophysics Centre, Orenburg State University, Orenburg, Russia

Kuritnyk I.P., Department of Electronics and Automation, High school in Oswiecim, Poland

Kushpil S., Heavy Ion Group, Nuclear Physics Institute of the Czech Academy of Science, Řež near Prague, Czech Republic

Miau J.J., Department of Aeronautics and Astronautics, National Cheng Kung University, Tainan, Taiwan

Miroshnichenko A.S., Department of Physics and Astronomy, University of North Carolina at Greensboro, North Carolina, USA

Saulebekov A.O., Kazakhstan Branch of Lomonosov Moscow State University, Astana, Kazakhstan

Senyut V.T., Joint Institute of Mechanical Engineering of National Academy of Sciences of Belarus, Minsk, Belarus

Shrager E.R., National Research Tomsk State University, Tomsk, Russia

Stoev M., South-West University «Neofit Rilski», Blagoevgrad, Bulgaria

Suprun T., Institute of Engineering Thermophysics of NASU, Kyiv, Ukraine

Trubitsyn A.A., Ryazan State Radio Engineering University, Ryazan, Russia

Zeinidenov A.K., Buketov Karaganda National Research University, Karaganda, Kazakhstan

Zhanabaev Z.Zh., Al-Farabi Kazakh National State University, Almaty, Kazakhstan

TECHNICAL EDITOR

Kambarova Zh.T., Buketov Karaganda National Research University, Karaganda, Kazakhstan

© Buketov Karaganda National Research University, 2025

Eurasian Physical Technical Journal, 2025, Vol. 22, No. 3(53)

CONTENTS

PREFACE……..……..…….……...……... 3

MATERIALS SCIENCE		
1	***Ismatov A.A., Romanitan C., Ashurov Kh.B., Adilov M.M., Rahimov A.A.*** Annealing-induced morphological evolution of iron nanocatalysts for carbon nanotube growth……...…….	5
2	***Sereda D.B., Kruglyak I.V., Sereda B.P.*** Obtaining multicomponent chromium coatings using functionally active mixtures. …….	14
3	***Kozlovskiy A.L., Borgekov D.B., Tleulessova I.K., Zhumazhanova A.T., Moldabayeva G.Zh., Burkhanov B.Zh., Khametova A.A.*** Evaluation of the application efficiency of multicomponent ceramics as protective shielding and thermal barrier materials. …….....	24
4	***Turdiyev M.T., Kasenov B.K., Nukhuly A., Bekturganov Zh.S., Kasenova Sh.B., Sagintaeva Zh.I., Kuanyshbekov E.E.*** Thermodynamic and electrophysical properties of a new semiconductor based on oxides of rare-earth and transition metals……...	36
5	***Yusupova Zh.B.*** Synthesis of silver nanoparticles and their influence on the fluorescence and absorption of anthracene. ……..	48
ENERGY		
6	***Genbach A.A., Bondartsev D.Yu.*** A study of heat transfer generalization for a cooling system with mineral media coatings.....	55
7	***Baytelesov S.A., Tadjibaev D.P., Fayziyev T.B., Kungurov F.R., Alikulov Sh.A.*** Determination of the energy release distribution and temperature in the IRT-4M nuclear fuel when changing the configuration of the control and protection system channels in the WWR-SM reactor. ……	66
8	***Mohammed H. Jawad, Mohammed R. Abdulameer*** Optical spectroscopic diagnosis of electron temperature and density for Zn-Al alloy plasma: effect of laser energy on plasma parameters.……..	75
9	***Sharipov M.Z., Majitov J.A., Ergashev Sh.H., Shodiyev E.B., Narzullayeva Z.M.*** Substitution of thermal-technical and geometric parameters of a small-scale biogas plant. …….	84
ENGINEERING		
10	***Askaruly R., Faizulla T., Abylkanov M., Syzdykov A.B., Sakhanov K.*** Enhancing the durability of robotic ARM using composite materials and additive manufacturing in harsh environmental conditions. ……..	91
11	***Sarsenbayev Y., Ostretsov K., Baktybekov K., Mussina A., Yskak A.*** Universal modular onboard control complex OBCARM G2 NANO for nano-class spacecraft…….	101
12	***Zhumazhanov B.R., Zhetpisbayeva A., Kulakayeva A., Makhanov K., Zhumazhanov B.S.*** Development and optimization of optical payload for nanosatellites with strict constraints. ……	111
13	***Baibolatov Y.Z., Nalibayev Y.D., Kozhagulov Y.T.*** A dynamical system approach to language bias evolution on complex networks. ……	120
14	***Usibe B.E., Iserom B.F., Iwuji P.C., Aigberemhon M.E., Iwuanyanwu I.O., Ushie A.I., Ettah E.E.*** Design Analysis of a Wien-Bridge Oscillator: From Prototype to Temperature Performance…….	127
PHYSICS AND ASTRONOMY		
15	***Aimanova G.K., Serebryanskiy A.V., Shcherbina M.P., Krugov M.A.*** Spectrophotometric studies of asteroids I: Taxonomic type. ……..…	138
16	***Saulebekov A.O., Kambarova Zh.T., Kassymov S.S.*** A novel design of an energy analyzer for charged particles based on a non-uniform electrostatic field……	148
17	***Shugayeva T., Amantaeva A., Spivak-Lavrov I.*** Numerical analysis and chaos control: a study of Lorentz systems with visual basic for application implementation…….	156
SUMMARIES…….....		163

Dear authors and readers!
Dear colleagues!

In Preface, we traditionally inform the authors and readers about the important achievements and status of the Eurasian Physical Technical Journal, that published by the E. A. Buketov Karaganda University. On the eve of the preparation and release of the current issue, a historic event occurred: by Decree No. 1399-D of the President of the Republic of Kazakhstan, K.-Zh. Tokayev, dated August 12, 2025, our university was granted the status of a National University.

It is no coincidence and symbolic that this event takes place in the year of the 100th anniversary of the birth of Academician Buketov E.A., the first rector who stood at the origins of the university's founding and development. Being granted the status of a national university is a well-deserved recognition of the many years of work by the entire university staff aimed at improving the quality of education and research. At the same time, it is a great responsibility, requiring further efforts to strengthen international competitiveness and make a significant contribution to the development of our Kazakhstan.

Since 2015, the university has been included in the QS World Universities Rankings and QS Asia. In the international Webometrics ranking, the university is among the top ten universities in the Republic of Kazakhstan. The university enrolls over 14,000 undergraduate, graduate, and doctoral students. Around 200 educational programs are offered across 12 faculties.

The Eurasian Physical Technical Journal, in which authors from over 50 countries publish original research articles on current issues in modern technical physics, also contributes to the development and growth of the university, facilitating the expansion and strengthening of international scientific collaboration. We hope and are confident that achieving national university status will open up new opportunities for implementing innovative programs, conducting cutting-edge research, and training competitive specialists.

This issue contains 17 articles. The Materials Science section discusses the challenges and prospects of nanotechnology for the production of new materials, nanocatalysts for carbon nanotube growth, and multicomponent chromium coatings; the creation of new semiconductors based on rare-earth and transition metal oxides; and the synthesis of silver nanoparticles.

In the Energy section, the authors propose solutions to problems related to optimizing heat transfer processes in the cooling system; replacing various components without compromising the nuclear safety of the VVR-SM reactor; spectroscopic diagnostics of the temperature and electron density in the plasma of a Zn-Al alloy; and an analysis of the possibilities of changing the thermal and geometric parameters for the operation of a small-scale biogas plant.

The Engineering section addresses a wide range of issues in payload optimization for nanosatellites, development of universal control systems for nano-class spacecraft, enhancing the durability of robotic manipulators using composite materials in harsh climates, modeling dynamic systems to study language competition and the evolution of language bias in structured agent populations, and analysis of the design modeling of a Wien bridge oscillator circuit.

The Physics and Astronomy section presents the results of an analysis of spectral observations of a number of Main Belt asteroids, the Apollo family asteroid 30825, and the rare asteroid Lick, with the aim of determining their taxonomic types; a new design for an energy analyzer based on an axisymmetric inhomogeneous field is proposed; the results of a numerical analysis and control of

the chaotic dynamics of Lorenz systems using the Visual Basic for Applications package are also shown.

We hope the presented articles will be of interest to scientists, teachers, doctoral and master's students.

We will be glad to see you among our readers and authors of the next issues, in which it is planned to publish articles by leading scientists on the most relevant and priority areas of modern physics and technology.

With respect and best wishes for health and well-being to our authors and readers,

Editor-in-Chief, Professor Sakipova S.E.
September, 2025

EURASIAN PHYSICAL TECHNICAL JOURNAL

2025, Volume 22, No. 3 (53)

https://doi.org/10.31489/2025N3/5-13

Received: 10/04/2025 Revised: 27/05/2025 Accepted: 25/09/2025 Published online: 30/09/2025

Research Article

Open Access under the CC BY -NC-ND 4.0 license

UDC 539.21; 541.16; 669.784

ANNEALING-INDUCED MORPHOLOGICAL EVOLUTION OF IRON NANOCATALYSTS FOR CARBON NANOTUBE GROWTH

Ismatov A.A.[1*], Romanitan C.[2*], Ashurov Kh.B.[1], Adilov M.M.[1], Rahimov A.A.[1]

[1] Institute of Ion-plasma and laser technologies, Tashkent, Uzbekistan,

[2] National Institute for Research and Development in Microtechnologies, Voluntari, Romania

*Corresponding author: asqarismatov878@gmail.com

Abstract. *The synthesis of iron nanocatalysts on silicon substrates via the Electron Beam Physical Vapor Deposition method has garnered significant attention due to its catalytic uses. The influence of annealing temperature (500°C, 550°C, and 600°C) on the structural and morphological characteristics of Fe nanocatalysts and their use in the growth of carbon nanotubes via Chemical Vapor Deposition is investigated in this study. Atomic Force Microscopy and Scanning Electron Microscopy measurements reveal that an increase in the annealing temperature reduces the average nanocluster size, and annealing at 600°C yields nanoclusters with an average size of approximately 30 nm; hence, they are more effective as catalysts. Raman spectroscopy proved that carbon nanotube growth was only observed on the 600°C-annealed substrate, and it exhibits a high* I_D/I_G *ratio (<1), indicating high crystallinity and low defect concentration. The absence of Radial Breathing Mode peaks represents additional evidence that the synthesized carbon nanotubes are multi-walled. These findings indicate that nanocluster size and distribution must be controlled with high accuracy using Electron Beam Physical Vapor Deposition and thermal treatment in order to maximize Fe nanocatalysts for carbon nanotubes growth.*

Keywords: Iron nanocatalysts, Carbon nanotube, Physical Vapor Deposition, Chemical Vapor Deposition, Raman spectroscopy, Atomic Force Microscopy, Scanning Electron Microscopy.

1. Introduction

In recent years, metallic nanomaterials have gained widespread popularity due to their physical, chemical, and catalytic properties which make them ideal for use in green chemistry, waste reduction, and environmental remediation [1- 3]. Iron (Fe) nanocatalysts are especially interesting due to the abundancy and low cost of iron, its favorable magnetic characteristics, and versatile reactivity [4,5]. Fe nanocatalysts have numerous applications in chemical synthesis, conversion of renewable energy, and even in cleaning up the environment [6]. Moreover, their involvement in the formation of carbon nanotubes (CNTs) has created a need to refine their synthesis and control their morphology, in order to increase catalytic activity [7] alongside these developments. Central to interest in Fe nanocatalysts is their application in the production of carbon nanotubes. Myriad approaches have been devised for the preparation of Fe nanocatalysts. The most common methods of chemical synthesis include: chemical reduction [8, 9], sol-gel technique [10], thermal evaporation [11], and sputter deposition [12]. Unfortunately, these techniques present important limitation related to the control over the particle size distribution, surface agglomeration, and contamination. It is clear that these features hamper the full potential of the synthesized nanomaterials thus being hampered their

effectiveness [13]. As response to these issues, Electron Beam Physical Vapor Deposition (EB-PVD) has been found to be a highly effective method due to its capacity to function under high vacuum conditions, thereby maintaining low levels of contamination and enabling deposition of very uniform and pure nanostructures [14]. The intrinsic control over deposition parameters of EB-PVD, such as the evaporation rate, substrate temperature or beam current enables the fine adjustment of catalyst morphology, which is a critical factor in optimizing the ensuing catalytic activity and CNT growth [15]. It was demonstrated the possibility to achieve high-purity films and nanostructures by using a ultraclean environment, thus minimizing the formation of defects and contaminants, and the same time promoting fast deposition with less material loss [16]. EB-PVD has also succeeded in optimizing the size and distribution of metallic nanocatalysts, which is essential for high surface area and active site requirements in applications [17]. It has been recently reported that alteration of the annealing conditions following deposition can impose severe changes in the morphology of Fe nanocatalysts, thus further enhancing their catalytic activity for CNT growth [18]. For instance, the reduction in particle size and enhancement in particle uniformity by annealing have been attributed to increased catalytic activity and enhanced crystallinity of CNTs [19]. The current state-of-the-art in CNT synthesis places higher priority on the construction of solid and scalable catalyst preparation methods that can form catalysts of suitable size, distribution, and purity [20]. Despite many physical and chemical methods being tried out, the EB-PVD method is unique in its ability to offer the best balance between controllability and efficiency, especially with the inclusion of subsequent thermal treatments [21]. This mixture not only improves the physical characteristics of the catalyst but also CNT quality and yield in Chemical Vapor Deposition (CVD) conditions [22]. Further, advances in in-situ characterization techniques have also enabled enhanced understanding of nanocatalyst structural evolution on annealing and CNT growth, thus enabling improved process optimization [23]. Despite these advancements, reproducibility of catalyst performance and elucidation of detailed mechanism underlying morphological evolution during the annealing process remains challenging. Numerous works have reported differences in various schemes of annealing and their implications on the character of catalyst, but relationship of deposition parameters with annealing treatment and the resulted synthesis efficiency of CNT remains unclear [24]. Filling this gap is a crucial step for the advancement of the nanocatalyst design field and for the broader application of CNTs in electronics, sensors, and energy storage [25].

In this paper, we report the optimization and synthesis of Fe nanocatalysts via EB-PVD followed by different annealing temperatures (500°C, 550°C, and 600°C). The novelty of our contribution is the rigorous investigation of the annealing-driven morphological evolution and its immediate impact on the growth of CNTs using CVD. With accurate tuning of annealing parameters, we demonstrate a critical temperature for which the nanocatalysts exhibit an ideal size distribution and geometric configuration beneficial for effective nucleation of CNTs. Our experimental outcomes, confirmed with Atomic Force Microscopy (AFM), Scanning Electron Microscopy (SEM), and Raman spectroscopy, reveal that only substrates annealed at 600°C exhibit the properties of the requisite nanoparticles and improved quality CNT growth [26]. This study not only offers a deeper understanding of the inherent mechanisms that control the development of nanocatalysts but also offers a pragmatic route to the synthesis of next-generation catalysts for new applications of CNTs [27].

2. Instrumentals Part

Figure 1 illustrates the setup of an EB-PVD system used for the deposition of Fe nanocatalysts on a silicon substrate. In this configuration, the core components include a vacuum chamber, an electron beam source, and pumping systems to maintain high vacuum conditions essential for precise deposition. The main components and their functions are as follows:

1. Electron Beam Source and Control Panel: The electron beam source is powered by a high-voltage supply, controlled through an interface that allows users to adjust the output voltage in kilovolts (kV). This high-voltage electron beam vaporizes the iron target material, creating a vapor that deposits on the silicon substrate within the vacuum chamber. The control panel includes switches for turning the high voltage (HV) on and off.

2. Vacuum Chamber: The deposition process occurs in the vacuum chamber, which isolates the deposition environment from atmospheric contaminants. Maintaining a high vacuum is crucial for creating uniform nanostructures, as it allows for a controlled deposition process with minimal interference from air particles.

3. Turbomolecular Pump: This pump creates and maintains the high vacuum required for EB-PVD by removing air and other gases from the chamber. It plays a critical role in ensuring that the vaporized material travels directly to the substrate without unwanted reactions or scattering.

4. Asynchronous Rotary Pump: Positioned before the turbomolecular pump, this pump performs initial evacuation, creating a lower vacuum that facilitates the turbomolecular pump's operation. Together, these pumps ensure a clean and stable vacuum environment essential for high-quality nanocatalyst deposition.

5. Cooling Water Lines: Cooling water flows through the system to prevent overheating, which can damage components or alter deposition parameters. This water flow is vital for maintaining temperature stability in both the electron beam source and the pumping system.

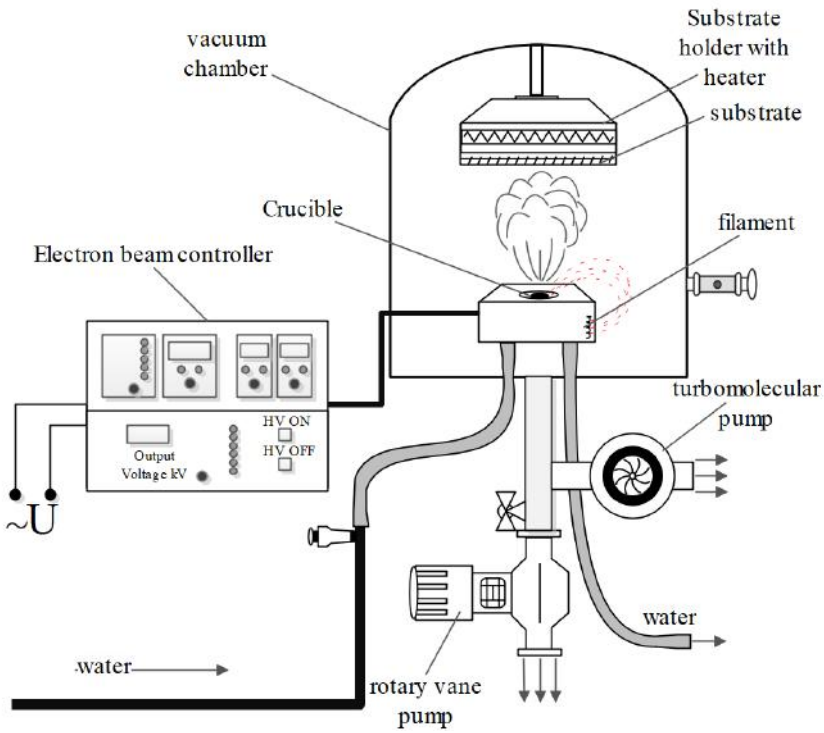

Fig.1. Schematic diagrams` setup of EB-PVD system.

The EB-PVD system operates under high-vacuum conditions, with a chamber pressure of 10^{-6} torr and an applied electron beam voltage of 10 kV, thus providing the precise and stable environment necessary for nanocatalyst deposition. This controlled environment allows a fine-tuning nanocatalyst properties, such as size and morphology, to enhance catalytic performance.

3. Experiment

Silicon wafers (KEC-001, 100, n-type) were sequentially cleaned in three stages, as schematically shown in Figure 2. To form a deposited buffer layer (DBL) on the obtained substrates, an oxide layer was grown using the Thermal Oxidation method. The DBL thickness was controlled by temperature and grown to various thicknesses over a period of 2–5 hours [28]. The substrates were cut into 2 × 1 cm pieces, with two samples taken from each (one directly for CVD after PVD, and the other for analytical characterization).

The prepared substrates were placed in an EB-PVD instrument, where a high-vacuum environment (2–4 $\times 10^{-6}$ Torr) was achieved. Iron material, placed in a crucible, was deposited onto the substrate surface for 3 seconds using a cathode filament operated at 10 kV and a current of 30–35 A. During the deposition process, the wafers were maintained at room temperature.

After deposition, under the same vacuum conditions, the iron-coated substrates were annealed at three different temperatures: 500°C, 550°C, and 600°C, each for 30 minutes. Upon completion of the annealing process, the substrates were allowed to cool to room temperature under vacuum before the chamber was opened. A portion of the obtained substrates was immediately transferred to the CVD system.

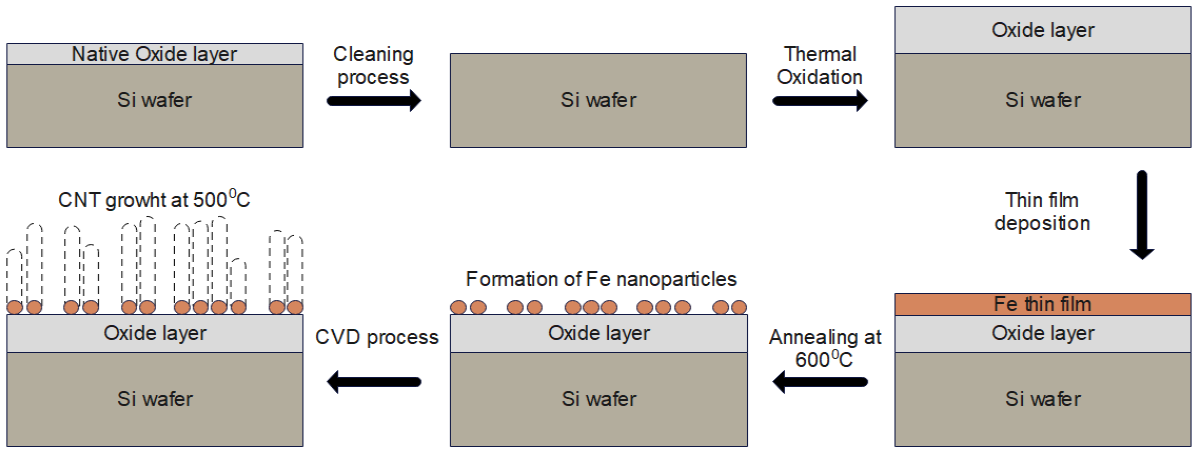

Fig.2. Fe nanocatalyst formation and CNT synthesis via CVD.

The CVD process was also conducted under vacuum conditions. To prevent oxidation of the Fe nanocatalysts' surface, the substrates were reduced in a hydrogen atmosphere at temperatures ranging from 400°C to 500°C for 45 minutes. Subsequently, Ar was introduced as a carrier gas, and an ethanol mixture was supplied as the carbon source into the quartz tube. Regardless of their annealing temperature, both sets of substrates underwent CNT synthesis at 500°C for 1 hour, followed by natural cooling to room temperature.

4. Characterization Techniques

The AFM micrographs were obtained with the equipment NT-MDT Next Solver, operated in semi-contact mode to minimize tip–sample interaction. The scans were performed at a frequency of 1 Hz with a resolution of 300 × 300 pixels, under ambient conditions. This setup enabled precise visualization of the surface morphology and height variations of the catalyst nanoparticles. SEM imaging was conducted using a Thermo Fisher Scientific Apreo 2S LoVac system, operated in low vacuum mode. The system provided a lateral resolution of up to 500 nm, which allowed clear observation of the nanocatalysts' size distribution, surface coverage, and structural uniformity. Raman spectra were acquired using a Renishaw inVia Raman microscope equipped with a 785 nm excitation laser. The measurements were taken in backscattering configuration under ambient conditions. The system offered a spectral resolution better than 1 cm^{-1}, enabling detailed analysis of the D, G, and 2D bands of CNTs to assess their degree of graphitization and structural defects.

5. Results and discussion

Figure 3 presents AFM images on $3 \times 3\ \mu m^2$ of iron nanoclusters annealed at 500°C and 550°C. .One can observe the presence of almost spherical grains distributed on the surface. The size analysis of the nanoclusters revealed that the average diameter of the particles annealed at 500°C was 250 nm (Figure 3a), while those annealed at 550°C exhibited an average diameter of 170 nm (Figure 3b). Only spherical Fe grains can be observed on the surface, without any features on the surface, indicating the absence of CNT growth. This can be attributed to the excessively large size of the nanoclusters, which prevents them from functioning effectively as nanocatalysts. Although carbon atoms adhered to the surface of the nanoclusters, no structured CNT growth was detected.

SEM imaging of iron nanoclusters on substrates annealed at 600°C (Figure 4) demonstrated a significant reduction in particle diameter compared to the samples annealed at the two lower temperatures. The minimum, maximum, and average diameters of the nanoparticles were determined to be 7 nm, 115 nm, and 30 nm, respectively, with a standard deviation (σ) of 15 nm.

This phenomenon indicates that the nanoparticles have reached the critical size required for their functionality as nanocatalysts. Additionally, their geometric shape closely resembles that of droplets (Figure 4a). The particle size distribution derived from SEM analysis indicates that the Fe nanocatalysts have an average diameter of approximately 30 nm. The histogram was constructed using ImageJ software, which

enabled accurate measurement and statistical analysis of nanoparticle dimensions. The distribution shows that the most frequently occurring particle sizes lie within the 15–25 nm range, which is close to the calculated mean. The data exhibits a positively skewed (right-skewed), log-normal distribution, commonly encountered in nanostructure synthesis.

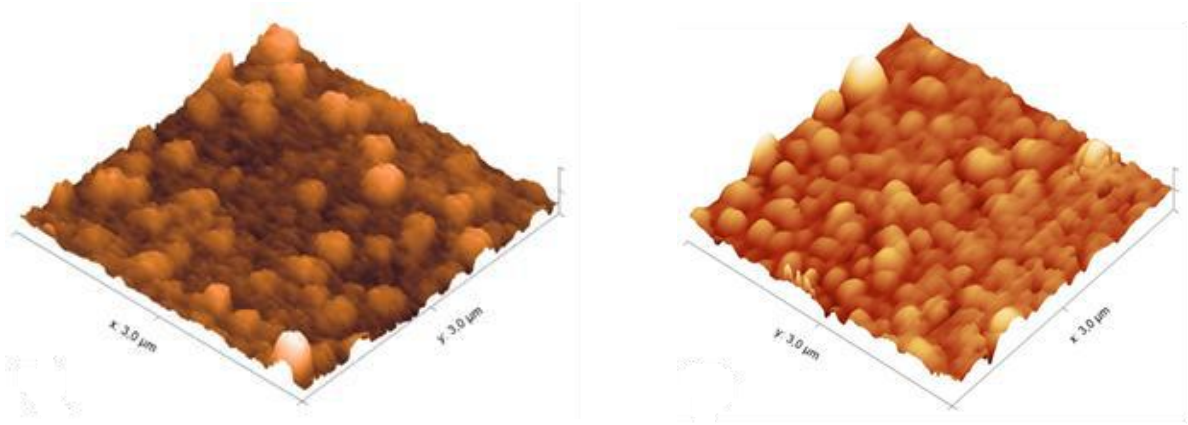

a) b)

Fig.3. AFM images of Fe nanoclusters annealed at 500°C (a) and 550°C (b).

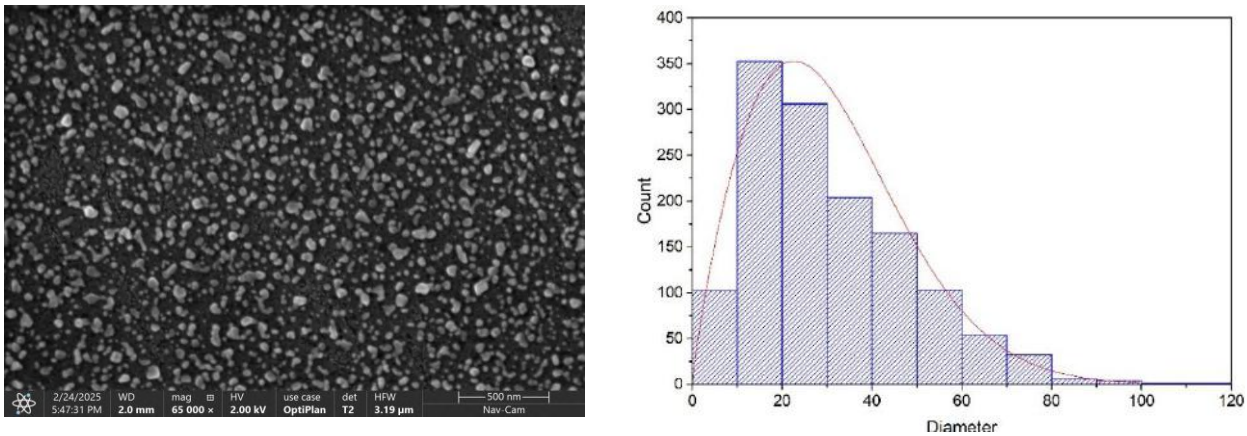

a) b)

Fig.4. (a) SEM image and (b) diameter distribution of Fe nanoparticles annealed at 600°C.

This suggests a high population of small particles, while larger particles are comparatively rare, indicating a polydisperse system. Such non-uniformity in particle size can significantly affect their catalytic behavior during CNT growth (Figure 4b). Furthermore, the appearance of a small number of particles in the 80–100 nm range may be attributed to agglomeration or sintering phenomena occurring during deposition or annealing processes. This confirms that 600°C represents the threshold temperature at which the iron thin film transforms into catalytically active nanoparticles.

EDX analysis further confirmed that the elemental composition of the substrate is uniformly distributed across the surface, as depicted in Figure 5a, b, and c. The absence of foreign elements in the sample serves as evidence of the high precision and purity maintained during the nanocatalyst preparation process.

Additionally, Figure 5d illustrates the percentage composition of the elements, providing insight into their relative abundance within the overall sample.

Raman spectroscopy (785 nm laser) analysis conducted after the CVD process confirmed that no CNT growth occurred on the surfaces of the substrates annealed at 500°C and 550°C. However, CNT formation was observed on the 600°C-annealed substrate after CVD at 500°C (Figure 6).

The Raman spectrum displayed a dominant G band at 1582 cm^{-1} compared to the D band at 1326 cm^{-1}. The intensity ratio of D to G (I_D/I_G) corresponded to 0,56 , indicating high crystallinity and low defectiveness in the CNTs. Compared to the MWCNTs grown in [29], the obtained results indicate significantly higher quality. According to the best Raman analysis results of MWCNTs synthesized by Miura

et al., the I_D/I_G ratio was found to be 1,11. Our results suggest an approximately twofold improvement in I_D/I_G over them, a finding that complements rather than contradicts their contributions. The smaller this ratio, the more ordered and high-quality the nanotubes are. If the intensity ratio of the D peak to the G peak is less than 0,5, it indicates highly ordered and high-quality nanotubes.

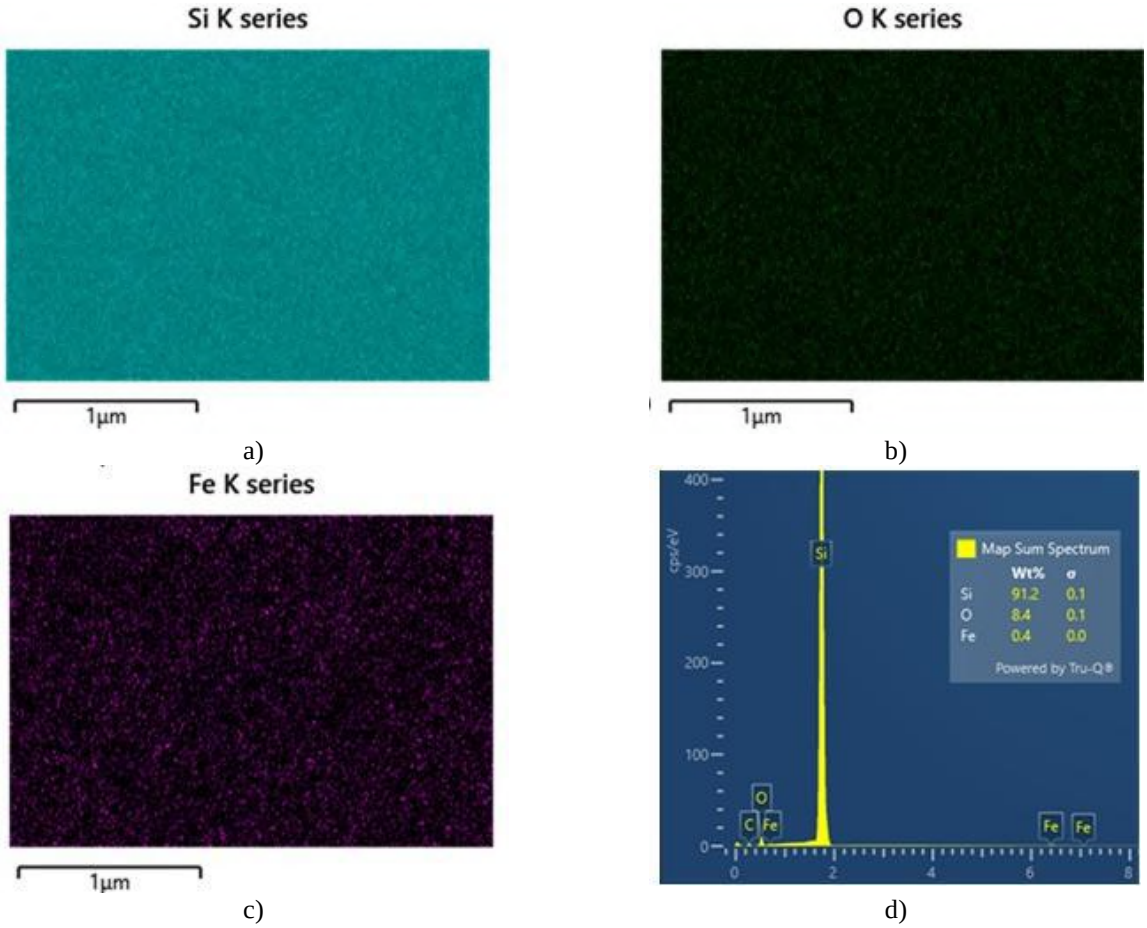

Fig.5. EDX analysis of nanoparticles annealed at 600°C: (a), (b), (c), and (d).

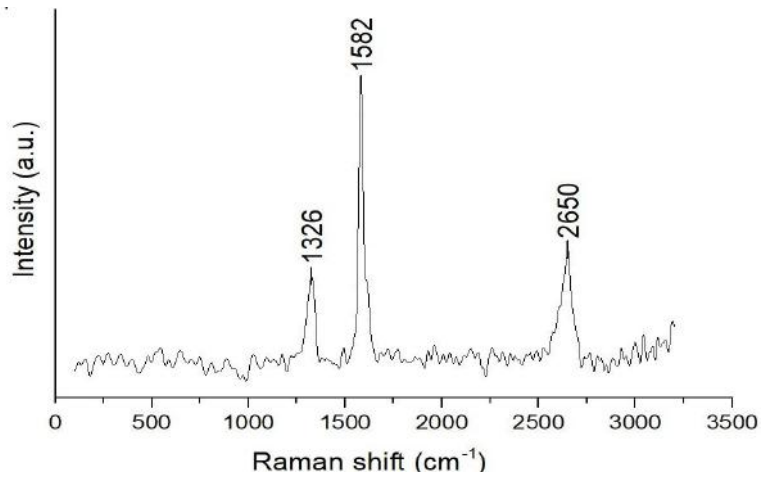

Fig.6. Raman spectrum of CNTs grown on Fe nanoparticles annealing at 600 ^{0}C.

If this ratio falls within the range of 0,5 to 1, it suggests the presence of some defects; however, the nanotubes remain structurally viable. Furthermore, the absence of RBM peaks in the 100–400 cm^{-1} range confirmed that the synthesized CNTs were multi-walled rather than single-walled.

6. Conclusion

In the present study, Fe nanocatalysts were successfully grown on Si substrates by means of Electron Beam Physical Vapor Deposition (EB-PVD) and subsequently subjected to annealing at various temperatures (500, 550, and 600 °C). The variation of annealing temperature was investigated for optimizing the structural and morphological characteristics of Fe nanoclusters to be used as catalysts in the growth of carbon nanotubes (CNTs). From Atomic Force Microscopy (AFM) and Scanning Electron Microscopy (SEM) investigations, it is confirmed that the higher annealing temperature attributed to the decrease in nanocluster size, with the most favorable size distribution at 600° ranging from 7–115 nm (average 30 nm). Raman spectra show CNTs only after annealing at 600°C with an ID/IG of 0.56, a value associated with high crystallinity and low defect levels. Taken together with prior studies under the same conditions, these data point to an approximate twofold reduction in ID/IG, implying enhanced structural quality. Based on the SEM-derived size distribution of the nanoparticles, the samples are consistent with multi-walled carbon nanotubes. In addition, the absence of Radial Breathing Mode peaks further elaborated this conclusion.

The iron nanocatalysts obtained in this study have great potential for various advanced fields such as nanoelectronics, nanomedicine, energy storage and conversion, environmental remediation, and sensor technologies, where precise control over nanoparticle size is crucial for optimizing performance; therefore, the method developed here, which enables fine-tuning of nanocluster dimensions, represents a highly valuable approach that not only advances these fields but also provides evidence that controlling the nanocatalyst size and distribution can optimize their use in carbon nanotube synthesis, with the EB-PVD technique under appropriate annealing conditions offering an effective way to produce high-quality nanocatalysts possessing uniform morphology and enhanced catalytic efficiency, while further refinement of deposition and annealing parameters is expected to enable even more precise control over nanostructure formation and catalytic performance, and in addition, exploring other catalyst materials and substrate modifications may open new avenues for improving processes related to CNT synthesis.

Conflict of interest statement

The authors declare that they have no conflict of interest in relation to this research, whether financial, personal, authorship or otherwise, that could affect the research and its results presented in this paper.

CRediT author statement

A.A. Ismatov: Writing – original draft, Investigation, Formal analysis, Visualization, **C. Romanitan**: Methodology, Formal analysis, Writing – review & editing, **Kh. B. Ashurov**: Supervision, Funding acquisition, **M.M. Adilov**: Conceptualization, Methodology, **A.A. Rahimov**: Investigation. The final manuscript was read and approved by all authors.

Funding

The authors gratefully acknowledge the financial and technical support provided by the Ministry of Higher Education, Science and Innovation under project number IL-5421101842

Acknowledgements

I would like to thank the team of the Institute of Ion-Plasma and Laser Technologies, Center for Collective Use of Scientific Instruments

References

1 Vaz C.A.F., Piamonteze C., Kleibert A. (2018) Enhanced mobility of iron nanoparticles deposited onto a xenon-buffered silicon substrate. *Journal of Magnetism and Magnetic Materials*, *459*, 2-6. https://doi.org/10.1016/J.JMMM.2018.02.021

2 Melchionna M., Fornasiero P., Cargnello M. (2017) Opportunities and Challenges in the Synthesis, Characterization, and Catalytic Properties of Controlled Nanostructures. *Studies in Surface Science and Catalysis*,177, 1-56. https://doi.org/10.1016/B978-0-12-805090-3.00001-2

3 Movchan B. A. (2016) Discrete nanosized metallic coatings produced by EB-PVD. *Surface Engineering*, 32, 4. https://doi.org/10.1179/1743294415Y.0000000092

4 Lehmann H.W., Frick K. (1988) Optimizing deposition parameters of electron beam evaporated TiO_2 films. *Applied Optics*, 27, 4920-4924**.** https://doi.org/10.1364/AO.27.004920

5 Minea T.M., Point S., Gohier A., Granier A., Godon C., Alvarez F. (2005) Single chamber PVD/PECVD process for in situ control of the catalyst activity on carbon nanotubes growth. *Surface and Coatings Technology*, *200*(1-4), 1101-1105. https://doi.org/10.1016/J.SURFCOAT.2005.01.053

6 Sharapov I., Omarova G., Sadykova A., Seliverstova E. (2025) Properties of Ag/TiO_2 AND Ag/SiO_2 nanoparticles and their effect on the photocatalytic properties of a semiconductor nanocomposite. *Eurasian Physical Technical Journal*, *22*(2 (52)), 25–32. https://doi.org/10.31489/2025N2/25-32

7 Berdiev U., Khudaykulov I., Iskandarov S., Amirova A., Ashurov K. (2025) Influence of SiO2 Nanoparticles on the Characteristics of a Polyvinyl Alcohol-Based Proton Exchange Composite Membrane. *East European Journal of Physics*, (1), 265-271. https://doi.org/10.26565/2312-4334-2025-1-30

8 Melchionna M., Beltram A., Stopin A., Montini T., Lodge R. W., Khlobystov A.N., . Fornasiero P. (2018) Magnetic shepherding of nanocatalysts through hierarchically-assembled Fe-filled CNTs hybrids. *Applied Catalysis B: Environmental*, 227, 356-365. https://doi.org/10.1016/j.apcatb.2018.01.049

9 Sharma P., Pavelyev V., Kumar S., Mishra P., Islam S.S., Tripathi N. (2020) Analysis on the synthesis of vertically aligned carbon nanotubes: growth mechanism and techniques. *Journal of Materials Science: Materials in Electronics*, *31*(6), 4399-4443. Available at: https://link.springer.com/article/10.1007/s10854-020-03021-6

10 Ju L., Chen Z., Fang L., Dong W., Zheng F., Shen M. (2011) Sol–gel synthesis and photo- Fenton- like catalytic activity of EuFeO3 nanoparticles. *Journal of the American Ceramic Society*, 94(10), 3418-3424. https://doi.org/10.1111/j.1551-2916.2011.04522.x

11 Dai Z.R., Pan Z.W., Wang Z.L. (2003) Novel nanostructures of functional oxides synthesized by thermal evaporation. *Advanced Functional Materials*, 13(1), 9-24. https://doi.org/10.1002/adfm.200390013

12 Bosso P., Del Sole R., Milella A., Mengucci P., Barucca G., Armenise V., & Palumbo F. (2023) Nanostructured iron oxide thin films deposited by RF sputtering as catalysts for the heterogeneous solar photo-Fenton reaction. *Vacuum*, *207*, 111646. https://doi.org/10.1016/j.vacuum.2022.111646

13 Zeng Xiaoliang, Yu Shuhui, Ye Lei, Li Mingyan, Pan Zhilong, Sun Rong, Xu J.B.. (2014) Encapsulating carbon nanotubes with SiO2: A strategy for applying them in polymer nanocomposites with high mechanical strength and electrical insulation. *J. Mater. Chem. C.*, 3, 187-195. http://dx.doi.org/10.1039/C4TC01051E

14 Zhang Q., Cheng G., Zheng R. (2018) The Internal Buckling Behavior Induced by Growth Self-restriction in Vertical Multi-walled Carbon Nanotube Arrays. *MRS Advances*, *3*(45–46), 2815–2823. https://doi.org/10.1557/adv.2018.429

15 Jing L., Li H., Lin J., Tay R.Y., Tsang S.H., Teo E.H.T., Tok A.I.Y. (2018) Supercompressible coaxial carbon nanotube@ graphene arrays with invariant viscoelasticity over− 100 to 500 C in ambient air. *ACS Applied Materials & Interfaces*, *10*(11), 9688-9695. Available at: https://pubs.acs.org/doi/abs/10.1021/acsami.8b01925

16 Eres G., Rouleau C. M., Puretzky A. A., Geohegan D.B., Wang H. (2018) Cooperative behavior in the evolution of alignment and structure in vertically aligned carbon-nanotube arrays grown using chemical vapor deposition. *Physical Review Applied*, *10*(2), 024010. https://doi.org/10.1103/PhysRevApplied.10.024010

17 Walsh P.J., Li H., Anaya de Parrodi C. (2007) A green chemistry approach to asymmetric catalysis: Solvent-free and highly concentrated reactions. *ChemInform*, 38(30), 112–118. https://doi.org/10.1002/chin.200736264

18 Păun C., Obreja C., Comănescu F., Tucureanu V., Tutunaru O., Romanițan C., Ionescu O. (2019). Epoxy nanocomposites based on MWCNT. *Proceeding of the IEEE 2019 International Semiconductor Conference (CAS)*, 237 – 240. https://doi.org/10.1109/SMICND.2019.8923947

19 Paun C., Obreja C., Comanescu F., Tucureanu V., Tutunaru O., Romanitan C., & Paltanea G. (2021) Studies on structural MWCNT/epoxy nanocomposites for EMI shielding applications. *Proceeding of the IOP Conference Series: Materials Science and Engineering*, 1009, 1, 012046. https://doi.org/10.1088/1757-899X/1009/1/012046

20 Hu H., Xin J.H., Hu H., Wang X., Miao D., Liu Y. (2015) Synthesis and stabilization of metal nanocatalysts for reduction reactions–a review. *Journal of materials chemistry A*, 3(21), 11157-11182. https://doi.org/10.1039/C5TA00753D

21 Rusevova K., Kopinke F.D., Georgi A. (2012) Nano-sized magnetic iron oxides as catalysts for heterogeneous Fenton-like reactions—Influence of Fe (II)/Fe (III) ratio on catalytic performance. *Journal of hazardous materials*, 241, 433-440. https://doi.org/10.1016/j.jhazmat.2012.09.068

22 Abdisaidov I., Khudaykulov Ilyos, Ashurov Kh. (2024) Low-temperature growth of carbon nanotubes using nickel catalyst. *East European Journal of Physics*., 355-358. https://doi.org/10.26565/2312-4334-2024-3-41

23 Mohapatra M., Anand S. (2010) Synthesis and applications of nano-structured iron oxides/hydroxides–a review. *International Journal of Engineering, Science and Technology*, 2(8). https://doi.org/10.4314/ijest.v2i8.63846

24 Ali A., Zafar H., Zia M., ul Haq I., Phull A.R., Ali J. S., Hussain A. (2016) Synthesis, characterization, applications, and challenges of iron oxide nanoparticles. *Nanotechnology, science and applications*, 49-67. https://doi.org/10.2147/NSA.S99986

25 Khan Y., Sadia H., Ali Shah S.Z., Khan M.N., Shah A.A., Ullah N., Khan M.I. (2022) Classification, synthetic, and characterization approaches to nanoparticles, and their applications in various fields of nanotechnology: a review. *Catalysts*, 12(11), 1386. https://doi.org/10.3390/catal12111386

26 Campos E. A., Pinto D.V.B.S., Oliveira J. I. S. D., Mattos E.D.C., Dutra R.D.C.L. (2015) Synthesis, characterization and applications of iron oxide nanoparticles-a short review. *Journal of Aerospace Technology and Management*, 7(3), 267-276. https://doi.org/10.5028/jatm.v7i3.471

27 Karakashov B., Mayne-L'Hermite M., Pinault M. (2022) Conducting interface for efficient growth of vertically aligned carbon nanotubes: Towards nano-engineered carbon composite. *Nanomaterials*, 12(13), 2300. https://doi.org/10.3390/nano12132300

28 Ashurov X., Adilov M., Ismatov A., Rakhimov A. (2025) Oxide layer growth on silicon substrates: effects of temperature and surface preparation. *Uzbek Journal of Physics*, 26(4). https://doi.org/10.52304/.v26i4.570

29 Miura S., Yoshihara Y., Asaka M., Hasegawa K., Sugime H., Ota A., Oshima H., Noda S. (2018) Millimeter-tall carbon nanotube arrays grown on aluminum substrates. *Carbon*, *130*, 834-842. https://doi.org/10.1016/j.carbon.2018.01.075

AUTHORS' INFORMATION

Ismatov, Askar Anvar o`g`li – Master (Sci.), Scientific Researcher, Institute of ion plasma and laser technologies, Tashkent, Uzbekistan; https://orcid.org/0009-0006-5005-4201; asqarismatov878@gmail.com

Romanitan, Cosmin - PhD, Physics Research Scientist, Voluntari, National Institute for Research and Development in Microtechnologies, Bucharest, Romania; Scopus Author ID: 56829395900, https://orcid.org/0000-0002-5615-6624; cosmin.romanitan@imt.ro

Adilov, Mukhammadjon Masharipovich - PhD, Head of the laboratory, Institute of ion plasma and laser technologies, Tashkent, Uzbekistan; Scopus Author ID: 55291303400, https://orcid.org/0000-0003-0312-2356, muhammad.84@mail.ru

Rakhimov, Abdulla Abdumurod o`g`li – Master (Sci.), Scientific Researcher, Durman street 33, Institute of ion plasma and laser technologies, Tashkent, Uzbekistan; https://orcid.org/0009-0004-1687-0454 , abdullarakhimov55@gmail.com

Ashurov, Khatam Baxronovich – D.Sc., Professor, Institute of ion plasma and laser technologies, Tashkent, Uzbekistan; Scopus Author ID: 23391831300, https://orcid.org/0000-0002-7604-2333; ashurov@iplt.uz

EURASIAN PHYSICAL TECHNICAL JOURNAL

2025, Volume 22, No. 3 (53)

https://doi.org/10.31489/2025N3/14-23

Received: 16/02/2025 Revised: 26/05/2025 Accepted: 25/09/2025 Published online: 30/09/2025

Research Article

Open Access under the CC BY -NC-ND 4.0 license

UDC 539.4.015; 621.793.6

OBTAINING MULTICOMPONENT CHROMIUM COATINGS USING FUNCTIONALLY ACTIVE MIXTURES

Sereda D.B.*, Kruglyak I.V., Sereda B.P.

Dnipro State Technical University, Kamenskoe, Ukraine,
*Corresponding author: seredabp@ukr.net

Abstract. *The purpose of our research is to obtain wear-resistant chrome coatings on carbon steels under non-stationary temperature conditions using functionally active powder mixtures, which allows reducing the chemical-thermal treatment time from 6-8 hours to 1 hour. The scientific novelty of the work lies in the original use of thermodynamic analysis to determine the composition of the gas phase formed during chemical-thermal treatment with functionally active charges, which made it possible to optimize the concentration of ammonium compounds for boron-alloyed chrome surface and predict its physical and mechanical characteristics. The practical significance of the developed technology is to increase the wear resistance of chrome coatings on steels with a ferrite-pearlite structure, which ensures their effective use under dynamic and impact loads. The proposed method opens up new opportunities for the creation of highly effective protective coatings for industrial applications. Optical microscopy (Neophot-32) and scanning electron microscopy (REM-106i) were used to study the microstructure and phase composition of the coatings. Tribotechnical tests were carried out on friction installations SMT-1 and MT-5. The composition of the gas medium formed during the chemical heat treatment was determined by thermodynamic modeling, and the optimization of the component composition of the charge materials was carried out using the methods of mathematical planning of experiments with the optimization criterion in the form of wear resistance of the boron-alloyed chrome surface. As a result, it was found that the addition of boron-containing components and ammonium gas transport reagents to the powder charge composition contributes to the generation of gaseous compounds and condensed phases. The proposed functionally active mixtures ensure the formation of protective chromium layers up to 150 μm thick within 15-60 minutes.*

Keywords: carbon steel, chromium plating, alloying, boron, protective coating, charge, thermodynamics, wear resistance.

1. Introduction

Modern materials science focuses on improving the performance of steels by applying chrome coatings, including boron-alloyed ones. One of the most promising methods is laser alloying of steel surfaces with chromium and boron, which produces coatings with high microhardness and corrosion resistance. Studies have shown that the use of a mixture of chromium and boron in different proportions during laser treatment contributes to the formation of coatings with a microhardness of 900 HV0.05 to 1300 HV0.005, depending on the laser treatment parameters [1]

Another approach involves the use of diffusion saturation of steel with boron and chromium. In particular, the study of the effect of chromium as a diffusion additive during boronizing of AISI 4140 steel showed that the formation of mixed boride phases, such as FeCrB, contributes to a significant increase in the

corrosion resistance of the coating. Evaluation by electrochemical impedance spectroscopy confirmed the improvement of the corrosion characteristics of boron-chromated samples compared to boron-only samples [2,3]. Boron is one of the most effective elements for increasing the hardness and wear resistance of steels. It forms solid boride phases (e.g., Fe_2B) that have high microhardness (up to 2000 HV) and excellent resistance to abrasive wear. Boron alloying is usually carried out using thermodiffusion methods such as boronizing in powder media or electrolytic boronizing. The resulting boride layers are characterized by considerable thickness (up to 150-200 microns) and high adhesion to the base metal [4,5].

Chrome plating is a classic method of applying protective coatings that provide high wear and corrosion resistance. Chrome coatings can be produced by electroplating or chemical deposition methods. The main advantages of chrome layers are high hardness (up to 1000-1200 HV), excellent corrosion resistance due to the formation of passive oxide films Cr_2O_3, and the ability to self-heal in case of surface damage [6,7].

The combination of boron and chrome plating is a promising area for creating multilayer coatings that combine the high wear resistance of boride layers with the corrosion resistance of chrome plated coatings. Such coatings are often called “hybrid” or “multifunctional”. Galvanic chrome plating is carried out in baths with chromic acid electrolytes, where the cathodic process is controlled by the deposition of metallic chromium. Process parameters such as temperature, electrolyte concentration and current density have a significant impact on the quality of the coating [8].

Researches [9] have shown that the application of a chromium layer on a boron surface significantly reduces the porosity of boride layers, which increases their corrosion resistance. The authors also noted that the optimal thickness of the chromium coating is 20-30 microns, which ensures maximum adhesion to the boride layer and a minimum number of defects. Hybrid coatings demonstrate high resistance to adhesive wear and contact fatigue. Research [10] found that the combination of boron and chromium plating provides a synergistic effect that significantly improves the wear and corrosion resistance of steels. The authors emphasized the importance of controlling process parameters to reduce internal stresses in coatings.

The use of electron beam surfacing of boron on chromium-nickel steels can increase their resistance to water-jet wear. The formation of a coating with densely arranged borides, mainly Fe_2B, increases the water-abrasive strength of steel by 1.5-2 times [11]. It is also worth noting that laser remelting of diffusion boron-chromium layers on 145Cr6 tool steel leads to the formation of zones with eutectic structures of boron and chromium, which improves the microhardness and wear resistance of surface layers [12].

Despite their numerous advantages, combined coatings have a number of problems that require further research. One of the key tasks is to control the porosity of boride layers before applying chromium, as excessive porosity can adversely affect the performance of the coating. In addition, an important aspect is to ensure the adhesion of the chrome coating to the boride layer, as strong adhesion between the layers is the key to the durability and reliability of the combined coating. Another issue that requires attention is the optimization of process parameters to reduce internal stresses in the coatings, which can lead to deformation or material failure during operation. Thus, overcoming these difficulties is an important step towards creating effective and reliable combined coatings.

The application of chrome coatings on boron-alloyed steels is a promising area for improving the service characteristics of steels. Hybrid coatings combine high wear resistance, corrosion resistance and mechanical strength, making them suitable for use in high-stress and aggressive environments. Further technology improvements and optimization of process parameters will expand the scope of such coatings. Increasing the durability and performance of steel materials is possible through the application of hard coatings that serve as protective layers. Such coatings modify the surface characteristics of the base material, giving it increased chemical resistance, increased hardness and reduced wear rates. Traditional methods of surface hardening are often characterized by significant energy consumption and process duration, which limits their practical application. In this context, the development of innovative chemical-thermal treatment technologies that allow controlling the composition and structure of protective coatings, providing the required performance parameters while minimizing the formation time, is a relevant area for Ukraine [13,14]. Particular attention is drawn to coatings formed under non-stationary thermal conditions, which exhibit high functionality due to the complex interaction of gas-phase deposition mechanisms and intense diffusion mass transfer. The formation of such coatings is based on the synergistic combination of two key processes: the formation of a film structure induced by gas-phase reactions and the formation of wide transient diffusion zones characteristic of diffusion saturation methods. This approach makes it possible to obtain materials with improved physical and chemical characteristics that exceed those of traditional coatings, which makes them promising for use under high mechanical loads [15].

2. Materials and methods of research

For the formation of protective coatings on samples from 45 and 40X steels we using functionally active (FA) powder mixtures included such components as chromium component (CC), boron, aluminum oxide, aluminum, ammonium fluoride, and ammonium iodine. The choice of the optimal powder fraction was based on preliminary experimental studies, which showed that particle sizes in the range of 100–120 μm are most effective for obtaining wear-resistant coatings and ensuring maximum completeness of chemical reactions. This range provides an optimal balance between the activity of the reagents and their processability for diffusion processes.

The process of forming protective coatings using functionally active charges was carried out on a specially designed experimental and industrial installation. The design of this unit was developed to meet modern requirements for process accuracy and safety. The unit integrates reaction equipment, a system for monitoring and controlling key process parameters (temperature, pressure and time), as well as a comprehensive gas cleaning system that ensures process safety and environmental friendliness. This approach made it possible to obtain coatings with high performance characteristics while minimizing the negative impact on the environment [16].

The evaluation of structural and phase changes in titanium-doped chrome coatings was carried out using optical and electron microscopy methods. A Neophot-32 optical microscope and a REM-106i scanning electron microscope were used to visualize the microstructure. To contrast the microstructure of the coatings obtained on the basis of steels, a 3% ethanol solution of picric acid in ethyl alcohol was used [17]. This method provided a clear visualization of the morphological features of the coatings, which made it possible to conduct a detailed analysis of their structure and identify characteristic defects.

X-ray structural analysis was used to analyze the phase composition of the diffusion zone on samples measuring 25×10×5 mm. To study the phase composition of the coatings, a DRO-3M X-ray machine was used in conjunction with a computer complex running the ARFA program. The tube emitted radiation with copper and cobalt anodes. The detector rotation speed was 1 deg/min in the angle range $2\theta = 15\text{-}163°$.

Wear resistance testing on the SMT-1 friction machine under conditions of limiting sliding friction with lubrication using automotive tractor oil according to the roller-block scheme, at a counterbody (roller) rotation speed of 500 rpm. The counter body was made of U8A steel with subsequent hardening and low tempering to a hardness of 61...63 HRC. The load on the sample was: P = 500 H.

Thermodynamic modeling of chemical transformations in the process of obtaining chrome coatings using functionally active charges included the calculation of the equilibrium composition of reaction products using the TERRA software package. This made it possible to predict possible phase transitions and assess the effect of temperature conditions on the formation of coatings [18,19]. To optimize the composition of powdered functionally active charges that allow obtaining the required coating thickness and high wear resistance, mathematical experiment planning methods were used. The study used a 3-factor, 3-level compositional asymmetric plan of the second order, which allowed us to systematically assess the effect of key parameters such as temperature, process duration, and reagent concentration on the characteristics of the resulting coatings [20]. This comprehensive approach to the study and optimization of coating formation processes not only improved their quality but also significantly reduced the time and cost of their manufacture, which is an important factor for industrial applications. In addition, the analysis of the results confirmed the possibility of obtaining coatings with improved physical and mechanical characteristics, which makes them promising for use under high mechanical and corrosion loads.

3. Results and discussion

Thermodynamic modeling of chemical processes entails a comprehensive assessment of the equilibrium state of a system that is treated as a quasi-isolated material domain. Within this framework, the system’s interaction with the external environment is constrained to energy and heat exchange only. The determination of thermodynamic equilibrium for arbitrary multi-component systems involves calculating the state variables and equilibrium parameters by minimizing the Gibbs free energy (G) under isobaric-isothermal conditions or, alternatively, by maximizing the system's entropy (S). This method takes into account the full set of potentially stable chemical species present in the system, providing a highly accurate prediction of the system’s chemical and phase composition under specific thermodynamic constraints.

In scenarios characterized by non-stationary temperature regimes, the kinetic behavior of chemical transformations is governed by both the thermal gradient and the diffusion mechanisms present within the system. It is generally assumed that during the thermal ramp-up phase, diffusion limitations in the gas phase are negligible, and the temporal rate of temperature change remains lower than that of gas-phase chemical reactions. This condition enables the presumption that a quasi-equilibrium composition is achieved at each discrete temperature interval. By performing calculations of equilibrium product distributions across a spectrum of temperatures, it becomes feasible to monitor the evolving chemical profile of the system, which is particularly advantageous in analyzing complex reaction pathways involving multiple intermediate steps influenced by both thermodynamics and kinetics.

However, the feasibility of utilizing combustion synthesis techniques in practical applications is constrained by the presence of threshold temperatures required for stable propagation of the combustion wave. These boundaries define the minimum thermal conditions necessary for reaction initiation and sustained front advancement. Failure to meet these thresholds can result in partial reaction inhibition or uncontrolled front propagation, thereby compromising process reliability. Consequently, precise identification of critical temperature limits and strategic optimization of operational parameters are essential to ensure both the functional efficiency and the thermal safety of combustion-based synthesis methods.

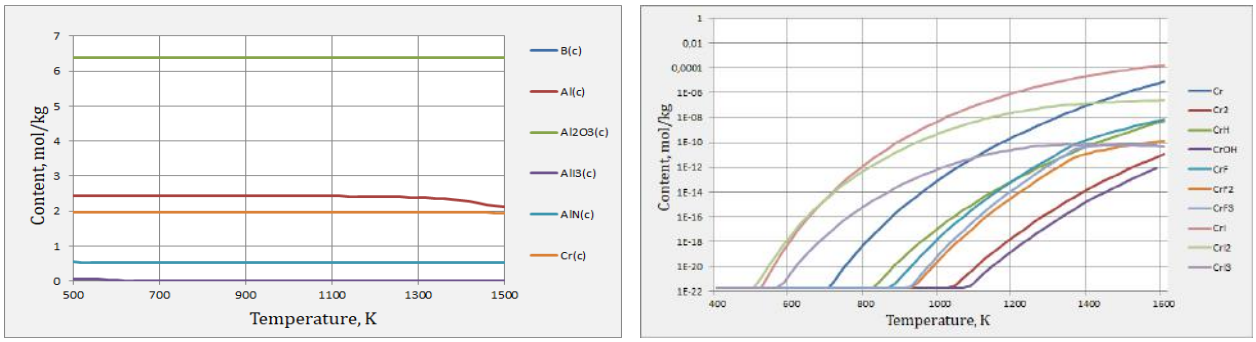

a) b)

Fig.1. Content of condensed products (a) and gaseous chromium compounds (b) in the reactor for the Cr-B system

Thermodynamic modeling, combined with the analysis of kinetic mechanisms, serves as a powerful tool for not only forecasting the outcomes of chemical reactions but also for optimizing the process parameters of synthesis technologies. This predictive capability is particularly valuable in the design and development of advanced materials, as it enables a substantial reduction in both the duration and financial investment typically associated with experimental research. Furthermore, the approach provides a reliable means of accurately estimating the physicochemical properties of final products, thereby facilitating more efficient process control and quality assurance. Unlike conventional combustion synthesis, which is constrained by the need for strict control over thermal conditions to ensure stable reaction propagation, thermally-induced spontaneous combustion offers enhanced flexibility in process adjustment. Specifically, the intentional dilution of the reactive powder mixture with inert additives—up to 45–50 wt.%—allows for effective modulation of the peak process temperature, thereby tailoring it to meet the requirements of particular technological applications.

As the system temperature increases, there is a notable shift in the product distribution, characterized by a rising fraction of gaseous products alongside the concurrent release of condensed species. Within the temperature interval of 400–1600 K, a progressive decline in the condensed phase content is observed. This phenomenon is largely attributed to the thermal evaporation of auxiliary materials or carriers integrated into the reactive system. Notably, when the temperature exceeds 800 K, a series of decomposition reactions are initiated, resulting in the evolution of secondary gaseous products and a pronounced increase in the overall molecular count of the gas phase (fig 1, 2). A thermodynamic system is conceptually defined as a physically bounded region of matter that exchanges only heat and mechanical work with its surroundings. Employing modern thermodynamic simulation techniques enables a rigorous, quantitative prediction of the behavior of complex heterogeneous, multi-phase, and multi-component systems across broad temperature and pressure ranges. Such models incorporate the influence of chemical equilibria and phase transitions, making them

indispensable for detailed thermochemical assessments. These methods significantly improve the efficiency of high-temperature process design, assist in the evaluation of interaction outcomes, and substantially decrease the dependence on repetitive empirical experimentation.

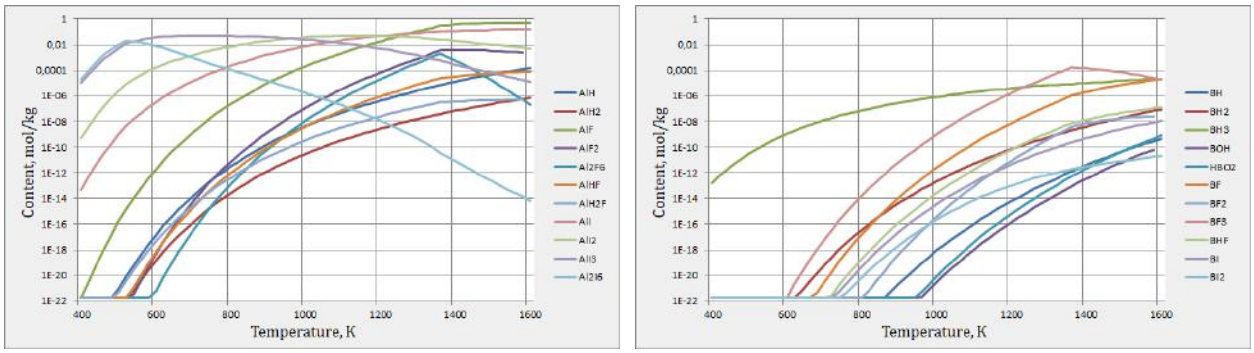

a) b)

Fig.2. Content of gaseous aluminum (a) and boron (b) compounds for the system Cr-B

Equilibrium calculations for arbitrary systems—encompassing all relevant thermodynamic parameters, physical properties, and the complete chemical and phase composition—are typically performed by minimizing the Gibbs free energy (at constant pressure and temperature) or by maximizing the system's entropy. This comprehensive approach ensures highly accurate forecasts of system behavior under prescribed environmental conditions. At temperatures exceeding 800 K, the relative amount of condensed phase products becomes nearly constant, which suggests that within the temperature range of 800–1600 K, chemical transformations occur without a significant change in the total molecular count of the system. This behavior is indicative of reaction mechanisms that predominantly involve condensed-phase dynamics, such as decomposition, disproportionation, and solid–substrate-mediated exchange reactions. These types of processes typically proceed without introducing additional gaseous species into the system, thereby maintaining molecular balance.

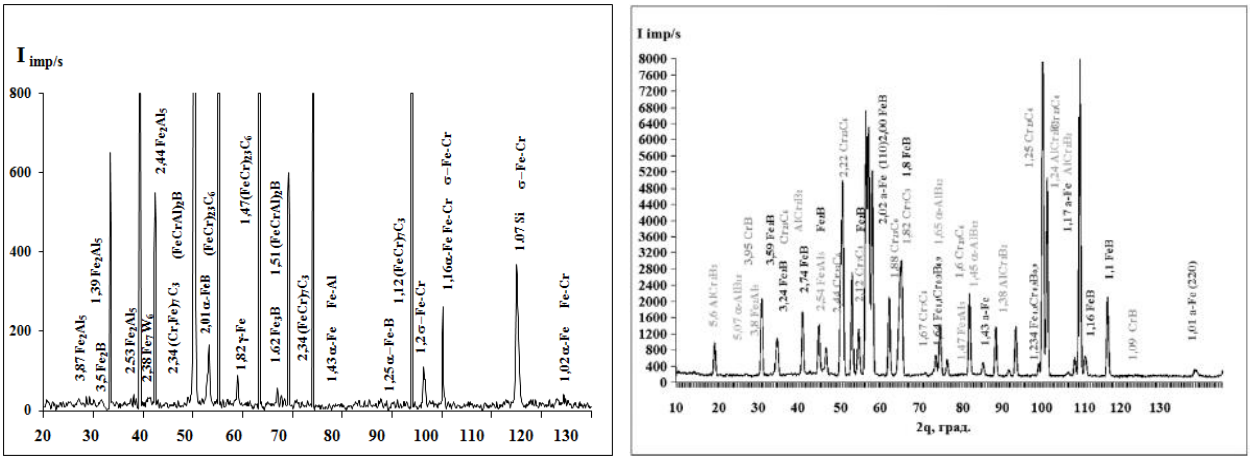

a) b)

Fig. 3. Diffraction pattern of a sample made of 45 steel (a) and 40X (b) with a protective chromium coating doped with boron

Such transformations often represent fundamental pathways for the chemical transport of elements within reactive media, especially in high-temperature powder metallurgy and self-propagating synthesis systems. The stabilization of the condensed phase in this regime also implies that the system has reached a thermodynamically favorable configuration, where the nature of chemical bonding and the structural stability of intermediate or final solid products become the dominant factors influencing phase evolution. Depending

on the amount of boron and ammonium gas transport agents, gaseous compounds (AlH, AlH_2 , AlF AlF_2 , Al_2 F6, AlHF, AlH_2 F, AlI, AlI_2 , AlI_3 , Al_2 I_6 , Cr, Cr_2 , CrH, CrOH, CrF, CrF_2 , CrF_3 , CrI, CrI_2 , CrI_3 , BH, BH_2 , BH_3, BOH, HBO_2 , BF, BF_2, BF_3, BHF BI, BI_2) and condensed phases (Al(c), B(c), Al2O3(c), AlI_3 (c), AlN(c), Cr(c)).

The task of the mathematical planning of the experiment was to study the effect of the technological mode of processing and the composition of functionally active charges on the wear resistance of protective coatings in order to optimize the mode of thermal spontaneous combustion and select the optimal composition of the powder charge.

Table 1. Experiment planning matrix

Characteristic	Factors		
	CC %, wt.	B %, wt.	Al %, wt.
Code	X_3	X_2	X_1
Basic level	20	12	17
Variation interval	5	4	5
The lower level	15	8	12
The upper level	25	16	22

Wear parameter (ΔI) was evaluated by measuring the mass loss of a steel 50 specimen, upon which the coating was deposited under process conditions defined by a peak temperature *tp* = 1100°C and an isothermal holding time τ = 30 min. The selection of both the baseline values and the variation intervals of the technological parameters was guided by empirical data, which established that the inclusion of less than 10 wt.% of chromium does not yield coatings with the requisite mechanical and physical performance. Consequently, the threshold value of chromium content was set to ensure structural integrity and functionality of the protective layer.

By analyzing the evolution of characteristic temperature values during processing under non-isothermal conditions, the optimal proportion of the chromium-containing component was empirically determined. Additionally, aluminum oxide (Al_2O_3) was employed as an inert ballast phase to ensure a stoichiometric completion of the powdered functional mixture. This approach guarantees the reproducibility and thermal stability of the coating formation process by maintaining a controlled heat balance and phase distribution.

As a result of the conducted investigations, a regression model was derived that quantitatively describes the influence of technological parameters and charge composition on the resulting structural, mechanical, and service properties of the coatings. The empirical model is expressed by the following equation:

$$\Delta I = 72{,}711 - 0{,}4X_1 - 1{,}1X_2 - 0{,}1X_3 + 0{,}1111X_1^2 + 5{,}6111X_2^2 - 5{,}3889X_3^2 - 5{,}5X_1X_3 + 0{,}25X_2X_3$$

This expression enables a detailed evaluation of the contribution of individual factors and their mutual interactions to the overall wear resistance and performance of the coating. The inclusion of quadratic terms and cross-factor interaction components significantly enhances the fidelity of the model by capturing nonlinearities inherent in real thermochemical systems.

The effectiveness of thermodynamic and statistical modeling for predictive analysis and optimization is thus convincingly demonstrated. This methodology facilitates the rational design of novel functional coatings by minimizing experimental effort and expediting process development. To visualize the influence of each factor on wear resistance, a set of three-dimensional response surface plots was constructed (fig. 4), enabling intuitive analysis and informed decision-making in material selection and process tuning.

Drawing upon comprehensive thermodynamic assessments and phase composition analyses of boron-enriched chromium-based protective layers, a detailed physicochemical model has been developed to describe the formation mechanism of such coatings under conditions of thermal self-propagating combustion of functionally active charges.

Stage 1. The process initiates with a steady temperature rise, during which the steel substrate is subjected to thermal exposure. As the temperature surpasses threshold values, the decomposition of volatile gas transport agents—specifically ammonium fluoride (NH_4F) and ammonium iodine (NH_4I)—is triggered. This decomposition results in the generation of chemically active species that will subsequently contribute to halide-mediated transport processes.

Stage 2. A self-sustaining combustion reaction of the functional powder blend is ignited, releasing a substantial amount of thermal energy. This exothermic reaction causes further elevation of the system temperature and leads to the formation of a halide-rich gaseous phase. The primary gaseous products at this stage include chromium and aluminum halides such as CrF, CrF_2, CrF_4, AlI, AlI_2, AlI_3, and volatile boron species like BF_3. These volatile halides serve as key agents in transporting the coating-forming elements toward the substrate.

Stage 3. The generated thermal energy begins to dissipate, primarily through conduction into the steel substrate, causing the local temperature to decrease toward the designed steady-state value. Under these thermal conditions, the formation of a chromium-, aluminum-, and boron-doped α-solid solution initiates, serving as the structural basis for the protective layer.

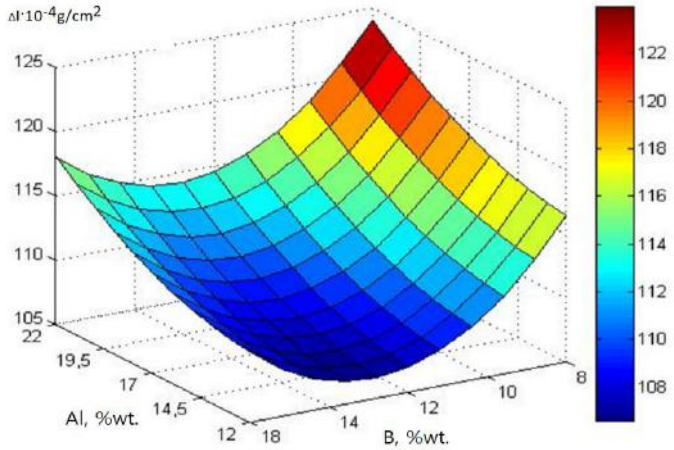

Fig.4. Influence of boron and aluminum content on the wear resistance of coatings

Stage 4. This stage is characterized by active interdiffusion processes. Thermally activated atoms of Cr, Al and B, begin to diffuse into the iron matrix of the steel component. As a result, a multicomponent solid solution enriched with these elements is formed, along with complex alloyed intermetallic phases A continuous and directed diffusion flux is established, promoting the development of thick, uniform coatings. Compared to conventional isothermal processes, coatings formed under transient thermal regimes exhibit significantly increased thickness. This is attributed to the fine-grained, submicron-block microstructure of austenite that forms under rapid heating. The austenitic matrix, developed under non-equilibrium conditions, features a high dislocation density localized at grain boundaries and a branched intergranular structure, enhancing the material's diffusion responsiveness. This stage is the most prolonged, extending up to 60 minutes, during which the bulk of the coating is synthesized.

Stage 5. In the final stage, the system undergoes cooling, and the temperature of the functionally active charge drops. As a consequence, the diffusion fluxes weaken, and the rate of coating formation diminishes. The protective layer solidifies with a stabilized phase composition comprising: $(Fe,Cr)_{23}(C,B)_6$, $(Fe,Cr)_7(C,B)_3$, (Fe,Cr,Al)B, $(Fe,Cr,Al)_2B$. Metallographic and X-ray spectral analysis of boron-doped chrome protective coatings obtained on 45 and 40X steel samples (fig. 5) showed that the following phases were formed on the surface: $(Fe,Cr)_{23}(C,B)_6$, $(Fe,Cr)_7(C,B)_3$, (Fe,Cr,Al)B $(Fe,Cr,Al)_2B$, and zones of α-solid solution of Cr, Al, B in Fe. Boron-modified chromium-based protective coatings deposited on steel grade 45 have gained substantial relevance in tribological applications due to their pronounced ability to reduce friction and significantly enhance resistance to wear. These coatings are especially valued in engineering systems subjected to intense mechanical contact, where surface durability and lubrication retention are crucial. As such, a key aspect of current research lies in assessing the wear resistance of steel 45 substrates following surface modification with boron-containing chromium coatings.

Experimental investigations conducted under dry sliding friction conditions using the SMT-1 tribometer revealed a pronounced enhancement in wear resistance when coatings were synthesized via thermal self-propagating modes using functionally active powder mixtures. Specifically, the coatings formed under dynamic temperature regimes demonstrated wear resistance approximately 1,4–1,6 times greater than their counterparts fabricated using conventional isothermal processes (fig. 6). This performance enhancement is attributed primarily to the superior microhardness of the thermally activated coatings.

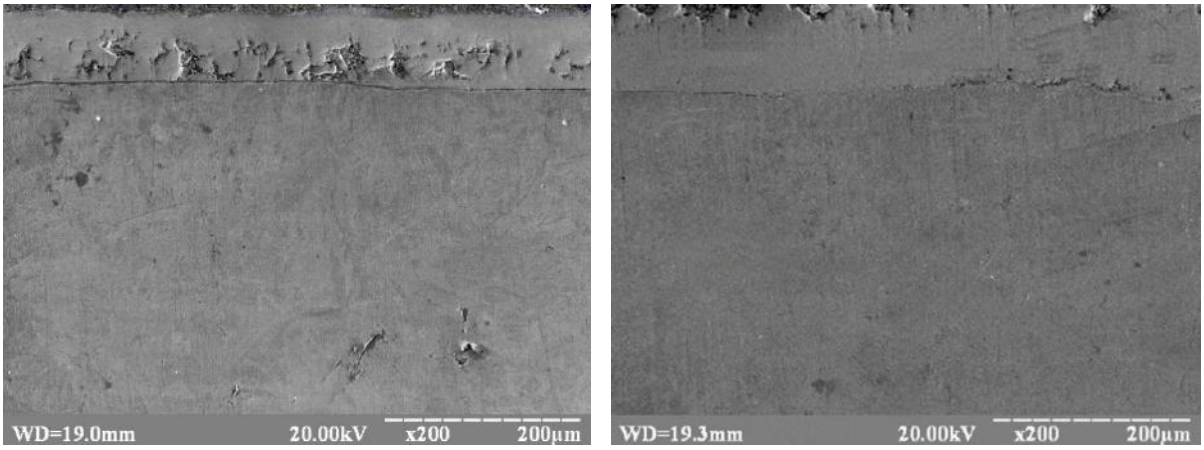

a) b)

Fig. 5. Boron-alloyed, chromium coatings on steel 40X(a) and 45 (b) (tp - 1050 ^{o}C, τ = 30 min).

Quantitatively, the microhardness values (measured under a 100 g load) for boron-doped coatings produced under steady-state thermal conditions were observed in the range of H100 = 15,000–15,500 MPa. In contrast, coatings formed under non-isothermal conditions utilizing exothermically reactive powder blends exhibited significantly higher microhardness, reaching values between H100 = 16,500–17,500 MPa. This substantial increase in surface hardness is one of the main factors contributing to the improved wear performance of the coatings. The increase in microhardness for coatings obtained using functionally active mixtures is due to an increase in the amount of chromium, aluminum, and boron alloying elements by 5-11% compared to known coatings obtained under isothermal conditions.

It is important to note, however, that although a clear trend correlating increased surface hardness with enhanced wear resistance exists, the relationship is not strictly linear. The wear behavior of metallic materials is inherently complex and influenced by numerous interacting variables, including contact pressure, sliding velocity, lubrication conditions, and surface topography. As a result, microhardness alone cannot fully account for all variations in wear behavior.

From a mechanistic perspective, wear under sliding friction conditions predominantly involves elastic and plastic deformation of the surface layer, along with subsurface fatigue processes that eventually lead to material removal. These processes manifest through microcrack initiation, propagation, and detachment of surface fragments. In contrast, when subjected to impact-dynamic loading, different wear mechanisms dominate, including brittle fracture, chipping, shearing of individual particles, and localized plastic deformation. These distinctions underscore the necessity of tailoring coating composition and structure to the specific mechanical and tribological demands of the intended application.

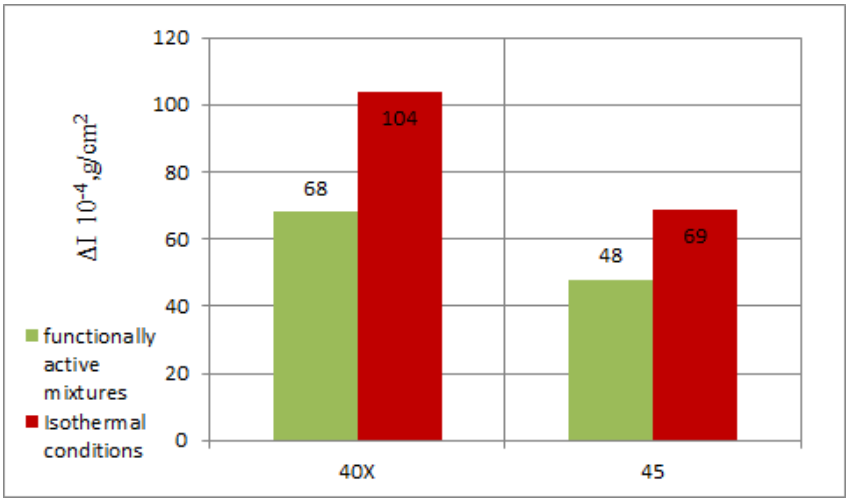

Fig.6. Comparative tribological tests on steel 40X and 45.

Consequently, the choice of coating technique and regime must be guided by a comprehensive understanding of the interaction between the operational environment and the mechanical behavior of the surface layer. The demonstrated ability of thermally generated boron-alloyed chromium coatings to resist wear under severe conditions positions this approach as highly promising for extending the service life of components in high-load, high-friction environments. Thus, the use of functionally active charges for the formation of boron-doped chromium coatings is a promising direction for improving the wear resistance of steel materials. The obtained results confirm the possibility of a significant improvement in the performance characteristics of steel 45 by optimizing the technological parameters and composition of coatings.

4. Conclusions

As a result of the research, the influence of boron alloying on the wear resistance of chrome coatings obtained using functionally active charges was determined. The effectiveness of the developed technology for applying multicomponent chrome coatings has been confirmed by both experimental and theoretical methods. The coatings formed under non-stationary temperature conditions demonstrated high characteristics in terms of wear resistance and thermal stability. A significant improvement in physical and mechanical properties was achieved on steel samples with a carbon content of 0.5% compared to traditional coatings, which was manifested in a reduction in wear under impact and dynamic loading. The amount of alloying compounds also depends on the initial composition of the material. Calculations of the thermodynamic equilibrium of reaction products and kinetic laws confirmed the possibility of forming coatings with specified properties at different temperature conditions. In the powdered, functionally active charge, gaseous compounds are formed (AlH, AlH_2 , AlF AlF_2 , Al_2 F6, AlHF, AlH_2 F, AlI, AlI_2 , AlI_3 , Al_2 I_6 , Cr, Cr_2 , CrH, CrOH, CrF, CrF_2 , CrF_3 , CrI, CrI_2 , CrI_3 , BH, BH_2 , BH_3, BOH, HBO_2 , BF, BF_2, BF_3, BHF BI, BI_2) and condensed phases (Al(c), B(c), Al2O3(c), AlI_3 (c), AlN(c), Cr(c)). The modeling showed that the selected powder mixtures and technological parameters ensure the effective formation of protective layers. Metallographic analysis confirmed the high quality and homogeneity of the coatings, their good adhesion to the steel base, and resistance to cracks and defects. According to the results of metallographic and X-ray spectral analysis, it was found that the following phases are formed on the surface of the chrome coatings of boron-doped coatings: $(Fe,Cr)_{2\ 3}$ C_6 , $(Fe,Cr)_7$ C_3 , Fe_3 Al, $(Fe,Cr,Al)_2$ B, as well as zones of α-solid solution of Cr, Al, B in Fe. During tests under sliding friction conditions on the friction machine SMT-1, it was found that the wear resistance of coatings obtained using functionally active charges was 1.9-2.1 times higher than that of coatings formed under isothermal conditions. A comparative analysis of wear resistance during tests on the friction machine MT-5 (under shock-dynamic loading) revealed that coatings obtained using functionally active charges have a 1.4-1.6 times lower wear than coatings obtained under isothermal conditions.

Conflict of interest statement

The authors declare that they have no conflict of interest in relation to this research, whether financial, personal, authorship or otherwise, that could affect the research and its results presented in this paper.

CRediT author statement

Sereda D.B.: Conceptualization, Data Curation; **Kruglyak I.V. -** Writing Original Draft, Methodology; **Sereda B.P.**: Investigation, Writing Review & Editing, Supervision. The final manuscript was read and approved by all authors.

References

1 Bartkowska A. (2021) Characteristics of Cr-B Coatings Produced on Vanadis® 6 Tool Steel Using Laser Processing. *Materials*, 14(10), 2621. https://doi.org/10.3390/ma14102621

2 Zagkliveris D. I., Mavropoulos A., Ntovinos E., Triantafyllidis G. K. (2020) The influence of chromium as a diffusive additive in the boronizing treatment of AISI 4140 steel on the corrosion resistance of the coating evaluated by Electrochemical Impedance Spectroscopy (EIS). *MATEC Web of Conferences*, 318, 01040. https://doi.org/10.1051/matecconf/202031801040

3 Masuda K.; Ishihara S.; Shibata H.; Sakamoto Y.; Oguma N.; Iwasaki M. (2024) Effect of surface coating on fatigue life and fatigue crack growth behavior of AISI D2 tool steel. *Int. J. Fatigue*, 183, 108230. https://doi.org/10.1016/j.ijfatigue .2024.108230

4 Muthiah P., Palaniappan G., Raj S. (2022) Boriding of steels: Improvement of mechanical properties – A review. *High Temperature Material Processes: An International Quarterly of High-Technology Plasma Processes*, 26 (2), 1–15. https://doi.org/10.1615/HighTempMatProc.2022041805

5 Xie Y., Medvedovski E., Joyce L., Simonton D., Frishholz E. (2024) Assessing boronized and aluminized thermal diffusion coatings in molten chloride salt and molten sodium environments. *Surface and Coatings Technology*, 487, 130973. https://doi.org/10.2139/ssrn. 4775692

6 Zhang Z., Wang L., Li Q. (2019) High-performance coatings for industrial applications. *Journal of Coating Technology*, 21(5), 1024-1035. https://doi.org/10.1007/s11998-019-00264-1

7 Sereda B., Sereda D. (2021) High-performance chrome coatings to protect against wear and corrosion. *Steel Properties and Applications in Conjunction with Materials Science and Technology*. 39 – 41. https://doi.org/10.33313/280/005

8 Merlo A., Leonard G. (2021) Magnetron Sputtering vs. *Electrodeposition for Hard Chrome Coatings: A Comparison of Environmental and Economic Performances. Materials*, 14(14), 3823. https://doi.org/10.3390/ma14143823

9 Hu J., Zeng J., Yang Y., Yang X., Li H., Guo N. (2019) Microstructures and wear resistance of boron-chromium duplex-alloyed coatings prepared by a two-step pack cementation process. *Coatings*, 9 (9), 529. https://doi.org/10.3390/coatings9090529

10 Adamaszek K., Jurasz Z., Swadzba L., Grzesik Z. (2011) The influence of hybrid coatings on scaling-resistant properties of X33CrNiMn23-8 steel. *High Temperature Materials and Processes*, 26 (2), 115–124. https://doi.org/10.1515/HTMP.2007.26.2.115

11 Bushueva E.G., Grinberg B.E., Bataev V.A., Drobyaz E.A. (2019) Raising the Resistance of Chromium-Nickel Steel to Hydroabrasive Wear by Non-Vacuum Electron-Beam Cladding with Boron. *Metal Science and Heat Treatment*, 60, 641–644. https://doi.org/10.1007/s11041-019-00331-3

12 Bartkowska A., Młynarczak A. (2021) Microstructural and Mechanical Properties of B-Cr Coatings Formed on 145Cr6 Tool Steel by Laser Remelting of Diffusion Borochromized Layer Using Diode Laser. *Coatings*, 11(5), 608. https://doi.org/10.3390/coatings1105060

13 Sereda B., Prolomov A., Sereda D. (2024) Corrosion Resistance of Zinc Coatings Obtained by Technology Using Complex Functionally Active Charges in Chemical Environments. *Proceeding of the Conf. Steel Properties & Applications in conjunction with Materials Science & Technology*. https://doi.org/10.33313/282/012

14 Zhang X., Wang,Y., Li J., Liu H. (2023) Development of SHS coatings for high-temperature applications. *Journal of Materials Science*. https://doi.org/10.1007/s10853-023-07456-9.

15 Sereda B., Sereda D., Kryhliyak I., Kryhliyak D. (2023) Modification of the surface of copper alloys with aluminum in the conditions of self-propagating high- temperature synthesis. *Problems of Atomic Science and Technology*, 2, 130 – 133. https://doi.org/10.46813/2023-144-130.

16 Sereda B., Sereda D., Udod A., Baskevych O. (2024) Quantum mechanical model of interaction of charges of metal atoms during creation of chrome coatings. *Naukovyi Visnyk Natsionalnoho Hirnychoho Universytetu*, 6, 38 – 44 https://doi.org/10.33271/nvngu/2024-6/038

17 ASM International. Dossett J.L., Totten G. E. (Eds.). (2014). Heat Treating of Irons and Steels. ASM Handbook Vol. 4D. ASM International. https://doi.org/10.31399/asm.hb.v04d.9781627081689

18 Tosun I. (2015) *Thermodynamics: Principles and Applications*. World Scientific Publishing. ISBN 978-9814696937

19 Fleischer M. T. (2018) *Thermodynamics: Fundamentals and Applications for Chemical Engineers*. World Scientific Publishing. ISBN 978-1516526680

20 Montgomery D.C. (2017) *Design and Analysis of Experiments Arisona*, State University. Ninth Edition, John Wiley & Sons, New York, 640. ISBN 9781119299363

AUTHORS' INFORMATION

Sereda, Borys P. - Doctor of Technical Sciences, Professor, Director of the Research Center for Materials Science and Innovative Technologies, Head of the Department of Automobiles and Transportation and Logistics Systems, Academician of the Academy of MST, Dnipro State Technical University, Kamenskoe, Ukraine, Scopus Author ID: 26428911900; https://orcid.org/0000-0002-9518-381X; seredabp@ukr.net

Kruglyak, Irina B. - Doctor of Technical Sciences, Professor, Head of the Department of Industrial Mechanical Engineering, Dnipro State Technical University, Kamenskoe, Ukraine, Scopus Author ID: 35196308100; https://orcid.org/0000-0001-8872-6778; irina6878@ukr.net

Sereda, Dmytro B. - PhD, Associate Professor of the Department of Industrial Mechanical Engineering, Dnipro State Technical University, Kamenskoe, Ukraine, Scopus Author ID: 36667256600; https://orcid.org/0000-0003-4353-1365; etohardcore@gmail.com

EURASIAN PHYSICAL TECHNICAL JOURNAL

2025, Volume 22, No. 3 (53)

https://doi.org/10.31489/2025N3/24-35

Received: 02/05/2025 Revised: 21/08/2025 Accepted: 25/09/2025 Published online: 30/09/2025

Research Article

Open Access under the CC BY -NC-ND 4.0 license

UDC 53.043

EVALUATION OF THE APPLICATION EFFICIENCY OF MULTICOMPONENT CERAMICS AS PROTECTIVE SHIELDING AND THERMAL BARRIER MATERIALS

Kozlovskiy A.L.[1,2,3*], Borgekov D.B.[1,2], Tleulessova I.K.[1,2], Zhumazhanova A.T.[1], Moldabayeva G.Zh.[3], Burkhanov B.Zh.[4], Khametova A.A.[1,2]

[1] Laboratory of Solid State Physics, The Institute of Nuclear Physics, Almaty, Kazakhstan
[2] Engineering Profile Laboratory, L.N. Gumilyov Eurasian National University, Astana, Kazakhstan
[3] Department of Chemical Processes and Industrial Ecology, Satbayev University, Almaty, Kazakhstan
[4] Agrarian and Technical University named after Zhangir Khan, Uralsk, Kazakhstan
*Corresponding author: kozlovskiy.a@inp.kz

Abstract. *The paper presents the comparative analysis results of the shielding characteristics of multicomponent ceramics obtained by mixing TeO_2, CeO_2, WO_3, ZnO, Bi_2O_3 and ZrO_2 oxides in various molar ratios, enabling acquisition of ceramics with a variable phase composition. According to the results of X-ray phase analysis, the addition of ZrO_2 to the composition of composite ceramics leads to the formation of a monoclinic substitution phase $ZrCeO_2$. The contribution growth of the latter results in strength properties growth due to a change in the concentration of interphase boundaries in the composition of ceramics. During the tests conducted for resistance to thermal effects capable of leading to destabilization of the crystalline structure, it was established that an increase in the contribution of ZrO_2 in the composition of ceramics leads to an increase in resistance to thermally induced softening processes, and an increase in the stress resistance of ceramics during tests for thermal shock effects. During determination of the shielding characteristics of the studied ceramics, it was found that the formation of a stabilizing $ZrCeO_2$ phase in the composition of multicomponent ceramics leads to an elevation in the shielding efficiency, as well as the stability of the preservation of shielding characteristics as a result of long-term thermal effects and thermal shock tests. Moreover, the greatest increase in the efficiency of the measured parameters is observed in the case of assessment of thermal insulation characteristics. The increase in the latter is more than 2.5 times compared to non-stabilized ceramics, which do not contain inclusions in the form of the $ZrCeO_2$ phase.*

Keywords*:* composite multicomponent ceramics, shielding materials, thermal shock exposure, stabilization, doping

1. Introduction

Interest in the creation of highly effective shielding materials is primarily due to the need to reduce the negative impact of ionizing radiation on living organisms and microelectronic devices, as well as the search for alternative materials to replace traditional lead and tungsten protective shields, which are highly effective in shielding, but have a number of disadvantages, including toxicity during prolonged contact (for lead) and high cost of manufacture (for tungsten). In recent years, much attention in this area of research has been paid to assessment of the possibilities of creation of shielding protective materials based on composite ceramics. Its concept includes combination of the properties of various oxide compounds, variation of the ratio of which makes it possible to obtain various materials that have high strength indicators, resistance to external influences [1-3], including aggressive environments, and have high shielding characteristics comparable to

those of lead. Interest in composite multicomponent ceramics and amorphous-like glasses is primarily due to the possibility of the material density reduction by variation of the components in the composition while maintaining high shielding efficiency indicators, with the possibility of bringing the parameters to values close to the shielding parameters of lead. In most cases, the density of composite multicomponent ceramics is about 3 – 5 g/cm^3, while the density of lead is about 11.3 g/cm^3. The reduction of density by more than 2 – 2.5 times compared to lead while maintaining high values of shielding characteristics, as well as the non-toxicity of ceramics in contrast to lead, allows their consideration as one of the key parameters in the field of shielding protective materials applicable in the medical sector, aerospace and energy industries [4,5]. It should also be noted that interest in composite ceramics in the field of protection of microelectronic devices is due to the need to reduce weight and overall dimensions, which play a very important role in spacecraft, for which any kilogram of weight when launched into orbit requires a large amount of fuel resources. In addition to shielding characteristics, recently much attention in the creation of composite multi-component shielding ceramics or glasses has been paid to their strength and heat-insulating parameters. These values determine their applicability in extreme operating conditions, including high mechanical loads, long-term mechanical friction, thermal effects and sudden changes in operating temperature conditions [6,7]. Elevation of strength characteristics, as well as resistance to external influences, along with high shielding characteristics, is one of the key areas of research, for the implementation of which methods of doping with high-strength components are used. The addition of these to the composition of ceramics or glasses can initiate the formation of inclusions that have a reinforcing effect, the occurrence of which increases resistance to external influences [8,9]. This effect is based on the possibility of filling the intergranular space with impurity inclusions in the form of new phases, which leads to the creation of interphase boundaries that prevent the spread of microcracks under external influences, as well as inhibition of oxidation processes caused by the diffusion of oxygen into the sample under high-temperature exposure. In this case, the choice of stabilizing components is usually based not only on the possibilities of alteration of the strength characteristics, but also enhancement of the shielding efficiency due to changes in the overall value of Z_{eff} [10-13], which plays a very important role in determination of the shielding characteristics, especially in the case of shielding gamma quanta with energies up to 1 MeV, which are the most common type of gamma quanta, and also have high penetrating power [14-16].

The main aim of this study is to determine the prospects for using composite 1- x(TeO_2 – CeO_2 – WO_3 – ZnO – Bi_2O_3) – xZrO_2 ceramics as shielding materials by comparative analysis of shielding efficiency depending on the variation of the ratio of components in the composition, as well as to determine the influence of external influences on maintenance of the stability of shielding and thermal insulation characteristics [17,18]. At the same time, much attention in the work is paid to assessment of the prospects for using these composite ceramics not only as shielding materials, but also as high-strength thermal barrier coatings, interest in which is due to the field of heat-resistant materials used in extreme conditions. The combination of the obtained results made it possible to evaluate both the prospects for using the proposed composite ceramics as protective materials and to expand the general understanding of the variation of phase composition in composite ceramics due to the observed phase transformations caused by changes in the ratio of components [19,20].

2. Material and Methods

The variation of components in the ceramics was carried out by addition of ZrO_2 to the five-component mixture in a molar fraction from 0.05 M to 0.25 M. In this case, all the initial oxides were purchased from Sigma-Aldrich (St. Louis, Missouri, USA), the chemical purity of the oxide powders was about 99.95 %. The synthesis of x(TeO_2 – CeO_2 – WO_3 – ZnO – Bi_2O_3) – xZrO_2 ceramics was carried out by mechanochemical solid-phase milling of oxide components in different molar fractions, the variation of which is due to the addition of ZrO_2 to the composite during mixing. Grinding for the purpose of obtaining a uniform distribution of all components in the volume was carried out using a PULVERISETTE 6 classic line planetary mill (Fritsch, Berlin, Germany), the grinding speed was about 250 rpm, the grinding time was 30 minutes. After grinding, the samples were removed from the grinding cup (tungsten carbide), divided into equal parts and annealed in a muffle furnace at a temperature of about 1000 °C (the heating rate until the final set temperature was reached was 20 °C/min). Annealing was carried out for 5 hours, after which the samples cooled together with the furnace for 24 hours until the furnace chamber had completely cooled.

After sintering, the obtained powders were subjected to a phase composition study, the changes of which in this case were due to a variation in the ratio of components in the composition of ceramics when ZrO_2 was added to them. The study of phase changes that occurred as a result of thermal sintering was carried out using the X-ray phase analysis method, performed using a D8 Advance ECO X-ray diffractometer (Bruker, Germany). To assess the phase composition, the Diffrac EVA v.4.2 software was used, the application of which made it possible to determine with high accuracy (at least 0.1 wt. %) changes in the phase ratio in the composition, the establishment of which was carried out using the method of comparative analysis of the observed diffraction reflections with the data of the card values taken from the PDF-2 (2016) database. Tests of heat resistance (resistance of ceramics to thermal shock effects), including a sharp change in the temperature of impact on the samples studied, were carried out according to the standard method. It consisted of rapid heating (heating rate 50 °C/min) of the samples to a given temperature of 1000 °C, 1300 °C and 1500 °C, holding at this temperature for 30 minutes and then quickly removing it into the air, which leads to the creation of a sharp temperature gradient. To determine the effect of thermal shock effects on ceramic samples, as well as to establish the relationship between the addition of ZrO_2 to the composition on resistance to high-temperature degradation, measurements of the hardness and bending strength of the samples under study were carried out before and after a specified number of cyclic tests. The number of test cycles was at least 10, which made it possible to evaluate the resistance of ceramics to high-temperature degradation, as well as to determine its effect on the softening degree of ceramics. Experimental work was also carried out to identify the effect of high-temperature degradation on the preservation of thermal insulation properties, which included testing samples when heated on one side and assessing the thermal insulation temperature parameters by calculating the temperature difference on both sides. These experiments were carried out at a test temperature of 1500 °C, and the temperature difference was controlled using thermocouples.

The shielding performance of the ceramic samples was evaluated using a Cs^{137} gamma source (E_γ = 662 keV) and a detector placed 10 cm from the source. From the measured intensity changes with and without the ceramic shielding, the linear and mass attenuation coefficients as well as the half-value layer thickness were determined.

3. Results and discussion

One of the important criteria playing a key role in determination of the applicability potential of composite ceramics is their phase composition, the change of which directly depends on the conditions of ceramic synthesis. In most cases, during production of telluride composite materials, the phase composition is represented by an amorphous nature, caused by the melt of tellurium oxide, the content of which plays a very important role in determination of the shielding parameters. Moreover, in the case of addition of cerium dioxide and tungsten oxide to the composition of composite glasses, the melting point of which is significantly higher, as a rule, the phase composition of composite telluride materials is represented by a mixture of different phases, the variation of the weight contributions of which determines the key role both in the shielding characteristics and in the strength parameters.

The circular diagrams (see Figure 1) show the X-ray phase analysis of the studied $x(TeO_2 – CeO_2 – WO_3 – ZnO – Bi_2O_3) – xZrO_2$ ceramics with varying component ratios, reflecting the role of adding ZrO_2 in the phase formation processes in ceramics during thermal sintering. According to the presented X-ray phase analysis data, the dominant phase in the composition of composite ceramics is the cubic phase CeO_2, the weight contribution of which varies from 61 to 40.5 wt. % depending on the concentration of ZrO_2, the addition of which, as is evident from these changes in weight contributions, leads to the formation of the monoclinic $ZrCeO_2$ phase with a subsequent increase in the share of its weight contribution. The samples also contain inclusions in the form of the orthorhombic $ZnTeO_3$ phase, the monoclinic phase of zinc tungstate ($ZnWO_4$), and the monoclinic $Bi_2Te_4O_{11}$ phase, associated with phase transformations of oxides during their thermal sintering. The formation of the $ZrCeO_2$ phase when ZrO_2 is added to the composite ceramics is due to the processes of cationic substitution of zirconium by cerium, which leads to the formation of a substitution solid solution phase, while the selected conditions of thermal annealing at a temperature of 1000 °C do not allow the initiation of polymorphic transformation processes in ZrO_2, which also maintains the stability of the crystal structure. Thus, it is possible to make a general conclusion that the selected conditions of thermal sintering of ceramics at a temperature of 1000 °C do not lead to amorphization or vitrification of the crystalline structure. Also, the observed phase changes are associated with the processes

of structural transformations caused by the formation of the substitution $ZrCeO_2$ phase, with the addition of ZrO_2 with a monoclinic type of crystal lattice. Its change occurs due to the partial substitution of zirconium cations (Zr^{4+}) by cerium cations (Ce^{4+}), as a result of which there is an increase in this phase in the composition of ceramics, and a decrease in the weight contribution of the CeO_2 phase due to its partial transformation.

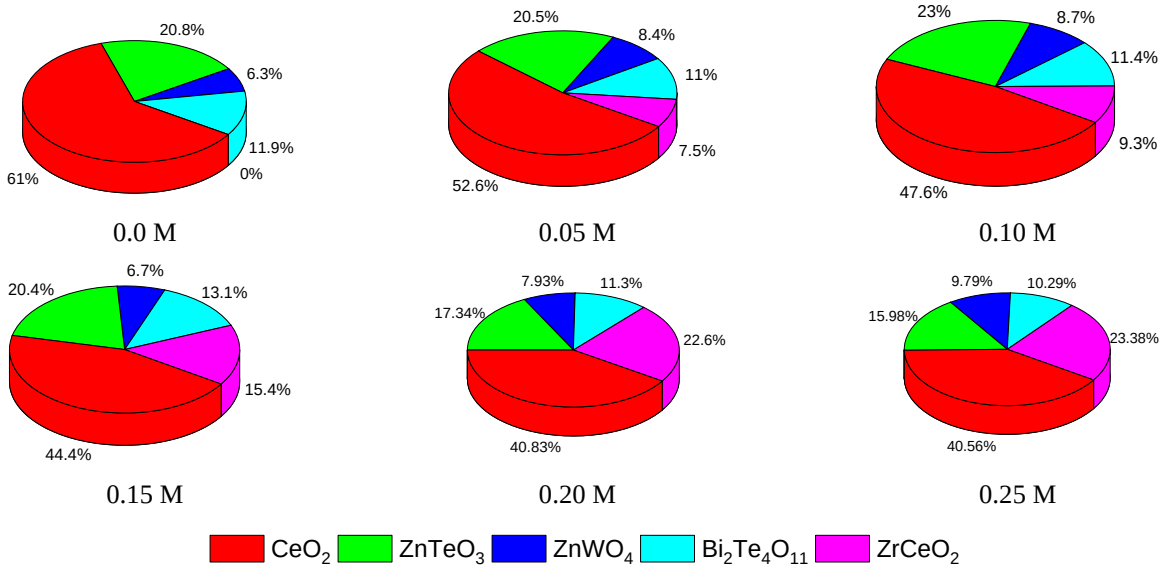

Fig.1. Results of X-ray phase analysis of the studied $x(TeO_2 – CeO_2 – WO_3 – ZnO – Bi_2O_3) – xZrO_2$ ceramics at varying ZrO_2 concentration

At the same time, the weight contributions of $ZnTeO_3$, $ZnWO_4$ and $Bi_2Te_4O_{11}$ in the composition of ceramics remain almost unchanged, and small variations in their weight contributions are due to the degree of manifestation of their diffraction reflexes on diffraction patterns, which affects the determination of the weight contribution. The formation of the zinc tungstate phase ($ZnWO_4$) in the composition of composite ceramics can contribute to an increase in the stability of both strength parameters and the accumulation of radiation damage, since it is known that tungstates have fairly high resistance to radiation exposure. In turn, the content of this phase in the composition of composite ceramics is stable regardless of the concentration of the ZrO_2 dopant, from which it can be concluded that the addition of a stabilizing dopant does not have a significant effect on its formation. Similar trends of small variations in weight contributions are also observed for the $ZnTeO_3$ and $Bi_2Te_4O_{11}$ phases, from which it can be concluded that the substitution processes occur in cerium dioxide. Some of the important parameters influencing the determination of the applicability potential of composite ceramics as protective or heat-insulating materials are their strength characteristics (hardness, bending strength), as well as maintenance of their stability under external influences, including a sharp change in temperature, the variation of which leads to the initialization of oxidation processes of the near-surface layer, leading to softening and destruction with subsequent embrittlement. In this case, determination of the resistance to external influences, including high-temperature ones, allows assessment of the possibilities of using composite ceramics during their operation in extreme conditions, the impact of which can result in destabilization of properties [21,22].

Figure 2 demonstrates the assessment results of changes in the values of hardness and bending strength determined during cyclic tests for heat resistance. The obtained dependences of changes in strength characteristics reflect the rate of degradation under high-temperature effects associated with temperature differences that initiate oxidation processes of samples due to a sharp change in the temperature gradient. The overall trend of the observed alterations in strength characteristics indicates a reduction in strength characteristics upon reaching a certain number of test cycles, from which it follows that oxidation processes have a cumulative effect associated with an increase in stress effects when the temperature of the sample changes. It should be noted that the addition of ZrO_2 to the composition of composite ceramics slows down the processes of destruction of strength characteristics, which can be due to the following factors. In the case of a sharp change in temperature, the resulting temperature gradient between the surface and internal layers

that are heated due to the effect of heating, the formation of thermal stresses occurs. At the same time, the presence of interphase boundaries can lead to uneven heating of samples due to low thermal conductivity coefficients, as well as differences in thermal expansion coefficients. The occurrence of thermal stresses in the near-surface layer with a sharp change in the exposure temperature (with rapid cooling) can lead to the formation of intergranular cracks, as well as extended intragranular cracks that arise along weakly bonded boundaries or defective inclusions, the presence of which is due to phase transformation processes.

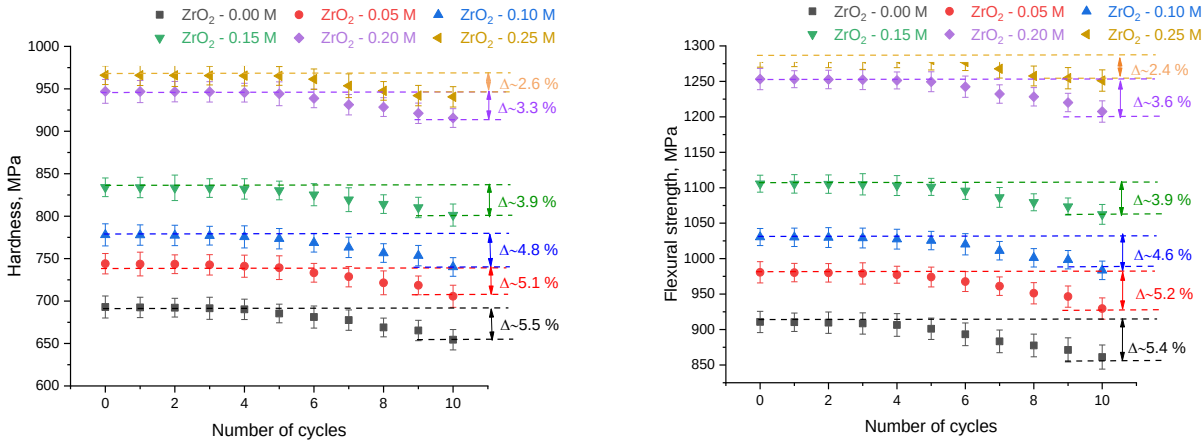

a) b)

Fig.2. Results of cyclic tests of composite ceramics, reflecting changes in strength properties under thermal shock exposure: a) results of changes in hardness; b) results of changes in bending strength

In this case, the emerging local redistribution of deformation stresses, the presence of which is associated with the processes of phase formation during sintering of ceramic samples, together with thermal stresses formed during a sharp change in the temperature gradient can lead to destabilization of the phase composition of ceramics. This is associated both with a change in the density of dislocations and microcracks in the near-surface layer, and the emergence of a gradient in the density of defects between the near-surface layer and the deep layers, which were subjected to less heating due to the low thermal conductivity of the samples. The formation of such a defect density gradient in combination with the generation of microcracks in the near-surface layer leads to destabilization of the surface, which in turn leads to a decrease in hardness and bending strength. In this case, effects associated with the formation of cavities in the damaged layer can also be observed, the occurrence of which occurs due to the deformation effect on the crystalline structure, as well as partial expulsion or destruction of individual grains from the near-surface layer, which in turn leads to surface erosion during long-term heat resistance tests. In the case of the formation of the $ZrCeO_2$ substitution phase in the composition of composite ceramics, the increase in the contribution of which, according to the presented measurement results, leads to an increase in the strength characteristics of the samples in the initial state (the observed change in hardness and bending strength with an increase in the weight contribution of the $ZrCeO_2$ substitution phase in the composition varies from 10 to 50 % compared to undoped ceramics). Such changes in the strength characteristics indicate that the change in the phase composition due to a change in the concentration of the ZrO_2 dopant (and, consequently, the weight contribution of the $ZrCeO_2$ substitution phase) about the positive dynamics of hardening of ceramics to external mechanical effects. In this case, the hardening mechanism is associated with the effects of the interphase (intergrain) boundaries contribution growth, which leads to an increase in the concentration of grain boundaries that prevent the propagation of microcracks and chips under external influences. This is evidenced by the change in the values of the difference in hardness and bending strength obtained by comparing these values after a certain number of cycles with the initial value. Formation of inclusions in the form of $ZrCeO_2$ with an increase in the concentration of the stabilizing additive allows to significantly increase both the resistance to external influences and to increase the strength parameters, which is a fairly significant indicator in the field of expanding the potential for the use of composite ceramics. Moreover, the obtained results of the resistance enhancement are in good agreement with the results of a number of works [23-26], in which an increase in the strength parameters was achieved by formation of a size effect in the structure, as well as alteration of the phase composition of the ceramics. According to the data presented, in

the case of unmodified composite ceramics, the difference in hardness and bending strength values, reflecting the degree of softening (degradation of strength properties), is about 5.4 ~ 5.5 %. At the same time, the addition of ZrO_2 to the ceramics, leading to the formation of the $ZrCeO_2$ phase in a small amount (within 10 wt. %), leads to a rise in the initial values of hardness and bending strength, but the softening degree changes insignificantly compared to unmodified ceramics (the difference is less than 10 %). An elevation in the weight contribution of $ZrCeO_2$ in the composition of composite ceramics above 10 % leads to a significant growth in the initial values of the strength parameters, as well as an increase in the degree of resistance to thermal shock effects, which consists in a decrease in the softening degree of less than 4.0 %, and in the case of a weight contribution of $ZrCeO_2$ phase of about 20 – 23 %, the observed change is more than 2 times less than in the case of unmodified ceramics. At the same time, the values of hardness and bending strength for these ceramics are also quite high compared to unmodified ceramics. Thus, it can be concluded that the formation of the $ZrCeO_2$ phase in the structure of ceramics results in emergence of additional interphase boundaries that restrain the effect of thermal expansion, and as a result, increases resistance to softening under thermal influence. It should also be noted that one of the factors restraining softening processes is the thermophysical properties, the change of which allows restraining high-temperature expansion processes. The decrease in the thermal conductivity of ceramics, caused by a change in the phase composition, expressed in the composite ceramics' thermal conductivity coefficient reduction from 26 W/(m×K) to 16 – 12 W/(m×K) leads to a slowdown in heat transfer processes, and therefore, an increase in thermal insulation due to the inhibition of phonon heat exchange mechanisms. As a result, the observed change in the softening degree can be explained by the fact that the restraint of heat exchange processes results in less pronounced destruction processes in the case of temperature differences.

Figure 3 shows the results of experimental work reflecting the change in temperature on the front and back side of ceramic samples and showing the thermal insulation properties of ceramics. These experiments were aimed at identifying the effect of variation in the phase composition of composite ceramics on the change in thermal insulation properties, as well as assessing the applicability of composite ceramics as thermal insulation materials capable of operating in extreme conditions.

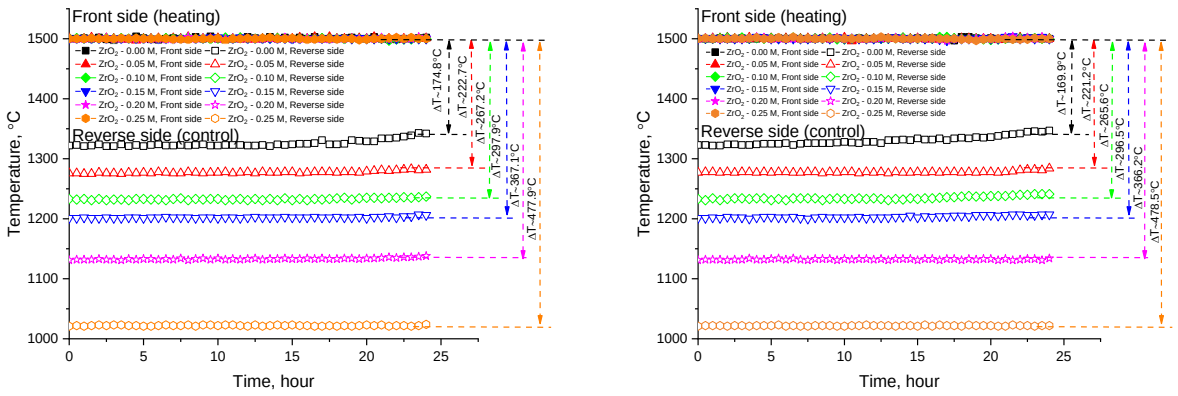

a) b)

Fig.3. The assessment results of changes in temperature values on the front and back sides of the sample, reflecting the results of thermal insulation of ceramics depending on the holding time at high temperatures: a) ceramics in the initial state; b) ceramics after testing for thermal resistance to thermal shock exposure.

The measurements were carried out by heating one of the sides (designated as the front side) with recording the surface temperature using a thermocouple and measuring the temperature on the back side of the samples, the difference between which (ΔT) determines the value of thermal insulation. Moreover, in the case of heating, the temperature difference was measured after stabilization of the surface temperature in a given temperature mode and recording stable temperature values on the back side. The time for stabilization of the temperature difference during heating of the samples was about 30 – 60 minutes. The total time of testing for thermal insulation and maintaining thermal insulation properties was 24 hours, with control temperature measurements taken every half hour on the front and back sides of the samples. According to the data presented, it is evident that in the case of non-stabilized composite ceramics, the temperature difference ΔT is about 175 °C, while after about 20 hours of cyclic testing, a decrease in the difference ΔT between the

front and back sides is observed. This means that with prolonged thermal exposure, the thermal insulation properties of the ceramics are lost. According to the analysis of the obtained experimental data, the addition of ZrO_2 to the composition leads to significant changes in the thermal insulation parameters, which are expressed both in the overall increase in the difference ΔT and in the increase in the stability of maintaining the temperature difference during long-term thermal exposure. At the same time, the ΔT value growth has a direct relationship with the change in the phase ratio in the composition of composite ceramics, due to the increase in the contribution of the monoclinic phase $ZrCeO_2$, formed as a result of the addition of ZrO_2 to the composition. The ΔT value growth in this case is due to a decrease in the thermal conductivity of ceramics, which in turn leads to a slowdown in the heat transfer mechanisms and, therefore, a reduction in heat transfer and heating of ceramic samples. The maximum ΔT value for the studied ceramics in which the weight contribution of the $ZrCeO_2$ phase is about 22 – 23 wt. % is equal to more than 475 °C, which is more than 2.5 times greater than the ΔT value established for unmodified ceramics. Such changes make it possible to consider modified composite ceramics as high-strength heat-insulating materials capable of withstanding both mechanical loads and temperature changes, as well as long-term high-temperature exposure. Figure 3b also reveals the assessment results of the change in the heat-insulating properties of ceramics after testing for heat resistance under thermal shock effects, reflecting the effect of high-temperature degradation on the heat-insulating properties of ceramics. The general trend of changes in the values of temperature differences between the front and back sides of ceramics subjected to heat resistance tests does not differ significantly from the results of thermal insulation tests in the case of the original samples, from which it can be concluded that the impact of oxidation processes caused by sudden changes in temperature does not have a significant negative impact on the stability of ceramics and the preservation of the stability of thermal insulation properties.

Figure 4 demonstrates the results of a comparative analysis of the ΔT values before and after testing the samples, reflecting the influence of high-temperature oxidation processes caused by thermal shock exposure on the preservation of thermal insulation characteristics. The obtained data showed that the thermal shock effect on the studied samples results in minor differences in the ΔT values, from the analysis of which it can be concluded that the observed processes of thermal oxidation and softening do not have a significant effect on the loss of thermal insulation characteristics, and in some cases lead to a slight increase in the difference ΔT, which may be due to a change in the thermophysical parameters of ceramics caused by oxidation.

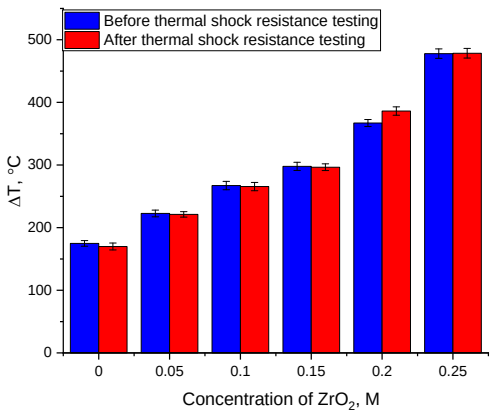

Fig.4. Results of comparative analysis of ΔT values before and after testing ceramic samples for thermal resistance to thermal shock exposure in the amount of 10 consecutive cycles

Determination of shielding characteristics reflecting the prospects of using the obtained multicomponent ceramics as protective shielding materials, allowing to reduce the negative impact of gamma radiation. As a source of gamma quanta, a Cs^{137} source, allowing the generation of gamma quanta with an energy of about 662 keV, which is characterized by the dominance of Compton scattering processes during the interaction of gamma quanta with materials, was used. The calculation was conducted by the assessment of changes in the intensity values of the registered gamma quanta without a protective shield and with a protective shield, on the basis of which the linear and mass absorption coefficients (LAC and MAC) and the thickness of the half-layer at which gamma quanta are absorbed (HVL) were estimated. The results of the experimentally determined values are given in Table 1.

According to the data presented, a change in the ratio of components in the composition of composite ceramics with the addition of ZrO_2 to the composition, followed by the formation of the $ZrCeO_2$ phase, leads to a growth in the shielding characteristics of LAC and MAC, an elevation in which indicates an increase in the shielding efficiency, and, as a consequence, a decrease in the negative effects of exposure to ionizing radiation. At the same time, the shielding efficiency growth due to the change in phase composition indicates a positive effect of modification not only on the strength and thermal insulation properties, but also on the shielding ability of ceramics. It is important to highlight that the order of magnitude of LAC, MAC and HVL itself indicates a fairly high shielding efficiency, since for most of the composite materials under consideration, the LAC value is usually about 0.2 – 0.5 cm^{-1}.

Table 1. Parameters of shielding characteristics depending on the ratio of components in the composition of ceramics

Shielding parameter	Concentration of ZrO_2 in ceramics, M					
	0.0	**0.05**	**0.10**	**0.15**	**0.20**	**0.25**
LAC, cm^{-1}	0.65±0.04	0.66±0.07	0.67±0.05	0.68±0.03	0.71±0.03	0.72±0.05
MAC, cm^2/g	0.096±0.009	0.097±0.004	0.098±0.005	0.101±0.006	0.108±0.005	0.109±0.007
HVL, cm	1.041±0.014	1.037±0.012	1.032±0.016	1.029±0.017	0.965±0.015	0.0964±0.012

A comparative analysis of the gamma radiation shielding efficiency was carried out using a number of literature data taken from works [27-31]. The choice of compositions of protective shielding materials is based on close ratios of components of the obtained samples, as well as their variations, which allowed the authors the estimation of the shielding efficiency. The results are shown in Figure 5; for comparison, the values of the LAC were selected in the case of shielding gamma quanta with energies of 662 keV, which are characterized by the dominance of Compton scattering in the mechanisms of interaction of gamma quanta with the shielding material. The comparison of the shielding efficiency was performed by comparison of the values of the LAC, which reflects the efficiency of gamma quanta absorption during shielding, while the choice of this value makes it possible to compare the efficiency without reference to density (the value of which, according to the results of these studies, varies within the range of 3.5 – 4.5 g/cm^2, which is significantly lower than the density of lead ~11.34 g/cm^3). The general appearance of the obtained comparison data shows that the shielding efficiency directly depends on the composition and quantity of components in the shielding glasses, in particular, the key role in increasing the efficiency is played by heavy oxide compounds (Bi_2O_3, WO_3, Nd_2O_3 et.al.), alongside compounds with rare earth elements, the addition of which makes it possible to increase the absorption capacity of the shielding materials. Moreover, the observed values, as well as their dependences of the LAC on the composition of the shielding materials, are in good agreement with the results presented in the relatively recently published mini-review of Recep Kurtulus [32], which indicates that the use of heavy oxide components allows for an increase in shielding efficiency, while eliminating lead or its oxide in the composition of glass, the addition of which allows for an increase in the density of shielding materials above 5 – 5.5 g/cm^3. The systematization provided in the work of Recep Kurtulus allows us to identify the most promising composites in this area, as well as to determine the role and potential applicability of various composite glasses and ceramics as shielding protective materials. The results of the comparative analysis of the values of the LAC obtained for the studied $x(TeO_2 – CeO_2 – WO_3 – ZnO – Bi_2O_3) – xZrO_2$ ceramics showed a significant superiority over other types of composite glasses considered as shielding protective coatings, which in turn is due to the presence of both heavy oxides such as Bi_2O_3, WO_3 in the composition of the glasses, and the difference in the charge state of the selected elements, which makes it possible to obtain sufficiently high values of Z_{eff} determining the shielding efficiency for the selected energies (in this case, the addition of heavy components and ZrO_2 to the composition leads to the value of Z_{eff} ~ 45 – 47). In this case, the high value of Z_{eff} in the region of gamma quanta energies, characteristic of the dominance of interaction mechanisms of the photoelectric effect type, allows for the effective absorption of low-energy gamma quanta, which in turn allows for the use of sufficiently thin layers of protective materials for shielding, which in the case of protecting microelectronic devices plays a very important role in determination of the mass and overall dimensions. In the energy range from 0.1 to 1 MeV, for which the dominant effect in the interaction mechanisms is Compton scattering, the influence of Z_{eff} on the absorption capacity is most pronounced, since the absorption efficiency is directly

proportional to the value of Z_{eff}. Thus, a large value of Z_{eff} for the synthesized ceramics provides a high absorption capacity, significantly different from a number of borate and telluride glasses selected for comparison. In the case of high-energy gamma quanta, the greatest contribution to the shielding efficiency is made by the density of the material and its thickness, which, together with high Z_{eff} values, makes it possible to significantly increase the prospects for using composite ceramics.

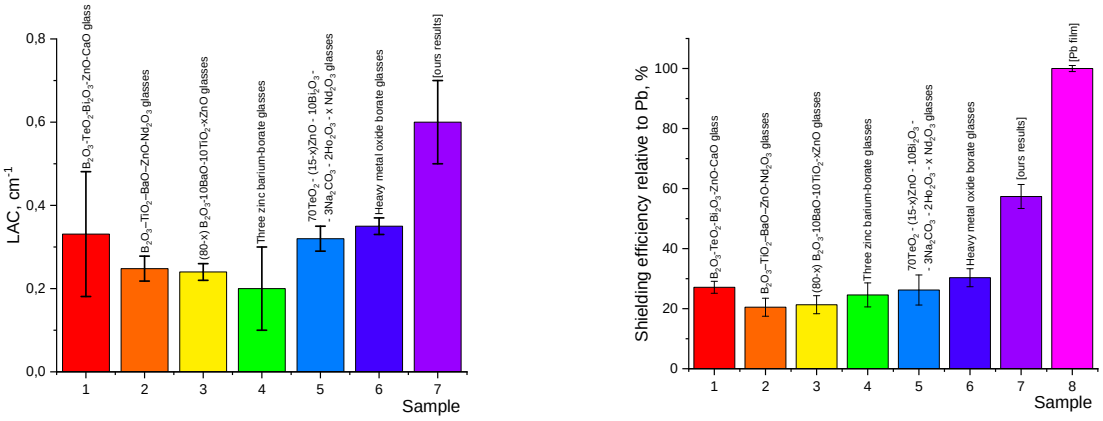

a) b)

Fig.5. Comparative analysis of shielding properties
a) results of a comparative analysis of the LAC taken from literature data with the results of the studies conducted;
b) results of the evaluation of the shielding efficiency in comparison with the LAC for lead

Figure 5b demonstrates the results of a comparative analysis of the shielding efficiency, determined on the basis of the measured LAC values in terms of the shielding efficiency of lead, which is a reference shielding material with the highest efficiency among the currently known protective shielding materials. In this case, the high efficiency of lead is primarily due to its high density, which leads to the maximum absorption of emitted gamma quanta. The results of the comparative analysis revealed that the efficiency of the obtained composite ceramics is about 60 – 65 % of the efficiency of lead, which is 1.5 – 2.0 times higher than the efficiency of the composite glasses and glass-like ceramics selected for comparison. This difference is primarily due to the difference in the density of the ceramics under consideration, as well as the Z_{eff} values, which play a very important role in determination of the absorption and shielding capacity.

Figure 6 shows the results of a comparative analysis reflecting changes in the strength (hardness and resistance to three-point bending), heat-insulating and shielding characteristics of the studied ceramics when modified with ZrO_2, the addition of which leads to a change in the phase composition of the ceramics due to the formation of the substitution phase $ZrCeO_2$.

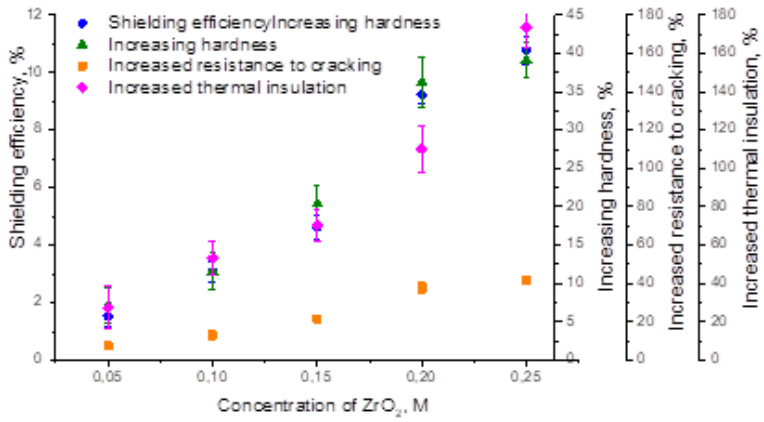

Fig.6. Results of comparative analysis of changes in strength, heat-insulating and shielding characteristics of the studied composite ceramics with the addition of ZrO_2, reflecting the effectiveness of alteration of properties in comparison with non-stabilized ceramics

According to the data presented, the change in phase composition due to the addition of ZrO_2 to the ceramics makes it possible to significantly increase the strength and mechanical properties, the increase of which is from 10 to 43 – 44 % depending on the concentration of the stabilizing additive in the composition. At the same time, the maximum achievement of efficiency is observed in thermal insulation characteristics, the growth of which is about 2.5 times compared to unmodified ceramics. In the case of assessment of the shielding characteristics, a change in the phase composition leads to an increase in the shielding efficiency, however, the increase in efficiency in the case of a change in the ratio of components in the composition is not as clearly expressed as in the case of strength and thermal parameters, and is no more than 10 – 12 % compared to unmodified ceramics. Such a difference between changes in the effectiveness of hardening and shielding is primarily due to the fact that hardening and thermal insulation growth is associated with the formation of impurity inclusions in the composition, which provide dispersion hardening due to size effects and the appearance of new inclusions, increasing the number of grain boundaries, restraining the spread of microcracks and oxidation processes.

Also, in the case of assessment of thermal insulation characteristics, the increase in efficiency is associated with a decrease in the thermal conductivity of ceramics due to impurity inclusions, which reduces the rate of heat exchange due to impurity inclusions, and therefore, inhibits heat transfer processes. In the case of shielding parameters, the main contribution is made by a change in the density of the material, which changes insignificantly with variations in the phase composition, which results in small changes in the shielding characteristics depending on the concentration of the component ratio. However, when compared with other samples of similar composite ceramics, as well as when recalculating the shielding characteristics in comparison with the parameters of lead, we can conclude that the absorption of gamma quanta and the containment of their negative impact are quite effective. Thus, it can be concluded that the proposed compositions of composite ceramics, as well as their modification due to the formation of inclusions in the form of the $ZrCeO_2$ phase, can constitute significant competition in the field of shielding and heat-insulating materials, which have great potential for use in extreme conditions.

4. Conclusion

In conclusion, we can summarize the main results of the experimental work carried out, reflecting the prospects for using composite multicomponent 1-x(TeO_2 – CeO_2 – WO_3 – ZnO – Bi_2O_3) – xZrO_2 ceramics as shielding and heat-insulating materials. During examination of the X-ray phase analysis of the studied ceramic samples, it was found that the addition of a stabilizing additive in the form of ZrO_2 leads to the formation of a substitution phase of the $ZrCeO_2$ type with a monoclinic crystal lattice type, the appearance of which in the composition of ceramics leads to an elevation in strength characteristics, alongside an increase in resistance to thermal effects and efficiency during their use as heat-insulating and shielding materials. According to the conducted experimental works aimed at study of resistance to thermal effects, it was found that the addition of ZrO_2 to the composition of composite ceramics leads to an increase not only in strength properties (hardness and bending strength), but also in resistance to high-temperature corrosion caused by cyclic tests.

In the case of tests to determine the effectiveness of thermal insulation characteristics, it was found that reduction in the thermal conductivity properties of ceramics during the formation of a new phase of $ZrCeO_2$ in the composition of ceramics leads to an increase in thermal insulation characteristics, as well as an increase in the retention of resistance to long-term temperature effects.

During determination of the shielding characteristics of the studied ceramics, it was found that the obtained ceramic samples have a high shielding capacity, amounting to about 60 – 70 % of the shielding efficiency of lead, which is 1.5 – 2 times higher than similar composite ceramics.

Conflict of interest statement.
The authors declare that they have no conflict of interest in relation to this research, whether financial, personal, authorship or otherwise, that could affect the research and its results presented in this paper.

CRediT author statement
Kozlovskiy A.L., Borgekov D.B., Moldabayeva G.Zh., Burkhanov B.Zh.: Conceptualization, Data Curation, Writing Original Draft; Methodology, Investigation; **Tleulessova I.K., Zhumazhanova A.T., Khametova A.A.:** Writing Review & Editing, Supervision. The final manuscript was read and approved by all authors.

Funding

This research was funded by the Committee of Science of the Ministry of Science and Higher Education of the Republic of Kazakhstan (No. BR21882390).

References

1. Al-Buriahi M.S., Olarinoye I.O., Yılmaz E., Çalıskan F., Sriwunkum C. (2025) Evaluation of the structural and radiation transmission parameters of recycled borosilicate waste glass system: An effective material for nuclear shielding. *Annals of Nuclear Energy*, *213*, 111136. https://doi.org/10.1016/j.anucene.2024.111136

2. Alrowaily A.W., Almuqrin A.H., Sayyed M.I., Albarzan B. (2025) Understanding radiation shielding performance through a comparative study of half value layer in novel and preexisting silicate glasses. *Nuclear Engineering and Technology*, *57*(3), 103268. https://doi.org/10.1016/j.net.2024.10.030

3. Sayyed M.I., Hamad M.K., Mhareb M.H.A. (2025) Radiation shielding properties for a borosilicate glass: Role of varying PbO. *Optical Materials*, *159*, 116602. https://doi.org/10.1016/j.optmat.2024.116602

4. Zhang M., Wang K., Cao Z., Yang S., Han Y., Lv H., Jia J. (2025) Environment-friendly glass with high refractive index and radiation resistance. *Ceramics International*, *51*(2), 1978-1987. https://doi.org/10.1016/j.ceramint.2024.11.172

5. Zughbi A., Kharita M.H., Shehada A.M. (2017) Determining optical and radiation characteristics of cathode ray tubes' glass to be reused as radiation shielding glass. *Radiation Physics and Chemistry*, *136*, 71-74. https://doi.org/10.1016/j.radphyschem.2017.02.035

6. Sayyed M.I., Kaky K.M., Şakar E., Akbaba U., Taki M.M., Agar O. (2019) Gamma radiation shielding investigations for selected germanate glasses. *Journal of Non-Crystalline Solids*, *512*, 33-40. https://doi.org/10.1016/j.jnoncrysol.2019.02.014

7. Madbouly A.M., Alazab H.A., Borham E., Ezz-ElDin F.M. (2021) Study of gamma radiation dosimeter and radiation shielding parameters of commercial window glass. *Applied Physics A*, *127*, 1-14. https://doi.org/10.1007/s00339-021-04889-9

8. Shamshad L., Rooh G., Limkitjaroenporn P., Srisittipokakun N., Chaiphaksa W., Kim H. J., Kaewkhao J. (2017) A comparative study of gadolinium based oxide and oxyfluoride glasses as low energy radiation shielding materials. *Progress in Nuclear Energy*, *97*, 53-59. https://doi.org/10.1016/j.pnucene.2016.12.014

9. Sayyed M.I., Mhareb M.H.A., Alajerami Y.S.M., Mahmoud K.A., Imheidat M.A., Alshahri F., Al-Abdullah T. (2021) Optical and radiation shielding features for a new series of borate glass samples. *Optik*, *239*, 166790. https://doi.org/10.1016/j.ijleo.2021.166790

10. Marltan W., Rao P.V., Klement R., Galusek D., Sayyed M. I., Tekin H.O., Veeraiah N. (2019) Spectroscopic and thermal analysis of lead-free multipurpose radiation shielding glasses. *Ceramics International*, *45*(5), 5332-5338. https://doi.org/10.1016/j.ceramint.2018.11.231

11. Wu Y., Wang Z. (2024) Progress in ionizing radiation shielding materials. *Advanced Engineering Materials*, *26*(21), 2400855. https://doi.org/10.1002/adem.202400855

12. Mhareb M.H.A., Sayyed M.I., Hashim S., Alshammari M., Alhugail S., Aldoukhi H., Khandaker M.U. (2022) Radiation shielding features for a new glass system based on tellurite oxide. *Radiation Physics and Chemistry*, *200*, 110094. https://doi.org/10.1016/j.radphyschem.2022.110094

13. Saeed A., El Shazly R.M., Elbashar Y.H., EL-AZM A.A., Comsan M.N. H., El-Okr M. M., Kansouh W.A. (2021) Glass Materials in Nuclear Technology for Gamma Ray and Neutron Radiation Shielding: a Review. *Nonlinear Optics, Quantum Optics: Concepts in Modern Optics*, *53*, 107–159. Available at: https://www.researchgate.net/publication/376409782

14. Kilicoglu O., Akman F., Ogul H., Agar O., Kara U. (2023) Nuclear radiation shielding performance of borosilicate glasses: Numerical simulations and theoretical analyses. *Radiation Physics and Chemistry*, *204*, 110676. https://doi.org/10.1016/j.radphyschem.2022.110676

15. Alalawi A., Al-Buriahi M.S., Sayyed M.I., Akyildirim H., Arslan H., Zaid M.H.M., Tonguç B.T. (2020) Influence of lead and zinc oxides on the radiation shielding properties of tellurite glass systems. *Ceramics International*, *46*(11), 17300-17306. https://doi.org/10.1016/j.ceramint.2020.04.017

16. Singh V.P., Badiger N.M., Kaewkhao J. (2014) Radiation shielding competence of silicate and borate heavy metal oxide glasses: comparative study. *Journal of non-crystalline solids*, *404*, 167-173. https://doi.org/10.1016/j.jnoncrysol.2014.08.003

17. Cheewasukhanont W., Limkitjaroenporn P., Kothan S., Kedkaew C., Kaewkhao J. (2020) The effect of particle size on radiation shielding properties for bismuth borosilicate glass. *Radiation Physics and Chemistry*, *172*, 108791. https://doi.org/10.1016/j.radphyschem.2020.108791

18. Abdelghany Y.A., Kassab M.M., Radwan M.M., Abdel-Latif M.A. (2022) Borotellurite glass system doped with ZrO2, potential use for radiation shielding. *Progress in Nuclear Energy*, *149*, 104256. https://doi.org/10.1016/j.pnucene.2022.104256

19. Imheidat M.A., KhHamad M., Naseer K.A., Sayyed M.I., Dwaikat N., Cornish K., .. Mhareb M.H.A. (2022) Radiation shielding, mechanical, optical, and structural properties for tellurite glass samples. *Optik*, *268*, 169774. https://doi.org/10.1016/j.ijleo.2022.169774

20. Temir A., Zhumadilov K.S., Zdorovets M.V., Kozlovskiy A., Trukhanov A.V. (2021) Study of the effect of doping CeO2 in TeO2–MoO–Bi2O3 ceramics on the phase composition, optical properties and shielding efficiency of gamma radiation. *Optical Materials*, *115*, 111037. https://doi.org/10.1016/j.optmat.2021.111037

21. Alpyssova G.K., Denisov I.P., Bakiyeva Z.K., Kaneva E.V., Domarov E.V., Tussupbekova A.K. (2024) Dependence of the Radiation Synthesis Efficiency of Ceramics Based on Tungstates on the Flow Power. *Bulletin of the Karaganda University" Physics Series", 11629*(4), 9-19. https://doi.org/10.31489/2024ph4/9-19

22. Belli P., Bernabei R., Borovlev Y.A., Cappella F., Caracciolo V., Cerulli R., Shlegel V.N. (2022) Optical, luminescence, and scintillation properties of advanced ZnWO4 crystal scintillators. *Nuclear Instruments and Methods in Physics Research Section A: Accelerators, Spectrometers, Detectors and Associated Equipment*, *1029*, 166400. https://doi.org/10.1016/j.nima.2022.166400

23. Nguyen T. N., Thong H.C., Zhu Z.X., Nie J.K., Liu Y.X., Xu Z., Wang K. (2021) Hardening effect in lead-free piezoelectric ceramics. *Journal of Materials Research*, *36*, 996-1014. https://doi.org/10.1557/s43578-020-00016-1

24. Alzahrani J.S., Alrowaili Z.A., Olarinoye I.O., Sriwunkum C., Kebaili I., Al-Buriahi M.S. (2025) Gamma-radiation insulating performance of AlON-hardened Na2O–Bi2O3–SiO2–BaO–Fe2O3–ZrO2 glasses. *Scientific Reports*, *15*(1), 6537. https://doi.org/10.1038/s41598-025-90902-7

25. Sayyed M.I. (2025) Modulation of optical, mechanical and radiation shielding characteristics in TeO_2 -B2O3–BaO–CeO_2 glasses with varying CeO_2 level. *Optical Materials*, *158*, 116492. https://doi.org/10.1016/j.optmat.2024.116492

26. Almuqrin A.H., Sayyed M.I., Elsafi M. (2025) Experimental investigation for radiation shielding performance of B2O3-TeO2-Bi2O3-ZnO-CaO glass system. *Annals of Nuclear Energy*, *215*, 111276. https://doi.org/10.1016/j.anucene.2025.111276

27. Al Huwayz M., Almuqrin A.H., Alharbi F.F., Sayyed M.I., Albarzan B. (2025) Unveiling the potential of Nd2O3 in optimizing the radiation shielding performance of B2O3–TiO2–BaO–ZnO-Nd2O3 glasses. *Nuclear Engineering and Technology*, *57*(1), 103135. https://doi.org/10.1016/j.net.2024.08.004

28. Ruiz E.L. (2024) Radiation shielding analysis of barium-titanium-borate glasses doped with zinc oxide. *Nexus of Future Materials*, *1*, 584050. https://doi.org/10.70128/584050

29. Alawaideh S.E.L., Sayyed M.I., Mahmoud K.A., Hanfi M., Imheidat M.A., Kaky K.M., Elsafi M. (2024) Effect of different metal oxides on the Radiation shielding features of borate glasses. *Radiation Physics and Chemistry*, *220*, 111720. https://doi.org/10.1016/j.radphyschem.2024.111720

30. Alvyanti F.A., Marzuki A., Purwanto H., Lathifah N., Fausta D.E., Rahmawati A.N., Ariyanti S. (2024) Properties of Gamma Ray Shielding Ho/Nd Codoped Tellurite Glasses. *Key Engineering Materials*, *993*, 25-34. https://doi.org/10.4028/p-2BlYr2

31. Kurudirek M. (2017) Heavy metal borate glasses: potential use for radiation shielding. *Journal of Alloys and Compounds*, *727*, 1227-1236. https://doi.org/10.1016/j.jallcom.2017.08.237

32. Kurtulus R. (2024) Recent developments in radiation shielding glass studies: a mini-review on various glass types. *Radiation Physics and Chemistry*, *220*, 111701. https://doi.org/10.1016/j.radphyschem.2024.111701

AUTHORS' INFORMATION

Kozlovskiy, Artem Leonidovich – PhD (Phys.), Associate Professor, Head of the Laboratory of Solid-State Physics, Astana Branch of the Institute of Nuclear Physics Agency of the Republic of Kazakhstan for Atomic Energy, Astana; Scopus Author ID: 55632118900; https://orcid.org/0000-0001-8832-7443; kozlovskiy.a@inp.kz

Borgekov, Daryn Boranbaevich – PhD (Phys.), Director of the Astana Branch of the Institute of Nuclear Physics Agency of the Republic of Kazakhstan for Atomic Energy, Astana; Scopus Author ID: 56440218700; https://orcid.org/0000-0002-9727-0511; d.borgekov@inp.kz

Tleulessova, I.K. – PhD student, Engineer of the Astana Branch of the Institute of Nuclear Physics Agency of the Republic of Kazakhstan for Atomic Energy, Astana; Scopus Author ID: 56178686600; ORCID iD: https://orcid.org/0009-0009-6739-6883

Zhumazhanova, Ainash Tyrlybekovna – PhD (Phys.), Senior Researcher of the Astana Branch of the Institute of Nuclear Physics Agency of the Republic of Kazakhstan for Atomic Energy, Astana; Scopus Author ID: 57090956700; https://orcid.org/0000-0002-5483-9552; a.zhumazhanova@inp.kz

Moldabayeva, G.Zh – D.Sc. (Tech.), Professor, Department of Chemical Processes and Industrial Ecology, Satbayev University, Almaty; Scopus Author ID: 55969768100; https://orcid.org/0000-0001-7331-1633; g.moldabayeva@satbayev.university

Burkhanov, B.Zh – Associate Professor, Ph.D. (Tech.), Agrarian and Technical University named after Zhangir Khan, Uralsk; Scopus Author ID: 57489799500; https://orcid.org/0000-0001-5407-9859; aruka73@mail.ru

Khametova, Ainagul Aitzhanovna – PhD (Phys.), Engineer of the Astana Branch of the Institute of Nuclear Physics Agency of the Republic of Kazakhstan for Atomic Energy, Astana; Scopus Author ID: 57731940800; https://orcid.org/0009-0005-9445-199X; a.khametova@inp.kz

EURASIAN PHYSICAL TECHNICAL JOURNAL

2025, Volume 22, No. 3 (53)

https://doi.org/10.31489/2025N3/36-47

Received: 19/02/2025 Revised: 19/05/2025 Accepted: 25/09/2025 Published online: 30/09/2025

Research Article

Open Access under the CC BY -NC-ND 4.0 license

UDC 536.7; 537.311; 546.654; 549.51

THERMODYNAMIC AND ELECTROPHYSICAL PROPERTIES OF A NEW SEMICONDUCTOR BASED ON OXIDES OF RARE-EARTH AND TRANSITION METALS

Turdiyev M.T.[1], Kasenov B.K.[2*], Nukhuly A.[1], Bekturganov Zh.S.[3]
Kasenova Sh.B.[2], Sagintaeva Zh.I.[2], Kuanyshbekov E.E.[2]

[1] L.N. Gumilyov Eurasian National University, Astana, Kazakhstan
[2] Zh. Abishev Chemical-Metallurgical Institute, Karaganda, Kazakhstan
[3] E.A. Buketov Karaganda University, Karaganda, Kazakhstan
*Corresponding author: kasenov1946@mail.ru

Abstract. *The study focuses on the investigation of a new compound that combines the properties of manganites and zirconates, paving the way for the development of highly efficient functional materials. The compound was synthesized through the interaction of lanthanum oxide, zirconium oxide, manganese oxide, and sodium carbonate at temperatures ranging from 800 to 1200 °C and studied using X-ray analysis methods, including the determination of cubic lattice parameters. The analysis of the temperature dependence of heat capacity revealed second-order phase transitions, based on which equations describing its variations were derived. Thermodynamic characteristics such as entropy and enthalpy were calculated. Electrophysical measurements confirmed the semiconductor nature of the material within a specific temperature range and revealed high values of dielectric permittivity, surpassing those of reference materials.*

Keywords: manganite, lanthanum, zirconium, sodium, heat capacity, thermodynamic functions, electrophysics.

1. Introduction

Due to their magnetoresistance (MS) and colossal magnetoresistance (CMS) properties, manganites can be utilized in compact devices that respond to magnetic field variations and serve as temperature sensors and other applications [1]. Manganites can also have semiconductor, ferroelectric, para-, ferro-, and antiferromagnetic characteristics with high RAM values [1-5]. Zirconium dioxide-based compounds are extensively utilized in contemporary technologies as solid electrolytes for various electrochemical applications. Their popularity stems from exceptional properties such as high ionic conductivity, excellent chemical resistance, low thermal conductivity, and superior mechanical and optical characteristics [5–8].

The effect of adding Er_2O_3 on the electrical conductivity of c-ZrO_2 was studied by analyzing the impedance spectra of undoped and various amounts of cubic zirconium dioxide doped with Er_2O_3 (c-ZrO_2). Doped c-ZrO_2 powders and powders containing 1-15 wt.% Er_2O_3 were prepared using a colloidal method. Subsequently, the doped powders were granulated under a pressure of 200 MPa. Additionally, undoped and Er_2O_3-doped samples of c-ZrO_2 were sintered at 1500 °C for 1 hour. The electrical conductivity of the samples was measured using an impedance analyzer in the frequency range of 100 Hz to 13 MHz within a temperature range of 300-800 °C. The results indicate that the electrical conductivity increases with an increase in the test temperature. Adding 1 wt.% Er_2O_3 to c-ZrO_2 led to an increase in grain interior, grain boundary, and overall conductivity. The distortion caused by the incorporation of Er^{3+} cations into the c-ZrO_2 lattice results in an increased concentration of oxygen vacancies in c-ZrO_2 [9].

The article [10] investigates the temperature dependencies of the thermal conductivity of cubic single crystals of ZrO_2 stabilized with yttrium oxide ranging from 8 to 40 mol.% within the temperature range of 50–300 K. The cubic crystals $(ZrO_2)_{1-x}$ $(Y_2O_3)_x$, where x = 0.08–0.40, were grown using directional melt crystallization in a cold container. For x = 0.08–0.15, the thermal conductivity values are similar, and the increase in thermal conductivity with temperature is negligible. These crystals exhibit the lowest thermal conductivity within the studied concentration range. When the temperature changes from 50 to 300K, the thermal conductivity values vary from approximately 1.2–1.4 to around 2.4 W/(m·K). The differences in thermal conductivity for these compositions are noticeable only at 50 K, where the thermal conductivity of 12YSZ and 15YSZ crystals is slightly higher than that of 8YSZ, 10YSZ, and 14YSZ. The thermal conductivity of 20YSZ crystals is higher than that of crystals with yttrium oxide content in the range of x = 0.08 to 0.15, with minimal variation in conductivity over the temperature range of 50 to 300K.

Reference [11] provides a review of the thermodynamic properties of complex oxides of lanthanides and zirconium $Ln_2 Zr_2 O_7$ (Ln = La, Pr, Sm, Eu, Gd), as well as solid solutions of $Ln_2 O_3 \cdot 2ZrO_2$ (Ln = Tb, Ho, Er, Tm). The heat capacity of $Ln_2 Zr_2 O_7$ samples, characterized using methods such as X-ray phase and elemental analysis, scanning electron microscopy, adiabatic and differential scanning calorimetry, is investigated. Based on the smoothed heat capacity values, the temperature dependencies of thermodynamic functions-including entropy, enthalpy changes, and reduced Gibbs energy-were determined over a broad temperature range. A comparative analysis of available thermodynamic data is presented, and recommended values are proposed. The contribution of low-temperature magnetic transitions for $Ln_2 Zr_2 O_7$ compounds (Ln = Pr, Nd, Sm, Gd) is taken into account, and the influence of the Schottky anomaly on the heat capacity of lanthanide compounds is explored. In study [12], the influence of the synthesis method on the microstructure of the resulting powders and ceramics of $La_{1.9}5Ca_{0.05}Zr_2O_{7-\delta}$ (LCZ) was established. In the above-mentioned and other literary sources, manganites and zirconates act as separate compounds. The article presents for the first time the compound $LaNa_2ZrMnO_6$, as combined from lanthanum (III), zirconium (IV), manganese (III) and sodium carbonate oxides to study its promising multifunctional properties.

2. Experimental technique

To synthesize the zircon-manganite $LaNa_2 ZrMnO_6$, the selected starting materials included lanthanum (III) oxide ("os.ch." grade), zirconium (IV) oxide, manganese (III) oxide, and sodium carbonate ("ch.d.a." grade). Before use, these materials were dehydrated at 400 °C, then thoroughly mixed and finely ground in an agate mortar. The resulting mixture was annealed in an alund crucible within a SNOL furnace under the following conditions: initially at 600 °C for 10 hours, then at 800 °C for 10 hours, followed by 1000 °C and 1200 °C for 20 hours each. After each annealing stage, the mixture was cooled to room temperature, remixed, reground, and reheated. To prevent the formation of nonequilibrium or metastable phases at high temperatures, a final low-temperature annealing step was performed at 400 °C for 10 hours, ensuring the stability of the phase at lower temperatures [8].

The equilibrium composition of the compound was examined using X-ray phase analysis performed on a DRON-2.0 diffractometer. The analysis utilized CuK_α radiation, filtered with a Ni filter, under the following conditions: U = 30 kV, J = 10 mA, pulse counter scale set at 1000 imp/s. The counter rotation speed was set to 2 degrees per minute, with a time constant (τ) of 5 seconds. Measurements were conducted over a 2θ angle range of 10° to 90°, and the intensity of the diffraction maxima was evaluated on a 100-point scale.

The microstructural analysis of the compound was carried out using a scanning electron microscope (SEM) (Figures 1, 2). SEM image of the synthesized $LaNa_2ZrMnO_6$ at 20,000× magnification, showing agglomerated particles with irregular morphology and rough surface texture. Measurement conditions: WD = 10.75 mm, HV = 20.00 kV, HFW = 20.7 µm. Scale bar: 5 µm.

SEM image of the synthesized $LaNa_2ZrMnO_6$ at 2400× magnification, showing agglomerated particles with irregular morphology and rough surface texture. Measurement conditions: WD = 10.77 mm, HV = 20.00 kV, HFW = 173 µm. Scale bar: 50 µm.

Taken together, both images complement each other: one provides insight into the micromorphology, while the other allows for the assessment of macroscopic particle distribution and agglomeration. This combination is valuable for a comprehensive interpretation of the material’s structure, particularly when discussing its functional properties such as ionic conductivity, catalytic activity, or magnetic behavior.

.

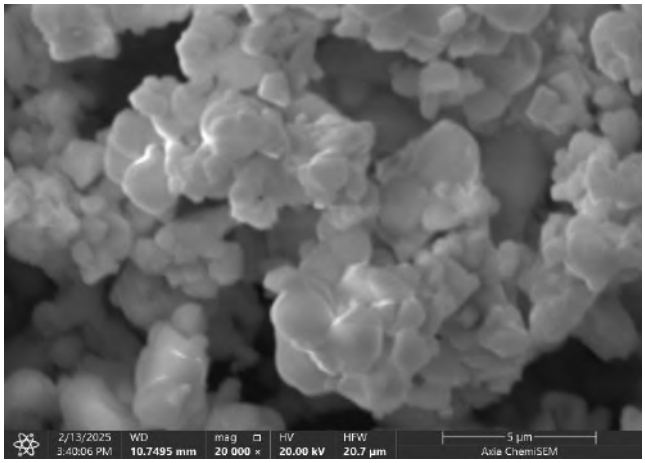

Fig. 1. Microstructure of $LaNa_2ZrMnO_6$ at a scale of 5 µm.

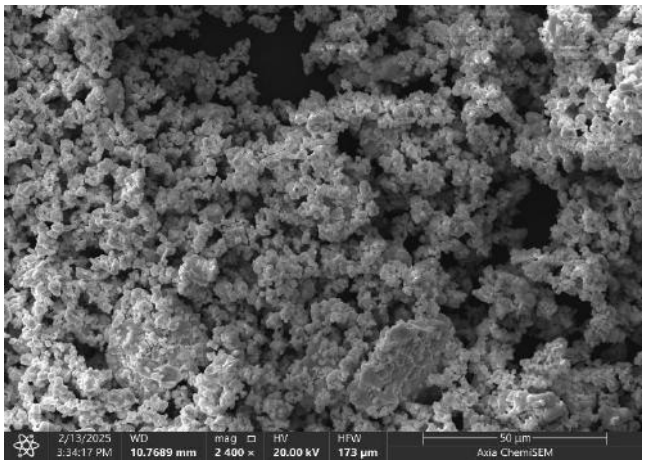

Fig. 2. Microstructure of $LaNa_2ZrMnO_6$ at a scale of 50 µm.

The isobaric heat capacity of $LaNa_2ZrMnO_6$ was investigated over the temperature range of 298–673 K using an IT-S-400 calorimeter. This instrument operates on the comparative principle of a dynamic calorimeter equipped with a heat meter. The measurement system allows temperature assessments at fixed intervals of 25 °C, utilizing a DC potentiometer and an integrated switch.

The volumetric heat capacity measurement range exceeds $1 \cdot 10^6$ J/K·m³, and the total measurement process, including experimental data processing, does not exceed 2.5 hours. The IT-S-400 calorimeter provides measurement accuracy within ±10% [8]. The device was calibrated by determining the thermal conductivity of the K_T heat meter, which represents an experimentally determined calorimeter constant [13–15]. For this purpose, experiments were performed using a copper sample and an empty ampoule. The thermal conductivity of the heat meter was calculated using the following formula [15]:

$$K_T = C_{rev.m} / (\bar{\tau}_{h.cop.} - \bar{\tau}_{h.}^{\circ}), \quad (1)$$

where $C_{rev.m}$ is the total heat capacity of the copper sample, J/(mol·K); $\bar{\tau}_{h.cop.}$ is the average delay time on the heat meter in experiments with the copper sample, s; and $\bar{\tau}_{h.}^{\circ}$ is the average delay time in experiments with an empty ampoule, s.

The total heat capacity of the copper sample was determined using the following formula [15]:

$$C_{rev.m} = C_m \cdot m_{rev}, \quad (2)$$

where C_m is the tabulated specific heat capacity of copper, J/(mol·K), and m_{rev} is the mass of the copper sample, kg.

The specific heat capacity of the substance was determined using the following formula [15]:

$$C_{spec.} = K_T / m_o(\tau_{h.} - \tau°_{h.}), \quad (3)$$

where K_T is the thermal conductivity of the heat meter, J/K; m_o is the mass of the test substance, g; $\tau_{h.}$ is the temperature delay time on the heat meter, s; and $\tau°_{h.}$ is the temperature delay time on the heat meter in experiments with an empty ampoule, s.

The molar heat capacity was obtained from the specific heat capacity by accounting for the molar mass. At each temperature, five parallel experiments were conducted, and the results were averaged and analyzed using mathematical statistical methods [15].

At each temperature, the standard deviation ($\bar{\delta}$) for the averaged values of the specific heat capacity was estimated according to [14, 15]:

$$\delta = \sqrt{\frac{\sum_{i=1}^{n}(C_i - \bar{C})^2}{n-1}}, \quad (4)$$

where n is the number of experiments, C_i is the measured value of the specific heat capacity, J/(g·K); $\bar{C}$, J/(g·K) is the arithmetic mean of the measured specific heat capacity values.

For the averaged values of the molar heat capacity, the random error component was calculated according to [14, 15] using the following formula:

$$\overset{\circ}{\Delta} = \frac{\delta \cdot t_p}{\bar{C}} \cdot 100, \quad (5)$$

where $\overset{\circ}{\Delta}$ - represents the random error component in percentage (%), and t□ is Student's coefficient. For n = 5, the value of t□ is 2.75 at a 95% confidence interval (p = 0.95) [15].

The functionality of the device was validated by measuring the heat capacity of α-Al_2O_3 (qualification "ch.d.a." in accordance with TU 6.09-426-75). Both during calibration and verification, repeated (parallel) measurements were conducted over the temperature range of 173–673K in 25K increments. At each temperature step, five parallel measurements were performed, and the results were averaged and analyzed using mathematical statistical methods [15]. To ensure the reliability of the α-Al_2O_3 heat capacity measurements, the obtained data were compared with recent literature values [16] (Table 1).

Table 1. Comparison of the measured heat capacity of α-Al_2O_3, used to verify the calorimeter's performance, with literature data [16].

T, K	$C_p°(T)$, J/(mol·K)		T, K	$C_p°(T)$, J/(mol·K)	
	Our results	By [16]		Our results	By [16]
180	44.50	43.83	400	94.12	95.21
230	64.86	61.18	450	100.26	101.8
250	70.37	67.08	500	105.47	106.1
280	77.07	74.82	550	110.09	109.7
300	76.31	79.41	600	114.29	112.5
350	86.49	88.86	650	118.20	114.9

As shown in the data presented in Table 1, our results on the temperature dependence of the heat capacity of α-Al_2O_3 within the range of 173–673K are in satisfactory agreement with the findings from [16], remaining within the accuracy limits of the IT-S-400 calorimeter. For ease of comparison, between our experimentally obtained heat capacity values for α-Al_2O_3 and the data from [16], we recalculated our results into intervals of 10 and 50 K using the equations $C°_p \sim f(T)$, derived from the experimental data. This adjustment was necessary because the data in [16] are presented in 10 and 50 K increments, while our measurements were conducted at ΔT = 25 K. It is worth noting that the actual errors in our experimental heat

.

capacity data, determined using formulas (4, 5), are significantly smaller than the maximum device accuracy, being less than 10%. The same device was also employed for investigating the heat capacities of several compounds, as described in [17–21].

Tables 2 and 3, along with Figure 3, present the results obtained from the calorimetric studies and thermodynamic calculations.

Table 2. Experimentally determined heat capacity values for $LaNa_2ZrMnO_6$

T, K	$C_p \pm \overline{\delta}$, J/(g·K)	$C_p{}^o \pm \overset{o}{\Delta}$, J/(mol·K)	T, K	$C_p \pm \overline{\delta}$, J/(g·K)	$C_p{}^o \pm \overset{o}{\Delta}$, J/(mol·K)
298.15	0.5657 ± 0.0105	242 ± 12	498	0.5777 ± 0.0140	247 ± 17
323	0.7219 ± 0.0097	308 ± 11	523	0.6315 ± 0.0170	270 ± 20
348	0.7830 ± 0.0103	334 ± 12	548	0.2791 ± 0.0080	119 ± 9
373	0.8567 ± 0.0111	366 ± 13	573	0.3513 ± 0.0082	150 ± 10
398	0.9552 ± 0.0113	408 ± 13	598	0.3916 ± 0.0102	167 ± 12
423	0.7697 ± 0.0163	329 ± 19	623	0.4264 ± 0.0087	182 ±10
448	0.5649 ± 0.0055	241 ± 6	648	0.4740 ± 0.0102	202 ± 12
473	0.4338 ± 0.0077	185 ± 9	673	0.5089 ± 0.0088	217 ± 10

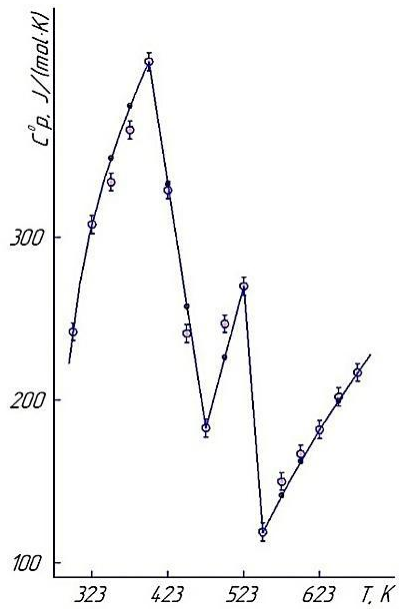

Fig. 3. Temperature dependence of the heat capacity of $LaNa_2ZrMnO_6$.
- experimental data, ● - calculated data

The electrophysical properties of $LaNa_2$ $ZrMnO_6$ were investigated in [22] by measuring its electrical capacitance using an LCR-781, operating at a frequency of 1 kHz within a temperature range of 293-483K. According to the device specifications, the measurement accuracy for electrophysical characteristics is ±0.05% [23]. For the measurements, a plane-parallel disk-shaped sample was prepared with a diameter of 10 mm and a thickness of 5-6 mm, incorporating a binder additive. The sample was pressed under a pressure of 20 kg/cm³ and subsequently annealed in a silite furnace at 673 K for 6 hours. After annealing, the disk was ground on both sides to ensure uniformity.

The dielectric constant was calculated based on the electrical capacity of the sample. The relationship between electrical induction and the electric field strength was analyzed using the Sawyer-Tower scheme.

Table 3. Thermodynamic functions of $LaNa_2ZrMnO_6$

T, K	$C_p°(T) \pm \overset{\circ}{\Delta}$, J/(mol·K)	$S°(T) \pm \overset{\circ}{\Delta}$, J/(mol·K)	$H°(T)-H°(298.15) \pm \overset{\circ}{\Delta}$, J/mol	$\Phi^{xx}(T) \pm \overset{\circ}{\Delta}$, J/(mol·K)
298	242 ± 13	238 ± 7	–	238 ± 20
300	248 ± 13	240 ± 20	490 ± 30	238 ± 20
325	313 ± 17	262 ± 22	7540 ± 400	239 ± 20
350	358 ± 19	287 ± 24	15960 ± 850	242 ± 20
375	389 ± 21	313 ± 26	25330 ± 1350	246 ± 20
400	409 ± 22	339 ± 28	35320 ± 1880	251 ± 21
425	328 ± 17	361 ± 30	44450 ± 2370	256 ± 21
450	254 ± 14	378 ± 31	51710 ± 2760	263 ± 22
475	179 ± 10	389 ± 32	57120 ± 3040	269 ± 22
500	231 ± 12	400 ± 33	62370 ± 3320	275 ± 23
525	273 ± 15	412 ± 34	68670 ± 3660	282 ± 23
550	107 ± 6	421 ± 35	73220 ± 3900	288 ± 24
575	144 ± 8	427 ± 36	76540 ± 4080	294 ± 24
600	164 ± 9	433 ± 36	80390 ± 4280	299 ± 25
625	184 ± 10	440 ± 37	84740 ± 4510	305 ± 25
650	202 ± 11	448 ± 37	89560 ± 4770	310 ± 26
675	219 ± 12	456 ± 38	94810 ± 5050	315 ± 26

To validate the accuracy and reliability of the obtained data, the dielectric constant of barium titanate, a standard substance, was measured within the temperature range of 293–483 K at a frequency of 1 kHz.

The measured dielectric constant of $BaTiO_3$ at 293 K and 1 kHz was found to be 1296, which aligns satisfactorily with the recommended value of 1400 ± 250 [24–26]. It is worth mentioning that the electrophysical characteristics of similar manganites were also investigated using this device in studies [27, 28]. Figure 4 and Table 4 below present the results of the electrophysical studies.

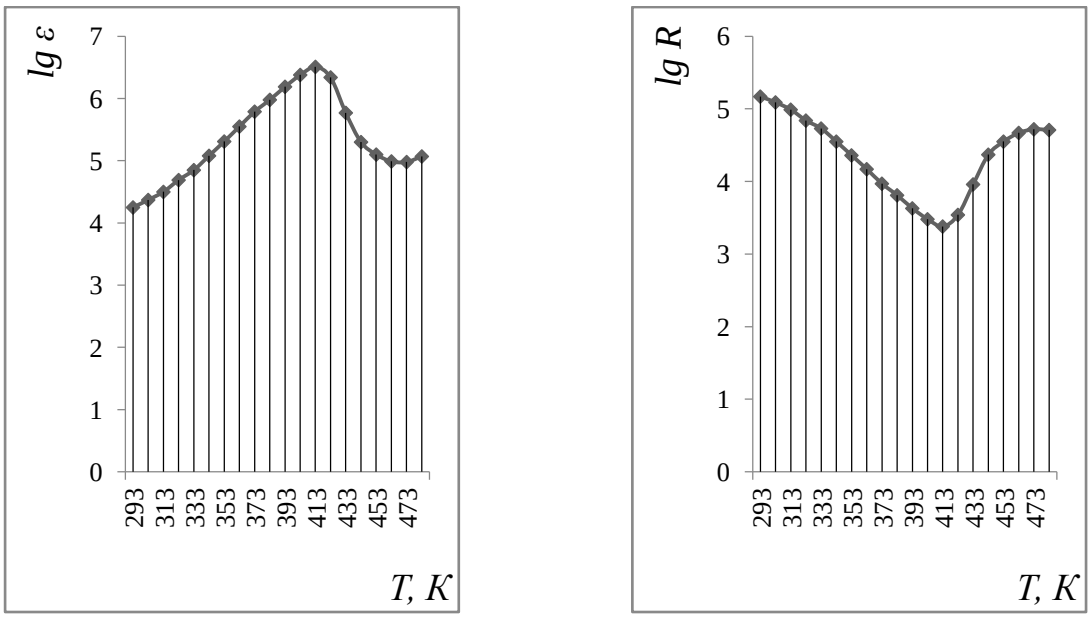

a) b)

Fig. 4. Temperature dependencies of lgε (a) and lgR (b) for $LaNa_2ZrMnO_6$ (measured at a frequency of 1 kHz)

.

Table 4. The variation of electrical capacity (C), electrical resistance (R), and dielectric constant (ε) of $LaNa_2ZrMnO_6$ within the temperature range of 293–483 K at a frequency of 1 kHz

T, K	R, Ом	ε	lgε	lgR
293	148300	17819	4.25	5.17
303	121700	23188	4.37	5.09
313	96810	31849	4.50	4.99
323	69950	49343	4.69	4.84
333	53210	70768	4.85	4.73
343	35290	120019	5.08	4.55
353	22790	206349	5.31	4.36
363	14810	353176	5.55	4.17
373	9324	612617	5.79	3.97
383	6425	965360	5.98	3.81
393	4298	1561193	6.19	3.63
403	3008	2395941	6.38	3.48
413	2384	3208176	6.51	3.38
423	3474	2212127	6.34	3.54
433	9190	592580	5.77	3.96
443	23470	197557	5.30	4.37
453	35280	124671	5.10	4.55
463	46460	97860	4.99	4.67
473	52110	95612	4.98	4.72
483	51390	117508	5.07	4.71

3. Results and discussion

By analyzing the X-ray diffraction data of $LaNa_2ZrMnO_6$ using the method described in [29], it was revealed that this zircono-manganite crystallizes with a cubic symmetry. The corresponding lattice parameters are as follows: a = 16.85 ± 0.02 Å; V^0 = 4785.46 ± 0.02 Å^3; Z = 6; $V°_{elem\ cell}$ = 795.58 ± 0.02 Å^3; $\rho_{x\text{-ray.}}$ = 5.35 g/cm^3; and $\rho_{picn.}$ = 5.30 ± 0.04 g/cm^3 [30].

The pycnometric density was determined according to [31]. Toluene was used as an indifferent liquid.

Based on the calorimetric studies presented in Fig. 3 and Table 2, $LaNa_2ZrMnO_6$ exhibits distinct anomalies in its heat capacity at temperatures of approximately 300 K and 523 K. These discontinuities in the heat capacity curve ($C°_p \sim f(T)$) likely indicate second-order phase transitions. Such transitions may be influenced by factors such as Schottky effects, variations in magnetoresistance, electrical resistance, and permittivity, potentially associated with Curie and Néel points [32, 33], as well as other contributing phenomena [34]. Considering the temperatures at which these phase transitions occur, the equations describing the temperature dependence of the heat capacity of $LaNa_2ZrMnO_6$ have been derived and are expressed as the following polynomials (J/(mol·K)):

$$C^0_{p(1)} = (1235 \pm 66) - (1169.6 \pm 62.3)\cdot 10^{-3}T - (572.5 \pm 30.5)\cdot 10^5 T^{-2} \text{ (298-398 K)}, \quad (6)$$

$$C^0_{p(2)} = (1589 \pm 85) - (2968.7 \pm 158.2)\cdot 10^{-3}T \quad \text{(398-473 K)}, \quad (7)$$

$$C^0_{p(3)} = -(619 \pm 33) + (1688.4 \pm 90.0)\cdot 10^{-3}T \quad \text{(623-673 K)}. \quad (8)$$

$$C^0_{p(4)} = (3418 \pm 182) - (6020.0 \pm 320.9)\cdot 10^{-3}T \quad \text{(523-548 K)}, \quad (9)$$

$$C^0_{p(5)} = (104 \pm 5.6) - (333.9 \pm 17.8)\cdot 10^{-3}T - (502.8 \pm 26.8)\cdot 10^5 T^{-2} \quad \text{(548 – 673 K)}, \quad (10)$$

Due to the limitations of the calorimeter's technical specifications, the standard entropy of $LaNa_2ZrMnO_6$ was determined by estimating ionic entropy increments: La^{3+} (40.4), Na^+ (34.6), Zr^{4+} (23.6), Mn^{3+} (34.7), and O^{2-} (11.7) J/(mol·K) [35].

These values were applied according to the following scheme:

$$S^o(298.15)\ LaNa_2ZrMnO_6 = S^i(298.15)\ La^{3+} + 2S^i(298.15)\ Na^+ + \\ + S^i(298.15)\ Zr^{4+} + S^i(298.15)\ Mn^{3+} + 6S^i(298.15)\ O^{2-}, \quad (11)$$

where $S^i(298.15)$ – entropic increments of ions entropic increments of ions.

The standard entropy of $LaNa_2ZrMnO_6$, calculated according to scheme (11) is 238 ± 7 J/(mol·K). The standard heat capacity of $LaNa_2\ ZrMnO_6$ was determined using an independent method based on ionic increments of heat capacity [35]. The input values for $C^i_p(298.15)$ were as follows: La^{3+} = 29.3, Na^+ = 26.8, Zr^{4+} = 22.9, Mn^{3+} = 25.0, and O^{2-} = 16.7 J/(mol·K). The calculated heat capacity was found to be 231.0 J/(mol·K), which aligns well with the experimental result of 242 ± 12 J/(mol·K), showing a deviation of only 4.8%.

Using experimental heat capacity data and the calculated standard entropy values at 25 K increments, the temperature dependencies of $C^o_p(T)$ and the thermodynamic functions S°(T), H°(T) - H°(298.15), and Φ^{xx}(T) were determined. The activation energy of electrical conductivity (ΔE) was determined by utilizing the following approach: Experimental values of temperature (T) and resistance (R) were plotted as a dot chart with markers. An exponential trend line was then added to the graph to verify that the experimental data aligns with a function of the form:

$$R_{nn} = R_0 e^{\frac{\Delta E}{2KT}}. \quad (12)$$

Using the least squares method and linear regression, we will construct a dot diagram of the dependence of lgR_{nn} от $10^4/T$ based on experimental data. Next, we add a linear trend line or create a system of equations: lgy = a + bx, где y = lg R, x = $10^4/T$ (Figure 5).

We obtain for $LaNa_2ZrMnO_6$ in the range 293-413 K the dependence lgR~*f*(1/T) (Figure 4a), which is described by the equation:

$$y = -1.2139 + \frac{1932}{T} \quad (13)$$

and let's compare it with the shape:

$$lgR_n = \frac{\Delta E}{2K} \cdot T + lgR, \quad (14)$$

then $\frac{\Delta E}{2K} = 1932K$, lgR_0=-1.2139 from where:

$$\Delta Ea = \frac{1932 \cdot 2 \cdot 1.38 \cdot 10^{-23}}{1.6 \cdot 10^{-19}} = 0.333\ eV, \quad (15)$$

where $k = 1.38 \cdot 10^{-23}$ Дж·К$^{-1}$ – Boltzmann's constant, e = $1.6 \cdot 10^{-19}$ KL – elementary charge.

The band gap width (ΔE_g) of the test substance was calculated using the formula:

$$\Delta E_g = \frac{2k\ T_1 T_2}{0.43(T_2 - T_1)} lg \frac{R_1}{R_2}, \quad (16)$$

where k - Boltzmann's constant, equal to $8.617302 \cdot 10^5$ eV. K^{-1}, R_1 – resistance at T_1, R_2 - resistance at T_2.

$$\Delta E_g = \frac{2 \cdot 0.000086173 \cdot 293 \cdot 413}{0.43(413-293)} \cdot \frac{5.17}{4.71} = 0.44\ eV. \quad (17)$$

The $LaNa_2ZrMnO_6$ compound in the range of 293-413 K has a band gap of 0.44 eV. The activation energy shows how much energy is required to transfer charge carriers (electrons or holes) in a material A value of 0.333 eV indicates that at room temperature (293 K) and above, the $LaNa_2ZrMnO_6$ material has a moderate energy required to activate conduction. This value helps to understand how easily a material can conduct electric current when heated. The band gap width determines the energy gap between the valence and conductive zones in the material. A value of 0.44 eV indicates that $LaNa_2ZrMnO_6$ is a semiconductor with a narrow band gap. Materials with these characteristics can be used in a variety of applications, including thermal sensors and devices operating at low temperatures.

.

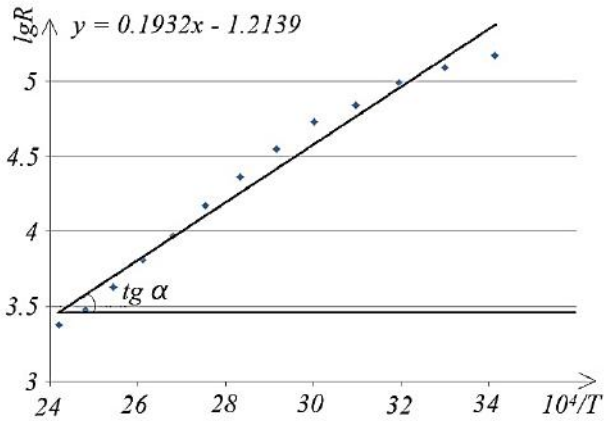

Fig. 5. Linear dependence of lg R ~ 10^4/T in the range - 293-413 K α

Electrophysical studies reveal that the material demonstrates semiconductor conductivity within the temperature range of 293–413 K. Beyond this range, from 413 to 473 K, it transitions to metallic conductivity. The dielectric constant of this zircono-manganite at 293 K and a frequency of 1 kHz is 14 times higher than that of the standard $BaTiO_3$ (1296), and 54 times higher at 483 K ($BaTiO_3$, ε = 2159) ($LaNa_2ZrMnO_6$, ε = 117508). At the transition temperature of 413 K, where the material shifts from semiconductor to metallic conductivity, the highest value of ε is observed at 3208176. This remarkable value surpasses the dielectric constant of the reference material $BaTiO_3$ at the same temperature (1626) by an impressive factor of 1973, highlighting the material's exceptional dielectric properties in this range.

The conduction mechanism for La and Zr in $LaNa_2ZrMnO_6$.

When La and Zr atoms are partially replaced, lanthanum and zirconium atoms can interact with other elements in the crystal lattice, creating unique energy levels. In this case, the conduction mechanism may look like this. La and Zr atoms have different charge states that affect the conductivity of the material. For example, the La atom may be in the La^{3+} state, and the Zr atom in the Zr^{4+} state. La and Zr atoms can create acceptor levels inside the band gap. These levels will be close to the valence band and separated by an energy gap that determines the activation energy.

When the bonds between atoms are heated and weakened, new covalent bonds can form. An electron can move from one atom to another, forming additional covalent bonds. Such a transition requires energy ΔE_a, which can be significantly less than the energy ΔE required for the transition of an electron into the conduction band.

When an electron leaves an atom and moves to another, the atom from which the electron left forms a hole. In the case of substitution of La and Zr atoms, they can serve as acceptors, and the holes they create will be located inside the band gap.

When an external electric field is applied, the holes in the valence band move due to the abrupt transition of electrons. This leads to p-type conductivity, in which holes are the main charge carriers. Thus, with partial substitution of La and Zr atoms, a conduction mechanism associated with the formation of acceptor levels and hole conduction is possible. The above studies show that this compound is of interest for semiconductor technology and as a RAM material.

4. Conclusions

1. $LaNa_2ZrMnO_6$ zircono-manganites, which crystallizes in cubic syngony, were synthesized for the first time by high-temperature synthesis.
2. The temperature dependence of the heat capacity of $LaNa_2ZrMnO_6$ was investigated using dynamic calorimetry over the temperature range of 298-673 K.
3. It was found that the $C^\circ_p \sim f(T)$ curve exhibits anomalous jumps in heat capacity at 398 K and 523 K, likely corresponding to second-order phase transitions, which indicate the presence of valuable physicochemical properties.

4. Taking into account the phase transition temperatures, the equations describing the temperature dependence of heat capacity have been calculated.

5. Fundamental values have been determined, including the experimental standard heat capacity and the calculated standard entropy of $LaNa_2\ ZrMnO_6$.

6. Based on the experimental $C^{\circ}_{p}(T)$ data and the estimated S°(298.15) values at 25 K intervals, the temperature dependence of $C^{\circ}_{p}(T)$ and the thermodynamic functions S°(T), H°(T) - H°(298.15), and Φ^{xx}(T) were calculated.

7. The band gap and activation energies of $LaNa_2ZrMnO_6$ conductivity are calculated and it is established that this semiconductor can be classified as a p- type semiconductor.

8. Electrophysical studies have shown that $LaNa_2ZrMnO_6$ is of interest for semiconductor technology with high RAM values.

9. The research results are valuable for the targeted synthesis of similar compounds with tailored properties, physicochemical modeling of processes involving the studied compound, and applications in the chemistry and technology of semiconductor materials. Additionally, the obtained data serve as source information for uploading fundamental thermodynamic constants into databases.

Conflict of interest statement

The authors declare that they have no conflict of interest in relation to this research, whether financial, personal, authorship or otherwise, that could affect the research and its results presented in this paper.

CRediT author statement

Turdiyev M.T., Kasenov B.K., Nukhuly A.: conceptualization, methodology, writing – review and editing; **Bekturganov Zh.S., Kasenova Sh.B.:** formal analysis, writing – original draft preparation; **Sagintaeva Zh.I., Kuanyshbekov E.E.:** investigation, writing – original draft preparation. The final manuscript was read and approved by all authors.

References

1 Karpasyuk V.K., Smirnov A.M., Badelin A.G. (2015) Features of constructing magnetic field sensors based on the colossal magnetoresistance effect. *Caspian Journal: Management and High Technologies*, 4, 291 – 297. [in Russian]. Available at: https://hi-tech.asu-edu.ru/files/4(32)/291-297.pdf

2 Menglei Li, Hengxin Tan, Wenhui Duan (2020) Hexagonal rare-earth manganites and ferrites: a review of improper ferroelectricity, magnetoelectric coupling, and unusual domain walls. *Phys. Chem. Chem. Phys.*, 22, 14415 – 14432. https://doi.org/10.1039/D0CP02195D

3 Yang Shen, Ce-Wen Nan. (2023) High thermal conductivity dielectric polymers show record high capacitive performance at high temperatures. *National Science Review*, 10 (11), nwad224. https://doi.org/10.1093/nsr/nwad224

4 Chabushkin A.N., Lyapin A.A., Ryabochkina P.A., Antipov O.L., Artemov S.A., Lomonova E.E. (2018) CW and Q-switched 2 m solid-state laser on ZrO_2–Y_2O_3–HO crystals pumped by a Tm fiber laser. *Laser Phys*, 28 (3), 035803. https://doi.org/10.1088/1555-6611/aa962f

5 Zhirenkina N.V. (2022) Technology of Powder Synthesis Based on Zirconium Dioxide for the Production of High-Density Ceramics. 2.6.14. Technology of Silicate and Refractory Nonmetallic Materials. Dissertation for the Degree of Candidate of Technical Sciences. Yekaterinburg, 159.

6 Arachi Y., Sakai H., Yamamoto O., Takeda Y., Imanishai N. (1999) Electrical conductivity of the ZrO_2–Ln_2O_3 (Ln=lanthanides) system. *Solid State Ionics*, 121, 1-4, 133 –139. https://doi.org/10.1016/s0167-2738(98)00540-2

7 Borik M.A, Bublik V.T., Kulebyakin A.V., Lomonova E.E., Milovich F.O., Myzina V.A., Osiko V.V., Tabachkova N.Y. (2014) Phase composition, structure and mechanical properties of PSZ (partially stabilized zirconia) crystals as a function of stabilizing impurity content. *Alloys and Compounds*, 586, 231 – 235. https://doi.org/10.1016/j.jallcom.2013.01.126

8 Zadorozhnaya O.Y., Napochatov Y.K., Agarkova E.A., Tiunova O.V. (2020) Layered sold-electrolyte membranes based on zirconia: production technology. *Russian Journal of Electrochemistry*, 56 (2), 124 – 131. https://doi.org/10.1134/S1023193520020123

9 Aktas B., Tekeli S., Kucuktuvek M. (2014) Electrical Conductivity of Er_2O_3-Doped c-ZrO_2 Ceramics. *J. of Materi Eng and Perform*, 23, 349–355. https://doi.org/10.1007/s11665-013-0750-5

10 Borik M.A., Volkova T.V., Kulebyakin A.V., Kuritsyna I.E., Lomonova E.E., Myzina V.A., Milovich F.O., Ryabochkina P.A., Tabachkova N.Yu., Zentsova A.I., Popov P.A. (2020) Thermal Conductivity of Cubic ZrO_2 Single Crystals Stabilized with Yttrium Oxide. *Physics of the Solid State*, 62, 1, 235 – 239. https://doi.org/10.1134/s1063783420010072

.

11 Guskov V.N. Gavrichev K.S. Gagarin P.G., Guskov A.V. (2019) Thermodynamic Functions of Complex Zirconia Based Lanthanide Oxides-Pyrochlores $Ln_2Zr_2O_7$ (Ln = La, Pr, Sm, Eu, Gd) and Fluorites $Ln_2O_3 \cdot 2ZrO_2$ (Ln = Tb, Ho, Er, Tm). *Russ. J. Inorg. Chem*, 64, 10, 1265 - 1281. https://doi.org/10.1134/S0036023619100048

12 Stroeva A.Yu., Vorotnikov V.A., Bervitskaya O.S., Ichetovkina V.A., Ichetovkin Z.N., Duvakin A.M., Ananchenko B.A., Kuzmin A.V. (2024) The effect of synthesis technique on the microstructure of doped lanthanum zirconate materials. *Electrochemical Energetics*, 24, 4, 185 - 190. [in Russian]. https://doi.org/10.18500/1608-4039-2024-24-4-185-190

13 Proshkin S. (2018) Multipurpose calorimeter to measure thermophysical properties ARPN *Journal of Engineering and Applied Sciences*, 2018, 13, 5, 1827 – 1832.

14 Bychinskii V.A., Tupitsyn A.A., Mukhetdinova A.V., Chudnenko K.V., Fomichev S.V., Krenev V.A. (2013) Estimation of the heat capacity of individual substances on the basis of experimental enthalpy increments. *Russian Journal of Inorganic Chemistry*, 58(9), 1079 – 1084. https://doi.org/10.1134/s0036023613090040

15 Rustembekov K.T., Sharipova Z.M., Dyusekeeva A.T. (2012) Thermochemistry of selenates of some s- d-elements. *Journal of international Scientific Publications: Materials, Methods & Technologies*, 6, 286 - 295. Available at: https://www.scientific-publications.net/download/materials-methods-and-technologies-2012-2.pdf

16 Bodryakov V.Yu., Bykov A.A. (2015) Correlation characteristics of the temperature coefficient of volumetric expansion and heat capacity of corundum. *Glass and ceramics*, 2, 30. [in Russian]. https://doi.org/10.1007/s10717-015-9726-2

17 Kassenov B.K., Kassenova Sh.B., Sagintaeva Zh.I., Kuanyshbekov E.E., Turtubaeva M.O. (2020) Calorimetric Research into the Heat Capacity of Novel Nano-sized Cobalt(Nickelite)-Cuprate-Manganites of $LaBaMe^{II}CuMnO_6$ (Me^{II}= Co, Ni) and their Thermodynamic Properties. *Eurasian Chemico-Technological Journal*, 22, 27 – 33. https://doi.org/10.18321/ectj927

18 Rustembekov K.T., Kasymova M.S., Kaikenov D.A., Fomin V.N., Aldabergenova S.K., Toybek A.A. (2019) Calorimetry of new double dysprosium tellurite. *Bulletin of Karaganda university. Chemistry series*, 93, 1, 60 – 65. https://doi.org/10.31489/2019ch1/60-65

19 Kasenova Sh.B., Sagintaeva Zh.I., Kasenov B.K., Ermaganbetov K.T., Kuanyshbekov E.E., Seisenova A.A., Smagulova D.I. (2013) Calorimetry and thermodynamic properties of nanostructured cuprate-manganite of lanthanum and strontium $LaSr_2CuMnO_6$. *News of NAS RK. Chemical sciences series*, 401, 5, 85 - 89. [in Russian]. Available at: https://nauka.kz/page.php?page_id=964&new&page=7845

20 Kasenov B.K., Kasenova Sh. B., Sagintaeva Zh.I., Kuanyshbekov E.E., Nuhuly A. Heat capacity of the new nano-size cobalt-cuprato-manganite $LaLi_2CoCuMnO_6$ in the interval of 298.15-673 K and its thermodynamic properties. *Applied solid state Chemistry*, 2018, 5 (4), 82-85. https://doi.org/10.18572/2619-0141-2018-4-5-82-85

21 Rustembekov K., Dyusekeyeva A., Sharipova Z., Amanzhan A. (2012) Syntesis and thermochemistry of new metal-mixed tellurites. *Chemical Bulletin of Kazakh National University*, 65(1), 170-174. https://doi.org/10.15328/chemb_2012_1170-174

22 Kasenov B., Kasenova S., Sagintaeva Z., Kuanyshbekov E., Bekturganov Z., Zeynidenov A. (2022) Electrophysical properties of new nanostuctured copper-zinc manganite of lanthanum and magnesium. *Eurasian Physical Technical Journal*, 2022, *19*(2(40), 42–47. https://doi.org/10.31489/2022No2/42-47

23 *Operation Manual. RLC meter (LCR-781)*. Moscow: PriST CJSC, 2012, 3 [in Russian]. Available at: https://prist.ru/upload/iblock/5a9/zv6bz0pv1oji5hdghyqzf8jwi26uaizw/Izmeritel-LCR_78200_5-mod._.pdf

24 Al Jaafari F.M.D., Korotkov L.N., Tolstykh N.A., Emelianov N.A., Pankova M.A., Popov S.V. (2023) Dielectric properties of mixed $BaTiO_3$–$SrTiO_3$ nanocomposites. *Bulletin of the Russian Academy of Sciences: Physics*, 87, 9, 1302 - 1307. https://doi.org/10.3103/S1062873823703197

25 Dikov R.V. (2022) Study of the Electrophysical Properties of Ferroelectric Piezo-Ceramics Based on Barium Titanate. Dissertation for the Degree of Candidate of Physical and Mathematical Sciences. 1.3.5. *Physical Electronics*. Volgograd, 128. [in Russian]. Available at: https://www.vstu.ru/upload/iblock/67e/67e5be44aa5e9d2ed1fecbb761609f3a.pdf

26 Wang J.J., Meng F.Y., Ma X.Q., Xu M.X., Chen L.Q. (2010) Lattice, elastic, polarization, and electrostrictive properties of $BaTiO_3$ from first-principles *J. Appl. Phys.* 108, 034107. https://doi.org/10.1063/1.3462441

27 Mataev M., Madiyarova A., Patrin G., Abdraimova M., Nurbekova M. Durmenbayeva Zh. (2024) Synthesis of New Complex Ferrite $Li_{0.5}MnFe_{1.5}O_4$: Chemical-Physical and Electrophysical Research, *Materials*, 17, 3754. https://doi.org/10.3390/ma17153754

28 Kasenov B.K., Kasenova Sh.B., Sagintaeva Zh.I., Kuanyshbekov E.E., Mukhtar A.A. (2022) Thermodynamic and Electrophysics of New $LaCaCuZnMnO_6$ Copper – Zinc Manganite of Lanthanum and Calcium. *High Temperature*, 60, 4, 474 - 478. https://doi.org/10.1134/S0018151X22020225

29 Guo G., Goldfeder J., Lan L., Ray A., Hanming Yang A., Chen B., J. L. Billinge S., Lipson H. (2024) Towards end-to-end structure determination from x-ray diffraction data using deep learning. *npj Comput Mater*, 10, 209. https://doi.org/10.1038/s41524-024-01401-8

30 Turdiyev M.T., Kasenov B.K., Nukhuly A., Stoev M., Sagintaeva Zh.I., Kasenova Sh.B., Kuanyshbekov E.E. (2024) New zircon-manganites of lanthanum and alkali metals. *Chemical Bulletin of Kazakh National University,* 111, 1-2, 23 - 27. https://doi.org/10.15328/cb1372

31 Viana, M,. Jouannin P., Pontier C., Chulia D. (2002) About pycnometric density measurements. *Talanta*, 57(3), 583 – 593. https://doi.org/10.1016/S0039-9140(02)00058-9

32 Hemminger W., Höhne G. (1984) *Calorimetry: Fundamentals and Practice.* Weinheim: Verlag Chemie, 310 p.

33 Goldenfeld N. *Lectures on Phase Transitions and the Renormalization Group*. CRC Press, Taylor & Francis Group, 1992. eBook published 2018. 420 p. https://doi.org/10.1201/9780429493492

34 Xue Y., Shen Z., Wu Z., Song C. (2023) Thickness dependence of the critical temperature and magnetic coupling in multilayer Cr_2 Sn_2 Te_6 . *Physical Review B.*, 108, 064416. https://doi.org/10.1103/PhysRevB.108.064416

35 Melchakova O.V., Zaitseva P.V., Mayorova A.V., Kulikova T.V., Pechishcheva N.V., Shunyaev K.Yu. (2019) Calculation of the Thermodynamic Properties of Metal Perrhenates and Their Use in Modeling Sample Preparation for Chemical Analysis. *Analytics and Control,* 23, 4, 570 – 579. https://doi.org/10.15826/analitika.2019.23.4.015 [in Russian].

AUTHORS' INFORMATION

Turdiyev, Myktybek Tolkynbayuly – PhD student, Master, L.N. Gumilyov Eurasian National University, Astana, Kazakhstan, https://orcid.org/0009-0007-0187-6804; turdiev.miktibek@gmail.com

Kasenov, Bulat Kunurovich – Doctor of chemical sciences, Professor, Head of the Laboratory of thermochemical processes, Abishev Chemical-Metallurgical Institute, Karaganda, Kazakhstan; https://doi.org/0000-0001-9394-0592; kasenov1946@mail.ru

Nukhuly, Altynbek – Doctor of chemical sciences, Professor, L.N. Gumilyov Eurasian National University, Astana, Kazakhstan; https://doi.org/0000-0001-5006-879X; nukhuly@mail.ru

Bekturganov, Zhanaly Sultanovich – Doctor of chemical sciences, Professor, Department of radiophysics and electronics, E.A. Buketov Karaganda University, Karaganda, Kazakhstan; https://doi.org/0000-0002-6487-7835; zhbekturganov@gmail.com

Kasenova, Shuga Bulatovna – Doctor of chemical sciences, Professor, Chief researcher, Laboratory of thermochemical processes, Abishev Chemical-Metallurgical Institute, Karaganda, Kazakhstan; https://doi.org/0000-0001-9755-7478; kasenovashuga@mail.ru

Sagintaeva, Zhenisgul Imangalievna – Candidate of chemical sciences, Associate Professor, Leading Researcher, Laboratory of thermochemical processes, Abishev Chemical-Metallurgical Institute, Karaganda, Kazakhstan; https://doi.org/0000-0001-8655-356X; kai_sagintaeva@mail.ru

Kuanyshbekov, Erbolat Ermekovich – Master (Eng.), Senior Researcher, Laboratory of thermochemical processes, Abishev Chemical-Metallurgical Institute, Karaganda, Kazakhstan; https://doi.org/0000-0001-9172-9566, mr.ero1986@mail.ru

.

EURASIAN PHYSICAL TECHNICAL JOURNAL

2025, Volume 22, No. 3 (53)

https://doi.org/10.31489/2025N3/48-54

Received: 16/02/2025 Revised: 12/08/2025 Accepted: 25/09/2025 Published online: 30/09/2025

Research Article

Open Access under the CC BY -NC-ND 4.0 license

UDC 535.37

SYNTHESIS OF SILVER NANOPARTICLES AND THEIR INFLUENCE ON THE FLUORESCENCE AND ABSORPTION OF ANTHRACENE

Yusupova Zh.B.

Institute of Molecular Nanophotonics, Karaganda Buketov University, Karaganda, Kazakhstan
Corresponding author: yusupova-zh@mail.ru

Abstract. *The synthesis process of island silver films was investigated, with a focus on the role of solution pH as a key parameter for successful film formation. It was determined that the optimal pH for effective synthesis is 8. The results of particle distribution analysis by Feret diameter, performed using the ImageJ software, are also presented. The distribution histogram confirmed that the chemically deposited film is of high quality. The developed synthesis method enables the fabrication of silver nanoparticle films with tailored properties. The influence of the synthesized silver films on the luminescent properties of anthracene was studied, highlighting their potential applications in photonics and sensor technologies.*

Keywords: island films, silver nanoparticles, anthracene, pH, ImageJ.

1. Introduction

In recent years, there has been rapid development in research devoted to localized surface plasmon resonance (LSPR) of metallic nanoparticles (NPs), which has contributed to the emergence of advanced analytical techniques and technological solutions [1]. When interacting with a light source, NPs made of metals such as silver, gold, copper, or aluminum exhibit collective oscillations of free electrons, leading to a significant enhancement of the electromagnetic field in their vicinity. It has been reported that the electric field intensity near such nanoparticles can increase by a factor of up to 10^4 [2]. Fluorophore or analyte molecules located in close proximity to these NPs experience intense external influence, which accelerates photocatalytic reactions [3], enhances luminescence, and facilitates surface-enhanced Raman scattering (SERS) [4, 5].

Plasmon-enhanced fluorescence is a well-studied phenomenon. Research shows that the fluorescence of dye molecules can either be enhanced or quenched depending on the distance between the nanoparticles and the emitting species, as well as their mutual dipole orientation. This effect finds applications in devices based on the control of radiative processes. The LSPR of metallic nanoparticles influences the relaxation dynamics of photoexcited emitters through the Purcell effect [6, 7] and also contributes to the reduction of the lasing threshold in dye-based lasers. Plasmonic effects are employed in the development of materials with tailored optical properties, in sensing technologies, and in optoelectronic devices [8, 9].

Particular interest lies in the influence of plasmons on long-lived luminescence processes associated with spin effects. Long-lived triplet states are crucial for fundamental processes and have significant practical relevance. For instance, prolonged emission of molecular probes is used in bioimaging to improve the signal-to-noise ratio. Triplet states are also utilized in photosynthetic systems for the generation of singlet oxygen, which is essential in photodynamic therapy, antibacterial treatments, and in the treatment of skin and

respiratory diseases. Moreover, triplet states of organic compounds find applications in OLED technologies, solar cells, and transistors [10, 11].

This article presents the results of silver nanoparticle film synthesis, surface analysis, and measurement data demonstrating the positive effect of plasmonic enhancement on the luminescent properties of anthracene.

2. Experimental section and measurements details

Anthracene was selected as the luminescent molecule and was purchased from Sigma-Aldrich. For the synthesis of silver island films, the following reagents were used: $AgNO_3$, NaOH, NH_4 OH, D-glucose, and polyvinyl alcohol (PVA), all of analytical grade (Sigma-Aldrich). Ultrapure water obtained using the Smart S15 UVF system (Drawell) was used for sample preparation.

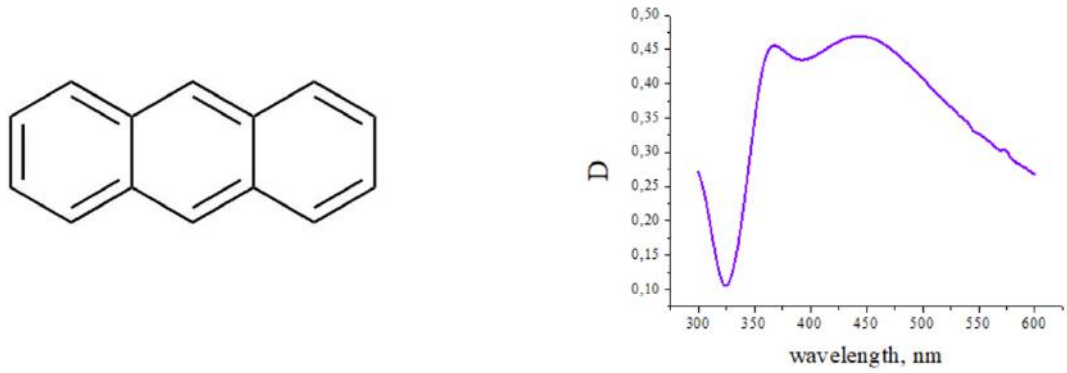

a) b)

Fig. 1. Molecular structure (a) of the studied compound and the absorption spectrum (b) of the silver island film (SIF).

The chemical deposition procedure used for the fabrication of silver island films (SIFs) was based on the method described in [12]. The synthesis involves several key steps (fig. 2):

Fig. 2. Key steps of synthesis process

When the synthesis is carried out correctly, it is assumed that the process can be controlled. Key factors that influence the process include the pH of the solution and the amount of reducing agent.

A 5% sodium hydroxide (NaOH) solution is added to the silver nitrate ($AgNO_3$) solution (process 1), resulting in the formation of a brown precipitate — silver oxide (Ag_2 O).

$$2AgNO_3 + 2NaOH = Ag_2O\downarrow + 2NaNO_3 + H_2O \quad (1)$$

Next, ammonium hydroxide (NH_4 OH) was added to the solution (process 2), dissolving the silver precipitates and forming an ammonia complex. A 25% solution of ammonium hydroxide was used for the synthesis. Previous studies have shown a relationship between the size of silver nanoparticles and the concentration of ammonia, as well as the pH of the medium during the reduction process.

When ammonium hydroxide was introduced into the silver nitrate solution, the pH initially reached 10, indicating an alkaline environment typical for ammonia solutions. However, over time, the pH gradually decreased to 8 and continued to lower, suggesting the release of ammonium ions (NH_4^+) and their reaction with water. This may indicate a weakening of the buffer capacity of the solution, affecting the pH

.

stabilization during synthesis. The decrease in pH accelerates the synthesis of silver nanoparticles and facilitates the formation of high-quality silver films. The possible reason for the acceleration of the reaction is the optimal conditions for the silver-ammonia complex and more efficient reduction of silver at pH 8 [13]. Furthermore, continuous mechanical stirring on a magnetic stirrer might have enhanced the contact between the components and accelerated the chemical reactions, which could also have contributed to the further reduction of pH.

$$Ag_2O + 4NH_4OH \rightarrow 2[Ag(NH_3)_2]OH + 3H_2O \quad (2)$$

The transparent solution is placed in a cooling bath to cool down to a temperature of -5°C. This step is necessary to ensure that the synthesis of silver nanoparticles occurs slowly until the temperature rises to 30°C. Under these conditions, the reduction of silver nanoparticles proceeds gradually and uniformly. Once the solution reaches the low temperature, the substrates are immersed, and glucose is added (process 3), which aids in the reduction of silver.

$$2[(NH_3)_2OH + C_2H_{12}O_6 \rightarrow 2Ag\downarrow + 4NH_3 + C_2H_{12}O_7 + H_2O] \quad (3)$$

After the addition of glucose, the pH level remained at 8, which is an ideal condition for synthesis. The solution was then heated to 30°C. Once the temperature reached 14-16°C, the solution began to change color from transparent to golden-yellow. At temperatures between 18-19°C, the solution turned dark green. At this stage, the films obtained had an optical density of 0.3-0.5. If the temperature was allowed to rise to 21-25°C, the film would compact further, and the optical density would increase to 0.4-0.8. After the synthesis was completed, the subsequent steps were carried out according to the procedure described in the literature [12]. This study refined the key stages of the synthesis, particularly the conditions for the reduction of silver nanoparticles. The annealing was performed at 200°C for 90 minutes.

Figure 3 presents images of silver nanoparticles, the absorption spectrum, and the particle size distribution histogram based on Feret's method. The SEM image was obtained using a Helios 5 CX scanning electron microscope. According to the data from the scanning electron microscope, the average particle size was found to be 95±30 nm. These films are characterized by the presence of an absorption band in the visible region of the spectrum (see Figure 2). The polymer coatings with an anthracene concentration of 1×10^{-3} mol/l were applied using the drop-casting method.

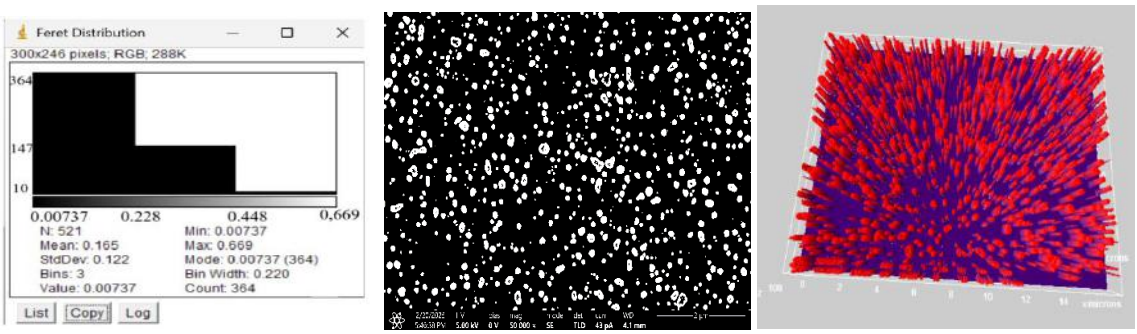

a) b) c)

Fig. 3. Histogram (a), SEM image (b), and 3D image of the particles (c).

For further investigation of the film surface, the ImageJ software was used to analyze the images obtained via scanning electron microscopy (SEM). The program provided data on the distribution of particles based on Feret's diameters. However, it is important to note that while ImageJ effectively analyzes SEM images, the results may depend on the size and orientation of the particles, which can affect their visibility and measurement accuracy. Therefore, SEM remains the primary method for detailed observation and analysis of particle structure.

In the process of analyzing 521 particles found in an image measuring 16 × 11.40 μm, the following results were obtained: for each particle, the Feret diameter (the largest distance between two points on the outer boundary of the particle) was measured. The minimum Feret value was 0.00737 μm, and the maximum

was 0.669 μm, indicating a wide range of particle sizes. The average particle diameter was 0.165 μm, and the standard deviation was 0.122 μm, suggesting significant variability in particle sizes. The modal value for the particles was 0.00737 μm, which represents the most frequently occurring size.

The histogram of particle distribution showed that 364 particles have a size corresponding to the bin of 0.00737 μm (the most frequent value), 124 particles correspond to the bin of 0.228 μm, 10 particles correspond to the bin of 0.448 μm, and fewer than 10 particles have a size around 0.669 μm. The bin size in the histogram was 0.220 μm, which defines the resolution of the histogram and allows for the assessment of the distribution of particle sizes.

The program determines the particle sizes in pixels/microns, which is incorrect to directly compare these units with the actual particle sizes in the film. A total of 521 particles were involved in the analysis, and the program determined that 73% showed smaller sizes, 25% showed medium sizes, and 2% showed large sizes. Based on the obtained results, it can be concluded that 73% of the particles correspond to the average size of 95±30 nm, which indicates the high quality of the synthesis process.

Additionally, the 3D image (fig.2, (c)) was generated based on SEM images using the ImageJ software, which allows surface topography visualization. Specifically, the "3D Surface Plot" module was used to create a volumetric reconstruction based on the brightness contrast of the image.

Particles with a diameter in the range of 50–100 nm are considered high-quality for various applications such as sensors, catalysts, and optical materials. According to research, particle size within this range is optimal for achieving high performance in these areas due to their enhanced optical, chemical, and catalytic properties. Silver particles with sizes ranging from 50–150 nm can effectively interact with the surrounding environment, especially in the context of plasmonic resonance. This interaction leads to fluorescence enhancement, which is particularly important for the application of nanoparticles in photonics and other optical devices [14, 15].

The absorption spectra of the samples were recorded using a Cary-300 spectrophotometer (Agilent Technologies). Fluorescent and long-lived luminescent spectra were recorded using an Eclipse spectrofluorometer (Agilent Technologies). In the case of long-lived luminescence, the spectra were recorded with a delay of 300 μs after the pulse from the xenon lamp.

Fluorescence decay kinetics measurements were conducted using the time-correlated single-photon counting (TCSPC) method with an FLS1000 spectrometer (Edinburgh Instruments). Excitation was performed with a laser at a wavelength of 375 nm and a pulse duration of 120 ps. The fluorescence lifetime analysis was performed using Fluoracle software (Edinburgh Instruments). For the registration of long-lived luminescence decay kinetics, the FLS1000 spectrometer was also used. The sample was excited at 362 nm using an Nd:YAG laser system LQ529, equipped with an optical parametric generator LP604 and a second-harmonic generator LG350 (SolarLS). To prevent contact with oxygen, the samples were vacuumed in an Optistat DN-V cryostat (Oxford Instruments). All measurements were carried out at a temperature of 293 K.

3. Results and Discussion

The absorption spectrum of silver nanoparticles (Figure 4, curve 3) in the film shows a broad band with maxima at 368 and 444 nm, which coincides well with the absorption and fluorescence spectra of anthracene (Figure 4, curves 1, 2). This indicates that the conditions for the manifestation of plasmon resonance in the photonics of lumophore molecules are met [16-18]. The absorption maxima of anthracene occur at 362 nm, and the fluorescence maxima occur at 404 nm.

Illustration 5 shows the influence of silver nanoparticles on the optical properties of anthracene. The silver nanoparticles contributed to a 1.2-fold increase in the absorption intensity of anthracene, and the fluorescence intensity of anthracene increased by 2.5 times. An increase in the electric field intensity near the surface during the excitation of surface plasmons leads to an increase in the intensity of fluorescence spectra [19].

Figure 6 shows the fluorescence decay kinetics of anthracene (1) and in the presence of silver nanoparticles (2). The presence of silver nanoparticles increased the fluorescence intensity and also shortened the fluorescence lifetime by a factor of 1.3. In silver island films, an increase in the decay rate of fast fluorescence of molecules is often observed [20, 21]. The reason for this phenomenon lies in the interaction between the electrons of silver particles and the fluorophore molecule.

.

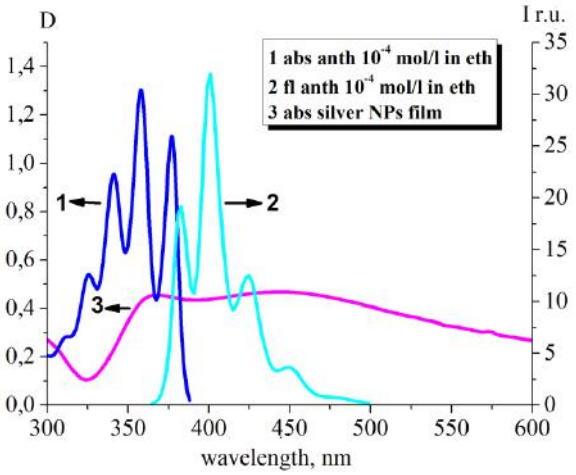

Fig. 4. Absorption and fluorescence spectra of anthracene (C = 10^{-4} mol/L in ethanol) and the absorption spectrum of the silver nanoparticle film.

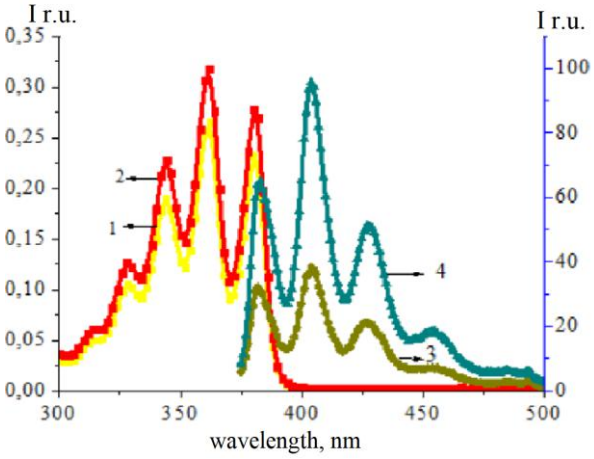

Fig. 5. Influence of silver nanoparticles on the absorption spectra (1,2) and fluorescence spectra (3,4) of anthracene in PVB films (C = 10^{-3}, 4% PVB). Curves 1 and 3 represent anthracene films on quartz substrates; curves 2 and 4 represent anthracene on the surface of silver nanoparticles

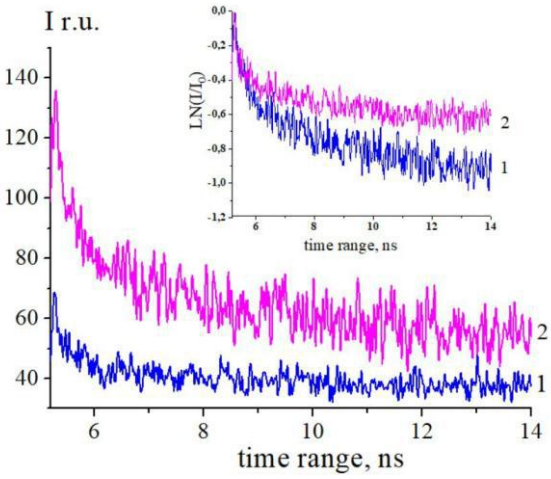

Fig. 6. Kinetics of fast fluorescence of anthracene (1) and in the presence of silver nanoparticles (2)

The process of transition between the excited and ground states of the fluorescent molecule is accelerated, which leads to a reduction in the fluorescence lifetime, an increase in its quantum yield, and a rise in the proportion of non-radiative processes in the transitions from the excited state [20-23].

The spectral characteristics of anthracene on quartz and in the presence of silver nanoparticles are summarized in Table 1. It can be seen that silver island films enhance the fluorescence intensity and influence the excited-state lifetime.

Table 1. Spectral data of anthracene in the presence of silver nanoparticles

	D	λ_{ex} *(nm)*	I_{fl}	λ_{em} *(nm)*	τ *(ns)*
Anthracene on Q	0,26	362	37	404	4,7
Anthracene on SIF	0,31	362	94	404	3,7

As can be seen from Table 1, the optical density (D) of anthracene on silver island films (SIF) shows a slight increase compared to quartz, rising from 0.26 to 0.31, indicating enhanced absorption properties. More significantly, the fluorescence intensity (I_f) increases by approximately 2.5 times, demonstrating a strong enhancement of emission in the presence of silver nanoparticles. Concurrently, the fluorescence lifetime (τ) decreases from 4.7 ns to 3.7 ns, an approximately 1.3-fold reduction, which suggests an acceleration of radiative decay processes. This phenomenon, known as plasmon–fluorophore coupling, arises from the interaction between the localized surface plasmons of silver nanoparticles and anthracene fluorophores, resulting in enhanced emission intensity and reduced fluorescence lifetime. These results underline the important role of silver nanoparticles in modifying the photophysical properties of anthracene, with potential applications in sensing and optoelectronic devices [8, 9].

4. Conclusions

As a result of the conducted research, island silver films were synthesized using the reduction method in a silver nitrate solution. Special attention was given to the role of the solution pH as a key parameter influencing the nanoparticle synthesis process. The use of ammonium hydroxide helped stabilize the pH at a level optimal for the formation of silver nanoparticles. The particle distribution histogram by Feret, obtained using the ImageJ program, showed that the film synthesized by the chemical deposition method was relatively homogeneous, with the majority of particles having an average size of silver nanoparticles.

The study of the influence of the synthesized island silver films on the luminescent properties of anthracene showed that the presence of silver nanoparticles leads to a significant increase in the fluorescence intensity of anthracene by 2.5 times. This enhancement is associated with the plasmon resonance effect and the intensification of the electric field near the surface of the nanoparticles. The lifetime of the excited state of anthracene molecules near silver nanoparticles is reduced by 1.3 times, confirming the impact of the plasmon effect on the transition between excited and ground states.The obtained results demonstrate that silver nanoparticles can effectively modify the fluorescence of anthracene molecules, opening up prospects for further research in the fields of photonics, sensor technologies, and biomedicine.

This study emphasizes the importance of optimizing nanoparticle synthesis conditions and their interaction with fluorophore molecules, which could form the basis for the development of new materials with enhanced optical characteristics.

Funding

This research is funded by the Science Committee of the Ministry of Science and Higher Education of the Republic of Kazakhstan (Grant No. AP23490195).

References

1. Novotny L., Hecht B. (2006) *Principles of nano-optics* (p. 539). Cambridge University Press. https://doi.org/10.1017/CBO9780511813535

2. Harrison R.K., Ben-Yakar A. (2010) Role of near-field enhancement in plasmonic laser nanoablation using gold nanorods on silicon substrate. *Optics Express*, 18**,** 22556–22571. https://doi.org/10.1364/OE.18.022556

.

3. Omarova G.S., Serikov T M., Seliverstova E.V., Auzhanova A.A., Ibrayev N.Kh. (2024) Influence of plasmon effect on the sensitization of titanium dioxide by dye molecules. *Eurasian Physical Technical Journal,* 21(47), 49–56. https://doi.org/10.31489/2024No1/49-56

4. Xiao X.H., Rodriguez R.S., Haynes C.L., Ozaki Y., Zhu B. (2021) *Surface-enhanced Raman spectroscopy***.** Springer Nature. https://doi.org/10.1038/s43586-021-00083-6

5. Brosseau C.L., Colina A., Perales-Rondon J.V., Wilson A.J., Joshi P.B., Ren B., Wang X. (2023) Electrochemical surface-enhanced Raman spectroscopy. *Nature Reviews,* 3(79). https://doi.org/10.1038/s43586-023-00263-6

6. Krivenkov V., Samokhvalov P., Nabiev I., Rakovich Y.P. (2020) Synergy of excitation enhancement and the Purcell effect for strong photoluminescence enhancement in a thin-film hybrid structure based on quantum dots and plasmon nanoparticles. *Journal of Physical Chemistry Letters***,** 11(19), 8018–8025. https://doi.org/10.1021/acs.jpclett.0c02296

7. Kumbhakar P., Biswas S. (2019) Resonance energy transfer-assisted random lasing in light-harvesting bio-antenna enhanced with a plasmonic local field. *RSC Advances,* 9(65), 37705–37713. https://doi.org/10.1039/c9ra08166f

8. Ibrayev N.K., Aimukhanov A.K. (2019) Influence of plasmon resonance in silver nanoparticles on the properties of stimulated emission of 1,3,5,7,8-pentamethyl-2,6-diethylpyrromethene-difluoroborate molecules in film of porous aluminum oxide. *Optics and Laser Technology***,** 115, 246–250. https://doi.org/10.1016/j.optlastec.2019.02.040

9. Seliverstova E.V., Ibrayev N.K. (2016) Plasmon-enhanced stimulated emission of chromene dye. *Journal of Physics: Conference Series***,** 735, 012018. https://doi.org/10.1088/1742-6596/735/1/012018

10. Temirbayeva D., Ibrayev N., Seliverstova E., Kudinova M., Ishchenko A. (2022) Plasmon effect on triplet-singlet energy transfer in the dye-doped Langmuir-Blodgett films. *Bulletin of the Karaganda University: Physics Series,* 4(108), 6–13. https://doi.org/10.31489/2022ph4/6-13

11. Seliverstova E.V., Ibrayev N.K., Zhumabekov A.Z. (2020) The effect of silver nanoparticles on the photodetecting properties of the TiO2/graphene oxide nanocomposite. *Optics and Spectroscopy*, 128**,** 1449–1457. https://doi.org/10.1134/s0030400x20090192

12. Kadir A., Leonenko Z., Lakowicz J.R., Geddes C.D. (2005) Annealed silver-island films for applications in metal-enhanced fluorescence: Interpretation in terms of radiating plasmons. *Journal of Fluorescence,* 15(5), 643–654. https://doi.org/10.1007/s10895-005-2970-z

13. Krutyakov Y.A., Kudrinsky A.A., Olenin A.Yu., Lisichkin G.V. (2008) Synthesis and properties of silver nanoparticles: Achievements and prospects. *ChemInform,* 77(3). https://doi.org/10.1002/chin.200835228

14. Liao D.L., Liao B.Q. (2007) Shape, size and photocatalytic activity control of TiO2 nanoparticles with surfactants. *Journal of Photochemistry and Photobiology A: Chemistry, 187,* 363–369. https://doi.org/10.1016/j.jphotochem.2006.11.003

15. Zhan C., Yi J., Hu S., et al. (2023) Plasmon-mediated chemical reactions. *Nature Reviews Methods Primers***,** 3(12). https://doi.org/10.1038/s43586-023-00195-1

16. Stranik O., McEvoy H. M., McDonagh C., MacCraith B.D. (2005) Plasmonic enhancement of fluorescence for sensor applications. *Sensors and Actuators B: Chemical, 107*(1), 148–153. https://doi.org/10.1016/j.snb.2004.08.032

17. Agrawal N., Saxena R., Kumar S. (2022) Recent advancements in plasmonic optical biosensors: A review. *ISSS Journal of Micro and Smart,* 11**,** 31–42. https://doi.org/10.1007/s41683-021-00079-0

18. Deng W., Goldys E.M. (2012) Plasmonic approach to enhanced fluorescence for applications in biotechnology and the life sciences. *Langmuir,* 28, 10152–10163. https://doi.org/10.1021/la300332x

19. Stranik O., Nooney R., McDonagh C., MacCraith B.D. (2007) Optimization of nanoparticle size for plasmonic enhancement of fluorescence. *Plasmonics, 2***,** 15–22. https://doi.org/10.1007/s11468-006-9020-9

20. Lakowicz J.R., Geddes C.D. (2005) Enhanced lanthanide luminescence using silver nanostructures: Opportunities for a new class of probes with exceptional spectral characteristics. *Journal of Fluorescence***,** 15**,** 53–59. https://doi.org/10.1007/s10895-005-0213-y

21. Lakowicz J.R., Maliwal B.P., Malicka J., Gryczynski Z., Gryczynski I. (2002) Effects of silver island films on the luminescent intensity and decay times of lanthanide chelates. *Journal of Fluorescence,* 12**,** 431–437. https://doi.org/10.1023/A:1021318127519

22. Lee I.-Y.S., Suzuki H., Ito K., Yasuda K. (2004) Surface-enhanced fluorescence and reverse saturable absorption on silver nanoparticles. *Journal of Physical Chemistry B***,** 108(50), 19368–19372. https://doi.org/10.1021/jp0471554

23. Aslan K., Holly P., Geddes C.D. (2006) Metal-enhanced fluorescence from silver nanoparticle-deposited polycarbonate substrates. *Journal of Materials Chemistry,* 16**,** 2846. https://doi.org/10.1039/B604650A

AUTHORS' INFORMATION

Yusupova, Zhanat Bahtierovna – PhD student, Institute of Molecular Nanophotonics, Buketov Karaganda University, Karaganda, Kazakhstan; Scopus ID: 57204979523, ORCID iD: 0009-0000-6178-5313; yusupova-zh@mail.ru

EURASIAN PHYSICAL TECHNICAL JOURNAL

2025, Volume22, No. 3 (53)

https://doi.org/10.31489/2025N3/55-65

Received: 16/02/2025 Revised: 21/08/2025 Accepted: 25/09/2025 Published online: 30/09/2025

Research Article

Open Access under the CC BY -NC-ND 4.0 license

UDC 536.421.1; 622.245.5(088.8)

A STUDY OF HEAT TRANSFER GENERALIZATION FOR A COOLING SYSTEM WITH MINERAL MEDIA COATINGS

Genbach A.A., Bondartsev D.Yu.

Almaty University of Power Engineering and Telecommunications named after G. Daukeev, Almaty, Kazakhstan
*Corresponding author: d.bondartsev@aues.kz

Abstract. *Studies of heat transfer in cooling systems with natural material coatings have been carried out. The phenomenon of flame spin detonation was observed at an oxidizer excess ratio below unity, with the spraying process being intensified up to sixfold. The coatings demonstrated high reliability compared to other accelerated systems. The maximum specific heat fluxes on the coating range from 2 to 20×10⁶ W/m², with oscillation frequencies reaching 200 Hz. The overheating range of the coating was (20–75) K. The granulometric composition of the materials was obtained, and the hydrodynamic operating modes of the burners were selected. A model was developed for the interaction of a supersonic detonation gas jet of the thermal tool acting normally to the coating. The experimentally determined heat transfer coefficients were found to be 5–6 times higher than those predicted by laminar theory, and several times lower than those predicted by turbulent heat transfer laws. The particle flight time, powder diameter, as well as the ultimate compressive and tensile stresses of the coating were determined. The main practical application of the research is thermal protection through cooling with natural coatings (quartzites, granites, teschenites, marbles, tuffs) for highly forced and high-intensity structures in the fields of energy, metallurgy, and mechanical engineering. The primary industrial implementation of the research is the use of a thermal tool for spraying, processing of rocks, drilling, and cutting of reinforced concrete structures during modernization and reconstruction of enterprises.*

Keywords: heat and mass transfer, coatings, thermal tools, combustion chamber, nozzles, detonation torch.

1. Introduction

In recent decades, the problem of protection against high temperatures has become increasingly important, especially in the context of the development of aviation, space technology, energy and other industries where exposure to extreme temperatures is inevitable. In the context of these technological processes, it is necessary to use materials that not only effectively protect against overheating, but also have high resilience, durability and environmental friendliness. The main difference of the performed work is the focus on natural mineral coatings such as quartzites [1], granites [2-3], tuffs [4] and marbles [5] in the context of creating porous cooling systems [6]. The authors consider not only well-known technologies, but also propose innovative solutions based on the application of supersonic detonation jets for sputtering.

One of the main equipment in both power and heat engineering is turbine units – steam [7] or gas turbines [8]. Today, the task of improving the efficiency of combined energy production [9], as well as cooling the turbine combustion chamber using various coolants to increase the coefficient of performance (CoP) of machines and cycles [10–11], remains relevant. The works [12-14] consider heat transfer in homogeneous and inhomogeneous coatings, in special wicks to increase the extraction q. Many authors describe studies of the influence of porous coating parameters such as thickness [15-17], porosity and size of

particles from which the structure is made [18], geometry of the structure [19] on boiling processes. There are studies on the influence of external conditions on the boiling intensity, system pressure [20] and surface orientation [21-22], including studies of special coatings of different designs. However, all the listed papers [1-5, 10-22] do not consider the action of capillary and mass forces (ΔP_g, ΔP_{g+cap}), and there is no connection between the bubble dynamics and the boiling curve in a porous medium. Combined cooling systems including powder spraying and capillary-porous structures with fluid boiling, including the use of jet methods of coolant supply with boiling on the cooling (heating) surface, that is, taking into account the speed and underheating of the flow, are not considered.

We introduce cooling elements for various thermal power units (choice of geometry and material of apparatuses, supply and type of energy). The application area of the new system is presented [23], which requires further research of new cooling systems with coatings made of natural materials.

2. Experimental study of the process of application of coatings by spraying

Burners for spraying natural materials have supersonic spin detonation jets [24]. Further development of powder spraying processes is required to create cooling of combustion chambers and increase the efficiency of the elements. Special design of supersonic nozzles with shortened diffuser part is used to carry out detonation mode of thermal tool operation. The cooling system of burners is very effective and allows increasing the resource of combustion chambers (from 100-150 to 500-600 hours).

2.1. Coating spraying tool (see Fig. 1) allows for fire spraying by supersonic detonation high-temperature jet. The powder was mineral particles (granite). The coatings were applied to the metal surface at temperatures up to 2500-3500 ^{0}C and flow velocity up to 2500 m/s.

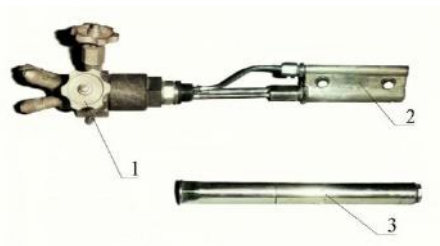

Fig.1. Unit for 1 an automated line. The combustion chamber is cooled by coatings 2 (granite); 3 – housing.

2.2. Conditions for conducting the experiment. A burner power supply circuit was assembled for conducting an experiment with a thermal tool (see Fig. 2): 1 – collector; 2 – pressure gauge; 3 – collector shut-off valve; 4 – oxygen intake shut-off valve; 5 – ramp reducer; 6 – oxygen cylinder; 7 – air cylinder; 8 – manifold pressure regulator; 9 – three-way valve; 10 – shut-off valve, 11 – water sump; 12 – water hose; 13 – air cylinder; 14 – kerosene cylinder; 15 – shut-off valve; 16 – kerosene sump; 17 – kerosene hose; 18 – plug; 19 – thermal tool; 20 – oxygen hose; 21, 25 – shut-off valves and command reducers; 22, 26 – check valves, 23, 27 – filters; 24 – reactive hose.

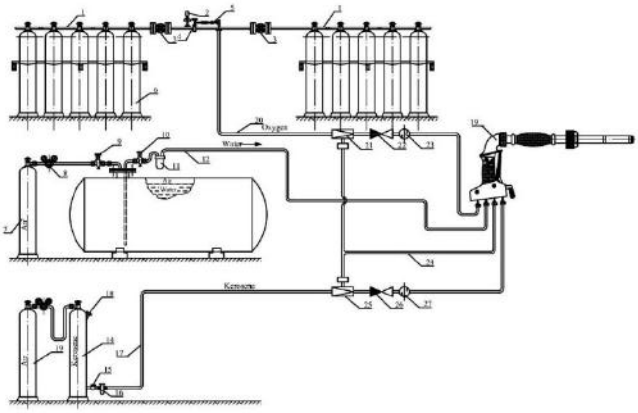

Fig.2. Displacing power supply circuit of thermal tool.

The heat flows q of the burner jet was measured by a sensor made of a copper cylinder, to which the heat flow of the burner jet is connected from one end, and from the other – the end of the cylinder is cooled by a heat pipe. Side surface of the cylinder is thermally insulated with ceramics based on zirconium dioxide. Two chromel-alumel thermocouples are placed in the cylinder. The cylinder was attached to a stationary cooled barrier (coating) having an area larger than the jet braking spot area and cooled by a heat pipe. To determine the specific heat flows q on the jet axis and in the braking spot (on the coating) along the radius r, the flow rate G, pressure P and temperature T of the cooler were measured in order to consolidate the heat balance. Flow rate, fuel and cooler pressure, and in-chamber pressure were also measured [23].

2.3. Samples of natural materials

The sample materials are made of natural mineral media, shown in Fig. 3. Stresses and deformations in the samples were studied, and three copper spirals were used as an energy source. The specific heat fluxes were (0.25÷4.2) $\times 10^6$ W/m^2.

Natural material	Type of material	Hole size, m	Drilling depth, m	Material features
Granite Sample №1		6×10^{-3}	12×10^{-3}	Crystalline rock formed from magma inside the earth's crust. It has characteristic large crystals and has high strength and resistance to wear.
Granite Sample №2		6×10^{-3}	12×10^{-3}	
Tuff Sample №3		6×10^{-3}	12×10^{-3}	Porous rock formed from sediments that contain small fragments of rocks and minerals. Light and porous.
Tuff Sample №4		6×10^{-3}	12×10^{-3}	
Marble Sample №5		6×10^{-3}	12×10^{-3}	Metamorphic rock formed from limestone under the influence of high pressure and temperature. It has characteristic patterns and textures.

Fig.3. Natural materials

3. Results of the experiment in application of coatings by spraying

Fig. 4 shows the structure of the jet flowing from a rocket-type burner (thermal tool). The phenomenon of spin detonation of a supersonic high-temperature multiphase jet has been recorded. The jet is designed for spraying a coating on a metal substrate with the strongest mineral media (powders of granite).

Fig.4. Jet outflow from the nozzle of a thermal tool (see Fig. 1) for spraying:
1 – strong flame swelling due to spin detonation of a supersonic high-temperature jet.

The flame is of an original shape, strongly inflated. The excess oxidant ratio is α < 1, the oxidant is additionally applied to the barrier and intensifies the particle spraying process by 2-6 times. The particles in powder form come from the hopper, ejected by a jet. The phenomenon of spin detonation of a supersonic high-temperature jet is presented in Fig. 5. The structure of the flooded jet is recorded.

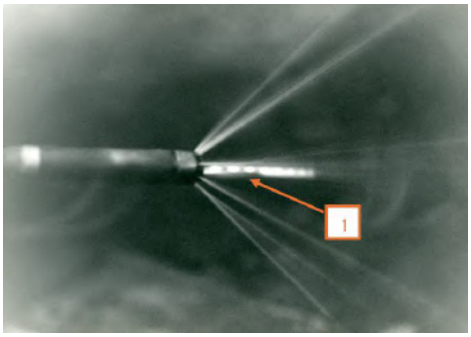

Fig.5. Spin detonation phenomenon of a supersonic high-temperature jet: 1 – spin detonation

Fig. 6 shows granite particles obtained by array processing with a thermal tool: G_{oxy} = 15 m^3/h, G_{ker}= 10 kg/h, P_{oxy}= 1.4 ÷ 1.5 MPa, d_{nt} = 4×10^{-3} m, α_{nt} = 0.8, T_g = 2780 K, W_g = 2410 m/s. For spraying the powder onto a metal substrate (stainless steel), the particles were selected by size: 0.1×10^{-3} m (2.9%); 0.25×10^{-3} m (3.8%); 0.5×10^{-3} m (7.1%) for spraying them in the form of powder on a heat exchange metal surface.

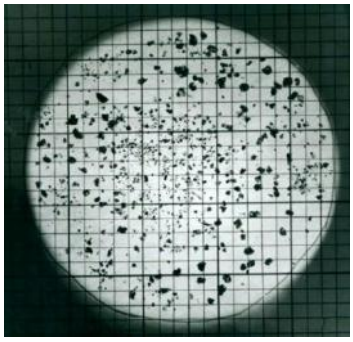

Fig.6. Granulometric composition of the «husk» obtained by processing Kurdai granite with a kerosene-oxygen burner.

3.1. Method of fuel combustion

Afterburning of fuel (kerosene, gasoline) is performed on a barrier (coating). Oxidizer excess coefficient α < 1, burner nozzle - shortened, combustion process - detonation. The afterburning process can be intensified up to two to six times. Maximum specific fluxes on the barrier: from (2 to 20)×10^6 W/m^2 (see Fig. 7). Application mode - without powder melting.

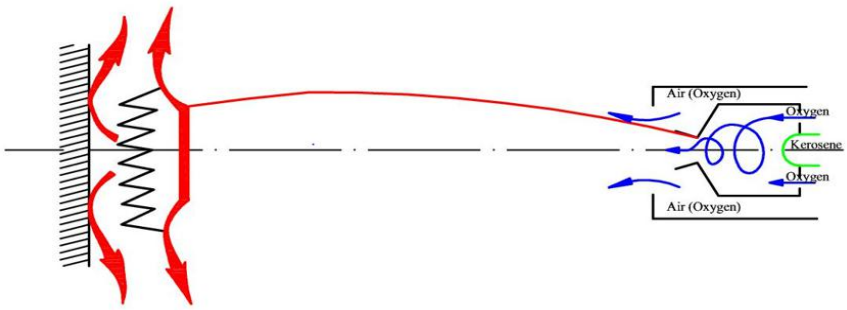

Fig.7. Detonation after-burning of fuel (kerosene) on the coating surface made of natural material (granite) and a stainless-steel substrate.

The afterburning scheme was constructed by observing the process using optical methods (holography [23], laser LG-38 [6], and high-speed filming SKS-1M [24]). For the gas pressure in the burner combustion chamber of 0.5 MPa (on the coating the gas pressure will be approximately the same), the frequency of pressure fluctuation in the chamber is ≈ (500÷600) Hz, and on the coating (obstacle) is reduced to 200 Hz.

Control of the length of the burner jet flowing out of the nozzle. The dimensionless jet length $\bar{z} = \frac{z}{r_n}$ (see Table 1). For the maximum value of the heat transfer coefficient from the jet to the coating for one of the modes we take α_1 = 1000 W/(m²×K).

Table 1. Dependence of α/α_1 on $\bar{z}$.

α/α_1	**0.8**	**1**	**0.7**	**0.4**	**0.3**
$\bar{z}$	0	10÷30	40	50	60

For $P_{c.c.}$ = 1 MPa, z = (0÷0.16) m, T = (3500÷850) ^{0}C, T_{st} = 3000 ^{0}C – braking temperature (on the coating), t_j = 300 ^{0}C – temperature at the end of the free jet, $r_n = 3\times10^{-3}$ m, $r_j = 10\times10^{-3}$ m (jet radius).

Adjustment of the jet angle to the coating. In Table 2, the following is accepted: α_{90^0} = 1000 W/(m²×K); T_{st} = 3500 ^{0}C; t_j = 300 ^{0}C; $P_{c.c.}$ = 1 MPa.

Table 2. Dependence of α/α_{90^0} on $\bar{z}$.

α/α_{90^0}	**1**	**1.1**	**1**	**0.8**	**0.5**	**0.35**	**0.3**	**0.25**
β, deg.	90	80 – 75	60	50	30	20	10	0

Characteristics of thermal tools and parameters of sprayed powders of mineral media. Dependences of thermal loads for natural mineral media are presented in Fig. 8 and Fig. 9 for granite. Temporal dependences of ultimate thermal loads and thermomechanical stresses depending on particle size distribution were investigated by us in [24].

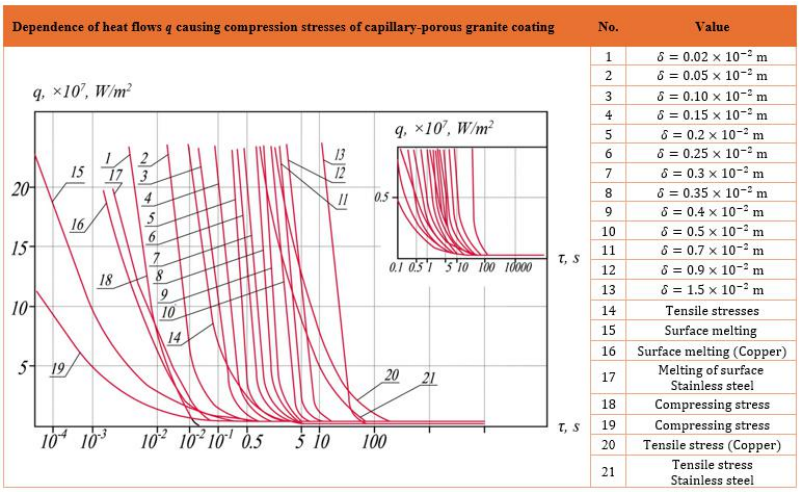

Fig.8. Limit ranges of thermal loads for granite coating

For the range of flight time of granite powder particles $\tau = (5\div9)\times10^{-2}$ s, the thicknesses of coatings were in the interval - $\delta = (0.2\div0.5)\times10^{-3}$ m, powder diameter - $d = (20\div100)\times10^{-6}$ m. The ultimate tensile stresses, MPa, respectively for granite coatings were - 21. Fig. 9 shows the dependence $q = f(\delta, \tau)$, presented in Fig. 8, in the range $q = (0.25...0.75)\times10^7$ W/m².

The dependences in Fig. 8, 9 have experimental confirmation [23]. The heat fluxes q of the burner jet were measured by a copper cylinder sensor, the process time τ and the size of the detached particle δ were measured by a high-speed movie camera SKS-1M [24]. The value of heat flows q can be reduced by one order when switching to another type of burner: benzo (kerosene) - air burners. Such burners are used for application of coating by spraying mineral medium with a lower strength value than that of granite, for example, teschenite, porphyrite or marble. The limiting ranges of thermal loads are presented in Section 4.

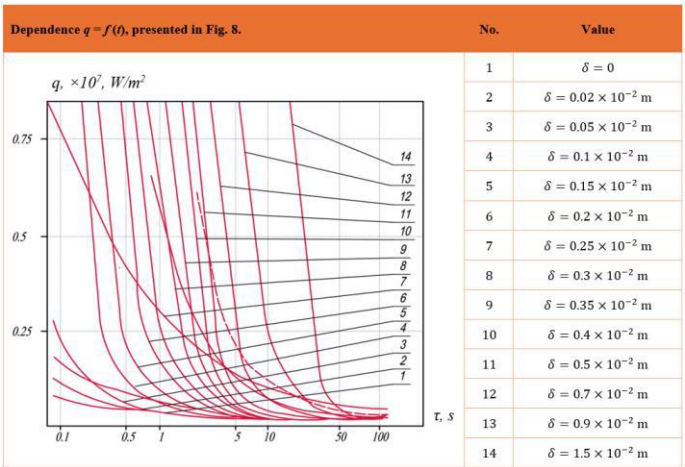

Fig.9. Limit ranges of thermal loads for granite coating $q = f(\delta, \tau)$.

3.2. Regulation of the power and type of burners.

For kerosene-oxygen burners of a thermal tool, we have the following characteristics: oxygen consumption G_{oxy} for pressure P_{oxy}= 1.2÷1.5 MPa, m^3/h – 15÷18; kerosene consumption G_{ker} for pressure P_{ker} = 1.3÷1.5 MPa, kg/h – 10÷12; nozzle critical diameter is d_{nt}, 10^{-3} m – 4÷5; combustion chamber diameter is $d_{c.c.}$, 10^{-3} m – 14. Gas-dynamic parameters of jets at the outlet of the nozzle are summarized in Table 3.

Table 3. Gas-dynamic parameters of jets at the outlet of the nozzle.

α	$P_{c.c.}$ = 1.5 MPa	
	T_g, K	W_g, m/s
0.7	2670	2420
0.8	2780	2410
0.9	2830	2400
1	2810	2320

Fig. 10 shows the technique and technology of thermal tool operation with d_{nt} = (4÷5)×10^{-3} m, $d_{c.c.}$ = 14×10^{-3} m to granite impact surface. The flame structure, jet spreading radius (braking spot), the distance from the nozzle edge (outlet part) of the burner to the coating are visible. Removal of cooling water from the impact surface in the form of jets is carried out for technological reasons of applying a protective coating.

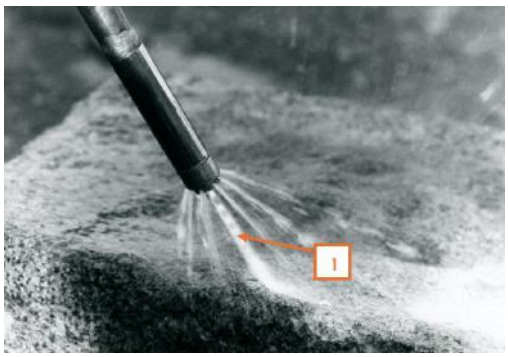

Fig. 10. Position of the torch to the granite processing surface, 1 - structure of the torch.

The protective shield is designed to protect the worker-operator of the thermal tool. Specific heat flows q on the coating surface were (5÷12) MW/m^2 for r = 0 and l = (4÷12)×10^{-2} m; (2÷5) MW/m^2 for r = 4×10^{-2} m and l = (4÷12)×10^{-2} m.

Distribution of q (r): q (r) = $q_{\max}$ × exp (-1000 × r^2), W/m^2. For a more powerful burner with d_{nt} = 6×10^{-3} m, $d_{c.c.}$ = 18×10^{-3} m: G_{oxy} for P_{oxy} = 1.8 MPa, m^3/h – 30÷55; G_{ker} for P_{ker} = (1.8-2) MPa, kg/h – 14÷18, we have q (r = 0) = (6÷13) MW/m^2.

4. Comparison of the results with existing data on the theme

Let us make a comparative evaluation of the coatings studied in this work (see Fig. 11) with other cooling systems. The studied thermal characteristics of coatings made of natural material are related to high-intensity cooling systems. The comparison shows the advantages of boiling in bulk, thin films and in heat pipes.

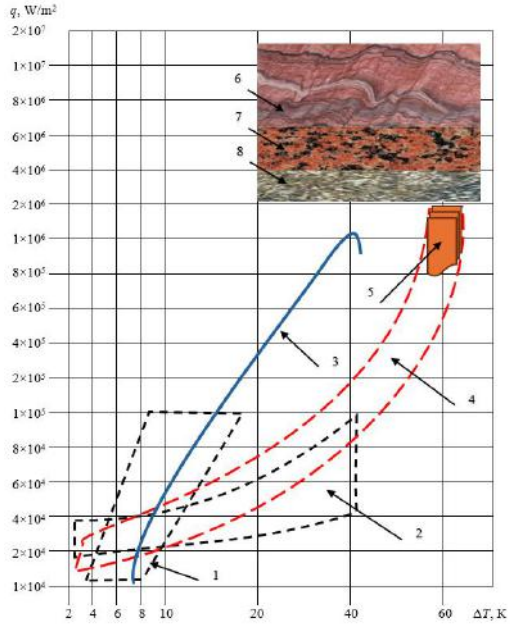

Fig. 11. Comparative evaluation of thermal load dependence on surface superheating

Fig. 11 shows the dependence of the thermal load on the wall superheat relative to the water vapor temperature (areas 1 - 4) (P = 0.1 MPa) [6], the designations in Fig. 11 are summarized in Table 4. As can be seen from Fig. 11, high $q_{cr.}$ are achieved in the case of the jet coolant supply, since in the jet braking zone there is high turbulence (intense pulsations), very thin boundary layer, negative pressure gradient dP/dx and active vapor film collapse.

Table 4. Comparative evaluation.

No. Area	Denomination	References to the authors' comparative scientific papers
1	Scope of work of thin-film evaporators	[11].
2	Scope of work of heat pipes with mesh wicks	[10], [12], [13], [14].
3	High-volume boiling on uncoated surfaces	[12], [13], [14], [15], [16], [17], [18], [19].
4	Researched mesh capillary-porous cooling system	[6].
5	Shaded area - application of intensifiers in a porous system	[24].
6	Thermal load limit areas for natural mineral medium with no surface melting for quartz coatings	[23].
7	Thermal load limit areas for natural mineral medium with no surface melting for granite coatings	See Fig. 8 and Fig. 9.
8	Thermal load limit areas for natural mineral medium with no surface melting for teschenite coatings	[26].

The thermal protection of CPCs (capillary porous coatings) is improved due to structural temperature gradients. Synthesis of powders of mineral media produced in the foci of elliptical cylinders, or due to impact processes and structural detonation, gives undeniable advantages in the creation of coatings with

gradient nanostructure. Such materials have high mechanical properties, combining the synergistic advantages of strength and plasticity, strain hardening, increased resistance to cracking, fracture and fatigue. Structural thermal gradients create thermal stress and strain gradients.

5. A model of interaction of an axisymmetric supersonic detonation jet of gases of a thermal instrument according to standards with the surface of a capillary-porous coating

Let us consider the interaction of the supersonic jet of the thermal tool (see Fig. 5 and Fig. 7) with the obstacle in the braking zone (the vicinity of the critical point) (see Fig. 10). The jet is located orthogonally (perpendicularly) to the coating surface. Let us write down for «standard conditions» the heat transfer equation [25] in the laminar boundary layer in the longitudinal flow of the plate:

$$Nu_x = K_1\sqrt{Re_x}\sqrt[3]{Pr}\,, \quad (1)$$

where $Re_x = W_\infty \cdot \frac{x}{\nu}$, $W_\infty = W_0$. Local heat transfer during longitudinal flow around the plate in a turbulent boundary layer [26]:

$$Nu_x = K_2 \cdot Re_x^{0.8} \cdot Pr^{0.43}, \quad (2)$$

where $T_{st} = const;\ 10^5 < Re_x < 10^7$. In the formula (1) $K_1 = 0.323$; in the formula (2) $K_2 = 0.0296$.

The thermo-physical properties of gas are assumed at an average temperature between T_∞ and T_{st}; more often in models, the temperature of the undisturbed flow T_∞, or T_{st} is selected as the determining temperature;

$Pr = \frac{\nu}{\alpha}$ – Prandtl number; Nu_x – Nusselt number;

$Nu_x = \alpha_x \cdot \frac{x}{\lambda}$.

Let us rewrite the number Nu_x and the criterion Re_x in a form which is more convenient for analysis.

The Reynolds Criterion:

$$Re_x = \frac{\rho_0 \cdot W_0 \cdot x}{\mu_x}.$$

The Nusselt number:

$$Nu_x = \frac{q(x) \cdot x}{\lambda_x \cdot (Ta_{st} - T_{st})},$$

Then we calculate the temperature Ta_{st}:

$$Ta_{st} = Tr_\infty, \text{ K}, \quad (3)$$

where Tr_∞ is the recovery temperature equal to:

$$Tr_\infty = T'_\infty + r \cdot \frac{W_\infty^2}{2Cp_\infty}, \text{ K}; \quad (4)$$

T'_∞ – the thermodynamic temperature of an undisturbed flow (this is the temperature that a thermometer moving with the flow at the same speed with it would show). For $Pr = 1$:

$$T_{0\infty} = T'_\infty + r \cdot \frac{W_\infty^2}{2Cp_\infty}, \text{ K}, \quad (5)$$

Ta_{st} – the temperature of the coating itself or the adiabatic temperature of the wall (the temperature of an ideally insulated, non-radiating solid surface, streamlined by a gas flow with internal heat sources or with the release of heat due to energy dissipation). When $Pr < 1$, $Ta_{st} < T_{0\infty}$.

Recovery factor:

$$r = \frac{Ta_{st} - T'_\infty}{T_{0\infty} - T'_\infty}. \quad (6)$$

For laminar layers:

$$r = \sqrt{Pr}. \quad (7)$$

The thermodynamic temperature is T'_∞ equal to:

$$T'_\infty = \frac{\alpha_\infty^2}{K \cdot R}, \text{ K}. \quad (8)$$

Braking temperature:

$$T_{0\infty} = T_\infty \cdot \left[1 + \frac{(K-1)}{2} \cdot M_\infty^2\right], \text{ K}. \quad (9)$$

The recovery temperature is equal to:

$$T_{r\infty} = T_\infty \cdot \left[1 + r \cdot \frac{(K-1)}{2} \cdot M_\infty^2\right], \text{ K}, \quad (10)$$

where $K = \frac{Cp}{C\vartheta}$.

5.1. Calculation of specific heat flows q_{st}

The heat flow of the gas streamlined by the high-speed flow is defined as:

$q_{st} = \alpha \cdot (Ta_{st} - T_{st})$, W/m^2. (11)

If $\neq 1$, then

$Ta_{st} = T_{r\infty}$, (12)

and $q_{st} = \alpha \cdot (T_{r\infty} - T_{st})$, W/m^2.

If $= 1$, then

$Ta_{st} = T_{0\infty}$, (13)

and $q_{st} = \alpha \cdot (T_{0\infty} - T_{st})$, W/m^2.

For a detonation supersonic flame, we conducted experiments using a micro-nozzle for measuring total and static pressures and a heat flow sensor for measuring $q(x)$, α_x, M_x and $\rho_0 W_0$ in a spraying jet. Mach numbers $M = \frac{W_g}{\alpha} = 2.3$. The degree of non-calculation of outflow $n_a = \frac{P_e}{P_b} = 0.8$. The number Re_a was calculated based on the parameters of the gas at the nozzle edge (index «*a*»):

$Re_a = \frac{W_a \cdot d_a}{\nu_a}$, where $Re = 1\times10^6$; $\bar{l} = \frac{l}{d_a} = 3$.

When a supersonic jet of the thermal tool interacts with an obstacle in the deceleration zone (near the critical point), a combined effect takes place: high turbulence intensity, negative pressure gradient, and wave structures that generate turbulence (pulsations), causing flow separation from the wall. Such a jet belongs to the impact type and affects the mechanism of heat transfer at the stagnation point of the coating. It increases turbulence (pulsations), and in the case of a boiling cooling system, destroys vapor conglomerates.

In the vicinity of the critical point (on the coating), a laminar flow regime is assumed, since the Reynolds number Re_x is not high and a negative pressure gradient is present. However, the Nusselt number Nu_x is found to be 5–6 times higher than that predicted by laminar theory (formula (1)). This may indicate a detonation effect of turbulent pulsations penetrating the laminar boundary layer from the outer flow. At $Re_x \geq 4\times10^5$, the points lie below the curve corresponding to the turbulent boundary layer ($10^5 < Re_x < 10^7$) for subsonic flows.

Thus, for the «standard conditions» of heat exchange, $K_1 = 0.323$ and $K_2 = 0.0296$. In case of a detonation supersonic wave, we have for $Re_x < 4\times10^5$, $K_1' = (5\div6)\times K_1$ and for $10^6 \geq Re_x \geq 4\times10^5$, $K_2' = 0.95\times K_2$.

6. Conclusions

1. Effective coating deposition from various natural materials is achieved through the use of a detonation burner. The main coating parameters have been determined.

2. The cooling system demonstrated high efficiency up to the critical state of the combustion chamber metals and nozzles.

3. A model was developed for the interaction of an axisymmetric supersonic detonation gas jet of the thermal tool acting normally to the coating. The experimentally obtained heat transfer coefficients were found to be 5-6 times higher than those predicted by laminar theory and several times lower than those predicted by turbulent heat transfer laws.

4. The developed surfaces in the form of coatings and mesh structures provide a positive effect due to the advantages of combined manufacturing technologies, enabling an increase in dissipated thermal loads.

5. A comparative evaluation of the coatings demonstrated their advantages over traditional cooling systems.

Conflict of interest statement

The authors declare that they have no conflict of interest in relation to this research, whether financial, personal, authorship or otherwise, that could affect the research and its results presented in this paper.

CRediT author statement

Genbach A.: Conceptualization, Mathematical model, Methodology, Writing - original draft; **Bondartsev D.**: Experimental method, Experimental data, Data creation, Investigation; Calculations, Supervision, review & editing.

The final manuscript was read and approved by all authors.

References

1 Wei Chen, Wuwen Liu, Yue Liang. (2024) An Investigation into the Compressive Strength, Permeability and Microstructure of Quartzite-Rock-Sand Mortar. *Fluid Dynamics and Materials Processing*, 20(4), 859-872. https://doi.org/10.32604/fdmp.2023.029310

2 Ramadji C., Messan A., Prud'Homme E. (2020) Influence of Granite Powder on Physico-Mechanical and Durability Properties of Mortar. *Materials,* 13, 5406. https://doi.org/10.3390/ma13235406

3 Ju Wang, Feng Dai, Yi Liu, Hao Tan, Pan Zhou. (2024) Thermophysical-mechanical behaviors of hot dry granite subjected to thermal shock cycles and dynamic loadings. *Journal of Rock Mechanics and Geotechnical Engineering,* https://doi.org/10.1016/j.jrmge.2024.09.007

4 Ting Zuo, Xianglong Li, Jianguo Wang, Qiwen Hu, Zihao Tao, Tao Hu. (2024) Insights into natural tuff as a building material: Effects of natural joints on fracture fractal characteristics and energy evolution of rocks under impact load. *Engineering Failure Analysis*, 163(Part A), 108584. https://doi.org/10.1016/j.engfailanal.2024.108584

5 Yan Zhang, Chunchi Ma, Yaohui Gao, Kai Meng. (2024) Investigation on mechanical behaviors and energy characteristics of deep-buried marble in a hydraulic tunnel in Southwest China. *Transportation Geotechnics*, 47, 101270. https://doi.org/10.1016/j.trgeo.2024.101270

6 Genbach A., Beloev H., Bondartsev D. (2021) Comparison of cooling systems in power plant units. *Energies,* 14, 6365. https://doi.org/10.3390/en14196365

7 Shavdinova M.D., Sharipov R.Zh., Meshherjakova T.Y. (2021) Enhancement of steam-turbine condenser steam-jet ejector. *Eurasian Physical Technical Journal,* 18, 4(38), 52-58. https://doi.org/10.31489/2021No4/52-58

8 Komarov I.I., Vegera A.N., Bryzgunov P.A., Makhmutov B.A., Smirnov A.O. (2022) Development and research of the topology of cooling baffles for blades of the axial carbon dioxide turbines. *Eurasian Physical Technical Journal*, 19, 2(40), 48-57. https://doi.org/10.31489/2022No2/48-57

9 Zlateva P., Terziev A., Murzova M., Mileva N., Vassilev M. (2025) Market Research on Waste Biomass Material for Combined Energy Production in Bulgaria: A Path Toward Enhanced Energy Efficiency. *Energies,* 18(15), 4153. https://doi.org/10.3390/en18154153

10 Riadh Boubaker, Vincent Platel. (2016) Dynamic model of capillary pumped loop with unsaturated porous wick for terrestrial application. *Energy*, 111, 402-413. https://doi.org/10.1016/j.energy.2016.05.102

11 Jamialahmadi M., Müller-Steinhagen H., Abdollahi H., Shariati A. (2008) Experimental and theoretical studies on subcooled flow boiling of pure liquids and multicomponent mixtures. *International Journal of Heat and Mass Transfer*, 51(9-10), 2482-2493. https://doi.org/10.1016/j.ijheatmasstransfer.2007.07.052

12 Mieczyslaw E. Poniewski. (2004) Peculiarities of boiling heat transfer on capillary-porous coverings. *International Journal of Thermal Sciences*, 43(5), 431-442. https://doi.org/10.1016/j.ijthermalsci.2003.10.002

13 Kimihide Odagiri, Hosei Nagano. (2019) Investigation on liquid-vapor interface behavior in capillary evaporator for high heat flux loop heat pipe. *International Journal of Thermal Sciences*, 140, 530-538. https://doi.org/10.1016/j.ijthermalsci.2019.03.008

14 Ji X., Xu J., Zhao Z., Yang W. (2013) Pool boiling heat transfer on uniform and non-uniform porous coating surfaces. *Experimental Thermal and Fluid Science*, 48, 198-212. https://doi.org/10.1016/j.expthermflusci.2013.03.002

15 Mohammad S.A., Prasad L., Gupta S.C., Agarwal V.K. (2008) Enhanced boiling of saturated water on copper coated heating tubes. *Chemical Engineering and Processing: Process Intensification*, 47(1), 159-167. https://doi.org/10.1016/j.cep.2007.07.021

16 Chen Li, Peterson G.P., Yaxiong Wang (2006) Evaporation/Boiling in Thin Capillary Wicks (l) - Wick Thickness Effects. *Journal of Heat Transfer*, 128(12), 1312-1319. https://doi.org/10.1115/1.2349507

17 Hanlon M.A., Ma H.B. (2003) Evaporation Heat Transfer in Sintered Porous Media. *Journal of Heat Transfer*, 125(4), 644-652. https://doi.org/10.1115/1.1560145

18 Chen Li, Peterson G.P. (2006) Evaporation/Boiling in Thin Capillary Wicks (II) - Effects of Volumetric Porosity and Mesh Size. *Journal of Heat Transfer*, 128(12), 1320-1328. https://doi.org/10.1115/1.2349508

19 Das A.K., Das P.K., Saha P. (2009) Performance of different structured surfaces in nucleate pool boiling. *Applied Thermal Engineering*, 29(17-18), 3643-3653. https://doi.org/10.1016/j.applthermaleng.2009.06.020

20 Mehmet Arik, Avram Bar-Cohen, Seung Mun You. (2007) Enhancement of pool boiling critical heat flux in dielectric liquids by microporous coatings. *International Journal of Heat and Mass Transfer*, 50(5-6), 997-1009. https://doi.org/10.1016/j.ijheatmasstransfer.2006.08.005

21 Mohammad S.S., Yong H.J., Soon H.C. (2007) Subcooled flow boiling CHF enhancement with porous surface coatings. *International Journal of Heat and Mass Transfer*, 50(17-18), 3649-3657. https://doi.org/10.1016/j.ijheatmasstransfer.2006.09.011

22 Forrest E., Williamson E., Buongiorno J., Hu L., Rubner M., Cohen R. (2010) Augmentation of nucleate boiling heat transfer and critical heat flux using nanoparticle thin-film coatings. *International Journal of Heat and Mass Transfer*, 53(1-3), 58-67. https://doi.org/10.1016/j.ijheatmasstransfer.2009.10.008

23 Genbach A.A., Bondartsev D.Y. (2020) Limiting Thermal State of Capillary-Porous Power-Plant Components. *Russian Engineering Research*, 40, 384-389. https://doi.org/10.3103/S1068798X20050093

24 Genbach A.A., Bondartsev D.Y., Iliev I.K. (2018) Modelling of capillary coatings and heat exchange surfaces of elements of thermal power plants. *Bulgarian Chemical Communications*, 50(G), 133-139. Available at: https://www.researchgate.net/profile/Iliya-Iliev-2/publication/330385900_Modelling_of_capillary_coatings_and_heat_exchange_surfaces_of_elements_of_thermal_power_plants/links/5c3dcf32458515a4c727ef12/Modelling-of-capillary-coatings-and-heat-exchange-surfaces-of-elements-of-thermal-power-plants.pdf

25 Kutateladze (1990) Heat transfer, mass transfer, and friction in turbulent boundary layers. *Hemisphere*, 367. https://discovery.hw.ac.uk/permalink/f/i526e0/44hwa_alma2127993300003206 [in Russian]

26 Genbatch A.A., Bondartsev D.Y. (2018) Experimental method of investigation of the heat transfer crisis in a capillary-porous cooling system. *News ofthe National Academy of Sciences of the Republic of Kazakhstan-Series of Geology and Technical Sciences,* (2), 81-88. Available at: http://www.geolog-technical.kz/images/pdf/g20182/229-235.pdf [in Russian]

AUTHORS' INFORMATION

Genbach, Aleksandr A. — Doctor of Science (Eng.), Professor, Professor, Department of Heat Power Engineering, Institute of Energy and Green Technologies, Almaty University of Power Engineering and Telecommunications named after G. Daukeev; Scopus Author ID: 6603206395; https://orcid.org/0009-0001-3819-4387, a.genbach@aues.kz

Bondartsev, David Yu. — Doctor of Philosophy (PhD), Associate Professor, Professor, Department of Heat Power Engineering, Institute of Energy and Green Technologies, Almaty University of Power Engineering and Telecommunications named after G. Daukeev; WoS Researcher ID: AFD-9189-2022, Scopus Author ID: 57202869716; https://orcid.org/0000-0001-8778-7851, d.bondartsev@aues.kz

EURASIAN PHYSICAL TECHNICAL JOURNAL

2025, Volume 22, No.3 (53)

https://doi.org/10.31489/2025N3/66-74

Received: 12/05/2024 Revised: 23/05/2025 Accepted: 25/09/2025 Published online: 30/09/2025

Original Research Article

Open Access under the CC BY -NC-ND 4.0 license

UDC 539.1; 621.039.573

DETERMINATION OF THE ENERGY RELEASE DISTRIBUTION AND TEMPERATURE IN THE IRT-4M NUCLEAR FUEL WHEN CHANGING THE CONFIGURATION OF THE CONTROL AND PROTECTION SYSTEM CHANNELS IN THE WWR-SM REACTOR

Baytelesov S.A., Tadjibaev D.P., Fayziyev T.B., Kungurov F.R., Alikulov Sh.A.

Institute of Nuclear Physics of Uzbekistan Academy of Sciences, Tashkent, Uzbekistan
*Corresponding author: baytel@inp.uz

Abstract. *The objective of this work is to determine the temperature distribution in the IRT-4M type fuel assembly with fuel 19.75% enriched in ^{235}U in the core of the WWR-SM reactor for the case of a square tube with rounded edges and a round hole in the center and the case of a round tube. In the case of installing a round tube inside the fuel assembly instead of a square tube with rounded edges and a round hole in the center, the volume of water in this space increases. On the one hand, this leads to improved heat removal, since the volume of cooling water increases, and on the other hand, an increase in the volume of water leads to an increase in thermal neutrons on this side of the fuel element, and this, in turn, leads to an increase in energy release. To determine these changes, we performed neutron-physical and thermal-hydraulic calculations for a channel with a square tube with rounded edges and a round hole in the center and for a round tube. It has been determined that replacing a square tube with rounded edges and a round hole in the center with a round tube as a guide for installing a compensating control rod will not affect the nuclear safety of the WWR-SM reactor operation.*

Keywords: fuel assembly, neutron-physical, thermal-hydraulic calculation, horizontal and vertical channels, reactor core, burnup.

1. Introduction

The results of neutron-physics and thermal-hydraulic calculations of a nuclear reactor core are among the key parameters that determine the nuclear safety of its operation. When developing new fuel, as well as when modifying the reactor core configuration or the geometry of structural elements, comprehensive neutron-physics and thermal-hydraulic calculations are a mandatory stage [1–6]. In global practice, continuous efforts are being made to improve the design of reactor cores for both research and power reactors. These efforts are accompanied by detailed calculations and analyses of neutron-physical and thermal-technical characteristics. Such studies are aimed at increasing fuel utilization efficiency, enhancing safety features, and expanding the application capabilities of reactors for both scientific and applied purposes.

In this study, neutron-physics and thermal-hydraulic calculations of the reactor core of the WWR-SM research reactor at the Institute of Nuclear Physics of the Academy of Sciences of the Republic of Uzbekistan (INP AS RUz) are presented. The calculations were carried out for a configuration loaded with 24 fuel assemblies (FAs) of the IRT-4M type containing low-enriched uranium (19.75% ^{235}U).

The reactor core uses six-tube IRT-4M type FAs. These assemblies contain fuel elements (FE) in the form of coaxial square-section tubular plates with a wall thickness of 1.6 mm and a length of 600 mm. The

cladding of the fuel elements is made of SAV-1 alloy with a thickness of 0.45 mm (minimum 0.3 mm). Inside the six-tube FAs, either control and protection system (CPS) rods or experimental channels with diameters of 24–26 mm are installed. Using the REBUS computational code, the axial distribution of power density was determined for each fuel element in the most power-intensive FA. For this purpose, the height of the assembly was conditionally divided into 15 sections.

Thermal-physics calculations of research reactors uses a mathematical model of the type [7], and include the determination of temperature fields, heat fluxes, and other parameters related to heat transfer in the reactor core and auxiliary systems. These calculations are essential to ensure safe and efficient operation, as well as to optimize the reactor design and operating conditions [8]. The main objectives of thermal-hydraulic analysis are:

– to determine the distribution of heat fluxes and temperatures within the reactor core;

– to establish the maximum fuel temperature in order to confirm the absence of a melting risk in the most heavily loaded fuel elements; to evaluate the safety margin to the onset of critical heat flux.

All thermal-hydraulic parameters (heat fluxes, temperatures, coolant characteristics) were calculated both for average values over the reactor core and for the most heavily loaded fuel elements. For spatial resolution, calculations were performed at 15 points along the fuel assembly height — from the bottom (0 mm) to the top (600 mm) with a step of 40 mm. The distribution of thermal power in the reactor core was analyzed both for all loaded FAs and for individual elements within each assembly. Knowledge of the thermal loads acting on the FAs and their components is a prerequisite for the safe operation of research reactors.

Thus, the purpose of this study is to determine the distribution of temperature and power generation in IRT-4M type fuel assemblies with uranium enrichment of 19.75% ^{235}U in the WWR-SM reactor core in order to justify thermal-technical reliability and safe operation.

2. Calculation of energy release in the WWR-SM reactor core

2.1 WWR-SM Reactor

The WWR-SM research reactor at INP AS RUz uses water as both moderator and coolant, with a primary circuit flow rate of 1250 m³/h and maximum core temperature of 50°C. The reactor's maximum thermal power is 10 MW. The facility supports various research activities using horizontal and vertical neutron beam channels.

The reactor features:

– 9 horizontal channels for heavy nucleus fission physics, neutron physics, solid-state physics, and materials structure research, including a thermal column [9]

– 32 vertical channels for radioisotope production and other applied research tasks.

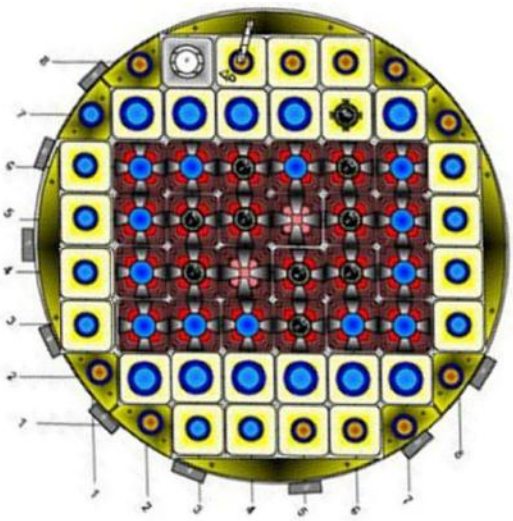

Fig. 1. Horizontal cross-section of the WWR-SM reactor core.

	6-tube fuel assembly (6-tube FA)
	8-tube fuel assembly (8-tube FA)
	6-tube FA with control rod drive mechanism (CRDM) or safety rod mechanism
	Beryllium reflector block with Be plug (Ø 44 mm)
	Horizontal dry channel
	9th dry irradiation channel
	Beryllium reflector block with channel (Ø 60 mm)
	Segmented Be reflector block with channel (Ø 44 mm)
	Beryllium reflector block with channel (Ø 44 mm)
	Automatic regulator mechanism in beryllium reflector block
	Lateral beryllium displacer

2.2 Neutron-Physics Calculations of the WWR-SM Reactor Core Loaded with 24 IRT-4M Fuel Assemblies

The calculation of power distribution and fuel burnup for the FAs was performed using the two-dimensional two-group code IRT-2D [10], developed by researchers at the Kurchatov Institute (Russia). The calculations were carried out under the condition of complete withdrawal of all control rods from the reactor core. Figure 2 shows the power distribution for the core configuration with 24 IRT-4M FAs, as calculated by the IRT-2D code [11].

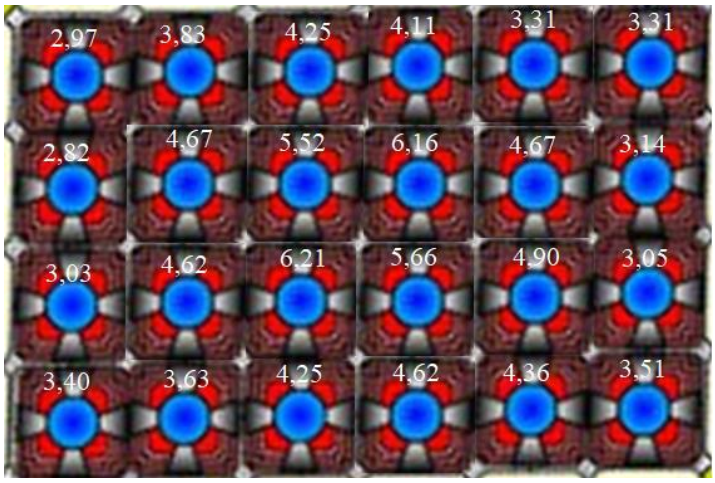

Fig.2. Thermal power distribution (%) for the 24-FA core configuration.

The calculations assumed that all 24 FAs in the core are of the six-tube type, with all control rods fully withdrawn from the core. This is because the control rod drive mechanisms can only be inserted into six-tube FAs. As seen in Figure 2, the most power-intensive FA with 6.212% power generation is located in the central part of the reactor core. Using the REBUS computational code developed at the Argonne National Laboratory in the United States, the axial distribution of power density was determined for each fuel element in the most power-intensive FA. For this purpose, the height of the assembly was conditionally divided into 15 sections. The axial power density distribution was determined for each six-tube fuel rod (FR) [12]. Figure 3 presents the axial power density distribution for each fuel rod in the most power-intensive FA (6.21%).

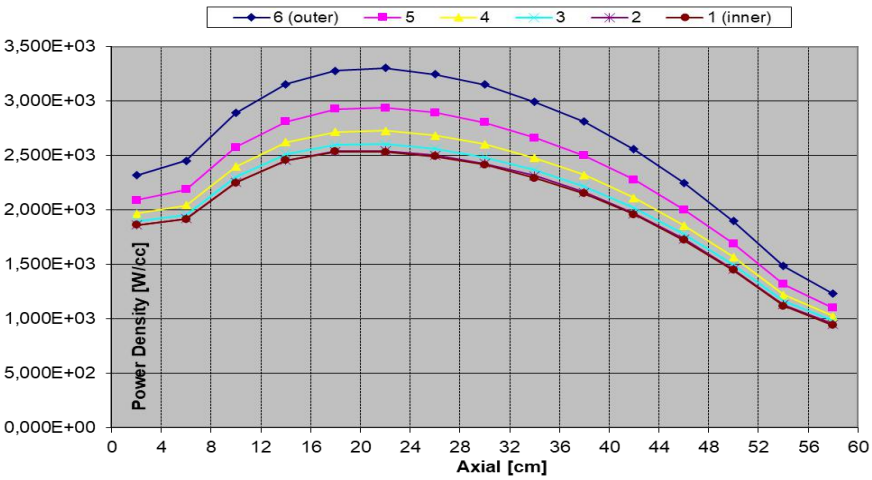

Fig.3. Axial power density distribution along the height of each fuel rod.

As shown in Figure 3, the minimum power density occurs in the inner fuel rod. Replacing the oval-square tube with a circular one alters the power density distribution in the inner tube, which may lead to increased temperatures.

Figure 4 presents:

(a) Horizontal cross-section of the IRT-4M fuel assembly with an oval-square central tube

(b) Cross-section with a circular central tube

Modified flow areas for water passage in the central part of the FA are highlighted in blue.

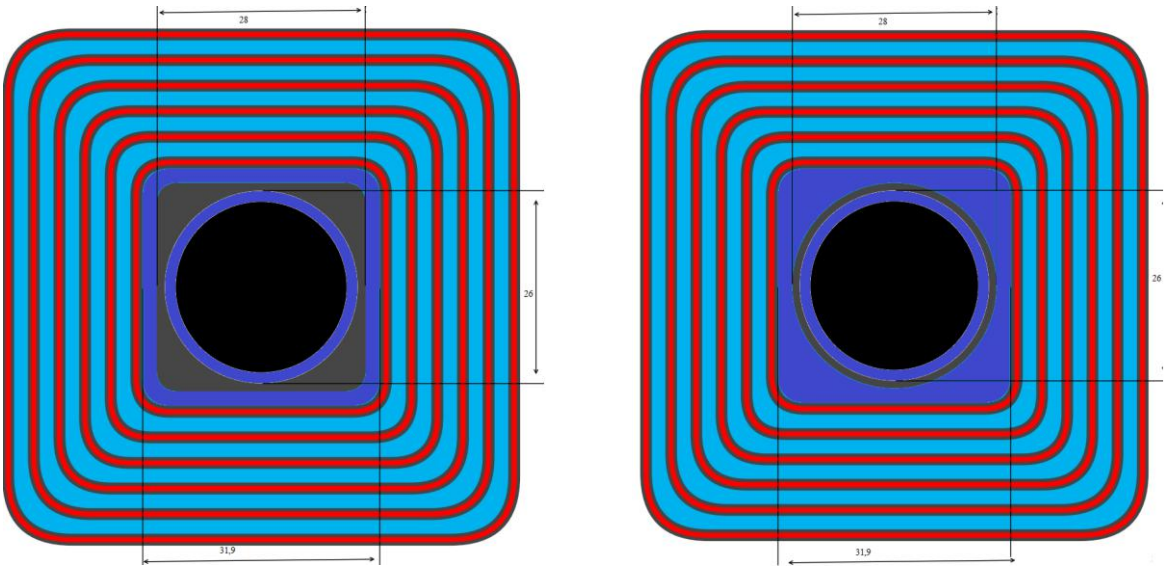

a) b)

Fig.4. Horizontal cross-section of IRT-4M - 6-tube fuel assembly with oval-square central tube for control and safety rods fuel assembly: (a) with oval-square central tube and (b) with circular central tube.

The area calculations were performed using the following formulas:

$S = S_{square(a)} - 4\,S_{square(r)} + S_{circle}$

$S_{square(a)} = a^2$

$S_{square(r)} = r^2$

$S_{circle} = \pi r^2$

$S = a^2 - 4\,r^2 + \pi r^2$

$S = a^2 - (4 - \pi) r^2$

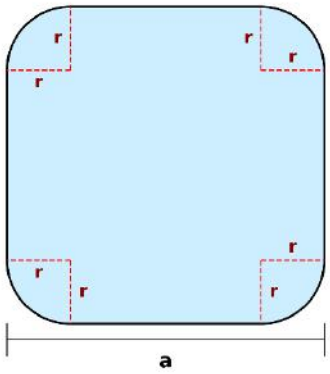

For the inner sixth fuel rod (FR): Radius: 2.9 mm

Rounded-square cross-sectional area: 1010.38 mm²

For the oval-square tube: Radius: 2.45 mm

Rounded-square cross-sectional area: 778.84 mm²

Central flow channel characteristics: Radius: 14 mm, Area: 615.44 mm²

Area difference compared to oval-square configuration: 163.4 mm²

The replacement of oval-square tubes with circular tubes within the fuel assembly (FA) increases the water volume in this region. This modification provides dual effects:

1. Enhanced heat removal due to greater coolant volume
2. Increased thermal neutron flux density near the fuel rod (FR), leading to:

– Higher power density

– Subsequent temperature elevation

Analysis Methodology:

– Computational study of power density redistribution following oval-square to circular channel conversion

– Axial power distribution analysis with 15 axial segments (4 cm each) along the FR height

– Complete results documented in Table

There are fresh fuel assemblies in the central parts of the core, and burnt-out fuel assemblies are on the periphery (Figure 1). The calculation of energy release and burnup in the fuel assembly was carried out using the two-dimensional and two-group program IRT-2D [10], developed by the National Research Center (NRC) "Kurchatov Institute", Russia. The table shows the results of calculations for reactor operation at 10 MW power. In case of installation of a round tube inside the FA instead of a square tube with rounded edges and a round hole in the center, the volume of water in this space increases. On the one hand, this leads to improvement of heat removal, since the volume of cooling water increases, and on the other hand, the increase in the volume of water leads to an increase in thermal neutrons on this side of the fuel element, and this, in turn, leads to an increase in energy release.

To take these changes into account, we calculated the energy release when replacing the channel with a square tube with rounded edges and a round hole in the center with a round tube. The energy release distribution by the height of the FE was calculated. For this, the FE was divided by height into 15 parts, each part having a length of 4 cm. The results of the calculations are presented in Table 1. As can be seen from Table 1, when replacing a square tube with rounded edges and a round hole in the center with a round tube, the energy release in the FA increases by an average of 5.5%.

Table 1. Energy release distribution by the height of the internal FE (60 cm is the upper part of the fuel element).

Height of FE, cm	Round tube, kW	Round hole, kW	The difference, %
60	2.79	2.60	6.81
56	2.96	2.76	6.76
52	3.61	3.45	4.43
48	4.39	4.19	4.56
44	4.97	4.74	4.63
40	5.59	5.33	4.65
36	6.17	5.87	4.86
32	6.6	6.27	5.00
28	7.03	6.66	5.26
24	7.24	6.83	5.66
20	7.13	6.73	5.61
16	6.73	6.37	5.35
12	6.01	5.65	5.99
8	5.12	4.81	6.05
4	4.69	4.40	6.18
Total	81.03	76.46	5.64

*Are given here: 1- Energy release in the center of FA with round tube, 2- Energy release in the center of FA with square tube with rounded edges and a round hole in the center, 3- The difference in energy output between square and round pipes.

3. Thermohydraulic calculations

For thermal hydraulic calculations, the ASTRA code [13] developed by NRC “Kurchatov Institute”, Russia, was used. Thermophysical parameters for calculations were taken from [13,14].

The thermal hydraulic calculations were performed for two cases: 1 – the case with a square tube with rounded edges and a round hole in the center and 2 – the case with a round tube.

Figure 5 shows a diagram of one side of the outer fuel element of the IRT-4M type fuel assembly. Water passes through the gaps in the fuel assembly from top to bottom.

The following notations are used in the figure:

TW1 - outer channel coolant temperature, °C

T1 - outer coolant/clad interface temperature, °C

T01 - outer clad/fuel meat interface temperature, °C

TM - maximum fuel meat temperature, °C

T02 - inner clad/fuel meat interface temperature, °C
T2 - inner clad/coolant interface temperature, °C
TW2 - inner channel coolant temperature, °C
All dimensions are given in millimeters.

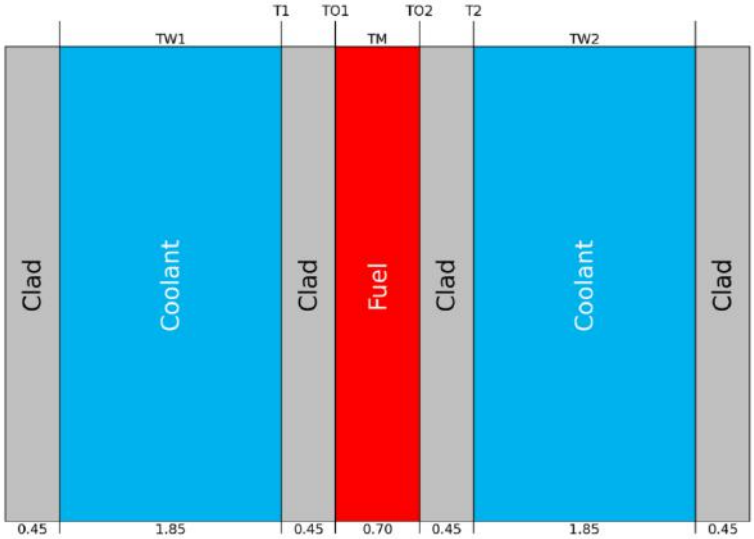

Fig.5. Schematic diagram of the fuel element side.

Table 2 shows the most heat-stressed side of the fuel element in cell 4-5 of the core, where a square tube with rounded edges and a round hole in the center is located in the center of the FA.

Table 2. Results of calculations using the ASTRA code of the most heat-stressed side of the fuel element in cell 4-5 of the cores, in the center of the FA, where there is a square tube with rounded edges and a round hole in the center.

TW1	T1	T01	TM	TO2	T2	TW2	QF1	QF2	SC1	SC2
45.0	54.6	54.8	55.0	54.9	54.9	45.0	91.	85.	7.54	7.28
45.8	57.7	58.1	58.3	58.1	58.1	45.2	116.	112.	5.72	5.55
46.7	62.3	62.8	63.0	62.8	62.8	45.5	154.	153.	4.27	4.15
48.0	66.2	66.7	67.0	66.7	66.7	46.0	183.	187.	3.52	3.43
49.5	69.9	70.5	70.8	70.5	70.5	46.4	210.	221.	3.02	2.95
51.1	72.9	73.6	73.9	73.6	73.6	47.0	228.	247.	2.70	2.65
52.9	75.3	76.1	76.4	76.0	76.0	47.6	237.	266.	2.49	2.45
54.6	75.4	76.1	76.4	76.0	76.0	48.2	221.	261.	2.47	2.45
56.2	73.4	74.0	74.2	73.8	73.8	48.8	183.	233.	2.61	2.61
57.5	70.8	71.2	71.4	71.1	71.1	49.3	139.	201.	2.84	2.86
58.6	70.8	71.2	71.3	71.0	71.0	49.8	128.	197.	2.83	2.87

The following designations are used:
QF1 - outer surface heat flow, kW/m*m
QF2 - inner surface heat flow, kW/m*m
SC1 - ONB margin on temperature for outer surface
SC2 - ONB margin on temperature for inner surface

Table 3 shows the most heat-stressed side of the fuel element in cell 4-5 of the core, where a round tube is located in the center of the FA. Table 4 shows the most heat-stressed parts of all 6 FEs of the FA. As can be seen from the table, when replacing a square tube with rounded edges and a round hole in the center with a round tube, the water temperature increases by about 2%.

Table 3. Results of calculations using the ASTRA code for the most heat-stressed side of the FE in cell 4-5 of the core, in the center of the FA where a round tube is located.

TW1	T1	T01	TM	TO2	T2	TW2	QF1	QF2	SC1	SC2
45.0	56.0	56.4	56.5	56.4	56.4	45.0	106	99	6.57	6.35
45.8	58.5	58.8	59.0	58.9	58.9	45.3	122	119	5.42	5.26
46.9	63.1	63.6	63.8	63.6	63.6	45.6	162	160	4.09	3.98
48.2	67.2	67.7	68.0	67.7	67.7	46.0	191	196	3.37	3.29
49.7	71.1	71.7	72.0	71.7	71.7	46.5	220	233	2.89	2.83
51.4	74.3	75.0	75.4	75.0	75.0	47.1	241	260	2.58	2.53
53.3	77.0	77.8	78.1	77.7	77.7	47.8	251	282	2.37	2.33
55.2	77.0	77.8	78.1	77.7	77.7	48.4	233	277	2.35	2.33
56.8	75.1	75.7	75.9	75.5	75.5	49.0	194	248	2.48	2.48
58.2	72.2	72.6	72.8	72.5	72.5	49.6	148	214	2.70	2.73
59.4	72.3	72.7	72.9	72.6	72.6	50.1	137	210	2.67	2.71

Table 4. Results of calculations using the ASTRA code for the most heat-stressed parts of all 6 FEs of the FA

# of FE tube	Round tube, °C	Square tube with rounded edges and a round hole in the center, °C	Difference in thermal stress, %
1	78.7	77	2.16
2	78.4	76.6	2.30
3	78.5	76.7	2.29
4	78.7	77	2.16
5	79	77.3	2.15
6	77.8	76.1	2.19

According to the performed calculations, the cladding surface temperatures are significantly lower than the values at which cladding damage may occur, and even lower than the temperature at which vapor bubbles begin to form in the coolant (124 °C, see [15]).

For IRT-4M nuclear fuel, the onset of nucleate boiling (ONB) safety factor according to the Bergles–Rohsenow correlation [16] should not be less than 1.3. According to the calculation results, when replacing the square tube with a circular one, this factor exceeds 2 for both the outer and inner surfaces.

In the case of installing a circular tube inside the fuel assembly instead of a square tube with rounded edges and a central circular hole, the volume of water in this region increases. On the one hand, this enhances heat removal due to the larger amount of coolant. On the other hand, the increased water volume leads to a higher fraction of thermal neutrons near the fuel rod surface, which in turn results in an increase in power generation. Calculations show that the power in the fuel elements rises by approximately 2%.

4. Conclusion

The performed neutron-physics and thermal-hydraulic calculations of the WWR-SM research reactor core with a loading of 24 IRT-4M type fuel assemblies containing low-enriched uranium (19.75% ^{235}U) made it possible to obtain the axial power density distribution for each fuel element and to determine the key thermal-technical parameters. It was shown that the maximum values of fuel temperature and heat flux in the most power-intensive fuel elements do not exceed the permissible design limits, thereby confirming the existence of sufficient margins for nuclear safety and thermal reliability. The calculation results confirm the correctness of the chosen reactor core configuration and applied design solutions. The obtained data can be used for optimizing reactor operating regimes, improving fuel utilization efficiency, as well as for further analysis of the feasibility of introducing new fuel types and conducting experimental studies in the reactor core.

Thus, the conducted study provides scientifically substantiated confirmation of the safe and reliable operation of the WWR-SM reactor with IRT-4M type fuel assemblies and forms the basis for further work aimed at improving its fuel cycle and design characteristics.

Conflict of interest statement

The authors declare that they have no conflict of interest in relation to this research, whether financial, personal, authorship or otherwise, that could affect the research and its results presented in this paper.

Credit author statement

Baytelesov S.A.: Writing - Original Draft; **Fayziev T.B:** Development of Facility and Measurements; **Kungurov F.R.:** Review & Editing; **Alikulov Sh.A.:** Conceptualization, Data Curation; **Tadjibaev D.P.:** Methodology, Investigation.
The final manuscript was read and approved by all authors.

References

1. Honghao Yu, Jiejin Cai, Sihong He, Xuezhong Li. (2021) Analysis of neutron physics and thermal hydraulics for fuel assembly of small modular reactor loaded with ATFs. *Annals of Nuclear Energy,* 152, 107957. https://doi.org/10. 1016/j.anucene.2020.107957
2. Malmir H., Vosoughi N., Zahedinejad E. (2010) Development of a 2-D 2-group neutron noise simulator for hexagonal geometries. *Annals of Nuclear Energy*, 37(8), 1089 – 1100. https://doi:10.1016/j.anucene.2010.04.007
3. Sidi-Ali K., Medouri E.M., Ailem D., Mazidi S. (2023) Neutronic calculations and thermalhydraulic application using CFD for the nuclear research reactor NUR at steady state mode. *Progress in Nuclear Energy,* 159, 104640. https://doi.org/10.1016/j.pnucene.2023.104640
4. Alzaben Y, Sanchez-Espinoza V.H., Stieglitz R. (2019) Analysis of a control rod ejection accident in a boron-free small modular reactor with coupled neutronics/thermal-hydraulics code. *Annals of Nuclear Energy,* 134, 114 – 124. https://doi.org/10.1016/j.anucene.2019.06.009
5. Erfaninia Ali, Hedayat Afshin, Mirvakili S.M. (2017) Nematollahi M.R. Neutronic-thermal hydraulic coupling analysis of the fuel channel of a new generation of the small modular pressurized water reactor including hexagonal and square fuel assemblies using MCNP and CFX. *Progress in Nuclear Energy*, 98, 213 – 227. https://doi.org/10.1016/ j.pnucene.2017.03.025
6. Xiaobei Xu, Zhouyu Liu, Hongchun Wu, Liangzhi Cao. (2022) Neutronics/thermal-hydraulics/fuel-performance coupling for light water reactors and its application to accident tolerant fuel. *Annals of Nuclear Energy,* 166, 108809. https://doi.org/10.1016/j.anucene.2021.108809
7. Yesbayev A.N., Yessenbayeva G.A.,Ramazanov M.I. (2019) Investigation of the model for the essentially loaded heat equation. *Eurasian Physical Technical Journal*, 16 , 1(31). https://doi.org/10.31489/2019No1/113-120
8. Shaimerdenov A.A., Shamanin I.V., Pribaturin N.A., Gizatulin Sh.Kh., Koltochnik S.N., Chekushina L.V. (2018) Thermophysical Justification for Conducting Lifetime Tests of Experimental Fuel Assemblies WWR-KN in the WWR-K Reactor. *Intern. Scientific Journal for Alternative Energy and Ecology,* https://doi.org/10.15518/isjaee.2018.10-12.023-033
9. Yusupov D.D., Abdullaev R.A. Research Nuclear Facility of Uzbekistan. [in Russian] Available at: file:///D:/Statya_2023_2024_2025/Statya_2025_Eura_Asian/71.pdf
10. Arkhangelsky N.V. (1985) *IRTNOW program for two-dimensional calculation of neutron flux densities in a two-group diffusion approximation*. Description of the application, Moscow, IAE. Available at: https://rusneb.ru/catalog/ 000200_000018_rc_682884/
11. Alikulov Sh.A., Baytelesov S.A., Boltaboev A.F., Osmanov B.S., Salikhbaev U.S. (2014) Experimental Studies of Spent Fuel Burn-up in the WWR-SM Reactor. *Nuclear Engineering and Design,* 277, 163 – 165. https://doi.org/10.1016/j.nucengdes.2014.06.020.
12. Baitelesov S.A., Dosimbaev A.A., Kungurov F.R., Salikhbaev U.S. (2008) Neutron-physical and thermal-hydraulic calculations of VVR-SM fuel assemblies from highly and low-enriched uranium. *Atomic Energy*, 104, 5. Available at: https://j-atomicenergy.ru/index.php/ae/article/view/1719
13. Taliev A.V. (2006) ASTRA modernized program for calculation of the thermal mode of the fuel assemblies of research reactors with tubular coaxial fuel elements. Available at: https://inis.iaea.org/records/m4cyv-40x35/
14. Baytelesov S.A., Kungurov F.R., Yuldashev B.S. (2020) Thermal-Hydraulic Calculations of the WWR-SM Research Reactor. *Nuclear Physics and Atomic Energy*, 21(2), 152–156. https://doi.org/10.15407/jnpae2020.02.152
15. Woodruff W.L., Warinner D.K., Matos J.E. (1992) Consequence Analysis Method. IAEA-TecDoc 643, *Research Reactor Core Conversion Guidebook. 2, Analysis, Appendices D; Radiological Consequence Analysis*. RERTR Program, Argonne National Laboratory, Argonne, Illinois, United States of America. Available at: https://www-pub.iaea.org/MTCD/Publications/PDF/te_643v2_prn.pdf

16.Li Dong Huang (2009) Evaluation Of Onset Of Nucleate Boiling Models. *ECI International Conference on Boiling Heat Transfer*. Available at: https://inis.iaea.org/records/c8grd-f8556

AUTHORS' INFORMATION

Baytelesov, Sapar Akimovich - Doctor (Sci.), Professor, Head of laboratory, Institute of Nuclear Physics, Uzbekistan Academy of Sciences, Ulugbek, Tashkent, Uzbekistan; Scopus Author iD: 9740002000; https://orcid.org/0000-0003-3926-9579; baytel@inp.uz

Kungurov, Fakhrulla Rakhmatullayevich – Doctor (Sci.), Senior researcher, Deputy Director; Institute of Nuclear Physics, Uzbekistan Academy of Sciences, Ulugbek, Tashkent, Uzbekistan; Scopus Author iD: 15021139600; https://orcid.org/0000-0003-4359-3523; fkungurov@inp.uz

Ajikulov, Sherali Abdusalomovich - PhD, Senior Researcher, Institute of Nuclear Physics, Uzbekistan Academy of Sciences, Ulugbek, Tashkent, Uzbekistan; Scopus Author iD: 55815707200; https://orcid.org/0000-0003-4028-6501; alikulov@inp.uz

Tadjibaev, Diyer Pulatovich – PhD, Senior researcher, Institute of Nuclear Physics, Uzbekistan Academy of Sciences, Ulugbek, Tashkent, Uzbekistan Scopus Author iD: 35305693000; https://orcid.org/0009-0001-9782-8079; tadjibaev@inp.uz

Fayziyev Temur Bahriddin o'g'li – PhD student, Institute of Nuclear Physics, Uzbekistan Academy of Sciences, Ulugbek, Tashkent, Uzbekistan; Scopus Author iD: 58427407800; https://orcid.org/0000-0002-8824-5488; temurfayziyev@outlook.com

EURASIAN PHYSICAL TECHNICAL JOURNAL

2025, Volume 22, No. 3 (53)

https://doi.org/10.31489/2025N3/75-83

Received: 18/04/2025 Revised: 05/06/2025 Accepted: 25/09/2025 Published online: 30/09/2025

Research Article

Open Access under the CC BY -NC-ND 4.0 license

UDC 537.521:535.372

OPTICAL SPECTROSCOPIC DIAGNOSIS OF ELECTRON TEMPERATURE AND DENSITY FOR ZN-AL ALLOY PLASMA: EFFECT OF LASER ENERGY ON PLASMA PARAMETERS

Jawad, Mohammed H*, Abdulameer, M.R

University of Baghdad, College of Science, Department of Physics, Baghdad, Iraq
* Corresponding Author: mohammed.hamza1204a@sc.uobaghdad.edu.iq

Abstract: *In this study, the properties of plasma produced from zinc and aluminum alloy were investigated using laser spectroscopy techniques. The alloy was locally manufactured and consisted of 20 to 80 percent zinc and aluminum, respectively. Neodymium-doped Yttrium Aluminum Garnet (Nd:YAG) laser with a fundamental wavelength of 1064 nm was used with a variable laser energy from 500 to 900 mJ In order to study the behavior of plasma and determine its general properties such as electron density and temperature. Boltzmann plot method was employed to ascertain the temperature of the electrons, in addition to using Stark expansion method to calculate the electron density. Based on these two basic parameters, the rest of the additional plasma parameters were calculated and determined. The results obtained from this study showed that there is a clear effect of laser energy on the plasma parameters, as the temperature and electron density increased significantly with the increase in laser energy, as these parameters gradually increased with the increase of laser energy. The maximum value of the electron temperature was 0.918 eV at 900 MJ, while the electron temperature was 0.537 eV at 500 mJ. On the other hand, the results showed an increase in both the Debye number and plasma frequency at high laser energies, while the Debye length showed a clear decrease at high power. The main purpose of this study is to contribute to a deeper understanding of the properties of plasma and how laser power affects these properties, which opens the way for many applications, including engraving and marking on metals and many industrial and technological applications.*

Keywords: Zn-Al Alloy, Optical spectroscopy of plasma (OES), Plasma properties and parameters.

1. Introduction

The analytical technique known as laser-induced plasma spectroscopy is well-established. used to determine samples' elemental compositions at a very high speed. This method can be categorized as a form of atomic emission spectroscopy, which is typically employed to examine materials, regardless of whether they are solid, liquid, or gaseous [1]. There are many uses for Laser-Induced Breakdown Spectroscopy (LIBS), an emission spectroscopic method for characterizing the elements in materials. When the surface of a sample is ablated by a high-intensity laser pulse, a plasma plume is created. The ablated mass of the substance falls between nanograms and micrograms [2]. The irradiation settings have a direct impact on the rapidly developing properties of the laser-generated plasma., which are transient by nature. These factors include the laser's wavelength, the duration of its pulse, the intensity of the laser incident on the target's surface, and the ambient pressure [3].To summarize, a high-intensity laser pulse targets a tiny area of the sample surface to excite the optical sample, which is then evaluated [4]. Recent years have seen a great deal of research on optical emission from laser-generated plasmas, and the sample target's interaction with the

laser was utilized to determine the atomic and ionic line emission [5]. The study of the generated emissions will contribute greatly to the identification of the elements using the spectrometer. The process of diagnosing the plasma is done by calculating its main parameters such as its temperature and electron density. On the other hand, there is a clear effect of the target material and the parameters of the laser used [6, 7]. The Boltzmann plot equation which is stated as follows, is one of the best methods for determining The local thermodynamic equilibrium's electron temperature, In contrast, one of the most popular approaches for the Optical spectroscopy of plasma (OES) in this study is the ratio approach [8].

$$\ln\left[\frac{\lambda_{ji} I_{ji}}{hcA_{ji} g_j}\right] = \frac{1}{k_B T}\left(E_j\right) + \ln\left[\frac{N}{U(T)}\right] \quad (1)$$

Here, I_{ji} is the emission line intensity, λ_{ji} the wavelength, gj the statistical weight of the upper level, Aji the transition probability, E_j the excitation energy, k_B Boltzmann's constant, and Te the electron temperature. The Stark expansion method is used to determine the electron density using the equation below: [9].

$$n_e = \left(\frac{\Delta\lambda_{FWHM}}{2w}\right) N_r \quad (2)$$

Here, Δλ is the full width at half maximum (FWHM) of the spectral line, ne the electron density, and w the Stark broadening parameter. The line w, $Nr \approx 10^{17}$ cm^{-3}, which theoretically represents the whole width of the Stark parameter, is represented by Full Width at Half Maximum (FWHM), which expresses the width at mid-intensity. The plasma frequency is adjusted so that electric fields are produced whenever its semi-neutral equilibrium is disturbed. Given that it solely depends on the plasma's density, this frequency is a very basic plasma factor. The plasma frequency can be computed using the formula below, which is inherently rather high due to the mince's small size [10]

One of the crucial factors is the Plasma frequency (fp) that are calculated in diagnostic processes, as the turbulent processes that occur lead to a disturbance of the quasi-equilibrium state in the plasma. The frequency is influenced by the density of plasma., can be calculated using the equation below [11].

$$f_p = \sqrt{\frac{e^2 n_e}{\varepsilon_0 m_e}} \quad (3)$$

Here, *fp* is the plasma frequency, *ne* the electron density, *e* the electron charge, *ε0* the permittivity of free space, and *me* the electron mass.

The main characteristic of plasma that is calculated is the Debye length (λD), which represents the distance at which the plasma is protected from the effects of the external electric field. The Debye length is inversely related to the electron density and is expressed mathematically using the equation below [12].

$$\lambda_D = \sqrt{\left(\frac{\epsilon_0 \mathbf{k}_B T_e}{n_e e^2}\right)} = 7430 * \sqrt{\frac{T_e}{n_e}} \quad (4)$$

Here, *λD* is the Debye length, *Te* the electron temperature, *ε0* the permittivity of free space, *kB* Boltzmann's constant, *ne* the electron density, and *e* the electron charge.

Comparing the system dimension to this basic prerequisite for plasma existence (λD < < < L), the Debye length should be relatively tiny. The second need for plasma existence (Debye number (ND)>>>1), which depends as follows on the electron temperature and density [13-15]

$$N_D = \frac{4}{3}\pi n_e \lambda_D^3 \quad (5)$$

Here, *ND* is the Debye number, *ne* the electron density, *λD* the Debye length, and *V* the plasma volume. The primary goal of this research is to investigate the effect of laser beam energy on the behavior of induced plasma produced from zinc and aluminum alloys in order to provide a deeper and more comprehensive understanding of how laser energy interacts with different materials, which could open up great horizons in many industrial and technological applications, especially those applications that include this type of process.

2. Experimental section

2.1 Preparing Zinc-aluminum alloy

A locally produced zinc-aluminum alloy with a purity of (99.99%) was prepared using a gas smelting method. This alloy consists of 80% zinc and 20% aluminum. The zinc was melted at a temperature of 550°C, after which aluminum was added in lumps, and the mixture was mixed using a diffusion method. The gas smelting method offers many advantages, as it provides better control over the temperature of the elements,

which helps in pouring the alloy evenly and accurately. In addition, it is cost-effective compared to other methods, and it provides a cleaner environment and is less polluted than traditional fuels. A square sample of the alloy, measuring (2 x 2 cm) and 3 mm thick, was positioned 10 cm away from the laser lens after that to get it ready for the procedure of ablation. Figure 1 shows the alloy used in the study.

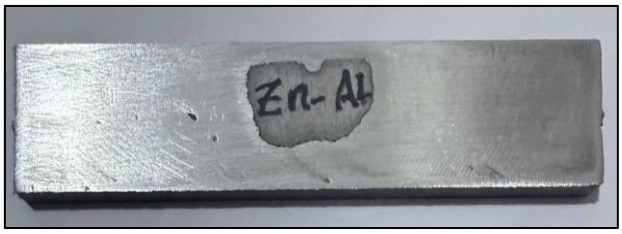

Fig 1: Cross section of zinc aluminum alloy

2.2 Configuring the laser-induced spectroscopy system

In this study, plasma was generated by a pulsed Nd:YAG laser operating at 6 Hz and a wavelength of 1064 nm. A target surface, placed 10 cm away, was illuminated by the beam at a 45° angle. This beam ionized and vaporized the material, creating plasma above the surface. This experiment was conducted at atmospheric pressure with pulse rates ranging from 15 to 30 pulses. Wavelength spectra were then obtained by placing a Sarwat (S3000)-UV-NIR spectrometer 1 cm from the target surface of the sample, as shown in Figure 2. These spectra were recorded for all laser energies used, ranging from 500 to 900 mJ, and compared with the National Institute of Standards and Technology (NIST) data shown in Table 1. This technique was used to determine the plasma parameters of the alloys used.

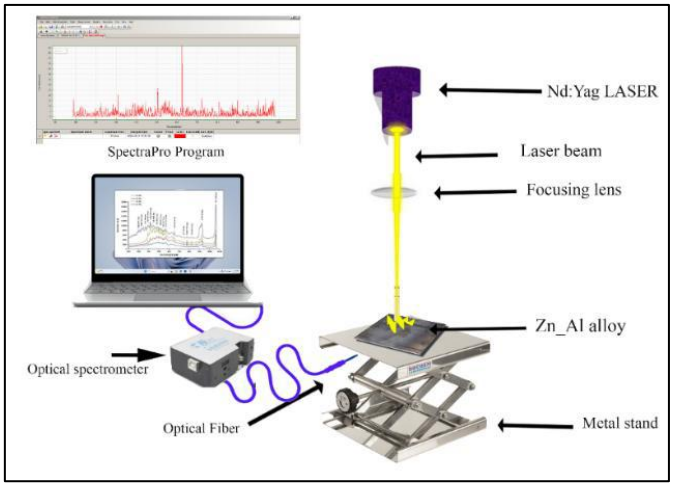

Fig 2: Basic components of an induced laser spectroscopy system

Table 1: Basic parameters of Zn-Al Alloy plasma

Element	Intensity	λ (nm)	g_kA_{ki} (S^{-1})	E_K (eV)
AL I	397.63	226.3462	8.80E+07	5.568835
	628.51	236.7052	5.58E+08	3.816692
	6530.41	308.2151	4.50E+08	6.192025
	7586.39	394.40058	8.72E+07	7.737027

3. Results and Discussion

The spectra in Figure 3 clearly show the increase in emission line intensities with increasing laser energy. The most pronounced variations were observed at the Al I line (394.40 nm) and the Zn I line (636.23 nm), which exhibit systematic intensity enhancement as the laser fluence increases. These lines were therefore selected as representative indicators of the effect of laser energy on plasma emission.

The above data shows that the emission lines of the spectrum increase with increasing laser power. The main reason for this is that as the power increases, the ablation of the metal (target) increases, resulting in increased plasma emission. More than one emission line was recorded for the alloying elements. The highest peak for aluminum was at a wavelength of 394.400 nm, while the highest peak for zinc was at a wavelength of 636.23 nm. Emissions from nitrogen and oxygen gases were also recorded. The nitrogen peak reached 480.0 nm, while the oxygen peak was recorded at 435.45 nm [16].

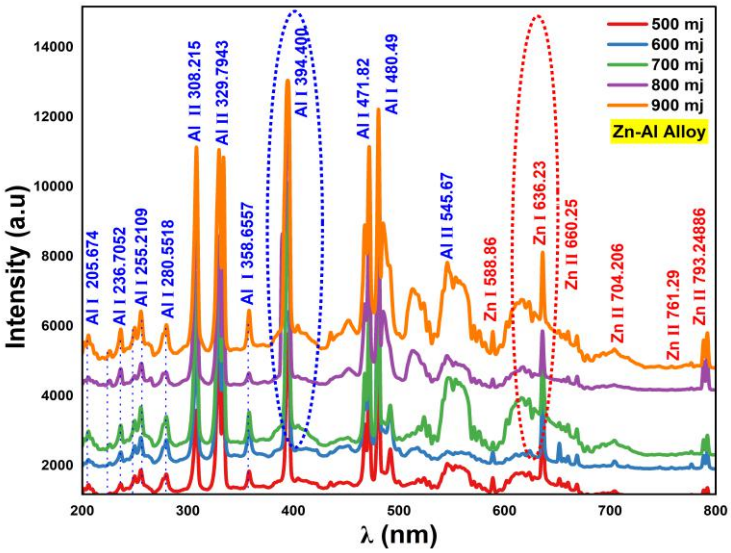

Fig.3. Laser-Induced Plasma Emission Spectra on an Al-Zn Alloy Target at Various Laser Energies

The variation of spectral line intensities with laser energy does not follow a strictly linear trend. This non-linearity can be explained by self-absorption of emitted radiation at higher plasma densities, plasma shielding effects that reduce the effective laser energy reaching the target, and enhanced collisional processes (electron–ion and electron–neutral) which modify the population of excited states. These combined mechanisms result in deviations from linear behavior for some spectral lines.

According to Equation 1, the Electron temperature (Te) in the zinc-aluminum alloy plasma in this study was determined using the Boltzmann diagram method. Considering the existence of thermodynamic equilibrium, the slope of the curve drawn between $Ln(\lambda jiIji/gjAji)$ and energy is the criterion for applying the Boltzmann diagram method. Four atomic lines of aluminum (Al I) were used, all in the same atomic transition state. The temperature was calculated by taking the reciprocal of the slope ($-1/kBT$). The R2 criterion is an indicator of the degree of agreement of the result, also known as the statistical coefficient, and its value always ranges from 0 to 1, with the best result being close to 1. Figure 4 shows the Boltzmann correlation diagram.

The findings indicated that the temperature of electrons is directly related to the laser beam energy, with a gradual increase observed at all laser energies used. This is because as the laser energy increases, more energy is transferred to the electrons [17]. The higher the energy, the greater the amount of energy transferred, and consequently, the mobility of these electrons increases, leading to an increase in their temperature. The temperature at an energy of 500 millijoules was found to be 0.537 electron volts, while at a temperature of 900 millijoules, it was 0.918 electron volts. The electron temperature (Te) shows an almost linear increase with laser energy.

This behavior can be explained by the direct coupling of the laser pulse with the plasma electrons. As the laser fluence increases, a larger number of free electrons are generated and these absorb the incident radiation mainly through inverse Bremsstrahlung and collisional excitation, converting the laser energy into electron thermal energy.

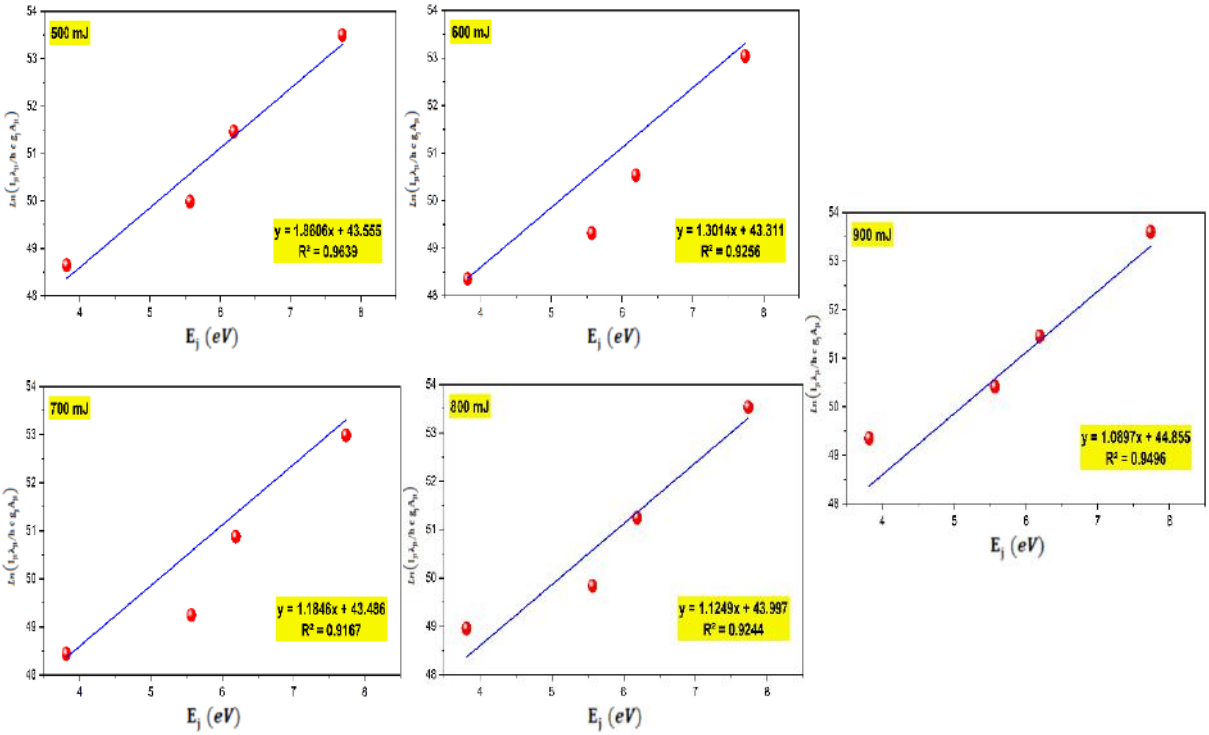

Fig 4. Zn-Al alloy plasma's Boltzmann plot was determined using a range of laser intensities.

Under the present experimental conditions, the rate of this energy transfer is approximately proportional to the laser energy, which results in the observed near-linear dependence. The figure 5 shows the electron temperature of a zinc-aluminum alloy in electron volts and kelvins.

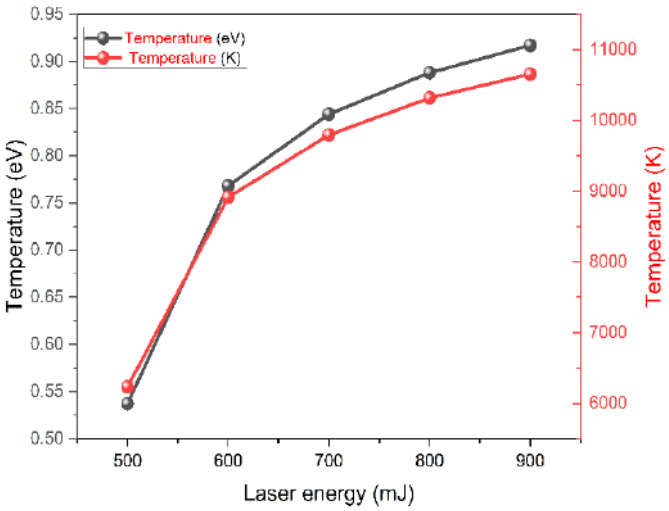

Fig 5. Electron temperature of zn-al alloy in electron volts and kelvin at varying laser intensities (500-900 mJ).

The Stark broadening method was used to calculate the Electron density (ne). This method is based on measuring he amplitude of the spectral lines and calculating the width at the midpoint of the intensity. The laser-induced emission spectrum of zinc and aluminum alloys exhibits broad lines, as shown in Figure 6.

These lines are primarily affected by their high amplitude. This is caused by collisions between charged particles and the emitting atoms. Equation (2) was used to calculate the electron density based on the spectral line width. The AL spectral emission line at 394.400 nm was used to calculate the electron density for the various energies used. The results obtained showed that the electron density is directly affected by the laser beam energy, showing a clear increase at higher energies. The maximum electron density at a laser energy of 500 mJ was $5.4*10^{17}$ (cm^{-3}), while the highest density at a laser energy of 900 mJ was $9.61*10^{17}$ (cm^{-3}). This demonstrates that when laser intensity increases, the electron density rises noticeably.

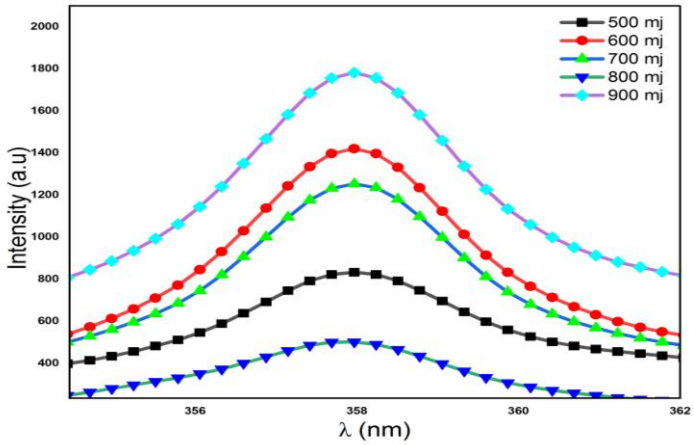

Fig.6. The Zn-Al alloy spectrum's full width at half maximum (FWHM) at 356-364 nm at various laser energy levels (Lorentzian Fitting).

To more accurately describe the properties of the zinc-aluminum plasma, Laser beam energy's impact on other plasma properties were examined. It was found that increasing the energy directly and significantly affects these other fundamental parameters, such as the (λD), (fp), and (N_D). Equations 3, 4, and 5 were used to obtain the data shown in Table 2, which indicate that the plasma frequency fp and N_D will increase significantly When the laser's energy increases. This is due to the fact that frequency and density are directly correlated, and the number of collisions increases at higher energies due to the increased amount of energy transferred from the laser beam to the resulting plasma. The peak plasma frequency was recorded at an energy of 500 mJ, while the peak frequency was recorded at an energy of 900 mJ. These findings also revealed a noteworthy increase in Nd with increasing laser beam energy. This is because that higher laser energy leads to increased interaction with the sample, resulting in the formation of more particles as a result of this interaction. On the other hand, increasing laser energy leads to a decrease in λD. This is because higher laser energy causes increased movement of plasma particles due to the greater energy they gain. This movement will cause the distance between the particles to decrease. The greater the energy, the more interactions between the particles increase, and the closer they become. In other words, the Debye length depends on the temperature of the electrons. Since increasing laser energy leads to an increase in the temperature of the electrons, this will in turn lead to a decrease in the Debye length [18].

Table 2: Features of the Zn-Al alloy plasma produced at various laser energies using a 1064 nm laser

E (mJ)	Te (eV)	n_e *10 ^{17} (cm^{-3})	f_p * 10^{+12} (Hz)	λ_D*10^{-6} (cm)	N_d *10^3
500	0.537	5.49	6.7	2.0	0.913
600	0.768	6.74	7.4	1.8	1.409
700	0.844	8.62	8.3	1.6	1.435
800	0.889	9.51	8.8	1.4	1.476
900	0.918	9.61	8.9	1.3	1.540

Figure 7 illustrates how laser power significantly affects the electron temperature and density. We observe that the Te gradually increases from 0.537 to 0.918 eV with increasing laser intensity. The results also show that the electron density increases from 5.49 to 9.61 with increasing laser power. The main reason

for this increase is the increase in laser pulse energy, which significantly affects the emission lines' intensity. This, in turn, affects the increase in these parameters.

Figure 8 shows the frequency of plasma rises and the Debye length decreases with increasing laser intensity. The frequency values range from 6.7 * 10^{12} to 8.9 * 10^{12} Hz, and 500-900 mJ is the laser power range. Equation 3 states that since the frequency and density are directly related, the frequency increase is natural. Equation 4 asserts that the relationship between the Debye length and the electron density is inverse. and decreases as the laser power increases. Its values are between 1.5 * 10^{-6} cm-3 and 2 * 10^{-6}. These results are consistent with the results of Maryam and Khadem (2021) [1].

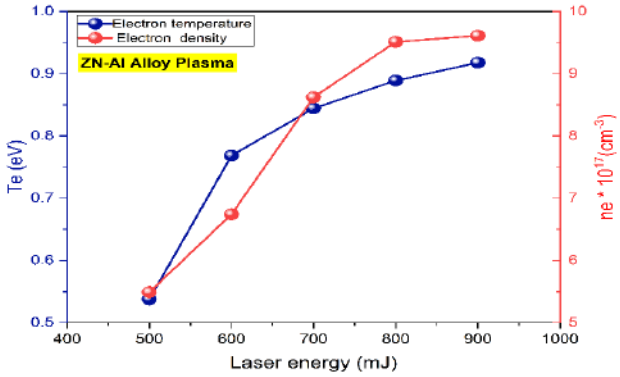

Fig.7. Zn-Al alloy's Te and Ne differences as a function of laser power at various energy levels

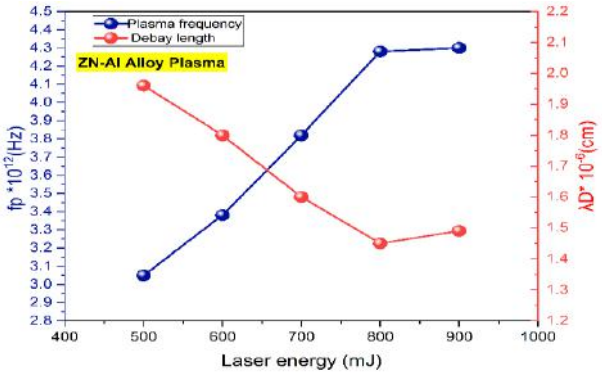

Fig.8. Zn-Al alloy's fp and λD differences with laser power at various energy levels

Figure 9 shows the clear increase in the number of particles in the Debye sphere in relation to laser intensity. This can be explained by the fact that increasing the laser power will have a significant effect on the particles that make up the plasma, making them move at a faster speed, which increases their interactions in the medium.

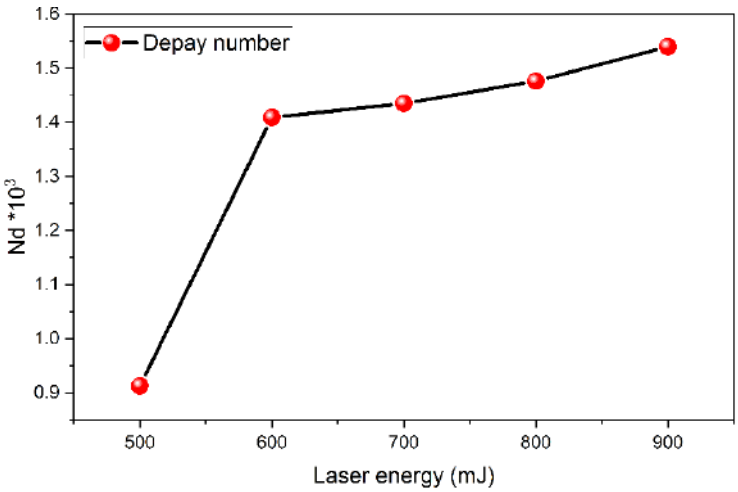

Fig. 9. Zn-Al alloy plasma's Debye number at varying laser energies

That is, the distances that the particles penetrate will be larger, meaning that the number of ionized atoms will become greater, and thus additional quantities of charged particles (electrons or ions) will be released. these results are consistent with [19].

4. Conclusion

This study focused on optical spectroscopy (OES) to characterize the plasma properties generated using a 1064 nm Nd:YAG laser from locally manufactured zinc-aluminum alloys with fabrication percentages ranging from 20% to 80%. The primary objective was to determine the basic plasma parameters, such as electron density and electron temperature, and to study the effect of laser beam energy on these properties

and the emissions associated with plasma formation. The Boltzmann diagram and Stark expansion were used to calculate both the electron density and temperature. The results showed that the highest value was obtained at 900 mJ, with the electron temperature reaching 0.918 eV, compared to 0.537 eV at 500 mJ. The results also showed that increasing laser power significantly affects secondary plasma properties, such as the Debye length, plasma frequency, and Debye number. Both the plasma frequency and Debye number increase with increasing energy, while the Debye length decreases with increasing energy. Thus, it is clear that the laser power plays a crucial role in controlling the plasma properties and parameters in locally manufactured Zn–Al alloys.

Conflict of interest statement

The authors declare that they have no conflict of interest in relation to this research, whether financial, personal, authorship or otherwise, that could affect the research and its results presented in this paper.

Credit author statement

Jawad, Mohammed H.: Conceptualization, Methodology, Writing - original draft; **Abdulameer, Mohammed R.:** Data Curation, Investigation; Review & Editing, Validation.

The final manuscript was read and approved by all authors.

References

1. Abbas Z.M., Abbas Q.A. (2024) Aluminum-doped ZnO nano-laminar structures by pulsed laser ablation for gas sensing application. *Journal of Optics, 53*(2), 544–557. https://doi.org/10.1007/s12596-023-01192-z
2. Aadim K.A. (2019) Spectroscopic studying of plasma parameters for SnO_2 doped ZnO prepared by pulse Nd:YAG laser deposition. *Iraqi Journal of Physics, 17*(42), 125–135. https://doi.org/10.30723/ijp.v17i42.447
3. Ahmed R.T., Ahmed A.F. (2024) Optical emission spectroscopy characteristics of chromium plasma parameters. *Journal of Optics, 53*(2), 1590–1597. https://doi.org/10.1007/s12596-023-01336-1
4. Ahmed R.T., Ahmed A. F., Aadim K.A. (2024) Influence of laser energy on structural and morphology properties of CdO and CdO: Sn production by -induced plasma. *Journal of Optics, 53*(2), 1564–1573. https://doi.org/10.1007/s12596-023-01291-x
5. Alkareem R.A., Ahmed B.M. (2025) Influence of laser energy on optical emission spectroscopy characteristics for zinc plasma parameters. *Journal of Optics, 29,* 1–6.https://doi.org/10.1007/s12596-025-02472-6
6. AlRashid S.N., Majeed N.F., Azeez M.A., Mazhir S.N. (2025) Calculating plasma parameters for Zn target using laser-induced breakdown spectroscopy. *Journal of Optics, 28,* 1–7. https://doi.org/10.1007/s12596-025-02644-4
7. Chen F.F. (2015) *Introduction to plasma physics.* Springer Science & Business Media. https://doi.org/10.1007/978-3-319-22309-4
8. Fahem M.Q., Jawad M.H., Abdulsada R.O., et al. (2025) The structure and electrical properties of $NiFe_2O_4$ and $NiMgFe_2O_4$ prepared via sol–gel method. *Ionics, 31,* 6475–6481. https://doi.org/10.1007/s11581-025-06333-x
9. Iftikhar A., Jamil Y., Nazeer N., Tahir M.S., Amin N. (2021) Optical emission spectroscopy of nickel-substituted cobalt–zinc ferrite. *Journal of Superconductivity and Novel Magnetism, 34,* 1849–1854. https://doi.org/10.1007/s10948-020-05734-5
10. Jamali S., Khoso M. A., Zaman M. H., Jamil Y., Bhutto W.A., Abbas A., Mari R.H., Kalhoro M.S., Shaikh N.M. (2021) Elemental analysis of kohl using laser ablation and atomic absorption spectroscopy (AAS) techniques. *Physica B: Condensed Matter, 620,* 413278. https://doi.org/10.1016/j.physb.2021.413278
11. Jawad M.H., Abdulameer M.R. (2023) The effect of background argon gas pressure on parameters of plasma produced by DC glow discharge. *Iraqi Journal of Science, 64*(3), 1210–1218. https://doi.org/10.24996/ijs.2023.64.3.17
12. Jawad M.H., Abdulameer M.R. (2024) Study the effect of external voltage on some plasma parameters produced by DC glow xenon gas discharge. *AIP Conference Proceedings, 2922*(1), 150003. https://doi.org/10.1063/5.0183126
13. Jawad M.H., Abdulameer M.R. (2025) Spectral analysis of brass plasma generated by a Nd:YAQ laser at $\lambda = 1064$ nm. *Russian Physics Journal, 68,* 903-911. https://doi.org/10.1007/s11182-025-03509-w
14. Jawad M.H., Abdulameer M.R. (2025) Spectroscopic investigation of plasma from Al–Ni alloy using OES technique: Influence of voltage on plasma parameters. *Indian Journal of Physics,* https://doi.org/10.1007/s12648-025-03738-2
15. Jawad M.H., Abdulameer M.R., Aadim K.A. (2025) Spectral diagnostics of Al–Ni alloys under laser irradiation: Effect of laser energy on plasma parameters. *Scientific and Technical Journal of Information Technologies, Mechanics and Optics, 25*(4), 626–634. https://doi.org/10.17586/2226-1494-2025-25-4-626-634
16. Kadhem S.J. (2023) Preparation of Al_2O_3/PVA nanocomposite thin films by a plasma jet method. *Science and Technology Indonesia, 8*(3), 471–478. https://doi.org/10.26554/sti.2023.8.3.471-478

17. Khaleel S.F., Aadim K.A. (2025) Investigation study of the plasma parameters for bronze produced by Nd:YAG laser at wavelength 1064 nm: Effect of laser energies. *Journal of Optics,* 1–6. https://doi.org/10.1007/s12596-025-02698-4

18. Mansour S.A.M. (2015) Self-absorption effects on electron temperature-measurements utilizing laser induced breakdown spectroscopy (LIBS) techniques. *Optics & Photonics Journal, 5*(3), 79–90. https://doi.org/10.4236/opj.2015.53007

19. Mohammed R.S., Aadim K.A., Ahmed K.A. (2022) Spectroscopy diagnostic of laser intensity effect on Zn plasma parameters generated by Nd:YAG laser. *Iraqi Journal of Science, 63*(9), 3711–3718. https://doi.org/10.24996/ijs.2022.63.9.5

20. Murtaza G., Shaikh N.M., Kandhro G.A., Ashraf M. (2019) Laser induced breakdown optical emission spectroscopic study of silicon plasma. *Spectrochimica Acta Part A: Molecular and Biomolecular Spectroscopy, 223,* 117374. https://doi.org/10.1016/j.saa.2019.117374

21. Oyebola O.O. (2017) Long wave-infrared laser-induced breakdown spectroscopy emissions from potassium chloride (KCl) and sodium chloride (NaCl) tablets. *Journal of Scientific Research & Development, 17,* 54–56. https://doi.org/10.4302/plp.2011.4.15

22. Rashid T.M., Rahmah M.I., Mahmood W.K., Fahem M.Q., Jabir M.S., Bidan A.K., Adbalrazaq S., Jawad M.H., Awaid D.M., Qamandar M.A., Alsaffar S.M. (2025) Eco-friendly laser ablation for synthesis of CNF@ Au nanoparticles: Insights into enhancing NO_2 gas detection and antibacterial activity. *Plasmonics.* https://doi.org/10.1007/s11468-025-02874-z

23. Shehab M.M., Aadim K.A. (2021) Spectroscopic diagnosis of the CdO: CoO plasma produced by Nd:YAG laser. *Iraqi Journal of Science, 62*(9), 2948–2955. https://doi.org/10.24996/ijs.2021.62.9.11

24. Turki Z.T., Fahem M.Q., Mankhi Z.A., et al. (2025) Magnetic field effect on cadmium oxide plasma properties detected by laser spectroscopy. *Russian Physics Journal,* 68, 804-812. https://doi.org/10.1007/s11182-025-03497-x

25. Wang J., Li X., Wang C., Zhang L., Li X. (2018) Effect of laser wavelength and energy on the detecting of trace elements in steel alloy. *Optik, 166,* 199–206. https://doi.org/10.1016/j.ijleo.2018.04.018

AUTHORS' INFORMATION

Jawad, Mohammed H. – PhD, Professor, Department of Physics, University of Baghdad, Baghdad, Iraq; SCOPUS Author ID: 56971327800; https://orcid.org/0000-0002-7395-9840; mohammed_plasma@sc.uobaghdad.edu.iq

Abdulameer, Mohammed R. – PhD Student, Department of Physics, University of Baghdad, Baghdad, Iraq; SCOPUS Author ID: 58536603200; https://orcid.org/0009-0001-8111-8195; mohammed.hamza1204a@sc.uobaghdad.edu.iq

EURASIAN PHYSICAL TECHNICAL JOURNAL

2025, Volume 22, No. 3 (53)

https://doi.org/10.31489/2025N3/84-90

Received: 02/04/2025 Revised: 21/08/2025 Accepted: 25/09/2025 Published online: 30/09/2025

Research Article

Open Access under the CC BY -NC-ND 4.0 license

UDC 53.662

SUBSTITUTION OF THERMAL-TECHNICAL AND GEOMETRIC PARAMETERS OF A SMALL-SCALE BIOGAS PLANT

Sharipov M.Z.[1*,2], Majitov J.A.[3], Ergashev Sh.H.[4], Shodiyev E.B.[3], Narzullayeva Z.M.[1,5]

[1] Bukhara State University, Bukhara, Uzbekistan
[2] Bukhara State Pedagogical Institute, Bukhara, Uzbekistan
[3] Bukhara State Technical University, Bukhara, Uzbekistan
[4] Karshi State Technical University, Karshi, Uzbekistan
[5] Bukhara State Medical Institute, Bukhara, Uzbekistan
*Corresponding author: m.z.sharipov@buxdu.uz

Abstract. *This article is devoted to the issues of justification of thermal-technical and geometric parameters for small-scale biogas devices. The growing demand for sustainable and renewable energy resources has increased the importance of biogas technologies, particularly at the small-scale level for rural and agricultural applications. However, the efficiency and stability of biogas production largely depend on the thermal-technical conditions of the digester and the optimization of its geometric parameters. The purpose of this study is to analyze the effect of substituting thermal-technical and geometric parameters on the performance of a small-scale biogas plant. The research object is a laboratory-scale biogas digester with adjustable design features. Methodologically, the work is based on mathematical modeling, computational analysis, and experimental validation of heat transfer and mass balance processes inside the digester. From the results of the resulting study, it can be seen that the methods of determining the optimal geometric dimensions (diameter and length) of the bioreactor structure and reducing heat losses have been analyzed. Mathematical modeling methods have been used to calculate the optimal reactor diameter for various thermal insulation thicknesses and biomass dosing, and the optimal diameter for a 30 m^3 bioreactor is 2800 mm, while the length is 4900 mm, the proportion of biomass in the reactor volume is expressed by the central sector angle.*

Keywords: biogas plant, thermal parameters, reactor insulation, fermentation process, biomass, anaerobic conditions, energy efficiency.

1. Introduction

In recent decades, many countries around the world have been carrying out large-scale and long-term reforms in both the economic and social spheres, with the primary objective of increasing overall energy efficiency, ensuring sustainable use of resources, and at the same time improving the ecological balance as well as the epidemiological situation of the environment in which people live. Within these processes, special attention is being given to encouraging and supporting the widespread use of renewable energy source (RES)-based technologies and devices in different branches of the national economy, since this direction is recognized as one of the most important priorities of modern state policy.

Biomass is one such RES, encompassing organic materials such as agricultural, livestock, and poultry waste, as well as other biological products. Following solar, wind, hydro, and geothermal energy, bioenergy derived from biomass is ranked as the fifth most efficient RES. Approximately 170 billion tons of primary

biological mass are accumulated annually on the Earth's surface, with nearly the same amount of biomass being reprocessed and utilized for various purposes [1,2]. Harnessing biomass for energy production presents a complex challenge from the perspective of ecological sustainability and efficiency. The development and implementation of novel devices and technologies that minimize environmental impact, maximize energy output while utilizing resources most effectively, are of paramount importance [3]. Currently, various digester designs are employed worldwide to generate biogas through the anaerobic digestion of biomass. However, most of these digesters possess large volumes, leading to high energy consumption. The widespread adoption of such systems is limited under the conditions prevalent in our Republic.

This article is dedicated to the development of small-scale, energy-efficient biogas digesters based on renewable energy sources, designed for individual consumers. Research is focused on improving the design of the digester, enhancing operational productivity, optimizing thermotechnical parameters, and modeling heat transfer processes within the digester. The objective is to develop an energy-efficient design of a metered biogas digester, which ensures the effective anaerobic fermentation process through the regulated processing of organic waste under anaerobic conditions, and to optimize its key energy parameters. This constitutes an important and topical task in the field.

The development of small-scale biogas plants has attracted significant attention in recent years due to their potential to improve energy self-sufficiency in rural areas while contributing to environmental sustainability. Previous studies have demonstrated that the efficiency of biogas production is strongly dependent on the thermal stability of the digester and the optimization of its structural parameters. For instance, Yan et al. [1] investigated energy conversion from food waste and highlighted the decisive role of operating conditions and reactor configuration in maximizing gas yield. Tagne et al. [2] emphasized the challenges of biogas technology implementation in agricultural regions of China and Africa, pointing out that economic viability and simplified designs are critical factors for adoption. A number of engineering-focused works, such as those by Conti et al. [3] and Vesvikar et al. [4], revealed that optimization of geometric parameters, particularly reactor diameter and length, significantly reduces heat loss and enhances fermentation uniformity. Schmidt et al. [6] and Rojas et al. [7] highlighted the importance of substrate composition and mixing, which are also closely linked to thermal management and microbial activity in the anaerobic digestion process. Despite these contributions, most published studies have concentrated either on large-scale industrial digesters or on specific substrate-related issues, while the adaptation of design parameters for compact digesters suitable for small farms and household applications remains underexplored. In this context, the present study addresses a clear research gap by providing a systematic methodology for determining the optimal thermal and geometric characteristics of a 30 m³ small-scale reactor, considering both insulation thickness and the proportion of liquid and gas phases.

Unlike the work of Yan et al. [1], which focused primarily on the conversion efficiency of organic waste through supercritical processes, the present study concentrates on classical anaerobic digestion with an emphasis on engineering optimization. Compared to Tagne et al. [2], who investigated socioeconomic perspectives of biogas adoption, our work provides a more technical and quantitative analysis of digester design. The modeling approaches of Conti et al. [3] and Vesvikar et al. [4] relied heavily on computational fluid dynamics and flow visualization, whereas this study proposes an analytical framework for determining optimal reactor dimensions supported by experimental validation. Similarly, while Schmidt et al. [6] and Rojas et al. [7] examined operational parameters such as trace elements, mixing, and substrate preparation, the originality of this work lies in minimizing heat losses through the combined optimization of insulation thickness and geometric design. Therefore, the novelty of the present research consists in developing a straightforward yet practical method for improving the thermal efficiency of small-scale digesters. This approach not only provides theoretical insight but also offers direct applicability to household and farm-scale biogas systems, which makes it a valuable contribution to the sustainable energy sector.

2. Experimental research results

Biogas plants consist of equipment designed to process organic matter under anaerobic conditions, producing biogas and organic fertilizers. The reactor, typically a horizontal or vertical cylindrical vessel, serves as the core component where organic material is processed. Maintaining a consistent temperature inside the reactor is critical—for instance, 35–37°C for mesophilic operation—throughout the fermentation period [1–4].Processing livestock waste in biogas plants requires thermal energy to sustain the desired

operating temperature. The energy demand depends on multiple factors, making it essential to minimize reactor heat loss through optimized design parameters.

To reduce heat loss, the reactor's geometric parameters must be carefully justified. In the reactor's heat balance, heat loss primarily occurs through the heat exchange surface with the external environment [5–8].

$$Q = kF\Delta t \tag{1}$$

where, k is the heat transfer coefficient, W/(m^2·K); F is the surface area of the heat transfer (loss) surface, m^2; Δt is the temperature difference between the inside of the reactor and the outside air, ºC;

During the fermentation process, the reactor is not completely filled and two media can be distinguished according to its volume: liquid (biomass to be fermented) and biogas formed during the decomposition of biomass. In this case, the heat balance equation for an unfilled reactor can be written as follows:

$$Q_g = \left(k_s F_s + k_g F_g\right)\Delta t \tag{2}$$

where, $k_s -$ heat transfer coefficient from biomass to the external environment, Vt/(m^2·K); F_s – surface area of heat transfer through biomass to the external environment, m^2; $k_g -$ heat transfer coefficient from biogas to the external environment, W/(m^2·K); F_g – surface area of heat transfer through biogas to the external environment, m^2;

In this equation, the first term represents the heat loss from the biomass, and the second from the gas phase. The temperature difference Δt for biomass and biogas is assumed to be the same. In this case, the heat transfer coefficient through the reactor wall can be expressed as follows [9,10]:

$$k = \frac{1}{\frac{1}{\alpha_1} + \sum_{i=1}^{n} \frac{\delta_i}{\lambda_i} + \frac{1}{\alpha_2}} \tag{3}$$

The heat transfer coefficient for the biomass-filled part of the reactor is $\alpha_1 = 350\ W/(\mathrm{m}^2 \cdot \mathrm{K})$, for the gas part – $\alpha_1 = 8{,}7\ \mathrm{W/(m^2 \cdot K)}$. $\alpha_2 = 23\ \mathrm{W/(m^2 \cdot K)}$ –is the heat transfer coefficient from the reactor wall to the external environment, and the same value is obtained for both cases [4].

The bioreactor is made of chromium-molybdenum steel with a thickness of $\delta_d = 5\ mm$ a thermal conductivity coefficient $\lambda_d = 37{,}7\ \mathrm{W/(m \cdot K)}$ and a thermal conductivity coefficient of the external insulation material (glass wool) $\lambda_{iz} = 0{,}05\mathrm{W/(m \cdot K)}$ .Figure 1 shows the values of the heat transfer coefficient for the liquid and gas phases inside the reactor at different thicknesses of the external insulation layer.

3. Analysis of insulation thickness and heat loss reduction

Figure 1 demonstrates that with an external insulation layer thickness of 5 sm, the heat transfer coefficient to the external environment stabilizes across both phases (liquid and gaseous) and remains constant even with further increases in insulation thickness. This indicates that 5 sm is the optimal insulation thickness for the reactor, as additional layers do not yield further reductions in heat loss.

To enhance thermal efficiency, minimizing heat loss requires a holistic approach:

– Optimizing insulation thickness (with 5 cm being the cost-effective threshold).

– Reducing the heat-conducting surface area, since excessive insulation entails diminishing returns and added material costs.

Thus, reactor design should balance insulation efficacy with economic feasibility by considering both insulation thickness and surface area reduction strategies.

Then it is necessary to reduce the heat transfer surface to choose the optimal option. The optimal diameter can be chosen when the value representing the heat losses in a reactor with a horizontal location is minimal. The surface bounded by the liquid (biomass) part of the reactor is equal to the sum of the 2 side segments and segments and the front surfaces represented by the cylinder length, which can be expressed as [10 - 12]:

$$F_s = 2 \cdot F_{seg.1} + F_{old.1} \tag{4}$$

Depending on the degree of saturation of the reactor with biomass, the segment surface formed on the side of the cylinder can be written as

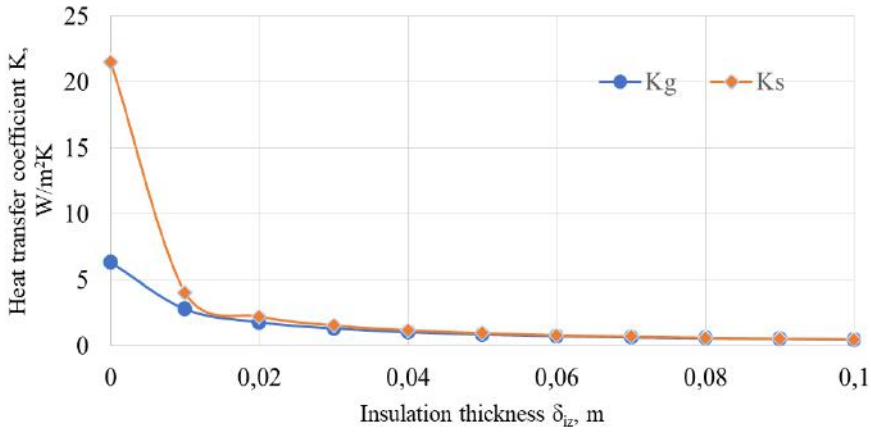

Fig. 1. Dependence of the heat transfer coefficient of the outer insulation layer for the liquid and gas phases inside the reactor.

$$F_{seg.1} = \frac{D^2}{8}(\beta - \sin(\beta)) = \frac{D^2}{8}\left(\frac{\pi\cdot\beta}{180} - \sin\left(\frac{\pi\cdot\beta}{180}\right)\right) \quad (5)$$

At the biomass saturation level, we represent the front surface as follows:

$$F_{old.1} = \beta\frac{D}{2}\cdot L = \frac{\pi\cdot\beta\cdot D}{360}L \quad (6)$$

For the non-fluid occupied part of the reactor i.e. for the biogas part, both (4)-(6) expressions are appropriate-the sector arc is represented by the retracted angle ($\gamma = 2\pi - \frac{\pi\cdot\beta}{180}$) - it is written as

$$F_g = 2\cdot F_{seg.2} + F_{old.2},\ F_{old.2} = \gamma\frac{D}{2}\cdot L = \frac{\left(2\pi - \frac{\pi\cdot\beta}{180}\right)\cdot D}{360}L$$

$$F_{seg.2} = \frac{D^2}{8}(\gamma - \sin(\gamma)) = \frac{D^2}{8}\left(2\pi - \frac{\pi\cdot\beta}{180} - \sin\left(2\pi - \frac{\pi\cdot\beta}{180}\right)\right), \quad (7)$$

Putting the expressions (4)-(7) in Equation (2) we obtain

$$Q = k_s\left[\frac{D^2}{4}(\beta - \sin(\beta)) + \beta\frac{D}{2}\cdot L\right]\Delta t + k_g\left[\frac{D^2}{4}(\gamma - \sin(\gamma)) + \gamma\frac{D}{2}\cdot L\right]\Delta t \quad (8)$$

For the liquid biomass in the cylinder and the total volume of the cylinder, we can write:

$$V_s = \frac{D^2}{8}(\beta - \sin(\beta))\cdot L,\quad V = \frac{\pi D^2}{4}\cdot L,\ V_g = \frac{D^2}{8}(\gamma - \sin(\gamma))\cdot L,\quad V = \frac{\pi D^2}{4}\cdot L,\ \ V = V_s + V_g \quad (9)$$

From this

$$\beta - \sin(\beta) = \frac{8V_s}{D^2\cdot L},\quad L = \frac{4V}{\pi D^2}\ ,\quad \beta - \sin(\beta) = \frac{2\pi V_s}{V} \quad (10)$$

$$\gamma - \sin(\gamma) = \frac{8V_g}{D^2\cdot L},\quad L = \frac{4V}{\pi D^2}\ ,\quad \gamma - \sin(\gamma) = \frac{2\pi V_g}{V} \quad (11)$$

Taking into account that by putting the expressions (8) and (9) in the expression (10), D = 2R, we obtain

$$Q = k_s\left[\frac{2\pi V_s}{V}R^2 + \beta\frac{V}{\pi R}\right]\Delta t + k_g\left[\frac{2\pi V_g}{V}R^2 + \gamma\frac{V}{\pi R}\right]\Delta t \quad (12)$$

To find the optimal radius, we examine this function to the extremum-that is, taking the derivative by radius from the amount of heat lost to zero:

$$\frac{dQ}{dR} = \left\{k_s\left[\frac{2\pi V_s}{V}R^2 + \beta\frac{V}{\pi R}\right]\Delta t + k_g\left[\frac{2\pi V_g}{V}R^2 + \gamma\frac{V}{\pi R}\right]\Delta t\right\} = 0 \quad (11)$$

After simplifications, we can write the optimal radius as:

$$R_{opt.} = \sqrt[3]{\frac{(\beta k_s + \gamma k_g)V^2}{(V_s k_s + V_g k_g)4\pi^2}} \quad (12)$$

The proportion of biomass in the reactor volume was represented by the central sector angle-$\beta = 2\pi, \gamma = 0$; 90 % in the full state; $\beta = 1{,}8\pi, \gamma = 0{,}2\pi$; 80 % full state,γ $\beta = 1{,}6\pi,\ \gamma = 0{,}4\pi$; 70 % in the full state, $\beta = 1{,}4\pi,\ \gamma = 0{,}6\pi$ in the full state, and hokazo.

Taking into account the above, we determine the optimal diameter of a 30 m^3 hajm reactor for an insulation coating of different thickness (Figure 4). For thermophilic and mesophilic modes on the basis of this diameter, we calculate the thermal loads depending on the insulation layer by formulas (3), (8) (figure 2,3).

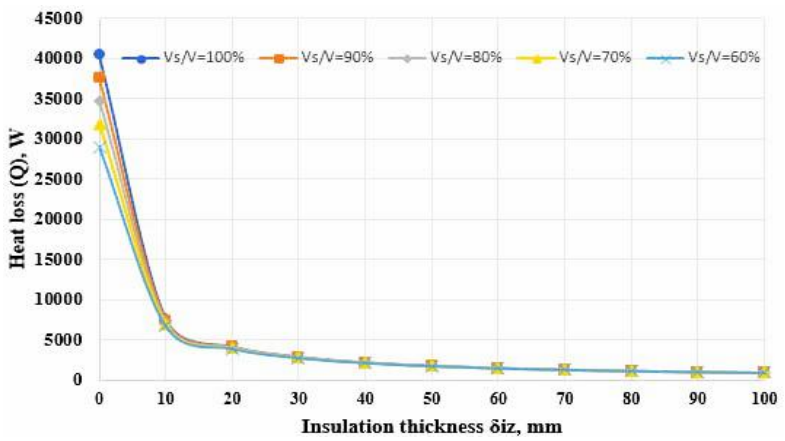

Fig. 2. Dependence of the thermal load on insulation thickness at a reactor volume of 30 m³ (thermophilic mode). The curves demonstrate that increasing the insulation thickness beyond 50 mm does not significantly reduce thermal losses, confirming that this value is the practical optimum.

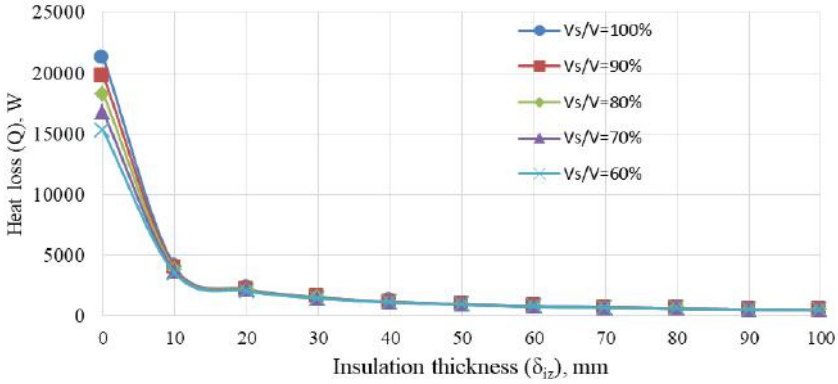

Fig. 3. Thermal load variation with insulation thickness at different biomass filling ratios in a 30 m³ digester (mesophilic mode). The graph highlights the effect of biomass distribution on energy demand and underlines the importance of insulation optimization for energy-efficient operation.

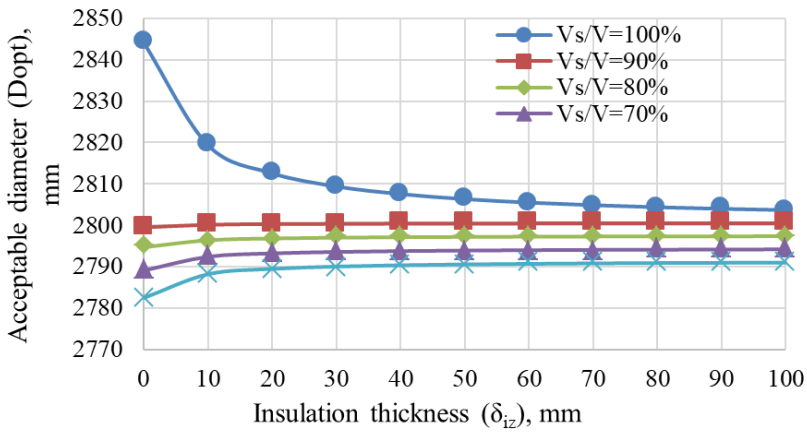

Fig. 4. Relationship between the optimal reactor diameter and insulation thickness for a 30 m³ digester. The analysis shows that an average diameter of 2800 mm ensures minimal heat loss under different biomass load conditions.

4. Conclusion

Based on the findings of this study, optimizing the thermal and geometric parameters is essential for enhancing the efficiency of small-scale biogas plants. The main outcomes include:

– Optimal insulation thickness: 50 mm for the reactor wall, which minimizes heat loss while avoiding unnecessary material costs.

– Reactor dimensions: For a 30 m³ bioreactor, the ideal diameter is 2800 mm and the length 4900 mm, ensuring a balance between heat retention and structural efficiency.

These parameters significantly improve energy efficiency and can be directly applied to the design and optimization of compact biogas plants.

– In addition to the immediate engineering benefits, the results of this research open several promising directions for application:

– Rural and household energy supply: The proposed methodology can be directly implemented in farm-scale or domestic digesters, helping to reduce reliance on traditional fossil fuels.

– Economic feasibility: Optimized designs with reduced thermal losses lower operational costs, increasing the competitiveness of small-scale biogas technology.

– Environmental impact: Improved reactor efficiency contributes to better utilization of organic waste streams, reducing greenhouse gas emissions and promoting sustainable agricultural practices.

– Scalability and adaptation: The analytical approach developed in this work can be adapted to other digester sizes and operational conditions, providing a flexible tool for engineers and policymakers.

Thus, the present study not only provides a practical framework for improving the technical performance of biogas digesters but also highlights the potential of optimized small-scale systems to play a significant role in advancing renewable energy adoption, particularly in rural and resource-constrained environments.

Conflict of interest statement

The authors declare that they have no conflict of interest in relation to this research, whether financial, personal, authorship or otherwise, that could affect the research and its results presented in this paper.

CRediT author statement

Sharipov M.Z. - Conceptualization, Methodology, Supervision; **Ergashev Sh.H., Shodiev E.B. -** Investigation, Formal Analysis, Writing-Reviewing and Editing; **Narzullayeva Z.M., Majitov J.A.** - Writing - original draft, Review and Editing; The final manuscript was read and approved by all authors.

Acknowledgements

The authors are grateful to Professor Sh.J.Imomov for attention to this work and useful advice.

References

1 Yan M., Su H., Hantoko D., Kanchanatip E., Shahul Hamid F.B., Zhang S., Wang G., Xu Z. (2019) Experimental study on the energy conversion of food waste via supercritical water gasification: *Improvement of hydrogen production Intern. Journal of Hydrogen Energy,* 44 (10), 4664-4673. https://doi.org/10.1016/j.ijhydene.2018.12.193

2 Tagne R.F.T., Dong X., Anagho S.G. Kaiser S., Ulgiati S. (2021) Technologies, challenges and perspectives of biogas production within an agricultural context. The case of China and Africa. *Environ Dev Sustain*, 23, 14799–14826. https://doi.org/10.1007/s10668-021-01272-9

3 Conti F., Wiedemannn L., Saidi A., Sonnleitner M., Goldbrunner M. (2018) Mixing of a model substrate in a scale-down laboratory digester and processing with a computational fluid dynamics model. *European Biomass Conference and Exhibition Proceedings, 26th EUBCE,* 811-814. https://doi.org/10.5071/26thEUBCE2018-2CV.5.34

4 Vesvikar M., Varma R., Karim K., Al-Dahhan M. H. (2005) Flow pattern visualization in a mimic anaerobic digester: Experimental and computational studies. *Water Science and Technology,* 52, 537-543. https://doi.org/10.2166/wst.2005.0564

5 Majitov J.A., Kamilov O.S., Yuliyev O.O. Solar biogas plant. Utility model patent No. FAP 2440. 19.03.2024. Available at: https://im.adliya.uz/document/check/e00d4d85-4e28-4988-917b-eb8f60e58fb7

6 Schmidt T., McCabe B.K., Harris P.W., Lee S. (2018) Effect of trace element addition and increasing organic loading rates on the anaerobic digestion of cattle slaughterhouse wastewater: *Bioresource Technology*, 264, 51-57. https://doi.org/10.1016/j.biortech.2018.05.050

7 Rojas C., Fang S., Uhlenhut F., Borchert A., Stein I., Schlaak M. (2010) Stirring and biomass starter influences the anaerobic digestion of different substrates for biogas production. *Eng. Life Sci.* 10, 339-347. https://doi.org/10.1002/elsc.200900107

8 Fosca Conti, Leonhard Wiedemann, Matthias Sonnleitner, Abdessamad Saidi, Markus Goldbrunner (2019) Monitoring the mixing of an artificial model substrate in a scale-down laboratory digester. *Renewable Energy*, 132, 351-362. https://doi.org/10.1016/j.renene.2018.08.013

9 Sharipov M., Hayitov D., Rizoqulov M., Islomov U., Raupova I. (2019) Domain structure and magnetic properties of terbium ferrite-garnet in the vicinity of the magnetic compensation point. *Eurasian Physical Technical Journal,* 16(2), 21-25. https://doi.org/10.31489/2019No2/21-25

10 Pivac G. (2015) Literature review of a LNG carrier machinery system, in Towards Green Marine Technology and Transport, *CRC Press*, 605–612. https://doi.org/10.1201/b18855-79

11 Pan W., Hongtao W., Yinquan Q., Lianhai R., Bin J. (2018) Microbial characteristics in anaerobic digestion process of food waste for methane production–A review. *Bioresource Technology, 248,* 29–36.

12 Majitov J.A. (2025) *Kichik quvvatli biogaz qurilmasining issiqlik-texnik parametrlarini asoslash. dis.PhD,* Qarshi. 51-63. Available at: https://library.ziyonet.uz/ru/book/135481

AUTHORS' INFORMATION

Sharipov, Mirzo - Doctor of Physical and Mathematical Sciences, Professor, Head of Department, Bukhara State University, Bukhara, Uzbekistan; SCOPUS Author ID: 24177719300, https://orcid.org/0000-0003-0370-8066; m.z.sharipov@buxdu.uz; m.z.sharipov@rambler.ru

Majitov, Jurabek – Doctor PhD (Eng), Associate professor, Physics Department Bukhara State Technical University, Bukhara, Uzbekistan; SCOPUS Author ID: 57221226030; https://orcid.org/0009-0005-9453-279X; majitov@mail.ru

Ergashev, Shakhrier – Doctor PhD (Eng), Associate professor, Karshi State Technical University, Karshi, Uzbekistan; SCOPUS Author ID: 57862905100; https://orcid.org/0000-0002-3336-9942; strong.shakhrier@mail.ru

Shodiyev, Erkin – Doctor PhD (Eng), Associate professor, Bukhara State Technical University, Bukhara, Uzbekistan; https://orcid.org/0009-0008-0433-0679; erkin@mail.ru

Narzullayeva, Zilola - PhD student, Bukhara State University, lecturer at Bukhara State Medical Institute. Bukhara, Uzbekistan; https://orcid.org/0009-0003-4706-8889; narzullayevazilola1487@gmail.com

EURASIAN PHYSICAL TECHNICAL JOURNAL

2025, Volume 22, No. 3 (53)

https://doi.org/10.31489/2025N3/91-100

Received: 25/01/2025 Revised: 10/06/2025 Accepted: 25/09/2025 Published online: 30/09/2025

Research Article

Open Access under the CC BY -NC-ND 4.0 license

UDC 62-52:620.22:621.988:620.9

ENHANCING THE DURABILITY OF ROBOTIC ARM USING COMPOSITE MATERIALS AND ADDITIVE MANUFACTURING IN HARSH ENVIRONMENTAL CONDITIONS

Askaruly R.[1*], Faizulla T.[2], Abylkanov M.[1], Syzdykov A.B.[3], Sakhanov K.[3]

[1] Nazarbayev University, Digital prototyping laboratory Fab Lab, Astana, Kazakhstan
[2] Nazarbayev Intellectual School of Physics and Mathematics, Astana, Kazakhstan
[3] L.N. Gumilyov Eurasian National University, Astana, Kazakhstan
*Corresponding author: rustam.askaruly@nu.edu.kz

Abstract. *Despite the harsh environmental conditions, such as strong winds, radiation exposure and frequent forest fires, pose serious challenges for the reliable operation of robotic systems. Despite growing interest in robotics for disaster relief and hazardous operations, the durability of additively manufactured components under such stresses remains insufficiently explored. This study investigates the use of composite materials and additive manufacturing techniques to improve the performance of robotic manipulators in harsh conditions. A modular rover equipped with a robotic arm made entirely of composite elements was developed and tested. The research focused on evaluating the structural reliability of PETG plastic and carbon fiber in terms of thermal exposure, static load, and radiation resistance. The study also presented a gesture-controlled interface for remote control and produced a functional prototype. The results of the study provide new insights into material selection and design strategies for sustainable robotic systems, contributing to the development of sustainable robotics in harsh environmental conditions.*

Keywords: Computer-Aided Design, Printed Circuit Board, Computer-Aided Manufacturing, Computer-Aided Engineering, Telecommunications Relay Service, Fused Deposition Modeling.

1. Introduction

Robotic systems are increasingly being used in hazardous and extreme conditions, including disaster zones, forest fire areas and regions with elevated radiation levels. Applications range from nuclear waste cleanup to firefighting support and contaminated site investigation. However, one of the main challenges is ensuring the durability of robotic components manufactured using additive manufacturing technologies. Polymers commonly used in 3D printing, such as PLA or ABS, have limitations when exposed to high temperatures or ionizing radiation [1-3]. Consequently, the search for suitable materials and design solutions for robust robotic manipulators remains an open question for research.

Kazakhstan is a unique testing ground for such technologies. The eastern regions of the country, which were severely affected by more than 460 nuclear tests during the Soviet era, are still exposed to high levels of radiation. In addition, large-scale forest fires in 2023, more than 116,000 hectares of forest were destroyed, highlight the urgent need for robotic systems capable of operating in extreme natural conditions. These challenges make the development of robust, affordable and adaptable robotic solutions particularly relevant at both the regional and global levels.

This study investigates the possibility of integrating composite materials and additive manufacturing to increase the strength of robotic manipulators designed to operate in conditions of radiation exposure and high temperatures. PETG was chosen as the polymer due to its superior resistance to gamma radiation compared to PLA, ABS and carbon composites were chosen for their high thermal stability and mechanical strength [4-6].

The novelty of this work lies in the combination of mechanical and thermal modeling with prototype development, which bridges the gap between material characteristics and functional robot design. Specific objectives:

- To evaluate the resistance of selected materials printed on a 3D printer of static and thermal loads;
- To design and assemble a modular robotic manipulator integrated with a gesture control interface;
- To manufacture and test a functional prototype suitable for use in hazardous environments

By addressing these challenges, this research contributes to the growing body of knowledge on sustainable robotic systems and provides practical insights for the use of composite based robotic manipulators in extreme operating conditions.

2. Methods

2.1 CAD and Simulation Framework

Autodesk Fusion was used as the primary platform for design and simulation to evaluate the strength of potential materials under mechanical and thermal loads. This software combined CAD, CAM and CAE tools, enabling iterative development from geometry design to mechanical validation.

The analysis focused on the servo motor mount, gripper and structural joints of the robotic arm, as these areas are subject to the highest static and thermal loads during operation. CAD models were created with parametric constraints, allowing for rapid changes to geometry and material properties during optimization.

Static Structural Analysis. Static structural analysis was performed to evaluate the ability of key components of the robotic arm, specifically the servo motor mount and gripper claws, to withstand operational loads under stationary conditions. In Fusion 360, the material properties (modulus of elasticity, yield strength and safety factor) were determined for PLA, ABS, ASA and PETG, which are among the most common polymers used in fused deposition modeling (FDM). As shown in Figure 1, boundary conditions were assigned to the locations of bolts and screws of the main platform of robotic arm, and forces up to 1000N were applied to simulate gripping and torque transmission loads. Fusion 360 generated a finite element mesh and calculated stress and displacement fields to identify the area's most susceptible to failure.

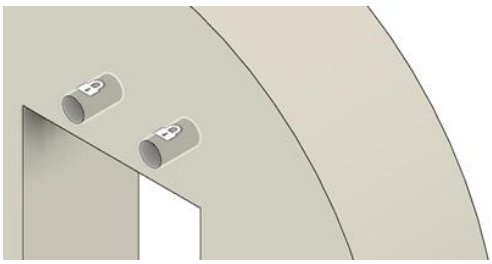

Fig.1. Boundary conditions

As can be seen in Figure 2, PLA plastic (a) demonstrated the highest safety factor under static loading of 1000 Newtons (the minimum result is about 0.5) than PET plastic (b), which has a result of about 0.44. Although PLA appeared to be more robust under static conditions, this did not account for thermal or radiation effects, which are critical for the intended application of the robotic arm. Therefore, additional analyses were required.

Thermal Stress Analysis. Thermal simulations were performed taking into account the effects of elevated ambient temperatures, which can exceed 200°C in forest fire conditions. The main focus was again on the servomotor mountings and structural connections, as these components are subjected to both thermal and mechanical stresses during operation.

Material parameters such as thermal conductivity, thermal expansion coefficient and heat capacity were included in the model. Boundary conditions simulated heat transfer from the motor housing and convection from the surrounding air.

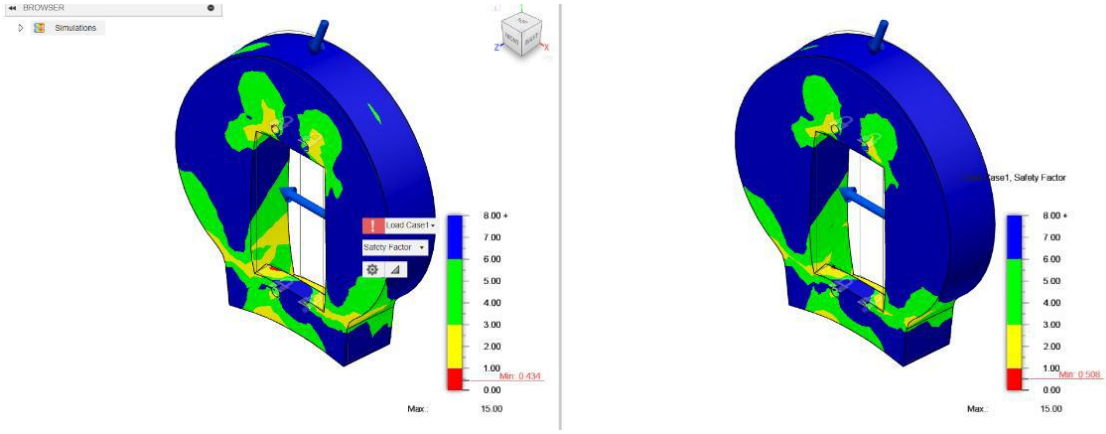

a) PLA b) PET

Fig.2. Difference of PLA and PET plastics

Combining Static and Thermal Analysis. In many cases, robotic components experience both mechanical and thermal loads simultaneously. Coupled thermal and structural analysis to evaluate the combined effects of these loads were performed. This analysis provides a more realistic assessment of component performance and helps identify potential failure modes. As shown in Figure 3, after a load of 100 newtons on the servo torque sides, and an ambient temperature of 200°C, ASA plastic (c) achieved the best result with a minimum safety factor of 0.183 with minimal critical zones, while PETG plastic (d) reached a comparable level 0.175 at significantly lower material cost. PLA shower only moderate resistance 0.15, with a larger vulnerable region, and ABS performed worst 0.099, failing in most of the tested areas.

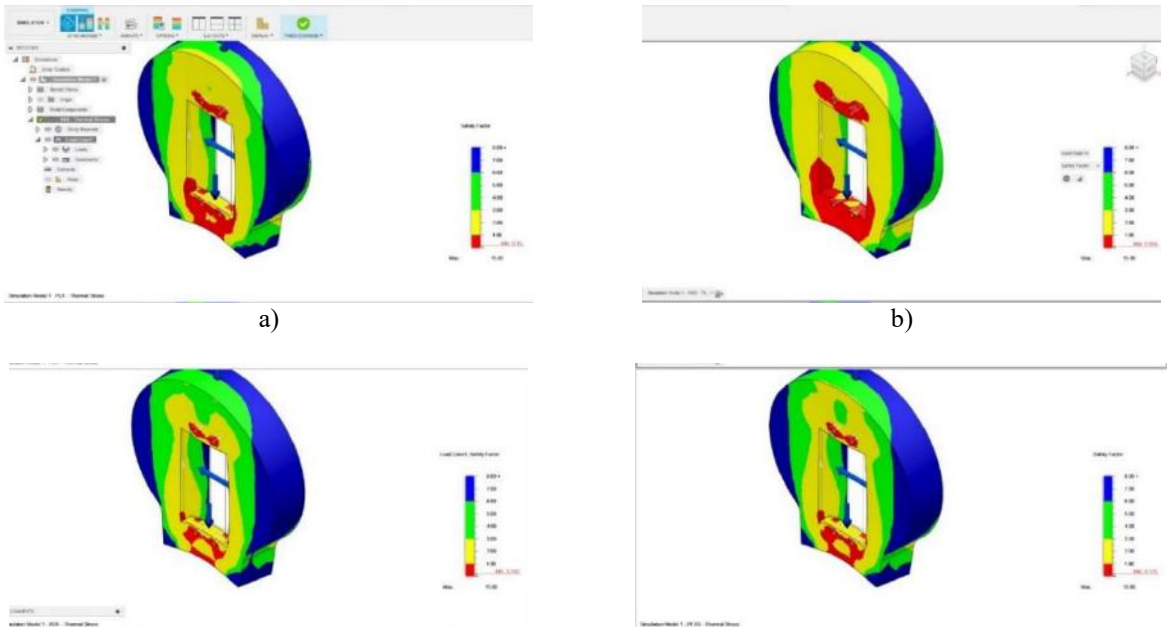

a) b)

c) d)

Fig.3. a) PLA, b) ABS, c) ASA and d) PETG under thermal stress conditions

These results confirmed that PETG represents a practical compromise, although not the strongest material in static testing, it provides sufficient load-bearing capacity and acceptable thermal resistance, while also being cost-effective and well suited for additive manufacturing.

3. Iteration and Optimization

The simulation results served as the basis for iterative improvements to the robotic arm design. Based on an analysis of static and thermal loads, the CAD geometry was adjusted to reinforce vulnerable areas such as servo mounts and grippers. Wall thickness, rib placement, and fill density were modified to maintain a safety factor above 0.15 under combined mechanical and thermal loads while minimizing material consumption and overall weight. Fusion 360 generative design tools were used to explore alternative configurations, providing geometry suggestions that balanced stiffness and mass efficiency. Several iterations demonstrated that even minor changes in rib geometry and layer orientation could reduce peak stress concentrations by more than 10% while remaining printable within standard fused deposition modeling parameters.

Thus, the iterative process not only improved the reliability of individual components, but also confirmed the choice of PETG as the primary polymer for the prototype. Although PLA demonstrated excellent static strength, its reduced heat resistance and brittleness under cyclic temperature changes limited its practical applicability. PETG, reinforced with optimized geometric shapes, provided the best compromise between strength, manufacturability and cost-effectiveness.

4. Academic Context

The suitability of components printed on a 3D printer for use in harsh conditions is determined both by internal properties of the materials used and by the external factors to which they are exposed. Previous studies show that polymers commonly used in FDM technology exhibit significant differences in their response to extreme conditions. For example, ABS is often preferred over PLA because of its comparatively higher resistance to radiation. However, PETG has been shown to outperform both ABS and PLA, retaining greater mechanical strength and plasticity after exposure to high-intensity gamma radiation [7-8]. These results indicate that PETG is a promising candidate for use in robotics in radiation-exposed environments.

In addition to radiation resistance, thermal stability is a critical factor for robotic systems designed to operate at elevated temperatures, such as those encountered in forest fires. Carbon composite materials have been extensively studied for their mechanical and thermal properties. Their high strength-to-weight ratio makes them attractive for use in lightweight structures, and their fire resistance is due to the formation of a protective carbon layer that reduces the heat release rate to a constant value of approximately 60 kW/m2 [9-10]. As a result, carbon fiber-reinforced composited can withstand temperatures exceeding 2000°C, ensuring structural integrity even under extreme thermal conditions [11].

Along with material characteristics, the choice of control strategy plays a decisive role in the effectiveness of robotic systems operating in complex environments. Traditional joystick interfaces are still widely used due to their reliability and simplicity, but they often lack flexibility and intuitiveness. Therefore, gesture-based control methods are attracting increasing interest. Such systems use cameras or sensor gloves to capture hand movements and translate them into corresponding robot actions [12]. A particularly promising approach is the use of strain-resistant sensors (TSR), which function by detecting changes in electrical resistance when bent [13]. These sensors provide continuous feedback corresponding to finger movements and are therefore well suited for intuitive human-robot interaction. For example, as shown in Figure 4 and Table 1, the resistance of a flexible sensor increases from approximately 30k Ohms in the straight position to approximately 70-80 Ohms when bent at 120° [14].

Overall, the analyzed studies show that PETG has superior radiation resistance, carbon composites provide exceptional thermal stability, and gesture-based TRS interfaces improve operator interaction with robotic systems. These considerations form the scientific basis for the present study, in which elastic materials and advanced control strategies are integrated into the design of a robotic manipulator intended for operation in extreme conditions.

5. Assemble

3D parts. The assembly of the manipulator began with the design of the end effector, which is a critical component for interacting with the environment. Various gripper concepts were evaluated, including angular jaw grippers, finger-based grippers, and parallel jaw grippers. Although angular and finger grippers have advantages when working with non-standard or fragile objects, their complexity and reduced gripping force did not meet the project's goal of developing on affordable and reliable prototype.

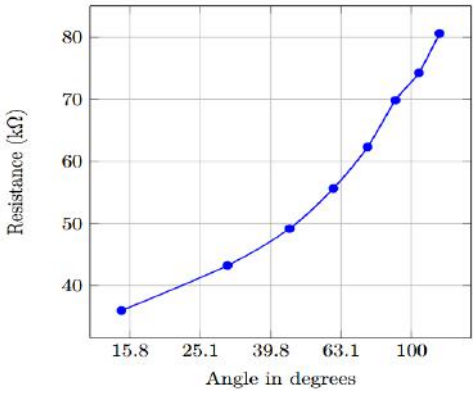

Fig.4. Dependence of the volt-ampere characteristics of a resistor on the degree of its bending.

Table 1: Angle versus Resistance

Angle [degrees]	Resistance [kΩ]
0	31.23
15	35.98
30	43.24
45	49.16
60	55.64
75	62.31
90	69.85
105	74.28
120	80.62

For this reason, a parallel gripper with toothed jaws was selected as the most suitable configuration, combining simplicity, versatility and reliability. The jaws were designed with a double gear transmission connected to a servomotor, which ensured synchronized movement in opposite directions. This design ensured constant gripping force and improved contact with objects, as shown in figure 5. The manipulator design was based on a three-coordinate system to provide sufficient freedom for practical tasks while maintaining the compactness of the overall design. Servo motors were used as drives because of their low cost, ease of control and compatibility with the proposed gesture-based interface. The base of the manipulator was designed as a large bearing with an internal cavity for electronic components, driven by a stepper motor to provide rotation. The design philosophy emphasized the balance between functionality and manufacturability, enabling the manipulator to be manufactured using additive technologies and assembled from readily available components.

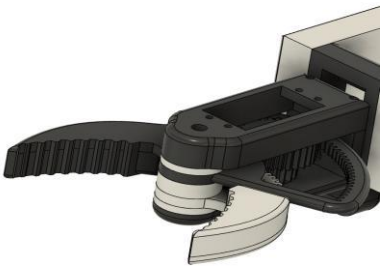

Fig.5. Crab type robotic arm

6. Electronics

The electronic subsystem was developed to ensure smooth interaction between the gesture-controlled glove and the robotic manipulator. As shown in Figure 6 (a), the glove is equipped with several sensors and microcontrollers that record the user's actions and transmit control commands via wireless communication.

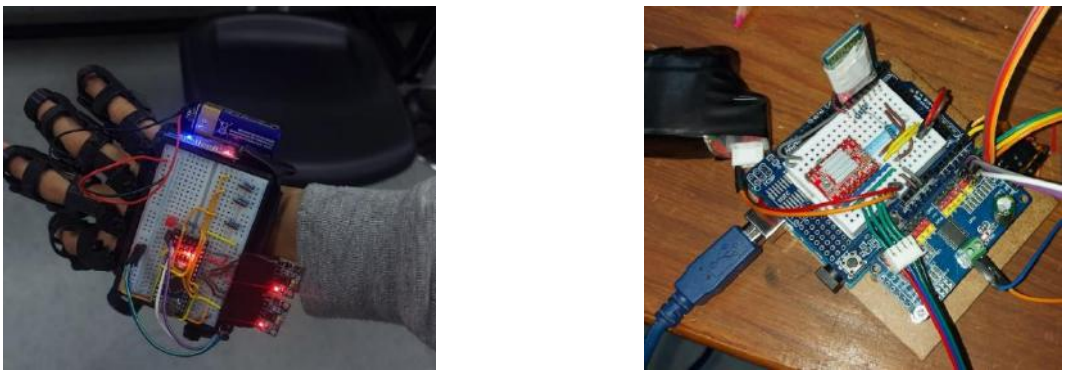

a) b)

Fig.6. a) Prototype of robotic glove and b) mainboard made on a breadboard

The glove's central processors are an Arduino Nano Rev3, which collects and processes raw data from the sensors and then transmits control signals via an HC-05 Bluetooth module. This wireless connection provides a reliable link between the glove and the manipulator, ensuring real-time responsiveness. Two MPU6050 inertial measurement units (IMUs) were built into the glove to collect acceleration and angular velocity data, allowing for accurate tracking of hand orientation. In parallel, three flexible sensors were installed along the fingers to measure bending angles, providing information about grip strength and finger position. Together, these sensors enabled intuitive control of the manipulator's joints and gripper using gestures. Initially, a breadboard was used for prototyping and rapid component integration, as shown in Figure 6 (b).

The sequence of operations included collecting signals from the sensors, analog-to-digital conversion using Arduino, filtering and processing the data, and then transmitting it to the manipulator control board, schematic view of the robotic glove is presented in Fig.7.

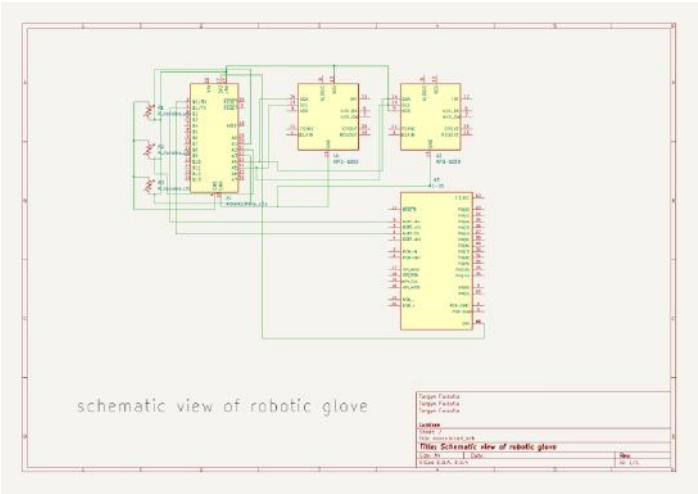

Fig.7. Schematic view of robotic glove

This represents a prototype of the electronics designed to control the manipulator. The board integrates key components that facilitate interaction between the controlling device (the glove mentioned earlier) and the mechanical parts of the manipulator, as shown in Figure 8.

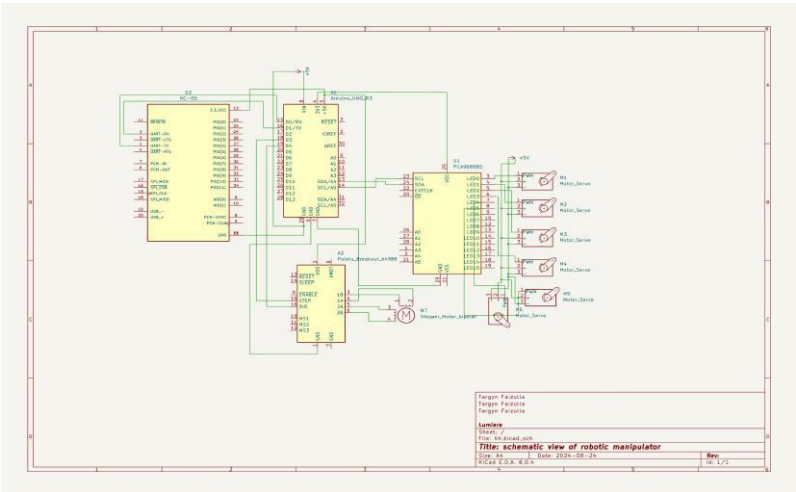

Fig.8. Schematic view of robotic manipulator

Key components and their functions include the Arduino Uno, which acts as the "brain" of the system, processing data from other components and sending commands to the manipulator's actuators:

– the Bluetooth module, which provides wireless communication between the controlling device (glove) and the manipulator, allowing commands from the glove to be transmitted to the Arduino Uno;

– the A4988 driver, designed to control stepper motors, likely used for controlling the manipulator's servos to ensure precise positioning;

– the PCA9685, a 16-channel 12-bit servo/PWM driver, used to control servos, providing smooth movement of the manipulator's joints; six servos, which are the actuators of the manipulator, driven by the PCA9685 driver to move the joints and grasp objects; and the breadboard, which is used for temporarily connecting components and facilitating the assembly and testing of the prototype.

The operation principle involves receiving commands through the Bluetooth module, which sends commands from the controlling device (glove) to the Arduino Uno. The Arduino Uno processes these commands to determine the necessary actions for the manipulator. It then sends signals to the PCA9685 driver, which controls the servos. The servos move the manipulator's joints, performing the required actions. The system is designed to control a manipulator with multiple degrees of freedom, allowing commands from the glove to control the position of each joint and the gripping force, enabling the manipulator to perform various tasks such as grasping and moving objects.

The integration of these components enabled the manipulator to respond to user gestures with several degrees of the freedom, converting natural hand movements into robot actions. This architecture not only demonstrated the possibility of gesture control in inexpensive robotic systems, but also laid the foundation for further adaptation of the system to harsh operating conditions, which is in line with the overall research goal of developing fault-tolerant robotic technologies.

7. Testing

The testing phase focused on verifying the power requirements and operational stability of the manipulator under various load conditions. Since the manipulator uses multiple servo motors for drive, ensuring sufficient power supply was identified as a critical step in system integration. Insufficient current supply can lead to voltage drops, uneven torque distribution or servo malfunction, which can affect the reliability of the robotic arm in practical applications.

Initial experiments involved powering the system form nickel batteries with a total output of 5V. Current consumption was measured for different numbers of active servomotors, as shown in Figure 9 (a) and summarized in Table 2. The results showed that as the number of connected servos increased, the batteries could not provide sufficient current, resulting in significant voltage drops. These drops were particularly noticeable in the first servo drives in the chain, which consumed disproportionately high currents. To overcome this limitation, the system was reconfigured using a regulated power supply and, alternatively, lithium-ion batteries with higher output power. Under these conditions, the current supply was significantly improved, and no voltage drops were observed on the servo drives. The stabilized results are shown in Figure 9 (b) and Table 3, which demonstrate a stable current distribution.

Table 2: Current Measurements for Different Numbers of Servo Drives without power supply.

Number of Servo Drives	Average Current [mA]	Maximum Current [mA]	Minimum Current [mA]
1	78.53	122.77	58.34
2	156.12	238.56	117.63
3	234.87	357.43	176.54
4	312.45	475.89	233.78
5	413.76	593.12	307.25
6	405.34	599.29	306.45

Table 3. Current Measurements for Different Numbers of Servo Drives with power supply.

Number of Servo Drives	Average Current [mA]	Maximum Current [mA]	Minimum Current [mA]
1	82.23	127.45	63.97
2	160.87	245.31	120.15
3	238.54	363.78	183.66
4	315.46	482.89	237.43
5	392.57	597.22	295.88
6	470.68	715.33	355.49

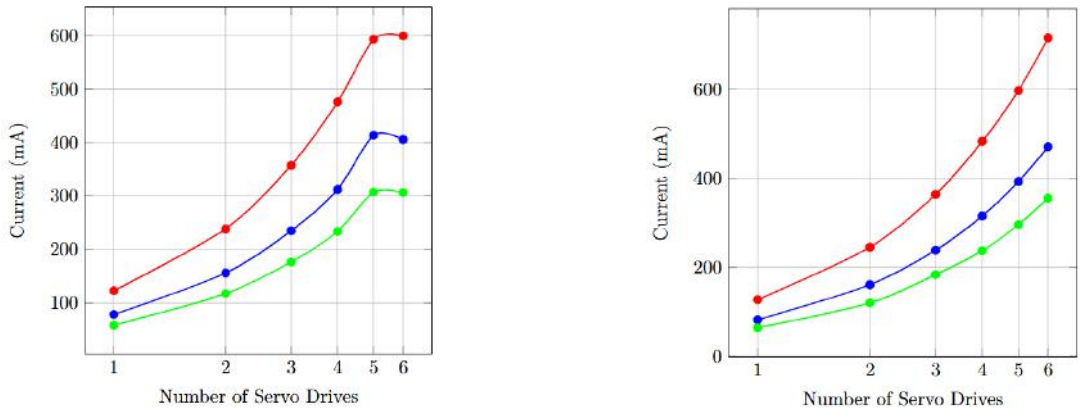

a) b)

Fig.9. a) Current vs Number of Servo Drives without power supply and b) Current vs Number of Servo Drives with power supply, where —●— is Average Current, —●— Maximum Current, —●— Minimum Current.

After ensuring a stable power supply, the manipulator successfully processed input signals from the gesture-controlled glove and converted them into coordinated servo movements. The prototype robotic arm in working condition is shown in Figure 10. These results confirmed the feasibility of the proposed electronic and mechanical integration and reinforced the importance of reliable power management for ensuring reliable operation.

Fig.10. Robotic arm

This testing phase laid the foundation for future developments in which the manipulator will be integrated with a mobile rover platform designed to operate in extreme conditions. This improvement will expand the capabilities of the system, allowing it to be used in hazardous situations such as search and rescue operations or disaster relief.

8. Conclusion

This study examined the problem of developing robotic manipulators capable of operating in extreme environmental conditions, such as those found in Kazakhstan, where high radiation exposure and frequent fires create significant obstacles for traditional robotic systems. The aim of the study was to evaluate the characteristics of materials under radiation, thermal and static loads, as well as to use the data obtained in the design and manufacture of a functional manipulator prototype.

The results of modeling and analysis of materials revealed the advantages of both PETG plastic and carbon composite materials. PETG demonstrated good plasticity and strength retention under simulated radiation exposure, making it a promising material for the manufacture of radiation-resistant components. Similarly, carbon composites demonstrated high thermal stability, forming a protective char layer when exposed to elevated temperatures, confirming their suitability for use in fire-hazardous environments. Simulation of static and thermal loads confirmed the mechanical acceptability of these materials, assembly and testing of the prototype confirmed the possibility of integrating gesture control electronics and mechanical design.

Although experimental testing of radiation and fire resistance was not conducted as part of the current project, the combination of simulation and prototyping results has created a solid foundation for future experimental research. The results obtained underscore the need to continue this work through controlled tests for exposure to radiation and high temperatures, as well as long-term assessment of strength under operating conditions.

In terms of practical results, the successful manufacture and testing of a gesture-controlled robotic arm demonstrated the potential for integrating composite materials, additive manufacturing, and intuitive control systems. This serves as proof of concept for the broader goal of developing mobile robotic platforms capable of performing tasks in hazardous environments, such as disaster relief and contaminated site investigation.

The present work is limited to simulation and protype-level validation. Direct experimental validation under radiation and fire exposure is essential and will form the next stage of this research.

In conclusion, this study contributes to the field of sustainable robotics by demonstrating how material selection, CAD simulation and low-cost electronic integration can collectively contribute to improving the design of robotic manipulators for harsh operating conditions. Despite limitations in experimentally verifying environmental resistance, the results provide practical insights and open avenues for further research. Future work should focus on experimental testing of materials under radiation and fire conditions, optimization of control systems, and development of a rover platform to extend the applicability of the manipulator in real-world extreme scenarios.

Conflict of interest statement

The authors declare that they have no conflict of interest in relation to this research, whether financial, personal, authorship or otherwise, that could affect the research and its results presented in this paper.

CRediT author statement

Askaruly R.: Conceptualization, Methodology, Validation, Investigation, Writing - Review & Editing; **Faizulla.T.:** Methodology, Resources, Investigation, Software, Writing – Original Draft; **Abylkanov M.:** Data Curation, Software; **Syzdykov A.B.:** Writing Review & Editing, Supervision, Funding acquisition; **Sakhanov K.:** Writing Review & Editing, Funding acquisition.The final manuscript was read and approved by all authors.

References

1 Torrado A.R., Roberson D.A. (2016) Failure analysis and mechanical characterization of 3D printed ABS and PLA filaments as a function of raster orientation. *Additive Manufacturing*, 6, 16 – 29. https://doi.org/10.1016/j.addma.2015.12.007

2 Spoerk M., Gonzalez-Gutierrez J., Sapkota J., Schuschnigg S., Holzer C. (2017) Effect of the printing bed temperature on the adhesion of parts produced by fused filament fabrication. *Journal of Applied Polymer Science*, 134(42), 1–9. https://doi.org/10.1002/app.45303

3 Han Y., Sun J., Liu Y., Liu J., Li H. (2012) Radiation effects on the thermal and mechanical properties of thermoplastic polymers. *Radiation Physics and Chemistry*, 81(12), 1923–1927. https://doi.org/10.1016/j.radphyschem.2012.08.004

4 Czarnecka-Komorowska D., Giełżecki J., Białas S. (2020) Properties and applications of PETG in additive manufacturing. *Polymers*, 12(12), 1–15. https://doi.org/10.3390/polym12122937

5 Lin K.C., Chen S.C., Wu C.S., Lin J.J. (2015) Gamma radiation resistance and mechanical properties of PETG and PLA-based polymers. *Journal of Applied Polymer Science*, 132(36), 1–8. https://doi.org/10.1002/app.42436

6 Li H., Zhang X., Wang B., Wang Y. (2019) High-temperature mechanical performance of carbon fiber reinforced composites. *Composites Science and Technology*, 182, 107 – 115. https://doi.org/10.1016/j.compscitech.2019.107703

7 Jakubczyk K., Szewczyk A., Plichta W., Gajewska H., Ławniczak M. (2019) Additive manufacturing for

extreme environments: Radiation resistance of polymers and composites. *Additive Manufacturing*, 60, 377 – 381. https://doi.org/10.1007/s00411-021-00892-z

8 Alfuraih A., Kadri O., Fakhouri F. (2023) The effect of high-intensity gamma radiation on PETG and ASA polymer-based fused deposition modelled 3D printed parts. *Journal of Materials Science*, 207, 111256. https://doi.org/10.1016/j.msea.2024.114256

9 Špitalská G., Hnatková P., Matějková J., Jirka I., Vovk M., Plichta R., Růžička J., Kočí D., Mičová E., Sedláček P. (2023) Quantitative structural investigation of thermal stability of carbon materials in air. *Carbon*, 206, 211 – 225. https://doi.org/10.1016/j.carbon.2023.01.119

10 Li W., Guo S., Giannopoulos I.K., He S., Liu Y. (2010) Strength and stiffness of composite laminates. *Composites Part B: Engineering*, 236, 111916. https://doi.org/10.1016/j.compositesb.2019.107703

11 Dodds N., Gibson A.G., Dewhurst D., Davies J.M. (2002) Fire resistance of a carbon fiber reinforced epoxy composite. *Composites Part A: Applied Science and Manufacturing*, 31(7), 689–702. https://doi.org/10.1016/S1359-835X(00)00154-2

12 Mohamed N., Mustafa M.B. (2021) Gesture recognition: A review of the hand gesture recognition system-current progress and future directions. *IEEE Access*, 9, 157422–157436. https://doi.org/10.1109/ACCESS.2021.3132223

13 SparkFun Electronics (2021) Flex Sensor Tutorial. Available at: https://learn.sparkfun.com/tutorials/flex-sensor-hookup-guide/all (accessed: 5 September 2025).

14 Hu W., Li Y., Liu S. (2023) Current designs of robotic arm grippers: A comprehensive systematic review. *Robotics*, 12(1), 5–37. https://doi.org/10.3390/robotics12010005

AUTHORS' INFORMATION

Askaruly, Rustam – Master, Engineer, Department of Research and Innovation System, Nazarbayev University, Astana, Kazakhstan; Scopus Author ID: 58250096600; https://orcid.org/0000-0002-9202-6528; rustam.askaruly@nu.edu.kz

Faizulla, Targyn Zh. – High School student, Nazarbayev Intellectual School of Physics and Mathematics, Astana, Kazakhstan; https://orcid.org/0009-0002-7518-0926

Abylkanov, Marat A. – Master, Engineer, Department of Research and Innovation System, Nazarbayev University, Astana, Kazakhstan; https://orcid.org/0009-0009-7890-9082, abylkanovm@gmail.com

Syzdykov, Arman B. – PhD, Senior Lecture, Department of Radio Engineering. Electronics and Telecommunications, L.N. Gumilyov Eurasian National University, Astana, Kazakhstan; Scopus Author ID: 57205435715; https://orcid.org/0009-0003-4111-5277, arman1978@bk.ru

Sakhanov, Kanat Zh. – Candidate of Technical Science, Head of the Department, Department of Space Engineering and Technics, Institute of Physics and Engineering Sciences, L.N. Gumilyov Eurasian National University, Astana, Kazakhstan; Scopus Author ID: 57217529929; https://orcid.org/0009-0000-8851-0889; sakhanov.kanat@enu.edu.kz

EURASIAN PHYSICAL TECHNICAL JOURNAL

2025, Volume 22, No. 3 (531)

https://doi.org/10.31489/2025N3/101-110

Received: 23/05/2025 Revised: 27/08/2025 Accepted: 25/09/2025 Published online: 30/09/2025

Research Article

Open Access under the CC BY -NC-ND 4.0 license

UDC 082.5; 629.7.05; 629.783

UNIVERSAL MODULAR ONBOARD CONTROL COMPLEX OBCARM G2 NANO FOR NANO-CLASS SPACECRAFT

Sarsenbayev Y., Ostretsov K., Baktybekov K.*, Mussina A., Yskak A.

Ghalam LLP, Astana, Kazakhstan
*Corresponding author: k.baktybekov@ghalam.kz

Abstract. *Universal modular onboard control system OBCARM G2 NANO has been developed for 3U-12U nano-class spacecraft designed for communications, Earth remote sensing, or the Internet of Things. OBCARM G2 NANO consists of interface and processor modules on separate printed circuit boards. The Zynq Ultra scale+ SoC-based processor mod-ule provides ARM TMS470-based module telemetry control support and necessary peripherals, including 500 MB DDR4 RAM for the CPU, 125 MB RAM for the programmable logic gate array field-programmable gate array 125 MB QSPI Flash for flight software storing, and 128 GB eMMC Flash as ROM. Interface module contains onboard control system modules power lines, interfaces of the control system and payload data transmitter and receiver, as well as drivers that provide con-version and buffering of payload data. The OBCARM G2 NANO uses QNX RTOS for flight software, and a high-performance AXI bus for interaction between the processor system and field-programmable gate array. CAN bus is used to ensure spacecraft subsystems operation in a single network. The dimensions of the OBCARM G2 NANO mechanical equipment, including a set of temperature monitoring sensors and a thermal bridge for removing excess heat from hot spots, are 95 mm x 95 mm x 35 mm.*

Keywords: on-board control complex, field-programmable gate array, processor, interface module, CubeSat.

1. Introduction

Today, the capabilities of small satellites and miniaturized payloads have increased significantly, along with the emergence of new business models based on large-scale low-orbit constellations composed of inexpensive, mass-produced spacecraft (SC). Small satellites typically require lower development and launch costs, making them more accessible to a wide range of organizations and countries. This accessibility has attracted the interest of both commercial companies and academic institutions, allowing them to contribute to space research.

These favorable factors allow all countries to actively participate in SC development and operation. Potential of CubeSats is widely used to accelerate scientific and technological progress in emerging market economies and developing countries. Analytical studies and forecasts indicate that at least 2,000 nano-class SC will be launched into space between 2023 and 2027 [1,2]. OBC, electrical power system (EPS), attitude and orbit control system (AOCS) and communication system are satellite platform fundamental components. At the same time, the choice of onboard control system (OBC) is critical, as it governs the operation of all systems of the SC and payload. When developing OBCARM G2 NANO, the objective was to create a high-performance, compact, versatile OBC capable of meeting the requirements of both low Earth orbit (LEO) communication satellites and CubeSat format remote sensing satellites. The design was based on a previous

version of the NANO model [3,4]. The OBCARM model was modernized taking into account the following requirements:

– development object miniaturization in accordance with the requirements and trends in the spacecraft and electronic systems design principles development [4];

– form factor and mechanical components unification, in accordance with the established standards of the global space community [5];

– increased performance by using field programmable gate arrays (FPGA) in addition to the central processing unit (CPU), either as a standalone unit or as part of a system-on-chip [6-9];

– modeling of operational processes at all stages of development to identify errors before board production, in accordance with industry-specific guidelines [10].

2. OBCARM G2 NANO Architecture

OBCARM G2 NANO consists of two modules - interface and processor, presented on separate printed circuit boards. Processor module (PM) contains the central processor responsible for executing onboard software (FSW), a service node that performs the functions of monitoring and controlling the module, RAM and ROM memory chips, as well as an FPGA for task-specific functionality. Processor module has a connector for interfacing with a radio module used for transmitting payload information and SC telemetry. Interface module includes power distribution across OBCARM G2 NANO modules, as well as a set of interfaces of various standards for communication with the satellite components.

OBCARM G2 NANO modular structure was chosen to achieve a unified and flexible OBC. Commercial OBCs are usually presented as a single solid module containing both external interfaces and processing units, with the possibility of purchasing additional mechanical equipment or a carrier board. However, such designs offer limited flexibility, and any modification or turnkey production significantly increase financial and project costs. Selected processor module based on a 16-layer printed circuit board [3] underwent minimal changes. Main changes were made to the software and FPGA configurations. Processor module is connected to the interface board via two 150-pin connectors and allows duplicating the control of AOCS.

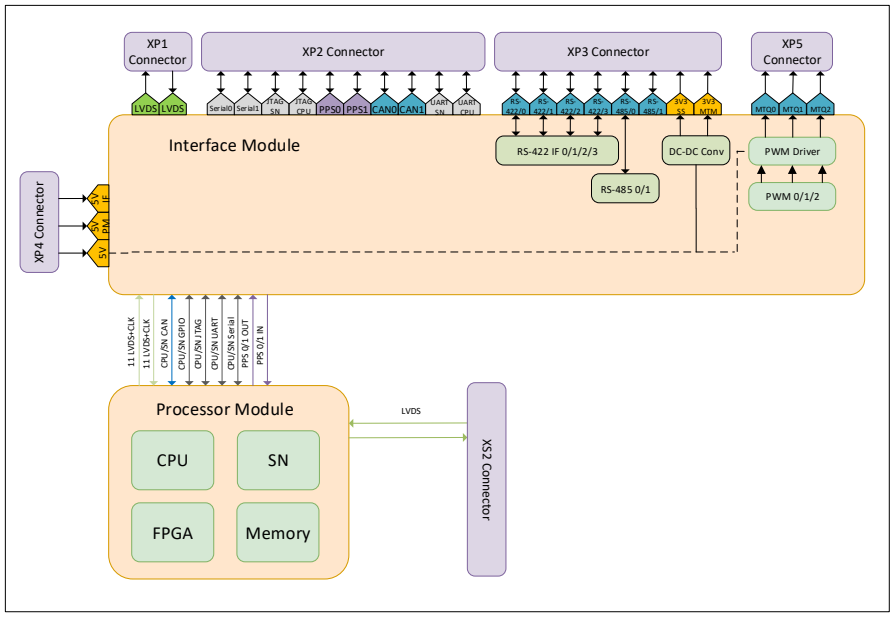

Fig.1. OBC general block-diagram

Interface module is designed on a 6-layer printed circuit board. In case of changes in project requirements or integration into other platforms, OBCARM G2 NANO can be redesigned through the interface module, ensuringits versatility. Unlike most similar solutions on the market, OBCARM G2 NANO offers significantly higher computing power. General, block diagram of the OBCARM G2 NANO is shown in Figure 1. The processor module is based on the Zynq UltraScale+ EG series chip. Computing segment of the ZU9EG chipset combines 4 ARM Cortex™-A53 processors with a frequency up to 1.3 GHz to support

L2 cache, as well as 2 Cortex-R5 processors with a frequency up to 533 MHz. XCZU9EG-2FFVB1156I microcircuit supports 32-bit or 64-bit DDR4, LPDDR4, DDR3, DDR3L memory, with high-speed interfaces such as PCIE Gen2, USB3.0, SATA 3.1, DisplayPort. as well as USB2.0, Gigabit Ethernet, SD / SDIO, I2C, CAN, UART, GPIO. The authors of the work [11,12] showed that Zynq UltraScale+ of the EG series are reliable in operation and implementation of fault mitigation systems. Radiation tolerance test of processors built on crystals of this series showed good results [13,14]. FPGA segment contains an array of programmable logic blocks, digital signal processing (DSP) and internal RAM. FPGA configurability allows flexible configuration of required intellectual property (IP) blocks within the system on a chip without affecting the hardware of processor module. For service node functions implementation microcontroller TMS 470 is used, which is resistant to external factors [15] and performs the following functions:

– Operating current, voltage and temperature of hot spots of the OBCARM G2 NANO monitoring. To ensure these tasks, 12 channels of the microcontroller with ADC for data collection are used;

– OBC components and CPU power supply power-on switching sequence control, ensuring correct initialization and eliminating a number of possible failures;

– CPU power activation, redundant hardware delay and voltage converter enable circuit, which is triggered if TMS is not enabled during platform initialization;

– CPU watchdog timer generates a pulse every minute and, in the event of a malfunction, the service controller will take action according to the embedded algorithms and fault Detection, isolation, and recovery (FDIR) actions;

– restoring the operation of OBCARM G2 NANO and its reconfiguration in case of emergency situations;

– CPU software image loading control;

– providing emergency telemetry.

Processor module uses 4 DDR4 Micron DDR4 MT40A512M16GE memory chips connected to the processor segment (PS), which are combined into a common 64-bit data bus with a capacity of 4 GB. One DDR4 MT40A256M16LY chip with a capacity of 512 MB is connected to the FPGA lines. DDR4 SDRAM on the PS and programmable logic (PL) side maximum operating speed is 1200 MHz (data transfer rate 2400 Mbit/s).

For non-volatile memory, a 128 GB eMMC Flash is used (two 64 GB chips connected in parallel), along with two 64 MB QSPI Flash chips for storing the boot image. The main interfaces of the processor module are 4 ERM8-075-08.0-S-DV-K-TR board-to-board connectors, two of which are located on the front side, two on the back. The front side is used for connection to the interface module, and the back side is intended for connection to the radio module with the corresponding pins. Interface module converts and buffers signal and power interfaces of processor module. Interface module uses 4 five-pin connectors for connection to external systems. List of interfaces is given in Table 1.

Table 1. OBC interfaces configuration.

#	Interface	Signal type	Protocol	Quantity	Max data rate per 1 interface
1	CAN	LVDS(3V3)	NSP	4	500 kbits
2	RS-422	Diff.pair(3V3)	UART	4	10 Mbits
3	RS-485	Diff.pair(3V3)	UART	2	10 Mbits
4	LVDS I/O	LVDS(3V3)	Serial+Clock	32	100 Mbits
5	SERIAL	LVDS(3V3)	Own development	4	1 Mbits
6	PPS	LVDS(3V3)	-	4	1 Hz
7	GTH	LVDS(1V2)	Serial+Clock	4	6.25 Gbits
8	UART	LVCMOS(3V3)	Own development	4	115.2 kbits
9	SPI	LVCMOS(3V3)	SPI	2	25 Mbits
10	I2C	LVCMOS(3V3)	I2C	2	100 kbits
11	JTAG	LVCMOS(3V3)	JTAG	2	115.2 kbits
12	PWM output	0 - +5v -5v – 0v	-	3	-
13	Analog Input	0-3.3V	-	5	-

The listed interfaces can be changed depending on the mission without redesigning OBC complex elements. The functionality of the interfaces is presented in Table 2.

Table 2. Interfaces functionality.

Interface		Processor module connection	Purpose
1	CAN	CPU and SN main and redundant CAN I/O	CPU and Service node connection to the main platform data bus
2	RS-422	FPGA configurable I/O	Subsystem elements connection, TM/TS
3	RS-485	FPGA configurable I/O	Subsystem elements connection, TM/TS
4	LVDS I/O	FPGA configurable I/O	High-speed, reliable data connection, focused on communication system and payload connection
5	SERIAL	FPGA configurable I/O and SN serial I/O	TM/TS Tx/Rx, ground debugging
6	PPS	FPGA configurable I/O	Synchronization signal
7	GTH	CPU multigigabit transceivers I/O	High-speed, reliable data connection, focused on communication system and payload connection
8	UART	FPGA configurable I/O and SN serial I/O	Ground debugging
9	SPI	CPU main and redundant SPI I/O	Additional peripherals connection
10	I2C	CPU and SN I2C I/O	Redundant data bus
11	JTAG	CPU and SN JTAG I/O	Ground debugging
12	PWM	FPGA configurable I/O	Magnetorquers (MTQ) control
13	Analog input	FPGA configurable I/O	ADC inputs of the interface module for connecting external analog sensors

3. Functional simulation

Electrical circuit simulations were conducted using LTspice and Altium Designer CAD environments. Figure 2 presents the results of the MTQ control simulation, Figures 3,4 show signal integrity in Altium Designer CAD. The main purpose of using LTspice is to simulate the power section and PWM drivers for MTQ control. This simulation is essential for considering the electrical operating parameters when designing the printed circuit board (PCB).

Fig. 2. MTQ control simulation in LTSpice:
Green line – MTQ coil output current, blue line – PWM control signal

Signal integrity simulation was performed to evaluate line termination and line coupling. This analysis was performed after completing the main PCB layout to evaluate performance and reliability, and identify potential issues before the manufacturing stage. Figure 4 shows the reflected signal amplitude in one of the output interfaces microstrip lines measured at 30 μV. Based on the data in Figure 3, it can be concluded that the line has the correct termination and ensuring that the transmitted signal will not experience significant degradation.

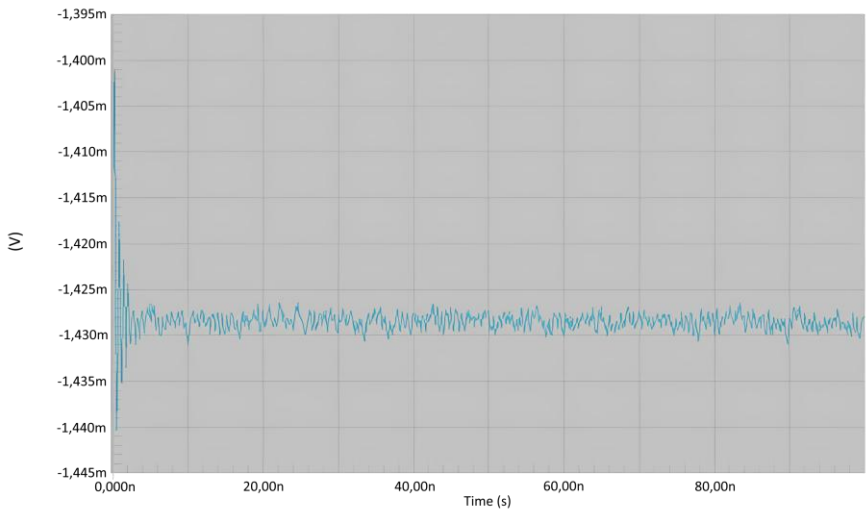

Fig. 3. Reflected signal values in one of output interface microstrip lines with 30 μV amplitude.

Figure 4 shows crosstalk values between two microstrip lines, where A is the shape and magnitude of the signal on the active line, B shows the induced signal on the passive line. With an active upper level of 5 V and the highest frequency component of 166 MHz, the value of the induced interference on the adjacent line does not exceed 2 mV, which is 0.04% of the maximum value and does not pose a threat to the integrity of the signal. Simulation data allow us to conclude that the OBCARM G2 NANO design is carried out in accordance with OBC requirements.

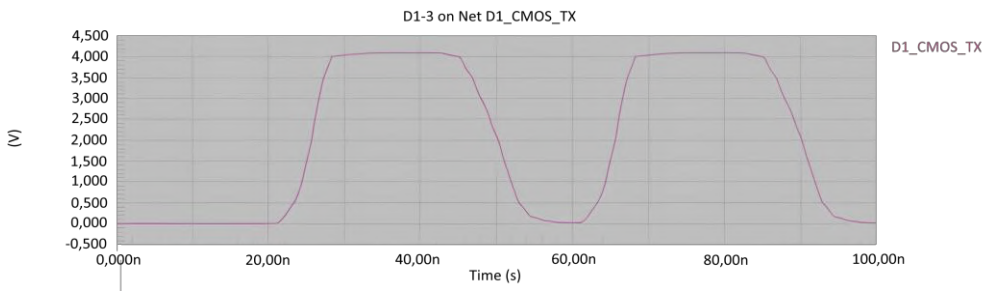

a)

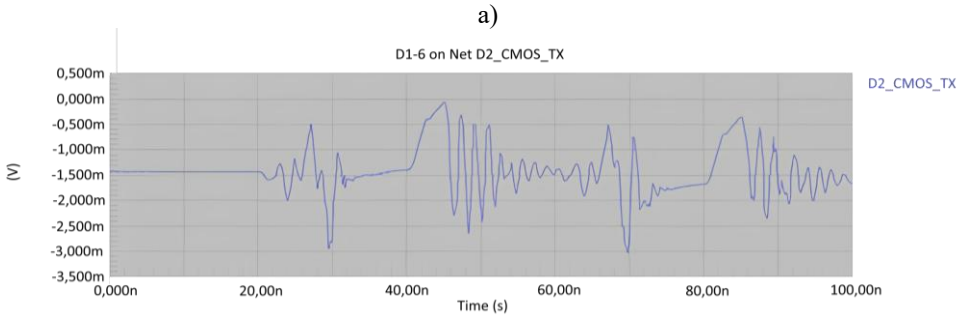

b)

Fig. 4. Crosstalk value between two adjacent microstrip lines:
a) - shape and magnitude of the signal on the active line, b) - shape and magnitude of the signal on the passive line.

4. OBC-Payload interaction

The OBC communicates with payload via three types of signal interfaces:

– Service channel using the RS-422 transmission standard and MODBUS protocol for transmitting TM/TC;

– Data link using the LVDS transmission standard and SpaceWire protocol for transmitting image data from an optical payload.

– Series of 3.3V logic-level signals transmit basic information about the state of the payload (power_ok – the state of the payload power supply, ready – readiness to take a photo) and control the main functions (enable/RST – the backlight and reset signal, trigger – the signal that activates shooting).

Optical payload information is initially saved in its own memory. Upon receiving a command from the OBC, this data is transferred to the FPGA (programmable logic) portion of the system. Images received on the FPGA are saved in OBC permanent memory. Then, according to the communication session schedule, these images are sent to the S-transmitter, which forms a data signal for the ground segment. Data transmission via the OBC is guided by the project's modular and universal design approach, which ensures that replacing the payload or transmitter requires only minimal redesign of the overall platform. In addition, payload and communication system direct connection possibility also remains available. Described interaction block diagram is shown in Figure 5.

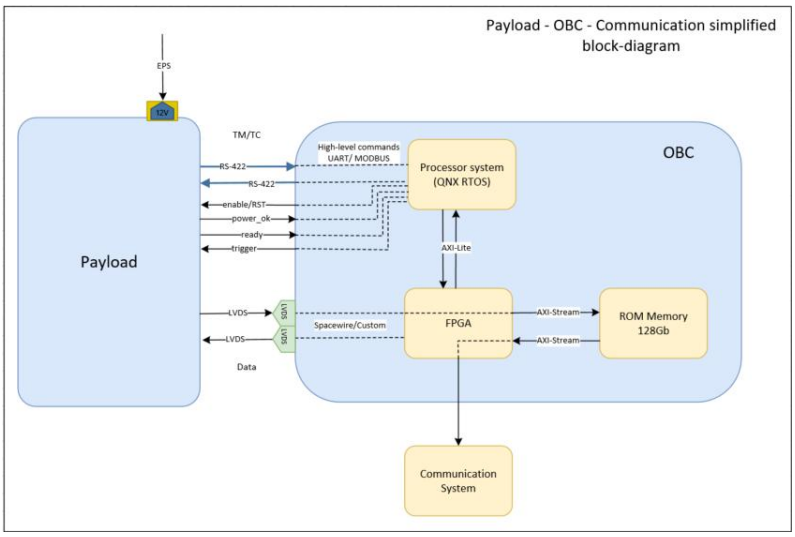

Fig. 5. OBC and payload interaction block-diagram.

5. FPGA architecture

Since the OBC combines a processor system for high-level software operation and programmable logic, it is necessary to develop an architecture for both systems. It was decided to attribute the FPGA architecture to the hardware part. Software architecture is described in the corresponding document. FPGA general architecture design is shown in Figure 6.

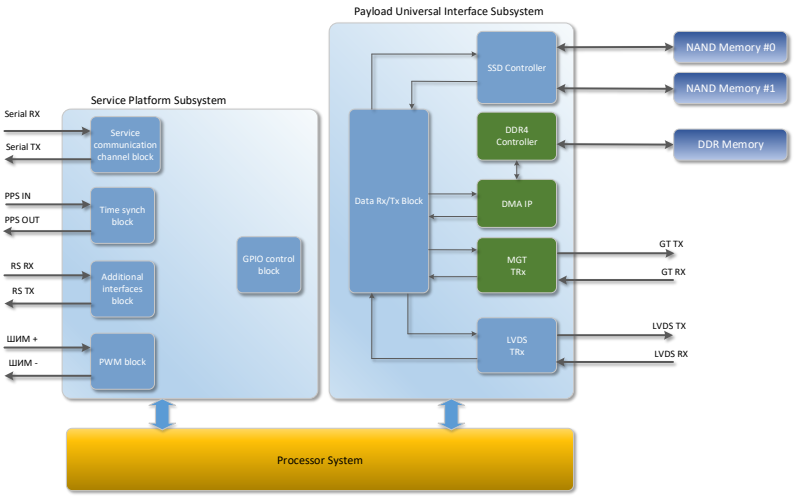

Fig. 6. FPGA general structure block diagram.

FPGA architecture can be divided into two large independent blocks that interact with the processor system via internal AXI bus. Processor system containing high-level software, controls the operation of FPGA blocks where required. Fast and reliable FPGA processes input and output data, removing the potential load from on-board software.

6. Service platform subsystem

The service platform subsystem is designed to receive and transmit telecommands, telemetry and control signals to systems located outside the processor. Service platform subsystem is shown in Figure 7. Its primary components include:

– Service Communication Channel Block: Interfaces with the transceiver, generates compatible protocols, transmits processor-generated telecommands, and decodes received signals.

– Payload Communication Unit: Acts as a backup channel to the optical payload using the Space Packet protocol, enabling command transmission.

– GPIO Control Unit: Generates simple digital control signals (e.g., ENABLE, RESET) for peripheral devices.

– Time Synchronization Unit: Synchronizes onboard time with Global Positioning System (GPS) using a Pulse-Per-Second (PPS) signal for timing of data exchange.

– PWM Generator: Provides adjustable PWM signals for MTQ control when applicable.

– RS-485 and RS-422 Buffers: Translate signals from legacy interfaces to AXI-compatible formats for the processor.

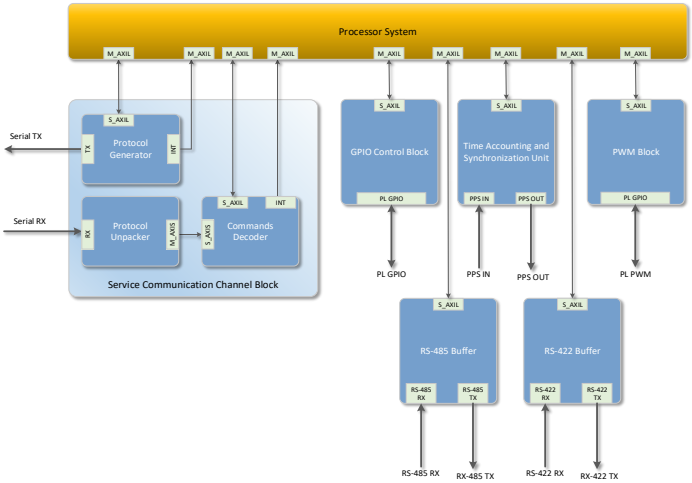

Fig. 7. Service platform subsystem block diagram

7. Universal Interface Subsystem

Universal interface subsystem is designed to form a transmission or reception with minimal redesign effort. Without changing the main configuration, only two IP blocks are requiring changes when adapting to different payload types: LVDS receiver and LVDS transmitter. Block diagram is shown in Figure 8.

– MGT transmitter/receiver blocks: are unused in the current implementation, their presence allows future integration of a custom radio module.

– LVDS Blocks: Handle protocol formation and decomposition, interfacing directly with payloads. These units are the object of redesign when payload type changes.

– Reception/Transmission Module: Operates using AXI protocol; routes data to/from ROM, RAM, or directly to communication channels. Includes its own FPGA-based RAM buffer.

– SSD Controller: Manages read/write operations on two NAND eMMC ROM chips.

– DMA and DDR4 Controller: Transfer data between memory and interface blocks with minimal processor intervention.

DMA, DDR4 controller, and MGT transmitter/receiver blocks are require configuration.

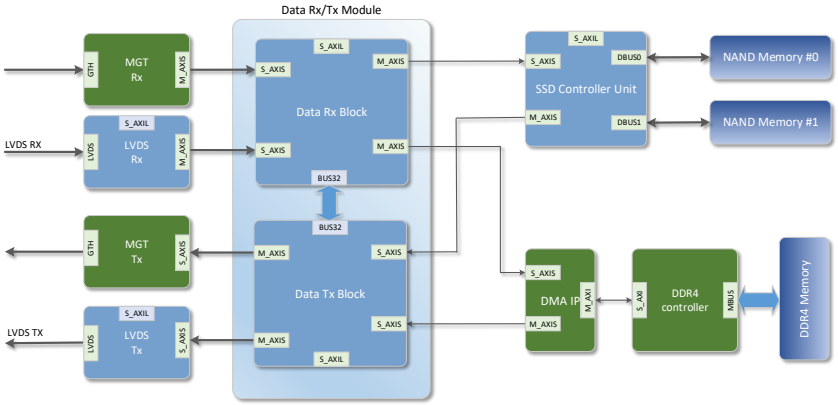

Fig. 8. Universal interface block diagram

8. Comparison of OBCARM G2 NANO with Existing analogues

During preliminary development, existing onboard computer systems were analyzed for benchmarking. Key comparisons are listed below:

– SpaceCube v3 Mini [16] uses previous generation memory, DDR3, and also replaces system-on-a-chip with separate FPGA modules, presented by Kintex Ultrascale and a processor system based on RT proASIC3. OBC has the ability to be installed into a motherboard, to which other modules of this developer can be connected. The breadth of use, comparable computing power is negated when it is necessary to obtain only OBC itself, and the gap in the processor system and FPGA excludes fast data exchange between them. Moreover, external drivers are still necessary to connect interfaces of different types. Considering all the parameters, it is an example of an excellently executed OBC technology.

– Many solutions, for example, the one specified in [17] suggest using the Zynq 7000 system-on-a-chip, which is significantly inferior in performance to the Zynq Ultrascale+, binds AOCS elements control only to OBC, while the OBCARM G2 NANO has the ability to work with AOCS computer as AOCS signals repeater. Also, the analog under consideration uses Linux and I2C as the main communication line.

– Sirius OBC [18], a commercial OBC, offers a robust solution with 64 MB of RAM, 50 MHz processors, and a 5-year orbital life. This OBC handles telemetry and stores payload data, but is not capable of combining the functions of a platform OBC and AOCS OBC.

– NanoMind A3200 [19], another commercial solution, with a larger amount of memory compared to [18], as well as the ability to control AOCS elements. NanoMind A3200 has extremely small dimensions, but will either require additional mechanical equipment for mounting in the platform, or the purchase of a motherboard for subsystems from the same manufacturer. A comparison brief summary is given in Table 3.

Table 3. Comparison of OBCARM G2 NANO and analogous systems

Parameter	OBCARM G2 NANO	SpaceCube v3 Mini [16]	Sirius OBC [18]	NanoMind A3200 [19]
CPU	Zynq Ultrascale+	RT proASIC3	32-bit LEON3FT	AVR32 MCU
FPGA	Zynq Ultrascale+	Kintex Ultrascale	-	-
RAM	500 MB DDR4 – CPU; 125 MB DDR4 - FPGA	2 GB DDR3 – ПЛИС;	64 MB	32 MB
ROM	128 MB QSPI Flash– FSW; 128 GB NAND Flash - ROM	16 ГБ NAND Flash – FSW; 16 ГБ NAND Flash – ROM;	2 ГБ Flash-ROM	128 МБ NOR Flash - ROM
Mass	260 g	-	130 g	24 g
Dimensions	95mm x 95mm x 35mm	95mm x 95mm x 95mm (motherboard included)	95mm x 90mmx 17mm	65mm x 40mm x 7.1mm
Integration difficulty	Low	Medium	Low	Low
AOCS OBC functions	Yes	No	No	Yes
Power	10 W/25 W max.	31 W	1.3 W	3.3 W max

9. Conclusion

The OBCARM G2 NANO is a versatile and modular onboard computer subsystem suitable for a wide range of space missions. Its separation of computational and integration components streamlines platform adaptation and scalability. Using a powerful system-on-a-chip allows execution of complex algorithms for high-performance platforms while remaining energy efficient for smaller spacecraft.

The project has resulted in a multifunctional, fault-tolerant computing solution with straightforward integration procedures, extensive computational resources, and a robust software framework. The OBCARM G2 NANO's modular and mechanically simple design ensures ease of installation across different satellite volumes. Although tailored to the CubeSat form factor, its specifications and flexibility make it equally viable for larger spacecraft platforms.

Conflict of interest statement

The authors declare that they have no conflict of interest in relation to this research, whether financial, personal, authorship or otherwise, that could affect the research and its results presented in this paper.

Credit Author Statement

Sarsenbayev Y.: Concept, Supervision, Architecture Development, Project administration; **Ostretsov K.:** Hardware Development, Hardware Simulation, Writing – Original Draft, Investigation, Resources; **Baktybekov K. (Corresponding Author):** Review & Editing, Validation, Resources. **Mussina A.:** Software Development, Review & Editing; **Yskak A.:** Software Development, Review & Editing;

Funding

This research has been/was/is funded by the Aerospace Committee of the Ministry of Digital Development, Innovations and Aerospace Industry of the Republic of Kazakhstan (BR 21982462)

References

1. Brycetech (2025) Smallsat by the numbers. Available at: https://brycetech.com/reports/report-documents/smallsats-2025/
2. Kulu E. (2022) Nanosatellite Launch Forecasts 2022 - Track Record and Latest Prediction. Available at: https://digitalcommons.usu.edu/cgi/viewcontent.cgi?article=5166&context=smallsat
3. Alipbayev K., Sarsenbayev Y., Mussina A., Nurgizat Y. (2022) Development of Onboard Control System Architecture for Nanosatellites. *Eurasian Physical Technical Journal*, 19, 4(42), 58 – 66. https://doi.org/10.31489/2022No4/58-66.
4. Sarsenbaev Y.Y., Mussina A.A., Ismailov U.M., Bychkov A.N. (2021) Patent for Utility Model, Republic of Kazakhstan № 6912, 27.12.2021.
5. Kulu E. (2024) Nanosats Database. Available at: https://www.nanosats.eu/
6. Furano G., Menicucci A. (2017) Roadmap for On-Board Processing and Data Handling Systems in Space. *Springer eBooks* (pp. 253–281). https://doi.org/10.1007/978-3-319-54422-9_10
7. Space Micro. Proton-600k Multi-Core Computer (2024). Available at: https://www.spacemicro.com/products/digital-systems.html
8. KP Labs. Antelope (2024). Available at: https://kplabs.space/antelope/
9. Space Inventor. Z7000-P4 (2024). Available at: https://space-inventor.com/modules/z7000
10. Bogatin E. (2020) *Bogatin's Practical Guide to transmission line design and characterization for signal Integrity applications*. Available at: https://ieeexplore.ieee.org/document/9118790/
11. Xilinx (2018) UltraScale Architecture Soft Error Mitigation Controller v3.1. *PG187*, San Jose, CA, USA, Available at: https://docs.amd.com/r/en-US/pg187-ultrascale-sem
12. Tambara L.A., Kastensmidt F.L., Medina N.H., Added N., Aguiar V.a.P., Aguirre F., Macchione E.L.A., Silveira M.a.G. (2015) Heavy Ions Induced Single Event Upsets Testing of the 28 nm Xilinx Zynq-7000 All Programmable SoC. *IEEE Radiation Effects Data Workshop (REDW)*, 1–6. https://doi.org/10.1109/redw.2015.7336716
13. Perez A., Otero A., De La Torre E. (2018) Performance Analysis of SEE Mitigation Techniques on Zynq Ultrascale + Hardened Processing Fabrics. *Proceeding of the NASA/ESA Conference on Adaptive Hardware and Systems (AHS)*, 51–58. https://doi.org/10.1109/ahs.2018.8541490
14. Anderson J.D., Leavitt J.C., Wirthlin M.J. (2018) Neutron Radiation Beam Results for the Xilinx UltraScale+ MPSoC. *IEEE Radiation Effects Data Workshop (REDW)*, 1–7. https://doi.org/10.1109/nsrec.2018.8584297

15. Larouche B.P. (2008) Design, simulation, and testing of the structural separation system for the CanX-3 CanX-4/-5 nanosatellite missions. Toronto. Available at: http://hdl.handle.net/1807/119907

16. Brewer C., Franconi N., Ripley R., Geist A., Wise T., Sabogal S., Crum G., Heyward S., Wilson C. (2020) NASA SpaceCube Intelligent Multi-Purpose system for enabling remote sensing, communication, and navigation in mission architectures. Available at: https://ntrs.nasa.gov/api/citations/20205005819/downloads/SSC20-VI-07-SC_Mini_Submitted.pdf

17. Raje S.M., Goel A., Sharma S., Aggarwal K., Mantri D., Kumar T. (2019) Development of on board computer for a nanosatellite. *Proceeding of the 68th International Astronautical Congress (IAC)*. https://doi.org/10.48550/arxiv.1911.11225

18. AAC Clyde Space (2025) SIRIUS-OBC-LEON3FT. Available at: https://www.aac-clyde.space/what-we-do/space-products-components/command-data-handling/smallsat-sirius-obc

19. GOMSpace (2025) Versatile Onboard Computer for Cube, Nano and Microsat missions. Available at: https://gomspace.com/shop/subsystems/command-and-data-handling/nanomind-a3200.aspx

AUTHORS' INFORMATION

Sarsenbayev, Yerbol Yericovich– Master of Robotic systems, Electronics and Energy Sector, Head of Electronics and Energy Sector, Ghalam LLP, Astana, Kazakhstan; https://orcid.org/0000-0002-2911-8200; y.sarsenbayev@ghalam.kz

Ostretsov, Kamil Igorevich – Master of Electronics & Nanoelectronics, Electronics and Energy Sector, Lead Design Engineer, Ghalam LLP, Astana, Kazakhstan; Scopus Author ID: 57426223200, https://orcid.org/0009-0003-5116-8129; k.ostretsov@ghalam.kz

Baktybekov, Kazbek Suleimenovich – Doctor of Phys. & Math. Sciences, Professor, Head of Payload, Research and Development Department, Research Fellow, Ghalam LLP, Astana, Kazakhstan; Scopus Author ID: 8926833000, https://orcid.org/0000- 0002-6401-8053; k.baktybekov@ghalam.kz

Mussina, Aiman Amanzholovna – Master of Engineering, Aerospace, Head of Software Development Sector, Ghalam LLP, Astana, Kazakhstan; https://orcid.org/0000-0002-0864-1238; a.mussina@ghalam.kz

Yskak, Asset Erikuly – Master of Engineering science, Lead Design Engineer, Ghalam LLP, Astana, Kazakhstan; Scopus Author ID: 57207202175, https://orcid.org/0000-0003-1196-3155; a.yskak@ghalam.kz

EURASIAN PHYSICAL TECHNICAL JOURNAL

2025, Volume 22, No. 3 (53)

https://doi.org/10.31489/2025N3/111-119

Received: 19/03/2025 Revised: 27/08/2025 Accepted: 25/09/2025 Published online: 30/09/2025

Research Article

Open Access under the CC BY -NC-ND 4.0 license

UDC 535.8

DEVELOPMENT AND OPTIMIZATION OF OPTICAL PAYLOAD FOR NANOSATELLITES WITH STRICT CONSTRAINTS

Zhumazhanov B.R.[1], Zhetpisbayeva A.[2*], Kulakayeva A.[3], Makhanov K.[2], Zhumazhanov B.S.[1]

[1] «Ghalam» LLP, Astana, Kazakhstan
[2] L.N. Gumilyov Eurasian national university, Astana, Kazakhstan
[3] International Information Technology University, Almaty, Kazakhstan
*Corresponding author: aigulji@mail.ru

Abstract. *This article presents the design and optimization of a compact, high-performance optical payload for Earth observation nanosatellites. The payload is based on a Ritchey-Chrétien telescope with corrective lenses, providing a ground sample distance (GSD) of 6 meters per pixel from a 600 km orbit while meeting strict constraints on mass, dimensions, power consumption, and operational conditions in the space environment. The design process, conducted using Zemax 2024 software, focuses on achieving high image quality within the limitations typical for a 12U CubeSat. The results confirm the feasibility of the project, ensuring a modulation transfer function value exceeding 0.26 at the Nyquist frequency. Several key performance indicators were evaluated, including the system modulation transfer function. Once the required parameters were achieved, a lens corrector system was added and the field angles were optimized. BK7 and Fused Silica were selected as lens materials. The simulation results confirm that the developed optical payload meets the requirements for use in space conditions, including resistance to vibration loads during launch vehicle launch.*

Keywords: Earth remote sensing, modulation transfer function, payload, nanosatellite, spacecraft.

1. Introduction

The growing demand for Earth remote sensing (ERS) data is driving the development of nanosatellites. Miniaturization requires the creation of compact and efficient optical payloads capable of delivering high-quality images while operating under strict constraints on mass, size, and power consumption. This article presents the design and optimization of such a payload for a CubeSat 12U, aimed at achieving high spatial resolution (6 m GSD) while meeting the stringent requirements typical of the nanosatellite environment.

12U CubeSats, typically ranging in mass from 10 to 24 kg, face significant resource limitations. Power generation within these platforms generally ranges within 20-60 Watts, thereby restricting payload capabilities. In contrast, larger small satellites offer substantially greater power budgets, typically ranging from 150 Watts, and can reach up to 2000 Watts. This disparity underscores the critical need for efficient power management and optimized performance in CubeSat payload designs.

Over the past decade, there has been a significant increase in the number of remote sensing satellites launched by various governments and commercial organizations. This trend reflects the growing demand for and importance of remote sensing technologies applied in fields such as cartography, agriculture, early warning systems, and natural resource monitoring [1].

As an integral part of information technology, ERS plays a key role in providing high-precision and reliable information products essential for industry, science, and society in the modern information economy. To meet the demand for high-quality ERS data, it is critical to develop a fully functional and advanced calibration system, including measurement instruments, measurement methodologies, and a dedicated test site [2]. Manufacturers of space systems apply various standards and methods to evaluate the performance of Earth observation (EO) satellite systems. A wide range of metrics is commonly used, with the most well-known being the modulation transfer function (MTF) [3], absolute signal-to-noise ratio (SNR) [4], and geometric resolution [5]. Additional approaches include differential SNR [6], frequency-dependent SNR [6], noise-equivalent change in reflectance (NE$\Delta\rho$) [7], and national image interpretability rating scales (NIIRS) for image quality assessment [2].

Thus, for a precise and comprehensive system analysis, it is necessary to integrate multiple evaluation metrics. Modern trends in the space industry, such as satellite miniaturization and the development of constellation missions, impose new requirements on optical systems. Compact and high-performance solutions are needed to ensure high-quality imaging while operating under strict mass and size constraints. The development of optical payloads for nanosatellites, such as CubeSats, presents numerous complex engineering challenges. Existing remote sensing systems provide invaluable information essential for scientific research and practical Earth-related applications [8]. In particular, multispectral images obtained from satellite systems play a key role in monitoring climate change and environmental conditions, representing the most common type of data collected by ERS satellite payloads [9].

The modern satellite systems market is characterized by a shift toward flexible and reconfigurable solutions, made possible by technological innovations such as embedded processors, active antennas, and photonic components. Satellite manufacturers are actively developing and exploring various payload configurations, striving to maximize flexibility through the use of embedded systems. This has led to an increasing number of possible configurations, requiring careful selection during satellite system design. The traditional approach to evaluating satellite system performance, based on predefined coverage characteristics and payload configurations, demands significant resources for implementation and testing. While this approach ensures high accuracy, it limits design flexibility by requiring the preselection of a limited number of configurations. This study proposes a software optimization tool that enables rapid parametric assessment of system throughput, considering different payload architectures [10].

High image quality is a critical requirement for high-precision remote sensing applications. Traditional design methods often rely on the experience of developers, which does not guarantee an optimal trade-off and may lead to suboptimal solutions [11]. In the work of Abolghasemi and Abbasi-Moghadam [12], an analysis and design methodology for an experimental remote sensing payload is presented, along with system performance results, including signal-to-noise ratio (SNR) and pre-MTF at a spatial resolution of 50 m in three spectral bands (green, red, and near-infrared). The obtained results demonstrate high image quality, with SNR > 100 and MTF > 40 for a push-broom scanner at an altitude of 700 km.

The study also describes a systematic approach to the development and performance evaluation of a multispectral payload, including an analysis of noise components such as photon noise, background noise, cold shield noise, and electronic noise. System performance was assessed using cascaded MTF, taking into account the effects of optics, image discretization, and satellite motion. The calculation results are provided for the SINA-1 satellite.

In study [13] presents the design of an optical telescope for CubeSats. The authors showed that reflector-based configurations can provide high image quality even within the strict size constraints of the platform. However, their analysis focused solely on the optical design and did not take into account thermo-mechanical stability or straylight, which limits the practical applicability of the results.

Similar limitations can be observed in the MeznSat project [14], where a SWIR spectrometer payload was implemented on a 3U CubeSat. Although the system demonstrated effectiveness for atmospheric monitoring, the study did not consider the combined impact of thermal and mechanical factors that determine image stability.

The importance of testing is highlighted in [15], which describes a thermal vacuum campaign on a CubeSat engineering model. Such experiments are valuable for identifying structural weaknesses, but the results were not directly linked to specific optical designs. This leaves open the question of how test data can be systematically integrated into the development of optical payloads.

A more detailed exploration of CubeSat optical instrumentation is presented in the KITSUNE mission [16]. A focusing mechanism was implemented that achieved image quality with a ground sampling distance

of several meters. At the same time, the issue of long-term focusing stability under thermal variations and vibrations remained unresolved, which limits the practical applicability of the results for Earth observation tasks. A similar conclusion can be drawn from the HiREV project [17], where a camera with a resolution of up to 3 m was demonstrated. This confirmed the potential of CubeSats for high-resolution Earth observation, but the study concentrated on imaging performance while leaving aside issues of straylight suppression and thermo-mechanical optimization.

Thermo-mechanical aspects were addressed in more depth in [18], where mechanical and thermal analyses of a 12U CubeSat carrying a LIDAR payload were conducted. Nevertheless, the authors did not assess how the identified deformations affected image quality, again underscoring the fragmented nature of existing approaches. Another line of research involves the use of phase change materials (PCM) for thermal stabilization. In [19], it was shown that PCM can smooth temperature peaks and improve the stability of multispectral payload performance. However, incorporating such solutions into small satellites remains difficult due to strict mass and volume constraints, as well as the lack of methodologies linking thermal control to optical performance.

Overall, the literature shows that research on CubeSat optical payloads is active and covers a wide spectrum of topics – from telescope and spectrometer design to testing campaigns and thermal stabilization methods. Yet, these efforts remain fragmented: optical systems are often analyzed without considering thermal effects, testing is performed without connection to specific designs, or stabilization methods are proposed without addressing straylight suppression. This indicates that the comprehensive problem of ensuring thermo-mechanical stability and minimizing straylight under the strict mass, size, and power constraints of CubeSats remains unresolved.

2. Materials and methods. Optical system design

The telescope was designed using Zemax 2024 based on the Ritchey-Chrétien configuration. This design was chosen for its effectiveness in minimizing spherical aberration and coma, which are critical for achieving high-quality imaging within the system's compact constraints. To meet the required spatial resolution of 6 m at an orbital altitude of 600 km, the optical system was developed with two hyperbolic mirrors and a corrective lens system. The lens materials selected were BK7 and fused silica. BK7 offers high transparency in the visible spectrum. Fused silica exhibits similar transparency but also features a wider spectral range, making it suitable for applications requiring broader wavelength coverage.

The Ritchey-Chrétien telescope design aims to achieve maximum resolving power while maintaining optimal mass and dimensional characteristics. This system represents a modified Cassegrain configuration, featuring hyperbolic primary and secondary mirrors, which effectively minimize spherical aberrations and coma, ensuring a wide field of view with high accuracy. A corrective lens system has been integrated to compensate for field curvature, which arises when using a flat detector.

As the imaging detector, we employed the CMV12000 CMOS sensor (ams/CMOSIS). The device provides a resolution of 4096 × 3072 pixels (≈12.5 MP) with a 5.5 μm pixel pitch, corresponding to an active area of 22.5 × 16.9 mm (diagonal ≈28.1 mm). The architecture is based on a global shutter with an 8T pixel design and correlated double sampling, which reduces fixed-pattern noise and enables exposure during readout. The sensor supports 8/10/12-bit quantization and features 64 LVDS outputs at up to 600 Mbit/s per channel, enabling frame rates of up to ≈132 fps at full resolution (12 bit) and ~300 fps in windowed readout modes.

The typical peak quantum efficiency of the monochrome version is 50–60% around 550 nm, enhanced further by microlenses that improve the effective fill factor. Key sensitivity parameters include temporal noise of about 13 e^- rms, dark current of approximately 70 e^-/s at 25 °C, a maximum SNR of ≈41 dB, and a dynamic range of ≈60 dB. The CMV12000 is an area-scan sensor without native TDI functionality; its use in push broom configurations is only possible with external scanning and does not provide charge accumulation along detector rows.

It is important to note that using classical manufacturing methods for such telescopes with relatively large apertures would lead to an increase in satellite mass and volume. However, several innovative techniques can reduce telescope size [20]. For example, the synthetic aperture concept allows for the segmentation of a monolithic primary mirror into smaller foldable segments, which are deployed after the satellite reaches orbit [21]. Another emerging technology, based on adaptive optics, enables the realization of a 1.5-meter mirror

[22]. Recently, a 1.3-meter large-aperture mirror was developed using lightweight space optical components [23].

3. Results

Calculation of key parameters:

The focal length of the telescope plays an important role in determining the quality and characteristics of the obtained images. The focal length (f) of the telescope is calculated using the formula:

$$f = \frac{H\Delta}{GSD}; \quad (1)$$

where H is the orbit height (600 km), Δ is the detector pixel size (5.5 μm), and GSD is the required ground sample distance (6 m). The calculation gives a focal length of approximately f ≈ 550 mm.

The minimum aperture diameter (D) of the telescope is determined by the formula:

$$D \geq \frac{1{,}22*\lambda*f}{\Delta}; \quad (2)$$

where λ is the minimum wavelength (450 nm for RGB). The calculation gives a minimum aperture diameter of approximately 54.9 mm. Considering dimensional constraints (the aperture diameter must fit within 1U of a CubeSat) and the need to accommodate additional components, the aperture diameter was set to 85 mm.

The field of view (FoV) of the telescope is calculated using the formula:

$$FoV = 2\,arctan\frac{SW}{2H}, ; \quad (3)$$

where SW is the swath width (30,720 m, calculated based on the detector resolution and GSD). The calculation gives FoV ≈ 3°.

The telescope's f-number (f#) is calculated as:

$$f\# = F/D = 6{,}47 \quad (4)$$

Based on the obtained parameters, the optical system was designed and simulated, with its schematic shown in Figure 1. The modulation transfer functions (MTF) graph for this system is presented in Figure 2.

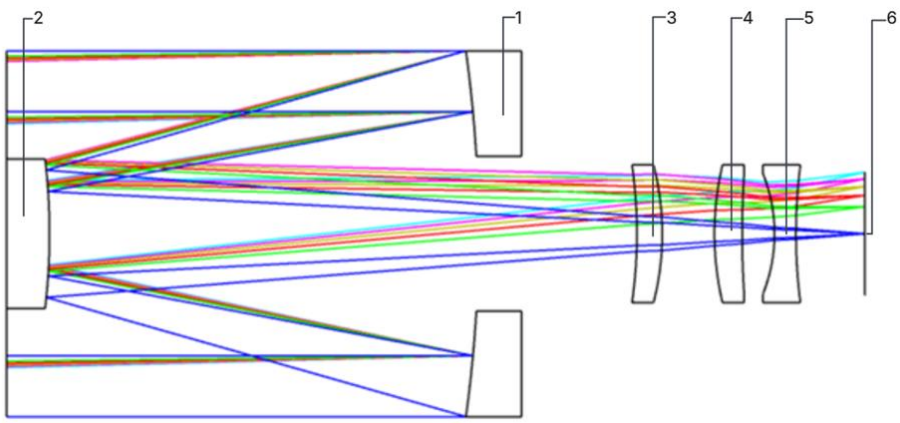

Fig.1. Optical diagram of the developed payload:
1 – primary mirror, 2 – secondary mirror, 3 – first lens corrector, 4 – second lens corrector, 5 – third lens corrector, 6 – detector plane.

The MTF is a key metric for assessing image quality in optoelectronic imaging systems. MTF is defined as the spatial frequency response of the system, representing its ability to reproduce sinusoidal test patterns of varying spatial frequencies. The overall image quality of the system—system MTF—is determined by the contributions of each of its components, as each element plays a role in shaping the final image.

Image quality is significantly affected by the optical system, the detector, blurring effects, and atmospheric conditions. According to the technical requirements, the MTF value of the designed telescope must exceed 0.1 at the Nyquist frequency (91 line pairs/mm). Simulation results have shown that the developed telescope achieves an optical system MTF value of 0.26 at the Nyquist frequency (Fig. 2).

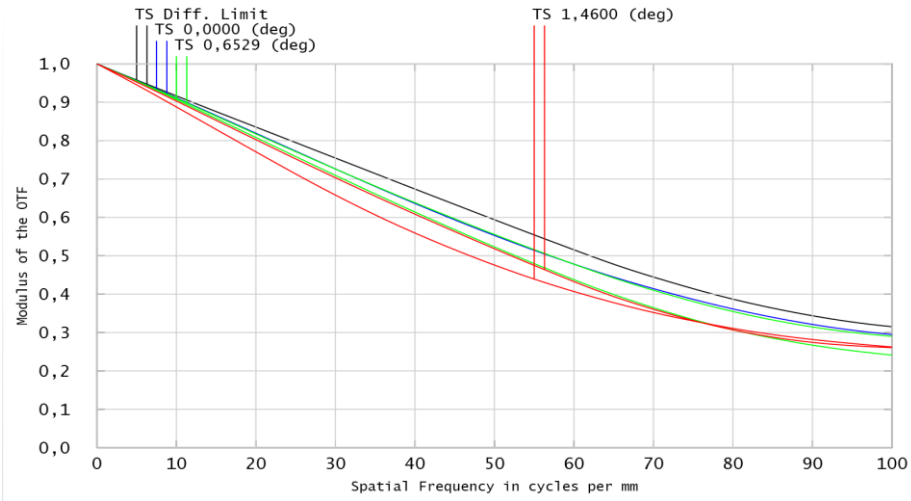

Fig.2. Modulation transfer function graph for the developed payload

The mirror segment of the system was designed and optimized independently of the corrective lens system, with calculations performed solely along the optical axis. This approach minimized the impact of lens defocusing on image quality. Once the required characteristics of the mirror system were achieved, corrective lenses were integrated, and additional optimization of the field angles was carried out.

BK7 and fused silica were selected as the lens materials.

BK7 provides high transparency in the visible spectral range.

Fused silica offers high transparency over a broader spectral range and exhibits enhanced radiation resistance.

Two materials were selected for the fabrication of corrective lenses: optical glass BK7 and fused silica. The choice was based on their optical and mechanical properties. BK7 is characterized by a high refractive index ($n_d = 1.5168$) and moderate dispersion ($\nu_d = 64.17$), providing sufficient transparency in the visible range (330–2100 nm). Fused silica exhibits a lower refractive index ($n_d = 1.4585$) and even lower dispersion ($\nu_d = 67.82$), while offering a significantly broader transmission range (180–3500 nm) and high thermal stability (thermal expansion coefficient of 0.55×10^{-6}/°C).

Additionally, fused silica has high chemical resistance and is highly resistant to UV radiation and laser exposure. Thus, the selection of these materials ensures an optimal combination of optical performance and durability for operation in space conditions.

The Point Spread Function (PSF) is one of the most important characteristics of an optical system, describing the distribution of light intensity in the image of a point source. PSF analysis allows for the assessment of image quality, which is determined by factors such as resolution, contrast, and the presence of aberrations. The graphical representation of the PSF is a scatter diagram that illustrates the distribution of light intensity in the focal plane depending on the position on the detector.

The shape and size of the scatter spot are directly related to the presence and magnitude of aberrations in the optical system, as well as diffraction effects. A compact and symmetrical scatter spot indicates high image quality, whereas a blurred or asymmetrical spot suggests the presence of aberrations and a decrease in image quality. Analyzing the PSF at various distances from the optical axis (across the field of view) allows for the evaluation of the uniformity of image quality across the entire frame.

Figures 3-4 present the PSF for the developed optical system, obtained through Zemax simulations. Figure 3 illustrates the PSF of the telescope without the corrective lens system, while Figure 4 shows the PSF with the corrective lens system integrated.

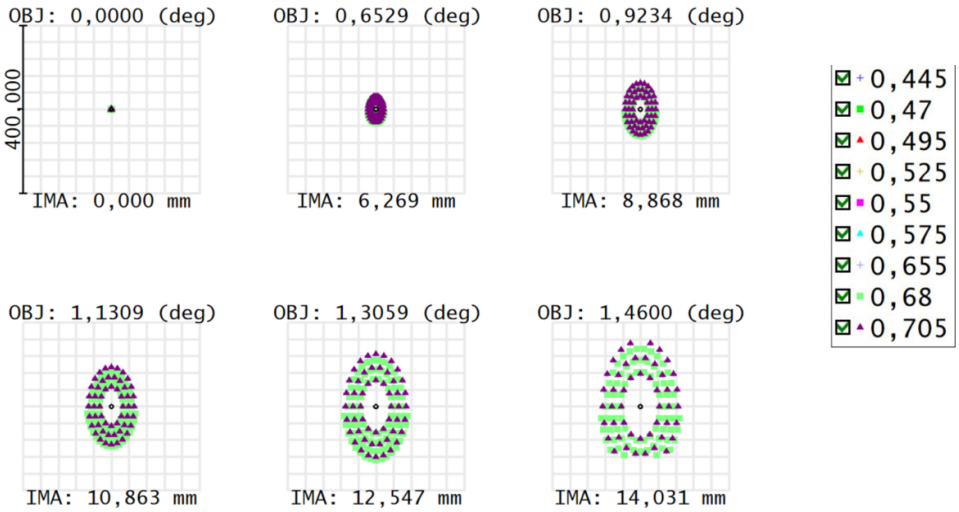

Fig.3. Ray spot diagram for telescope without a corrective lens system

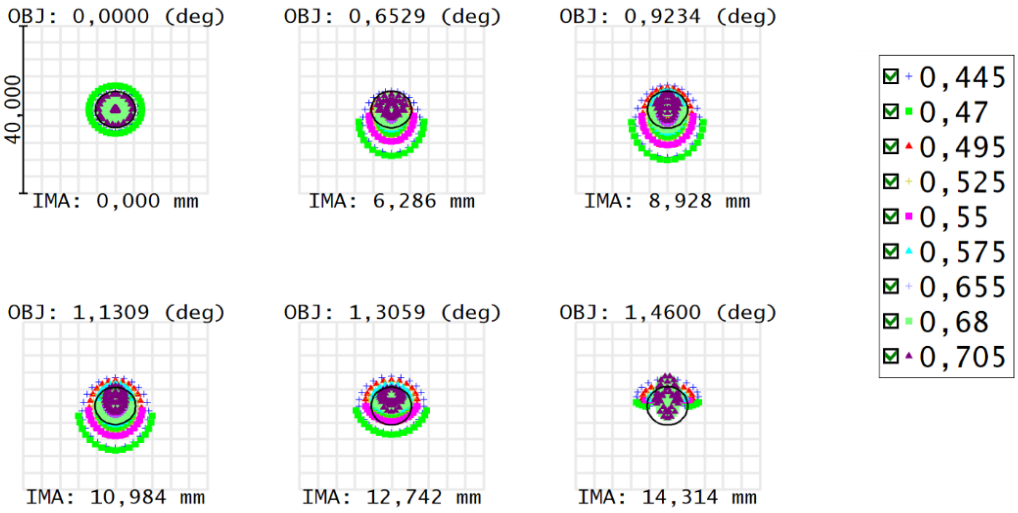

Fig.4. Ray spot diagram for telescope with a corrective lens system

Simulation results show that in the absence of corrective lenses (Fig. 3), the telescope forms an almost perfect image at the center of the field of view; however, a significant increase in spot size and distortion of its shape is observed toward the edges. The inclusion of a corrective lens system (Fig. 4) leads to a slight degradation of image quality at the center, characterized by a small increase in spot size. However, this degradation is minimal compared to the significant improvement in image quality at the periphery of the field of view, where a substantial reduction in spot size and a more symmetrical shape are observed. This confirms the effectiveness of the corrective lens system in minimizing aberrations and enhancing image quality across the entire field of view. The Table 1 summarizes the parameters of the optical payload.

To mitigate direct illumination of the detector via the front aperture of the system and the central aperture of the primary mirror, the straylight analysis was done, and by its results, the external and internal baffles were designed and implemented. The effectiveness of these elements was assessed using non-sequential ray tracing simulations within Zemax OpticStudio. The configuration of the baffles is illustrated in Figure 5.

While not providing complete shielding of direct flight paths, this baffle contributes to reducing the intensity of scattered light originating from external sources outside the primary field of view, thereby minimizing background stray light, particularly crucial in high-illumination environments.

Table 1. Parameters of optical payload.

#	**Payload parameters**	**Values**
1	Reference Orbit type	Sun Synchronous
2	Reference Orbit Altitude	600 km
3	Size	3U
4	Mass	<2,0 kg
5	Image size (from reference orbit)	18 km x 24 km
6	GSD (from reference orbit)	6 m
7	Onboard memory	128 GB
8	MTF	> 0.26
9	Life time	2 years

As an additional way of reduction of straylight, the Acktar foil was applied to the internal surfaces of the tube. Coating internal parts of the tube by Acktar foil allows to absorb an exceptionally high percentage of incident light. This greatly reduces the amount of light that can be reflected or scattered within the optical system.

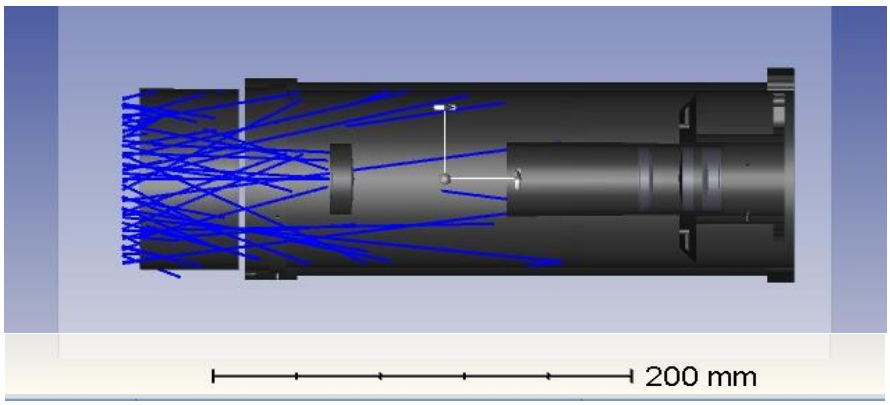

Fig. 5. Model of baffle placement within the optical system)

4. Discussion

The optimized optical system achieved the target GSD of 6 meters at an orbital altitude of 600 km. MTF analysis showed an exceeding of the target value, with an MTF of 0.26 at the Nyquist frequency. Scatter diagrams confirmed high image quality across the entire field of view. Detailed modeling assessed the structural stability under various space environment factors.

The presented work demonstrates the feasibility of developing a high-performance optical payload for nanosatellites capable of capturing high-quality images of Earth. The Ritchey-Chrétien design effectively balances high performance with constraints on mass, dimensions, and power consumption. Further research may focus on the application of advanced methods in the development of solutions for the payload electronics module. The Ritchey-Chrétien design was selected as it provides superior off-axis performance at compact size of the payload. This design corrects for coma and astigmatism to provide a wide enough, flat field of view crucial for efficient Earth observation. While the main mission was technology demonstration, obtaining a GSD of 6 meters enables a range of applications, including the identification of individual agricultural fields, allowing for precise monitoring of crop health, as well as object recognition of objects of the corresponding size, such as automobiles and trucks. The MTF analysis revealed a performance exceeding the design goal, achieving a value of 0.26 at the Nyquist frequency. This ensures the capture of sufficiently detailed images. The article covers the current status of optical design. The work will be continued with research of methods for the straylight analysis, mechanical analysis, integration of the sensor and electronics unit to the payload and integration of the payload to satellite platform.

5. Conclusion

In this article, the task of designing and optimizing a compact optical payload for a CubeSat 12U spacecraft was successfully accomplished. The use of a Ritchey-Chrétien telescope with corrective lenses enabled the creation of a system that effectively minimizes spherical aberration and coma, which is crucial for ensuring high image sharpness. It was established that even with significant constraints on mass and dimensions, achieving a high spatial resolution of 6 meters at an orbital altitude of 600 km is possible.

As a result of optimizing the optical design, significant efficiency in the use of photonic components was achieved, improving system performance while maintaining its compactness. These enhancements open new prospects for the development of future nanosatellites capable of performing complex remote sensing tasks with high precision and minimal resource consumption.

Further research and development may include the design of more advanced onboard control and data processing systems for remote sensing, enhancing the overall functionality and reliability of satellite systems.

Thus, this article highlights the importance of integrating the latest technological advancements in aerospace engineering and emphasizes the significance of scientific research in space technologies, contributing to the strengthening of technological independence and the development of the national space industry.

Conflict of interest statement

The authors declare that they have no conflict of interest in relation to this research, whether financial, personal, authorship or otherwise, that could affect the research and its results presented in this paper.

CRediT author statement

Zhumazhanov B.: Project administration, Supervision, Writing - Original Draft, Methodology. **Zhetpisbayeva A.:** Investigation, Writing- Original draft, Writing- Reviewing and Editing, Conceptualization**; Makhanov K., Kulakayeva A.:** Writing- Reviewing and Editing, Investigation**. Zhumazhanov Bexultan:** Conceptualization, Methodology, Validation, Formal analysis**.** The final manuscript was read and approved by all authors.

Acknowledgements

The work was carried out with financial support from the CS MES RK under the PTF program, grant BR27198365 "Development of an optoelectronic system in the short-wave infrared spectral range in the context of the development of Kazakhstan's remote sensing space systems" (2024–2026).

References

1 Simon Jones, Karin Reinke (2009). *Innovations in remote sensing and photogrammetry*. Springer Science & Business Media, 468. https://doi.org/10.1007/978-3-540-93962-7

2 Li, C.R., Tang, L.L., Ma, L.L., Zhou, Y.S., Gao, C.X., Wang, N., Zhu, X. H. (2015). Comprehensive calibration and validation site for information remote sensing. *The International Archives of the Photogrammetry, Remote Sensing and Spatial Information Sciences*, XL-7/W3, 1233-1240. https://doi.org/10.5194/isprsarchives-XL-7-W3-1233-2015

3 Xing, K., Cao, S. X., Yue, C. Y., Zhou, N. (2017). Optimization design method of optical remote sensor based on imaging chain simulation. *MATEC Web of Conf.*, 114, 04013. https://doi.org/10.1051/matecconf/ 201711404013

4 Kramer, H. J. (2002). *Observation of the Earth and Its Environment:* Survey of Missions and Sensors, Heidelberg, Berlin, New York Berlin: Springer, 1509. https://doi.org/10.1007/978-3-642-97678-0

5 Musabayev, T. A., Moldabekov, M. M., Nurguzhin, M. R., Dyussenev, S. T., Murushkin, S. A., Albazarov, B. S., & Ten, V. V. (2013). Earth observation system of the Republic of Kazkahstan. *Proceedings of the Intern. Astronautical Congress, IAC*, 2738-2740. https://www.eoportal.org/satellite-missions/kazeosat-2#eop-quick-facts-section

6 Fiete, R. D., & Tantalo, T. (2001). Comparison of SNR image quality metrics for remote sensing systems. *Optical Engineering*, 40(4), 574-585. https://doi.org/10.1117/1.1355251

7 Citroen, M., Raz, G., & Berger, M. (2008). Noise equivalent reflectance difference (NERD) vs. spatial resolution (SR) as a good measure for system performances. *Remote Sensing System Engineering*, 7087, 66-76. https://doi.org/10.1117/12.794632

8 Attia, W. A., Eltohamy, F., & Bazan, T. M. (2020). Design of very high resolution satellite telescopes part II: comprehensive performance assessment. *IEEE Transactions on Aerospace and Electronic Systems*, 56(5), 4049-4055. https://doi.org/10.1109/TAES.2020.2991622

9 Wong, S. (2014). Predicting image quality of surveillance sensors. *Defence Research and Development Canada*, 38. Available at: D68-2-97-2014-eng

10 Mengali, A., Ginesi, A., D'Addio, S. (2020). Computer-aided payload architecture optimization for HTS satellites. *Proceedings of the 10th Advanced Satellite Multimedia Systems Conference and the 16th Signal Processing for Space Communications Workshop (ASMS/SPSC)*, 1-8. https://doi.org/10.1109/ASMS/SPSC48805.2020.9268888

11 Jafarsalehi, A., Asl, E. P., & Mirshams, M. (2014). Satellite imaging payload design optimization. *Aerospace Science and Technology*, 39, 145-152. DOI:10.1016/j.ast.2014.09.003

12 Abolghasemi, M., & Abbasi-Moghadam, D. (2012). Design and performance evaluation of the imaging payload for a remote sensing satellite. Optics & Laser Technology, 44(8), 2418 - 2426. https://doi.org/10.1016/j.optlastec.2012.04.006

13 Şanlı, A., & Erkeç, T. Y. (2024). Design and Analysis of Optical Telescope Subsystem. *Journal of Aeronautics and Space Technologies*, *17*(Special Issue), 92-101. URL jast.hho.msu.edu.tr

14 Jallad, A. H., Marpu, P., Abdul Aziz, Z., Al Marar, A., & Awad, M. (2019). MeznSat—A 3U CubeSat for monitoring greenhouse gases using short wave infra-red spectrometry: Mission concept and analysis. *Aerospace*, *6*(11), 118. https://doi.org/10.3390/aerospace6110118

15 Dunwoody, R., Reilly, J., Murphy, D., Doyle, M., Thompson, J., Finneran, G., ... & McBreen, S. (2022). Thermal vacuum test campaign of the EIRSAT-1 engineering qualification model. *Aerospace*, *9*(2), 99. https://doi.org/10.3390/aerospace9020099

16 Jung, J., Sy, N. V., Lee, D., Joe, S., Hwang, J., & Kim, B. (2020). A single motor-driven focusing mechanism with flexure hinges for small satellite optical systems. *Applied Sciences*, *10*(20), 7087. 10. https://doi.org/10.3390/app10207087

17 Azami, M. H. B., Orger, N. C., Schulz, V. H., Oshiro, T., Alarcon, J. R. C., Maskey, A., ... & KITSUNE Team Members. (2022). Design and environmental testing of imaging payload for a 6 U CubeSat at low Earth orbit: KITSUNE mission. *Frontiers in Space Technologies*, *3*, 1000219. https://doi.org/10.3389/frspt.2022.1000219

18 Guentchev, G. N., Bayer, M. M., Li, X., & Boyraz, O. (2021, August). Mechanical design and thermal analysis of a 12U CubeSat MTCW lidar based optical measurement system for littoral ocean dynamics. *CubeSats and SmallSats for Remote Sensing V* ,Vol. 11832, 71-98. https://doi.org/10.1117/12.2597709

19 Geismayra, L., Schummera, F., Langer, M., Binder, M., & Schlick, G. (2020, October). Thermo-Mechanical Design and Analysis of a Multispectral Imaging Payload using Phase Change Material. *Proceeding of the Intern. Astronautical Congress (IAC) – The CyberSpace Edition, 1-17, IAC-20-C2.5.13* https://www.researchgate.net/publication/348603407

20 Woodruff, R. A., Hull, T., Heap, S. R., Danchi, W., Kendrick, S. E., & Purves, L. (2017). Optical design for CETUS: a wide-field 1.5 m aperture UV payload being studied for a NASA probe class mission study. *Astronomical Optics: Design, Manufacture, and Test of Space and Ground Systems*, 10401, 400 - 408. https://doi.org/10.48550/arXiv.1912.06763

Contreras, J. W., & Lightsey, P. A. (2004, October). Optical design and analysis of the James Webb Space Telescope: optical telescope element. *Novel Optical Systems Design and Optimization VII* 5524, 30 - 41. https://doi.org/10.1117/12.559871

21 Devilliers, C., Du Jeu, C., Costes, V., Suau, A., Girault, N., & Cornillon, L. (2017). New design and new challenge for space large ultralightweight and stable Zerodur mirror for future high resolution observation instruments. *Proceedings of the Intern. Conf. on Space Optics—ICSO 2014*, 10563, 442-450. https://doi.org/10.1117/12.2304187

22 Wang, X., Guo, C., Liu, Y., Chen, J., Wang, Y., & Hu, Y. (2019). Design and manufacture of 1.3 meter large caliber light-weighted Space optical components. *Proceedings of the Intern. Conf. on Space Optics—ICSO 2018*, 11180, 304-321. https://doi.org/10.1117/12.2535947

AUTHORS' INFORMATION

Zhumazhanov, Berik – Master (Sci.), Head of payload and scientific developments department, «Ghalam» LLP, Astana, Kazakhstan; SCOPUS Author ID: 57350754500; http://orcid.org/0000-0001-5926-9619; b.zhumazhanov@ghalam.kz

Zhetpisbayeva, Ainur – PhD, Associate Professor, Department of Radio engineering, electronics, and telecommunications, L.N. Gumilyov Eurasian National University, Astana, Kazakhstan; SCOPUS Author ID:57189702755; https://orcid.org/0000-0002-4525-5299; aigulji@mail.ru

Kulakayeva, Aigul – PhD, Associate Professor, Department of Radio engineering, electronics, and telecommunications, International Information Technology University, Almaty, Kazakhstan; SCOPUS Author ID: 56732962300; https://orcid.org/0000-0002-0143-085X; a.kulakayeva@iitu.edu.kz

Makhanov, Kanat – Candidate of Physical and Mathematical Sciences, Senior Lecturer, Department of Radio engineering, electronics, and telecommunications, L.N. Gumilyov Eurasian National University, Astana, Kazakhstan; Scopus Author ID: 57217354220; https://orcid.org/0000-0002-1263-0734; makanov@inbox.ru. +77009667591

Zhumazhanov, Bexultan – Master (Eng.), Design-engineer, «Ghalam» LLP, Astana, Kazakhstan, https://orcid.org/0009-0000-9493-7491; zhumazhanov.b@ghalam.kz

EURASIAN PHYSICAL TECHNICAL JOURNAL

2025, Volume 22, No. 3(53)

https://doi.org/10.31489/2025N3/120-126

Received: 07/04/2025 Revised: 28/08/2025 Accepted: 25/09/2025 Published online: 30/09/2025

Research Article

Open Access under the CC BY -NC-ND 4.0 license

UDC 530.1

A DYNAMICAL SYSTEM APPROACH TO LANGUAGE BIAS EVOLUTION ON COMPLEX NETWORKS

Baibolatov Y.Z., Nalibayev Y.D., Kozhagulov Y.T.*

Al-Farabi Kazakh National University, Almaty, Kazakhstan
*Corresponding author: eldos.kozhagulov@kaznu.kz

Abstract. *We propose a dynamical systems model to study language competition and bias evolution in structured agent populations. Each agent is characterized by a continuous bias variable representing their linguistic preference, evolving under the combined influence of peer interactions, native language retention, and external prestige forces. The model incorporates a nonlinear damping mechanism that confines the agent's bias within a fixed range between negative one and one, and allows for heterogeneous susceptibility and retention parameters. We analyze the model in its linear regime and perform a stability analysis of the fixed points under both symmetric and asymmetric network topologies. Simulations on fully connected and small-world networks reveal diverse dynamical scenarios, including language death, bilingual persistence, and spontaneous population bifurcation into opposing linguistic groups. The results provide insight into the interplay of social structure, identity, and external influence in shaping language dynamics.*

Keywords: Nonlinear dynamics, complex systems, networks.

1. Introduction

The evolution of languages in a globalized, interconnected society is shaped by complex interactions between individuals, their cultural identities, and external sociopolitical forces. As some languages grow in dominance while others face extinction, mathematical modeling offers a powerful framework to understand the mechanisms driving these dynamics. Previous studies have highlighted mechanisms of language death [1], bilingual coexistence [2], and the effects of social structure [3–10]. Language dynamics have also been explored using agent-based models [11], adaptive networks [12], and hybrid learning schemes [5,13]. The inclusion of prestige effects [1,14], inter-linguistic similarity [2], and stochasticity [13,15] enriches the modeling landscape. The study of language dynamics offers a compelling application of nonlinear dynamical systems, a core area in technical and applied physics. Our approach formalizes language bias evolution using continuous variables and differential equations on complex networks, employing techniques common in statistical physics, control theory, and systems engineering. Furthermore, the model's structure—governed by agent-level dynamics and influenced by network topology—parallels the analysis of synchronization [16], signal propagation, and collective behavior in engineered and physical systems [17–21]. This cross-disciplinary perspective aligns with the broader goal of applying physical modeling paradigms to complex social and technical systems.

In this work, we present a novel model of language bias evolution in agent-based populations, incorporating network-based peer influence, native language retention, and external prestige effects. The goal is to identify conditions that lead to outcomes such as language death, bilingualism, or stable language coexistence.

2. The Model

We consider a system of agents that speak either language A or language B, or both. Since in reality, even if people are bilingual, it is quite often that their language competence is not absolute for both languages. For example, if a person's native language is A, and at some point in his life, the person learns the language B, the level of competence is rarely the same as a native level. In this work, we construct a mathematical model of agents, with a dynamic variable being the "bias" ϕ_k towards one or the other language: $\phi_k = +1$ if the person speaks only language A, $\phi_k = -1$ if the person speaks only language B, and $-1 \prec \phi_k \prec +1$ if the person is bilingual. If the person perfectly speaks both languages at the same level, the value of $\phi_k = 0$, which means that the person does not have any preference in choosing the language. If the value of ϕ_k is positive, then we say that the person is bilingual, but with a preference for language A.

How does this bias change over time? The first and foremost purpose of a human language is communication with other people, and the bias naturally changes due to the social connections of the person. If a group of people speaks the same language at the same level, their bias and proficiency level do not change, hence $\dot{\phi}_k = 0$ for the agents of this group (a dot over a variable denotes derivative over time). But if a group of people with different levels of language proficiency and bias are connected, for example, a foreigner with an intermediate level of language proficiency is connected to a group of native speakers, then there is a natural drive to change the bias $\dot{\phi}_k \neq 0$. To model this behavior, we consider a simple diffusive coupling model

$$\dot{\phi}_k = \left(1-\phi_k^2\right)\sum_{j=1}^{N} L_{jk} f\left(\phi_j - \phi_k\right), \tag{1}$$

where f is the coupling strength, which is an odd function, and L_{jk} is the connectivity matrix, i.e., $L_{jk} = 0$ if agents j and k are not connected, and $L_{jk} = 1$ if they are connected. Naturally $L_{kk} = 0$. The term $1-\phi_k^2$ is added to introduce natural fixed points in the model at values $\phi_k = \pm 1$ and to dampen the dynamics near these points, so that the values of the bias remain in the domain $\phi_k \in [-1,1]$.

At this point, our model lacks individuality of the agents, such as preference of the native language. Let us introduce the new term, describing the native language retention

$$\dot{\phi}_k = \left(1-\phi_k^2\right)\left[\sum_{j=1}^{N} L_{jk} f\left(\phi_j - \phi_k\right) + \gamma_k g\left(\eta_k - \phi_k\right)\right], \tag{2}$$

where $\eta_k = \pm 1$ is the native language parameter, and $g\left(\eta_k - \phi_k\right)$ is the retention function that controls the bias towards the native language of the individual agent. We assume that people have a natural tendency to lean towards their native language, due to various reasons, like cultural heritage, historical, philosophical, or political influence, etc. The parameter γ_k is the strength of individual agents' retention. Small values γ_k indicate that an agent is easily biased toward the other language, while large values indicate that the agent is deeply rooted towards its native language, e.g., "zealot" or "patriotism" parameter. It is obvious that the function g has to be an odd function as well.

Last, but not least, we have to consider the "status" of the language, described in [1]. The idea is that in reality, different languages have different perceived status of prestige. This factor appears for various natural reasons, such as the number of people speaking the language, the media influence, the access to information and education, etc. In our model, we introduce the influence term as

$$\dot{\phi}_k = \left(1-\phi_k^2\right)\left[\sum_{j=1}^{N} L_{jk} f\left(\phi_j - \phi_k\right) + \gamma_k g\left(\eta_k - \phi_k\right) + \beta_k h\left(P - \phi_k\right)\right], \tag{3}$$

where $P \in [+1,+1]$ is the prestige field parameter, and β_k is the susceptibility parameter of an individual agent. Small values β_k indicate that an agent is not easily influenced by an external influence, while large values indicate that the person is easily manipulated by an external influence, e.g., "zombie" parameter. Here h is also an odd function.

In our model, the bias of an agent depends on three factors: (i) the social network; (ii) the retention strength of the native language and its "patriotism" parameter; (iii) the prestige factor of the language, influenced by external sources and the "zombie" parameter of an agent.

3. Linear model

Although, our model is built for arbitrary functions f, g and h, in this paper we analyze only the linear case

$$\dot{\phi}_k = \left(1-\phi_k^2\right)\left[\sum_{j=1}^{N} L_{jk}\cdot\left(\phi_j-\phi_k\right)+\gamma_k\cdot\left(\eta_k-\phi_k\right)+\beta_k\cdot\left(P-\phi_k\right)\right]. \tag{4}$$

As we will see, even the simplest linear model has rich behavior. Another advantage of a linear model, is that its stability can be treated analytically.

3.1. Stability analysis

The non-trivial fixed points ϕ_k^* of the model (4) are found as solutions of

$$\sum_{j=1}^{N} L_{jk}\phi_j^* - \left(c_k+\beta_k+\gamma_k\right)\phi_k^* + \gamma_k\eta_k + \beta_k P = 0, \tag{5}$$

where ϕ_j^* are the fixed points of all the other equations for agents and $c_k = \sum_{j=1}^{N} L_{jk}$. Writing $\vec{\phi}^* = \left(\phi_1^*,\ldots,\phi_N^*\right)^T$ the equation (5) can be expressed in the vector form

$$A\vec{\phi}^* = \vec{b}, \tag{6}$$

where

$$b_k = \gamma_k\eta_k + \beta_k P,$$
$$A_{jk} = \delta_{jk}\left(c_k+\beta_k+\gamma_k\right) - L_{jk}, \tag{7}$$

where δ_{jk} is the Kronecker's delta. Now, the fixed points are obtained as

$$\vec{\phi}^* = A^{-1}\vec{b}. \tag{8}$$

To perform the linear stability analysis, we can write the biases as $\phi_k(t) = \phi_k^* + \varepsilon_k(t)$, where ε_k is a small perturbation, and leave only the linear terms in ε_k. This procedure yields

$$\frac{d\varepsilon_k}{dt} \approx \left(1-\left(\phi_k^*\right)^2\right)\left[\sum_{j=1}^{N} L_{jk}\cdot\varepsilon_j - \varepsilon_k\left(c_k+\beta_k+\gamma_k\right)\right], \tag{9}$$

or in the matrix for

$$\frac{d\vec{\varepsilon}}{dt} = -MA\vec{\varepsilon}, \tag{10}$$

where $\vec{\varepsilon} = \left(\varepsilon_1,\ldots,\varepsilon_N\right)^T$ and M is a diagonal matrix

$$diag(M) = 1-\left(\phi_k^*\right)^2. \tag{11}$$

In the case of symmetric coupling $L_{jk} = L_{kj}$, or an undirected network, the matrix is also symmetric and strictly diagonally dominant, since

$$A_{kk} = c_k + \beta_k + \gamma_k, A_{jk} = -L_{jk}, \Rightarrow |A_{kk}| \succ \sum_{j=1}^{N} |A_{jk}|. \quad (12)$$

Assuming that $L_{jk} \in [0,1]$ and $\beta_k \geq 0, \gamma_k \geq 0$, we can say that the matrix A is positive definite, which means that all its eigenvalues are real and positive. The diagonal matrix M is also positive, since by definition $|\phi_k| \leq 1$. Although we cannot say that $-MA$ it is symmetric, it is similar to a symmetric negative-definite matrix. This means that all the eigenvalues of the system's Jacobian are real and negative, which implies global stability of the fixed points $\vec{\phi}^*$.

For the directed network case $L_{jk} \neq L_{kj}$, we cannot guarantee that all the eigenvalues are real and negative, and more complicated dynamics might arise. The special cases are the fixed points $\phi_k^* = \pm 1$. In that case $\dot{\varepsilon}_k = 0$, which indicates the marginal stability of these points.

3.2. Network topologies

It is obvious that our model crucially depends on the topology of the network connections L_{jk}. In general, the elements of the matrix L_{jk} can have arbitrary values, not only 0 or 1, and can describe the connection strength between agents j and k. In this work, we consider only the undirected network cases, meaning that the connection matrix is symmetric. It is, however, obvious that for arbitrary network topologies, whether the matrix L_{jk} is symmetric or not, its diagonal elements should always be zero. As a measure of the entire network behavior, we will use the mean field bias $\langle \phi(t) \rangle$ defined as

$$\langle \phi(t) \rangle = \frac{1}{N} \sum_{j=1}^{N} \phi_j(t), \quad (13)$$

and its standard deviation. Here, we consider a few models that mimic certain real-life scenarios.

3.2.1. Fully connected network

The fully connected network, when all agents are identically connected to all the other agents, is the simplest connection topology. This simplicity is useful for analytical predictions and benchmarks, despite being quite unrealistic. However, a fully connected network can be reasonably accurate to model small communities, when everyone knows each other, or specific corporate networks, when everyone is connected to the same internal communication network. Usually, such networks produce a very coherent state when all the agents are aligned together. In such cases, it can be interesting to influence the mean field of the system by an external field, to see if it is possible to drive the mean field to an opposite polarity.

3.2.2. Small-world network

A small-world network, as introduced by Watts and Strogatz [22], interpolates between regular lattices and random graphs by introducing a small probability of long-range rewiring. In the context of our work, this topology captures the balance between local clustering, representing tightly connected communities, and occasional long-range interactions, such as those enabled by modern communication or migration. The small-world structure is particularly relevant for modeling realistic social systems, where individuals tend to interact more frequently within close groups but still maintain weak ties across the broader population. This heterogeneity can give rise to rich dynamical phenomena, including the formation of linguistic clusters, polarization, or partial synchronization.

4. Results and discussion

Let us now consider a few typical scenarios that we could model using (4). One of the standard scenarios is the language death, when the entire population eventually starts to strongly prefer only one of

the languages. To achieve this scenario, we can construct a simple fully connected network of identical agents, meaning that they have the same native language η_k, and the same susceptibility to the prestige field β_k. Setting the prestige field P to an opposite language, we create a strong influence on the system.

To analyze the final state, we can draw certain thresholds for bias variables that mark danger zones for a language. This means that when the entire population's bias enters this zone, with a strong preference for a specific language, this puts the other language into danger of extinction.

In Figure 1, we have shown a simulation of the dynamics of a mean field $\langle \phi_k \rangle$ of $N = 100$ agents for different values of γ.

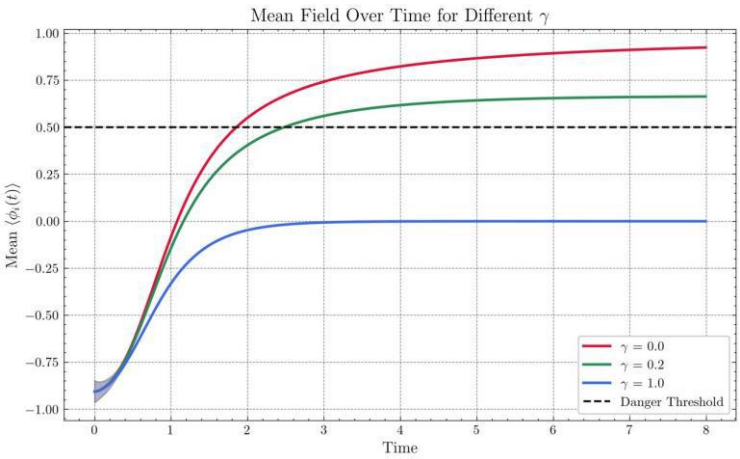

Fig. 1. The dynamics of the mean field $\langle \phi_k \rangle$ over time for different values of the parameter γ.

The simulation is performed for a fully connected network of identical agents, with native language parameters $\eta_k = -1$ and prestige susceptibility $\beta_k = 1.0$. The prestige field is set to $P = +1$, while the initial states of the agents are uniformly distributed within $\phi_k = U(-0.8, -1.0)$.

We can see that initially, the bias of all agents is strongly in favor of the native language. Exposed to an external prestige field P, their bias eventually leans towards the opposed language. We can see that if the patriotism parameter γ_k is small, the original preference for the native language can be overcome, putting it in danger of extinction. However, the strong patriotism ($\gamma_k = 1.0$ in the plot) can result in a bilingual outcome.

In the next scenario, we model a system initially localized at zero (bilingual bias), but eventually split the population into two distinct groups (Figure 2). To obtain such a state, we configured a system with half the population with a native language $A(\eta_k = +1)$, while the other half with a native language $B(\eta_k = -1)$.

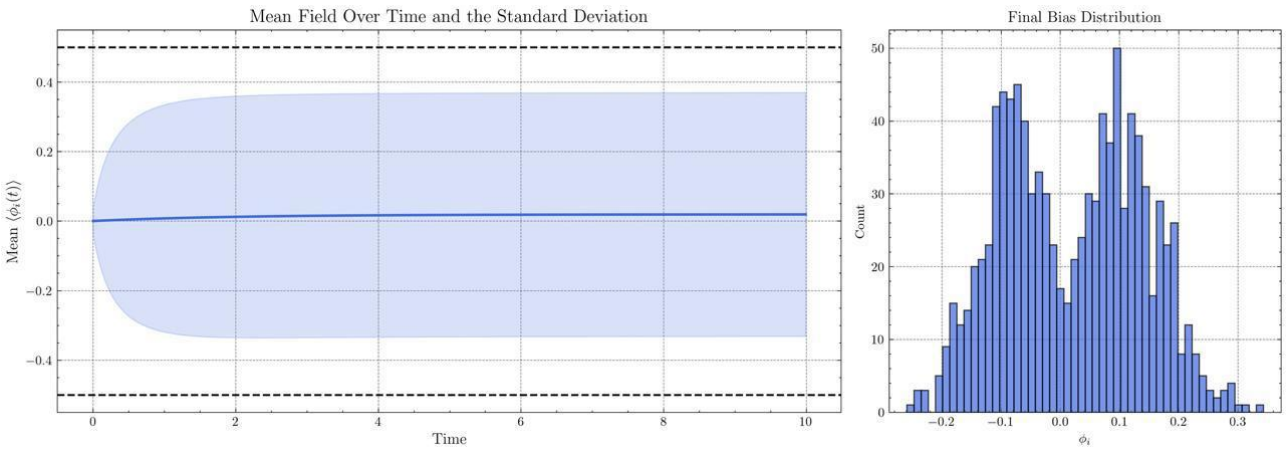

Fig. 2. The simulation of the linear system for $N = 1000$ agents. On the left, we can see the evolution of the mean field (solid line), and although it stays almost unchanged, the standard deviation (shaded area) becomes very large. On the right, there is a final distribution of the biases, with clear two separate peaks.

If the initial state of the system is strongly bilingual, then it generally tends to stay that way. In order to separate the population, we need to tweak the parameters in a specific way. First, in order to diminish the external influence, we set the zero-prestige field $P = 0$, and a very small susceptibility $\beta_k = 0.01$. Next, we set the entire population to be very patriotic, with a high value of $\gamma_k = 3.0$. Finally, the network topology was chosen to be a Watts-Strogatz small-world network.

5. Conclusion

In this work, we introduced a dynamical systems model to describe language bias evolution in populations embedded in social networks. By treating linguistic preference as a continuous variable and incorporating native identity retention, prestige influence, and agents' interactions, we developed a framework capable of capturing a wide range of realistic language dynamics scenarios.

Analytical results from the linearized model provide insight into the stability of fixed points. Numerical simulations on fully connected and small-world networks further illustrate how the interplay between topology and parameter heterogeneity governs the long-term outcomes.

This model not only advances the mathematical treatment of language competition but also exemplifies how methods from applied physics, particularly those related to networked systems and dynamical stability, can be effectively applied to social phenomena. Future work may extend this framework to incorporate dynamic networks, agent mobility, or feedback between bias and network structure, offering even deeper integration with techniques from complex systems and control theory.

References

1 Abrams D.M.,Strogatz S.H. (2003) Modelling the dynamics of language death. *Nature*, 424, 900. https://doi.org/10.1038/424900a

2 Castelló X., Eguíluz V.M., Miguel M.S. (2006) Ordering dynamics with two non-excluding options: Bilingualism in language competition. *New Journal of Physics,* 8, 308. https://doi:10.1088/1367-2630/8/12/308

3 Patriarca M., Leppänen T. (2004) Modeling language competition. *Physica A,* 338, 296. https://doi.org/10.1016/j.physa.2004.02.056

4 Kandler A., Steele J. (2008) Ecological models of language competition. *Biological Theory,* 3, 164. https://doi.org/10.1162/biot.2008.3.2.164

5 Mira J., Paredes A. (2005) Interlinguistic similarity and language death dynamics. *Europhysics Letters*, 69, 6. https://doi.org/10.1209/EPL/I2004-10438-4

6 Fagioli S., Radici E. (2021) Opinion formation systems via deterministic particles approximation. *Kinetic and Related Models, 14, 1.* https://doi:10.3934/krm.2020048

7 Sperlich S., Uriarte J. (2018) The Economics of Minority Language Use: Theory and Empirical Evidence for a Language Game Model. *SSRN Electronic Journal,* 1. https://doi:10.2139/ssrn.3445345

8 Marchetti G., Patriarca M., Heinsalu E. (2020) A bird's-eye view of naming game dynamics: From trait competition to Bayesian inference. *Chaos*, 30, 6, 063119. https://doi.org/10.1063/5.0009569

9 Marchetti G., Patriarca M., Heinsalu E. (2020) A Bayesian Approach to the Naming Game Model. *Front. Phys.*, 8, 00010. https://doi:10.3389/fphy.2020.00010

10 Marchetti G., Patriarca M., Heinsalu E. (2021) The role of bilinguals in the Bayesian naming game. *Physica D*, 428, 133062. https://doi.org/10.1016/j.physd.2021.133062

11 Mudd K., De Vos, C., De Boer, B. (2020) An agent-based model of sign language persistence informed by real-world data. *Language Dynamics and Change*, *10*(2), 158-187. https://doi.org/10.1163/22105832-bja10010

12 Charalambous C., Sanchez D., Toral R. (2023) Language dynamics within adaptive networks: an agent-based approach of nodes and links coevolution. *Frontiers in Complex Systems,* 1. https://doi.org/10.3389/fcpxs.2023.1304448

13 Gao Y, Liu W (2023) Measures to sustain endangered languages: A bilingual competition model with sliding mode control. *PLoS ONE*, 18(6): e0287850. https://doi.org/10.1371/journal.pone.0287850

14 Boissonneault M., Vogt P. (2021) A systematic and interdisciplinary review of mathematical models of language competition. *Humanit Soc Sci Commu,* 8, 21. https://doi.org/10.1057/s41599-020-00683-9

15 Soriano-Panos D., Lotero L., Arenas A., Gómez-Gardeñes J. (2018) Spreading Processes in Multiplex Metapopulations Containing Different Mobility Networks. *Phys. Rev. X*, 8, 031039. https://doi.org/10.1103/PhysRevX.8.031039

16 Zhanabaev Z.Z., Kozhagulov Y.T., Zhexebay D.M. (2016) FPGA implementations of scale-invariant models of neural networks. *Turkish Journal of Electrical Engineering and Computer Sciences,* 24, 6. doi:10.3906/elk-1504-204

17 Ibraimov M., Tynymbayev S., Skabylov A., Kozhagulov Y., Zhexebay D. (2022) Development and design of an FPGA-based encoder for NPN. *Cogent Engineering*, 9, 2008847. https://doi.org/10.1080/23311916.2021.2008847

18 Ussipov N., Akhtanov S., Zhanabaev Z., Turlykozhayeva D., Karibayev B., Namazbayev T., Almen D., Akhmetali A., Tang X. (2024) Automatic modulation classification for MIMO system based on the mutual information feature extraction. *IEEE Access,* 12, 68463 – 68470. doi:10.1109/access.2024.3400448

19 Turlykozhayeva D.A., Akhtanov S.N., Baigaliyeva A.N., Temesheva S.A., Zhexebay D.M., Zaidyn M., Ussipov N.M., Skabylov A.A. (2024) Evaluating routing algorithms across different wireless mesh network topologies using NS-3 simulator. *Eurasian Physical Technical Journal,* 21, 2(48). https://doi.org/10.31489/2024No2/70-82

20 Turlykozhayeva D., Temesheva S., Ussipov N., Bolysbay A., Akhmetali A., Akhtanov S., Tang X. (2024) Experimental performance comparison of proactive routing protocols in wireless mesh network using Raspberry Pi 4. *Telecom*, 5(4), 1008-1020. https://doi.org/10.3390/telecom5040051.

21 Ibraimov M.K., Kozhagulov Y.T., Zhexebay D.M., Sarmanbetov S.A. (2023) Implementation of functional block radio unit based on system-on-chip. *Eurasian Physical Technical Journal*, 20(4), 74–80. https://doi.org/10.31489/2023No4/74-80

22 Watts D., Strogatz S. (1998) Collective dynamics of 'small-world' networks. *Nature.* 393, 440–442. https://doi.org/10.1038/30918

AUTHORS' INFORMATION

Baibolatov, Yernur - PhD, Senior lecturer, al-Farabi Kazakh National University, Faculty of Physics and Technology, Department of Electronics and Astrophysics, Almaty, Kazakhstan; SCOPUS Author ID 35145187200; https://orcid.org/0009-0007-4125-898X, baibolatov.yernur@kaznu.kz

Yerkebulan Nalibayev - PhD, senior lecturer, al-Farabi Kazakh National University, Faculty of Physics and Technology, Department of Electronics and Astrophysics, Almaty, Kazakhstan; SCOPUS Author ID 55785834100, https://orcid.org/0000-0003-2217-4549; ednalibaev@gmail.com

Yeldos Kozhagulov - PhD, senior lecturer, al-Farabi Kazakh National University, Faculty of Physics and Technology, Department of Electronics and Astrophysics, Almaty, Kazakhstan; SCOPUS Author ID 57192878535, https://orcid.org/0000-0001-5714-832X; eldos.kozhagulov@kaznu.kz

EURASIAN PHYSICAL TECHNICAL JOURNAL

2025, Volume 22, No. 3 (53)

https://doi.org/10.31489/2025N3/127-137

Received: 12/04/2024 Revised: 22/04/2025 Accepted: 25/09/2025 Published online: 30/09/2025

Research Article

Open Access under the CC BY -NC-ND 4.0 license

UDC: 536.24; 621.382.3

DESIGN ANALYSIS OF A WIEN-BRIDGE OSCILLATOR: FROM PROTOTYPE TO TEMPERATURE PERFORMANCE

Usibe B.E.[1], Iserom B.F.[1], Iwuji P.C.[1], Aigberemhon M.E.[2], Iwuanyanwu I.O.[3], Ushie A.I.[4], Etta E.E.[4]

[1]Department of Physics, University of Calabar, Nigeria

[2]Department of Electrical and Electronics Engineering, University of Cross River State, Nigeria

[3]Department of Geography & Environmental Science, University of Calabar, Nigeria

[4]Department of Philosophy of Science, University of Calabar, Nigeria

***Corresponding author:** pciwuji@unical.edu.ng

Abstract. *A prototype Wien-bridge oscillator was designed and constructed using a single Op-Amp with a diode-bridge included in the degenerative-feedback path to provide amplitude stabilization of the output oscillations. A circuit simulator, PSpice version 10.0P was also used to simulate the circuit. The simulated results were compared with those measured with an oscilloscope for validation, and it had 90% accuracy. The relationships between the operating temperature and the settling time of the oscillator, as well as the resonant frequency, were investigated and derived. The resonant frequency of the constructed oscillator is adjustable between* $142.86Hz$ *and* $16.67KHz$. *The prototype circuit in this work that measures this range of frequencies was successfully analyzed, and the investigated effects of temperature variations on the output signals are presented in section 3. The results of the temperature response to the output bias voltage, source currents, and total power dissipation of the circuit are also presented. The overall results of the presented parameters show that the operating temperature of the oscillator (within a temperature limit) has an unpredictable effect on its output, which could adversely affect the performance of the oscillator where precision is of great importance.*

Keywords: Wien-Bridge Oscillator, Temperature Stability, Resonant Frequency, Transient Response, Circuit Simulation, PSpice

1. Introduction

An oscillator is an electronic circuit that creates a continuous alternating current waveform output when supplying power via a direct current input. This work that was developed to promote technical skills in circuit design and prototyping and to expand the limits of the development of local content in Nigeria consists of a direct current supply as the only external source of the oscillator. This was achieved by conversion of the alternating current supplied by the power grid (from the electricity supply company) into direct current [1]. One could question the need to convert the direct current back into an alternating current using the oscillator after the initial conversion process. The problem is that the alternating current supplied by the source companies in Nigeria, Europe and the United Kingdom works with a fixed frequency of 50 Hz (60 Hz in some other countries), while many devices such as electronic circuits, laboratory devices, communication systems

and microwave devices require internally generated frequencies in the range from 300 MHz to 1 GHz or higher. It is, therefore, important to have a device that can generate these frequencies.

On the other hand, a Wein-bridge oscillator is an electronic oscillator that generates sinus waves and uses a two-stage RC amplifier circuit, has a high-quality resonance frequency, low distortion and is useful when voting. It is an oscillator type that uses a resistance-capacitor network (RC) instead of the conventional inductor-capacitor swinging circle (LC) to create a sinus-shaped output waveform [2]. The Wein-Bridge, an alternating current version of the popular wheat stone bridge, is a combination of a standard/parallel RC network that is balanced at the frequency $f_o = {}^{1}/_{2\pi RC}$ [3]. Using the Wein-Bridge as positive feedback, the frequency-selective network creates an oscillator that works according to the Vienna Bridge principle with suitable negative feedback (resistance or non-linear network) with suitable negative feedback (resistance or non-linear network); Wein-Bridge-Oscillator [4].

The use of an operational amplifier in a Vienna Bridge Oscillator is one of the available methods for the construction of an oscillator. The project therefore aimed to use discrete components to create a prototype circuit that can measure a large range of frequencies by generating sinus waves, the results of which match the existing literature and also to examine how the results of the output signals can be influenced by different operating temperatures. Therefore, the main focus of this work is to simulate and create a prototype circuit with surgical amp and other discrete components and to examine the effect of temperature changes on the output of the Wein-Bridge Oscillator. The simulated results using PSPICE are then compared with those measured with the oscilloscope for validation.

Many RC oscillators, including the Wein-Bridge Oscillator, control the vibration amplitude by integrating a temperature-sensitive resistance into the negative feedback loop. Thermistors and tungsten lamps are typically used for this purpose, and some studies on the behavior of the Win lamp were carried out in a Wein-bridge oscillator and the effects of the temperature on the output of the oscillator [5]. In addition, [6] presented an RC oscillator that should maintain a stable frequency over a wide temperature range. The authors used a self-calibration oscillator to achieve ±0.4% temperature stability from 55°C to 125°C. This is a great example of how oscillator design can ensure low distortion even with temperature changes. [7] and [8] have also done some work on various aspects of Wein-bridge oscillators, including the use of temperature-sensitive RC networks in the negative feedback loop. They also provided solutions for the design and operation of Vienna bridge oscillators, taking into account temperature effects and component selection.

Temperature changes can influence the outcome of a Wein-Bridge oscillator by changing the resistance of the temperature-sensitive components, which influences the automatic reinforcement and negative feedback mechanisms. These changes can, in turn, influence the frequency and amplitude of the oscillator [2]. For example, the resistance of a resistance changes with temperature and influences the resonance frequency and amplitude of the oscillator. Similarly, the capacity of a capacitor can also vary with the temperature and influence the resonance frequency and amplitude of the oscillator. This is due to a temperature-dependent RC time constant and a fixed input frequency to attribute to the middle frequency of the oscillator. One significant aspect of considering the temperature effects on the output of a Wien-bridge oscillator is that the circuit's temperature-dependent properties can be used for measurement purposes in specific applications like temperature sensors [7, 8].

In summary, the impact of temperature on a Wien-bridge oscillator is mainly associated with the components used in the circuit, such as resistors, capacitors, and incandescent lamps used for automatic gain control. These components react to temperature changes in a way that contributes to maintaining the stability of the oscillator output and the low distortion [8]. However, fluctuating temperatures can affect the components of the oscillator, in particular the resistance and capacitors, which in turn can affect the outcome of the oscillator. In view of the fact that extreme temperature fluctuations could possibly affect the performance of the oscillator, it is recommended to select components based on the temperature range specified by the manufacturer during the design phase of electronic circuits in order to ensure optimal performance and longevity [9]. It is, therefore, important to take into account and examine the effects of the temperature when designing and operating a Wein-bridge oscillator and how these temperature changes change the output of the oscillator, especially if it is to be used in environments with considerable temperature fluctuations.

In order to simulate the behavioral properties of the oscillation circuit, the PSPICE simulator was used to record potential problems in design before the PCB was established. The PSPICE is a circuit simulation program that affects a personal simulation program with an integrated circulation [10]. The use of the PSPICE simulator works for the Wein-ridge oscillator when reaction to each DC input in the operational amplifier by

using models to display the components in the literature. PSPICE was used in [11] to emulate operational amplifiers in which the distortion of audio signals in a circuit was recognized via a wide frequency range. [12] also used an interactive ambient design of PSPICE to examine the parameters and properties of operational amplifier circuits and the various variants of trans-impedance amplifiers with photodiodes. In particular, an analogous PSPICE macro model technique was presented for the parametric dependence of the surgical ampere [13], which uses an easy use of internal equations in both time and frequency domains for non-linear control of voltage and power sources. The macro-model, which made up the temperature dependencies of the main amplifiers' electrical parameters, resulted in the basis of this work. The PSPICE simulator is one of the many commercial software programs available for engineers who can increase the design efficiency, save time and reduce defects and electronic waste. For recent applications of the PSPICE software in electronic circuit design, see [14]. Also, see [15] for details on other simulation and modelling techniques of electronic circuits.

Although the first operational amplifiers used complex vacuum tubes [16], they are versatile in their applications; they can sum, integrate, differentiate, or amplify a signal. These are the reasons they are termed operational amplifiers [17 - 19].

The pin configuration and circuit symbol of a typical eight-pin dual-in-line package (DIP) of an Op-Amp used in this project was adopted from [17]. Terminal 8 is unused, and terminals 1 and 5 are of little importance to this work. The five essential terminals include;

- Inverting input; pin 2: an input signal applied to this terminal appears inverted at the output.
- Non-inverting input; pin 3: signal applied to this terminal appears with the same polarity at the output.
- Other terminals include:
- Output; pin 6
- Positive power supply; pin 7
- Negative power supply; pin 4.

1.1 Op-amp operating mode and oscillator gain

As an active element, the Op-Amp must be powered by a voltage supply ($\pm V_{cc}$). One practical limitation worth noting here is that the magnitude of its output voltage cannot exceed $|V_{cc}|$ [20], [21]. In other words, the output is dependent on and is limited by the magnitude of the power supply voltage. Depending on the differential input voltage (V_d), an Op-Amp can operate in:

Positive saturation mode; $V_o = V_{cc}$ (1)

Linear mode; $-V_{cc} \leq V_o = G.V_d \leq V_{cc}$ (2)

Negative saturation region; $V_o = -V_{cc}$ (3)

In this work, it is assumed that Op-Amps operate in the linear mode. Thus, the output voltage of the oscillator is restricted by equation (1).

Applying the Op-Amp in any electronic circuit design involves configuring the Op-Amp as either an inverting amplifier with voltage gain;

$$G_v = \frac{V_o}{V_i} = -\frac{R_f}{R_i} \quad (4)$$

Or as a non-inverting amplifier with a voltage gain given as [14].

$$G_v = V_o/V_i = 1 + R_f/R_i \quad (5)$$

However, for sustained oscillation, the loop gain of the circuit must satisfy the Barkhausen criterion as shown in Equation 5, where R_f and R_i are resistors in the gain feedback network.

2. Materials and methods

The materials used during the construction of the circuit include electronic components listed in section 3.2, soldering iron, soldering lead, soldering pump, side cutter, picker, digital multi-meter, sandpaper, technician knife, laser jet printer, 12V mini hand-drill machine, electric iron, copper board, PCB foil, ferric chloride, as well as plastic Perspex and Uhu-plast adhesive gum for the casing and finishing. The construction was carried out in stages, which included the power supply, the oscillator circuit, amplitude stability, printed circuit board, and finally, the assembling stage. The block diagram of the Wien-bridge oscillator is shown in Figure 1.

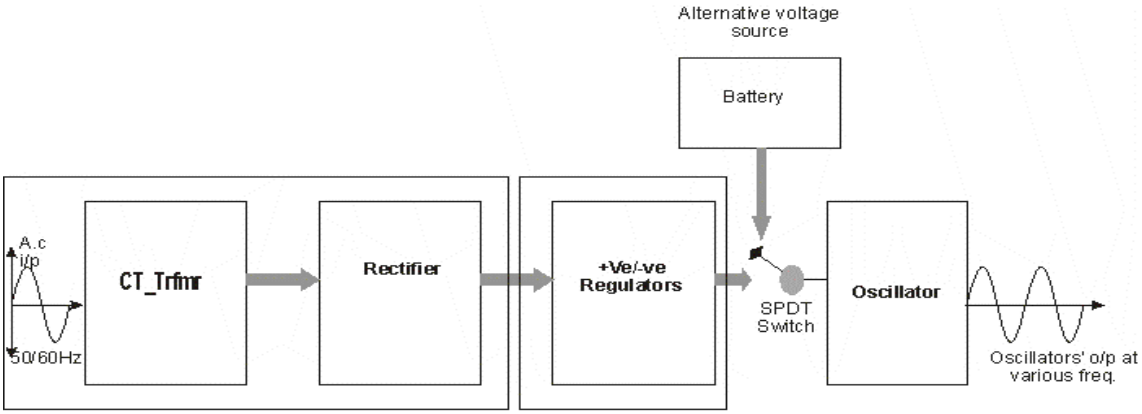

Fig.1. Block Diagram of the constructed Oscillator

2.1 Design methodology

Designing the Wien-bridge oscillator revolves around the operational amplifier (Op-Amp) IC chip [22], [23]. For this work, an Op-Amp (UA741 model) was used. It is an 8-pin DIP IC with a high input voltage range, high input impedance, and excellent temperature stability [17]. To determine the frequency of resonance (f_o), equation (6) was employed [24], [25] with a fixed capacitor $C = 22nF$ and a dual-gang variable resistor $R = 50K\Omega$.

$$\omega_o = {}^{1}/_{RC} = 2\pi f_0 \quad (6)$$

Thus, f_o can be varied for a range of frequencies determined by the variation in R.

Let $f_{o(\min)}$ be the minimum frequency obtainable for the maximum value of R called $R_{(max)}$

$$f_{o(min)} = \frac{1}{2\pi R_{(max)}C} = \frac{1}{2*\pi*50*10^3*22*10^{-9}} = 145Hz \quad (7)$$

The maximum resonance frequency $f_{o(\max)}$ is obtained when R is minimum (i.e. at $R_{(min)}$) thus:

$$f_{o(\max)} = \frac{1}{2\pi R_{(min)}C} = \frac{1}{2*\pi*390*22*10^{-9}} = 18.5KHz \quad (8)$$

Note: $R_{(max)} = 50K\Omega$, $R_{(min)} = 390\Omega$ and $C = 22nF = 22 * 10^{-9}F$

From Equation 5, where the amplitude gain is determined, the oscillator was found to produce fine-tuned oscillation with the chosen value of capacitance, C. To satisfy the Barkhausen criterion and keep the overall gain of the circuit as 1, the Op-Amp must compensate by providing a gain of 3 or greater [3, 26]. In other words, the amplifier gain must initially be set to 3 to start oscillation. This was achieved using equation 9, which is critical to maintaining oscillations and keeping the circuit stable at the desired frequency.

$$R_f = 2R_i \quad (9)$$

For numerical convenience and design purpose, R_i was chosen to be $10K\Omega$, thus, $R_f = 2 * 10K = 20K\Omega$.

Where R_f is the feedback resistor connected from the output to the inverting input of the Op-Amp and R_i is the resistor connected from the inverting input to the ground. The overall circuit is shown in Figure 2.

2.2. Construction steps

The building of the Wien-bridge oscillator involved the assembling of discreet components on a Printed Circuit Board (PCB), which was prepared before this construction using the method carefully adopted from [27 - 30]. A summary of the components used for the construction is given below.

Resistors	Voltage Regulators	Capacitors	Diodes
10KΩ x 2 (fixed)	LM317	22nF x 2 (fixed)	1N4007 x 10
1KΩ x 1 (fixed)	LM137	100µF/35v x 2 (fixed)	**IC**
50KΩ x 2 (dual-gang variable)	**Transformer**	10µF/35v x 2 (fixed)	UA741 Op-amp
220Ω x 3 (fixed)	15V/2A (center-taped)	2500µF/35v x 2 (fixed)	

The layout of the fabricated circuit is shown in Figure 2.

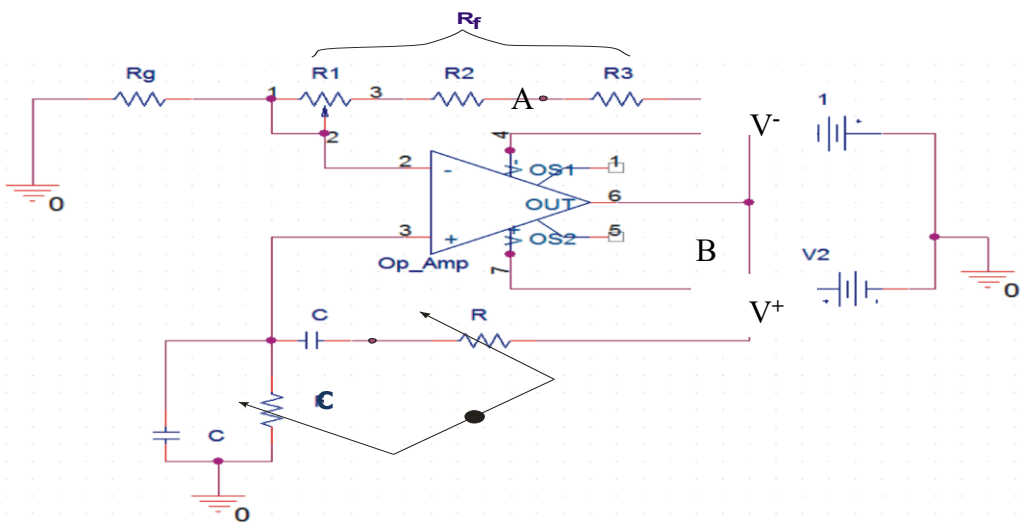

Fig. 2. Prototype Wien-bridge Oscillator using Op-Amp (Designed with PSPICE)

3. Results and discussion

Simulations were carried out on the Wien-bridge circuit using an equivalent model circuit with 90% accuracy. The value of the Resistor, R was fixed at 10KΩ and the Capacitor, C at 22nF in the modeled circuit. Measurements were initially made at room temperature, and subsequently at varying operating temperatures. Meanwhile, software limitations [31-33] placed some restrictions on the number of components that could be simulated in a single circuit diagram. So, the Wien-bridge was simulated without the amplitude stability and the power supply sections of the circuit, and these had no significant effects on the results. The results obtained are presented in the succeeding sections.

3.1. The oscillator output from PSPICE simulation at room temperature

Figure 3 shows the sinusoidal output obtained by simulation with PSPICE at room temperature (27˚C). Here, V_{cc} was set to ±10V, and the results of oscillation between t = 0 second and t = 100 milliseconds were skipped. This was because resultant waveforms within this time interval were found to be unstable and very low in amplitude.

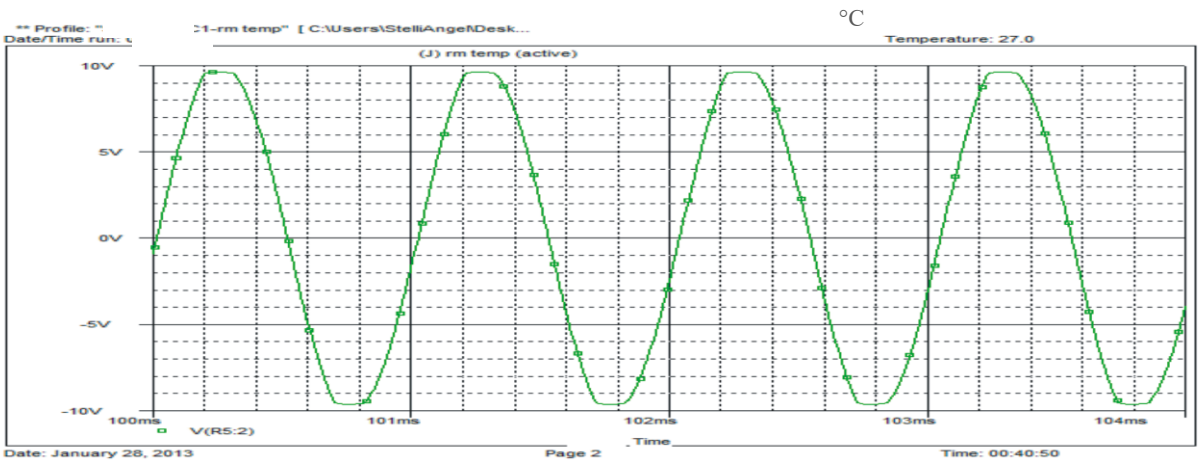

Fig. 3. Oscillator Output Waveform at Room Temperature from PSPICE (V_{cc} = ± 10v)

3.1.1. The oscillator output from oscilloscope

The image shown in Figure 4 is the output waveform obtained from the oscilloscope screen. It should be noted that this output was obtained from the complete oscillator circuit.

Figure 5 shows the prototype of the Wein-bridge oscillator.

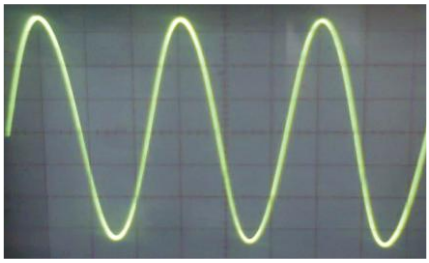

Fig. 4: Output Waveform of Wien-bridge Circuit

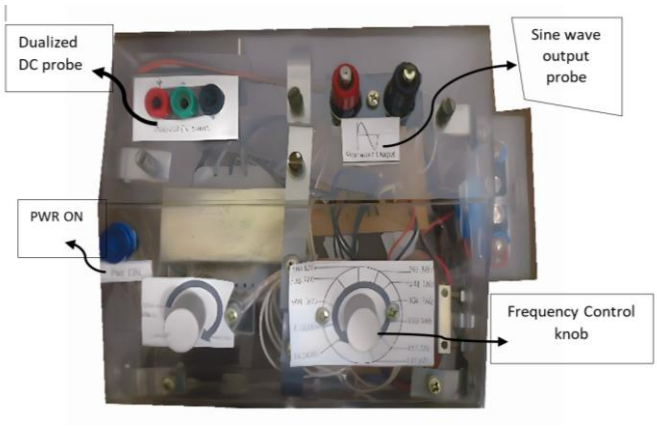

Fig. 5: Prototype Wien-bridge oscillator

3.1.2. Comparison of the PSPICE and oscilloscope outputs

The output waveforms from PSPICE and the measurement from the oscilloscope are shown in Figures 3 and 4, respectively. The output waveform of Figure 3 is seen to have flat amplitudes. This was because the diode bridge was not included in the circuit during the PSPICE simulation due to software limitations. In contrast, Figure 4 (output from the oscilloscope) shows a noise-free amplitude-stable waveform. This was because a diode-bridge was added to the Wien-bridge circuit before this oscilloscope output was obtained. Otherwise, both Figure 3 and Figure 4 are similar and they represent the desired sine wave outputs.

3.1.3 Results of DC bias point

The results shown in Table 1 were obtained by analyzing the circuit's response to the basic DC sources, operating in conjunction with the resistive elements in the circuit at different temperatures. Parameters of interest (i.e., output bias voltage, source currents, and total power dissipation of the circuit) and how they are affected by temperature changes are extracted and summarized in Table 1. This result shows that a change in the operating temperature of the oscillator affects the bias voltage of the oscillator circuit minimally but in an unpredictable manner. This effect may not be considered significant but could have adverse effects where precision is of great importance. The results further show that the source currents and total power dissipated in the circuit remain constant for a wide range of temperatures (-125°C to 200˚C) and increase slightly at temperatures above 200˚C.

Table 1. Resuls of DC Bias Point

Temperature (ºC)	Voltage at output (µV)	Source current (mA)		Total power dissipation (mW)
		V^+	V^-	
-125.0	-736.9	-1.006	-1.006	18.0
-100.0	-735.7	-1.006	-1.006	18.0
-75.0	-735.0	-1.006	-1.006	18.0
-50.0	-734.8	-1.006	-1.006	18.0
-25.0	-735.2	-1.006	-1.006	18.0
0.0	-735.2	-1.006	-1.006	18.0
25.0	-735.1	-1.006	-1.006	18.0
50.0	-734.8	-1.006	-1.006	18.0
75.0	-734.5	-1.006	-1.006	18.0
100.0	-734.0	-1.006	-1.006	18.1
125.0	-733.5	-1.006	-1.006	18.1
150.0	-732.7	-1.006	-1.006	18.1
175.0	-731.5	-1.006	-1.007	18.2
200.0	-730.0	-1.006	-1.007	18.2
225.0	-729.0	-1.007	-1.008	18.3

3.2. Transient Response at Different Temperatures

A transient time analysis was carried out on the circuit with a temperature sweep for a range of temperatures of -125°C to -300°C. The run time was 600ms and data were recorded from t = 100ms. The maximum step size was set to 10µs. A summary of the results obtained is shown in Table 2.

Table 2: Temperature Sweep for transient time, t = 0 to t = 600ms.

T (°C)	t (ms)	T (°C)	t (ms)
-125.0	350.0	100.0	310.0
-100.0	260.0	125.0	320.0
-75.0	300.0	150.0	318.0
-50.0	240.0	175.0	330.0
-25.0	270.0	200.0	340.0
00.0	276.0	225.0	375.0
25.0	280.0	250.0	348.0
50.0	288.0	275.0	376.0
75.0	300.0	300.0	335.0

Table 2 shows that transient time, t (ms) increases for a range of temperatures, T (-50°C to 125°C) and becomes unpredictable beyond this range. Thus, it was deduced that: if 't' is the amplitude stability time (settling time) in milliseconds, and 'T' is the operating temperature of the oscillator in degrees Celsius, then

$$t \propto T \qquad \text{Provided } (-50^{\circ}\text{C} \leq \text{T} \leq 125^{\circ}\text{C}) \tag{10}$$

Then,

$$t = Z\text{T}, \tag{11}$$

where Z is a constant

Equation (11) shows that for a unit time $t = 1ms$ and a unit temperature $T = 1$°C,

$$Z = {}^{t}/_{T} \ (ms/°C) \tag{12}$$

Equation (12) shows how the amplitude stability time is affected by a change in the operating temperature of the oscillator.

3.3. Results of Resonant Frequency from Fourier Analysis

Fast Fourier analysis was performed for the transient results presented in Table 2 using PSPICE, and the corresponding resonant frequencies (f_o) were recorded in Kilohertz (KHz) against the operating temperatures (T°C) as shown in Table 3.

Table 3: Resonant Frequencies at Different Temperatures

T (°C)	f_o (kHz)	T (°C)	f_o (kHz.)
-125.0	0.720	100.0	0.720
-100.0	0.720	125.0	0.718
-75.0	0.720	150.0	0.718
-50.0	0.720	175.0	0.718
-25.0	0.720	200.0	0.718
00.0	0.720	225.0	0.00
25.0	0.720	250.0	0.250
50.0	0.720	275.0	0.275
75.0	0.720	300.0	0.300

Results presented in Table 3 show that the resonant frequency is constant, provided -125°C≤T≤100°C. That is

$$f_o = \beta \qquad \text{Provided } (-125^{\circ}\text{C} \leq \text{T} \leq 100^{\circ}\text{C}), \tag{13}$$

where β is a constant with a unit in kHz.

Comparing Equation (13) and Equation (6), it can be seen that;

$$\beta = \frac{1}{2\pi RC} \tag{14}$$

Since R and C are known variables, β can be found from equation (14) as the resonant frequency.

4. Discussions

The DC bias point is crucial for proper circuit operation, particularly in oscillators like the Wien-Bridge. It determines the amplifier's operating point, affecting linearity and gain. Maintaining a stable bias point ensures consistent performance across varying temperatures. Table 1 illustrates the Wien-Bridge oscillator's thermal stability. The output voltage slightly decreases from -736.9 μV at -125°C to -735.2 μV at 0°C, reflecting minor but significant temperature-induced effects. This change, influenced by the temperature coefficients of circuit components, demonstrates adequate stability within the design's limits. However, a sharper decline to -175 μV at 225°C suggests the need for optimization at extreme temperatures due to parasitic effects. The source currents (V+ and V-) remain stable (~-1.006 mA) across the temperature range, ensuring consistent gain and reliable operation. Power dissipation stays nearly constant at 18 mW, with only a slight increase to 18.3 mW at 225°C, indicating high thermal efficiency. Overall, these results confirm a robust DC bias design suitable for the oscillator's intended range.

Transient response data in Table 2 reveal the relationship between temperature and settling time. Within -50°C to 125°C, settling time exhibits a linear trend, increasing from 240.0 ms to 320.0 ms as temperature rises. Beyond this range, transient behavior becomes unpredictable, highlighting the circuit's limitations at extreme temperatures. This nonlinearity may result from temperature-dependent variations in transconductance and carrier mobility, impacting active components.

The linear trend in settling times applies between -50°C and 125°C. Beyond this range, transient times become unstable, with significant variations at extreme temperatures. For instance, the transient time at -125°C is 350.0 ms, longer than 276.0 ms at 0°C but comparable to 375 ms at 225°C. This unpredictability suggests interactions among multiple variables, possibly due to active component behavior deviating from designed conditions or parasitic effects in extreme temperatures. The data show that outside -50°C to 125°C, the oscillator's response is unreliable. This limitation highlights the need to understand safe operating conditions and manage thermal impacts effectively. Additionally, Table 2 validates equation (10) only within the linear range of -50°C to 125°C. Managing thermal conditions remains crucial for wide-temperature applications.

The resonant frequency of the Wien-Bridge oscillator is governed by its frequency-determining components, as shown in Table 3. Between -125°C and 100°C, the resonant frequency remains stable at 0.720 kHz. However, it decreases slightly to 0.718 kHz at 150°C and significantly drops beyond 225°C. By 250°C, the frequency plummets to 0.250 kHz, suggesting component degradation or parasitic effects leading to operational failure. Extreme temperatures affect resistance, capacitance, and active device parameters like transconductance, preventing oscillations.

In summary, the Wien-Bridge oscillator in the current work demonstrates robust performance and frequency stability within moderate temperature ranges up to 100°C. Beyond this threshold, temperature-induced effects degrade stability, and it becomes unpredictable, necessitating design improvements such as effective heat management strategies, enhanced component selection, or temperature compensation techniques. These adjustments are critical for extending the functionality of the oscillator in high-temperature environments and ensuring its reliability under diverse operating conditions.

5. Conclusion

Since temperature variation impacts electronic components, the frequency of oscillation also shifts slightly due to changes in resistance and capacitance. Therefore, modelling these variations helps predict the performance of an oscillator circuit under thermal stress. While it is easy to design and build a sine-wave oscillator, such as the Wien-bridge oscillator, the results obtained have shown that a change in operating temperature unpredictably affects the bias voltage at the oscillator's output.

Further investigation into the temperature effect has shown that the amplitude stability time (t) and the resonant frequency (f_o) of the oscillator are proportional to the temperature with a given temperature limit.

The DC bias or operating point results in Table 1 showed that a change in temperature affects the "bias voltage at the output" of the oscillator. Though this observed effect was minimal, its effect is unpredictable and could pose a great challenge if not taken into consideration where precision and accuracy are of great concern in circuit design. The result further showed that the source current and the total power dissipated in the circuit remained constant except at very high temperatures above 225°C. Similarly, Table 2 gives a relationship between the operating temperature (T°C) and the stability time t (ms) of the oscillator. For temperatures greater than 125°C, the settling time becomes unpredictable. Therefore, equation (10) holds only when the operating temperature, T (°C) lies in the range -50°C→125°C. As shown in Table 3, a change in the operating temperature of the oscillator also affects the resonant frequency (f_o) significantly for T > 100°C.

Finally, in what follows the current work, implementing effective heat control strategies and utilizing electronic components with minimal temperature sensitivity is recommended to aid in reducing these impacts observed in the output results of the current work.

Conflict of interest statement

The authors declare that they have no conflict of interest in relation to this research, whether financial, personal, authorship or otherwise, that could affect the research and its results presented in this paper.

CRediT Author Statement

Usibe B.E.: Conceptualization, Methodology, Supervision, Writing – review & editing; **Iserom B.F.**: Investigation, Formal analysis, Data curation, Visualization; **Iwuji P.C.:** Validation, Software, Formal analysis, Project administration, Writing – review & editing; **Aigberemhon M.E.**: Investigation, Resources, Writing – original draft; **Iwuanyanwu I.O.**: Data curation, Methodology, Writing – original draft; **Ushie A.I.**: Software, Validation, Resources; **Etta E.E.**: Supervision, Funding acquisition, Writing – review & editing. The final manuscript was read and approved by all authors.

Acknowledgements

We sincerely thank the technologist and technicians in the Electronics Laboratory, Department of Physics, University of Calabar, Nigeria, for their consistent efforts in ensuring the laboratory was always ready for use and for their encouragement throughout the course of this work.

We also extend our appreciation to the other staff members of the department and other colleagues and acquaintances for their valuable support.

References

1 Moore J.H., Davis C.C., Coplan M.A., Greer S.C. (2009) Building Scientific Apparatus: A Practical Guide to Design and Construction., Cambridge: Cambridge University Press. Available at: https://assets.cambridge.org/97805218/78586/frontmatter/9780521878586_frontmatter.pdf

2 Electronic Tutorials. (2023) Wien Bridge Oscillator Tutorial and Theory. Available at: https://www.electronics-tutorials.ws [Accessed: 26-Jan-2023].

3 Sedra A.S., Smith K.C. (2020) Microelectronics Circuits: Introduction to Modern Electronics., Oxford University Press. Available at: https://books-library.website/files/books-library.net-02131527Lf1G9.pdf

4 Razavi B. (2021) Fundamentals of Microelectronics. John Wiley & Sons. Available at: https://scholar.google.com/scholar?q=Razavi+B.+(2021)+Fundamentals+of+Microelectronics

5 Skillen R.P. (1964) Transient Stability of the Wien Bridge Oscillator. MSc Thesis, McMaster University, Hamilton, Ontario.

6 Wang J., Koh L.H., Goh W.L. (2015) A 13.8-MHz RC Oscillator with Self-Calibration for ±0.4% Temperature Stability from -55 to 125°C. *IEEE Int. Conf. Electron Devices Solid-State Circuits (EDSSC)*, 423-428. Available at: A 13.8-MHz RC oscillator with self-calibration for ±0.4% temperature stability from −55 to 125°C | Request PDF

7 Pan S., Makinwa K.A.A. (2022) Wien Bridge–Based Temperature Sensors. *Resistor-Based Temperature Sensors in CMOS Technology, Analog Circuits and Signal Processing*, Springer. https://doi.org/10.1007/978-3-030-95284-6_3

8 Cristiano G., Livanelioglu C., Ji Y., Liao J., Jang T. (2023) RC Oscillators with Non-linear Temperature Compensation. *Biomedical Electronics, Noise Shaping ADCs, and Frequency References*, Springer, Cham. https://doi.org/10.1007/978-3-031-28912-5_14

9 Li Y., Du K., Zhang J. (2022) Design of ring oscillator with temperature compensation effect. *Proceeding of the Int. J. RF Microw. Comput. Aided Eng.*, 32(11). https://doi.org/10.1002/mmce.23374

10 Cadence. (2022) How Does SPICE Simulation Work? Available at: https://resources.pcb.cadence.com/blog/2022-how-does-spice-simulation-work [Accessed: 9-Dec-2022].

11 Shamsir S., Hasan M.S., Hassan O., Paul P.S., Hossain M.R., Islam S.K. (2020) Semiconductor Device Modeling and Simulation for Electronic Circuit Design. *Modeling and Simulation in Engineering - Selected Problems, Intech Open*. https://doi.org/10.5772/intechopen.92037

12 Asadi F. (2023) Op Amp Circuits and 555 Timer IC. *Analog Electronic Circuits Laboratory Manual*, Springer, Cham. https://doi.org/10.1007/978-3-031-25122-1_6

13 Maxim A., Andreu D. (2000) A Unified High Accuracy Behavioral SPICE Macromodel of Operational Amplifiers Featuring the Frequency, Temperature and Power Supply Influences and the Monte Carlo Simulation. *Proceeding of the IEEE Int. Symp. Circuits Syst*., 4, 697–700. https://www.researchgate.net/publication/224066383_

14 Pandey O.N. (2022) PSPICE. *Electronics Engineering*, Springer, https://doi.org/10.1007/978-3-030-78995-4_8

15 Shehova D., Asparuhova K., Lyubomirov S. (2021) Study of Electronic Circuits with Operational Amplifiers Using Interactive Environments for Design and Analysis. *Proceeding of the 12th Nat. Conf. with Int. Participation* (ELECTRONICA), 1–4. https://scispace.com/papers/study-of-electronic-circuits-with-operational-amplifiers-170g62o5

16 Darran D.R. (n.d.) Wien-bridge Oscillator Circuits. SlidePlayer. Available: https://slideplayer.com/slide/10856659/ [Accessed: 2-Oct-2021].

17 Nilsson J.W., Riedel S.A. (2020) Electric Circuits. Pearson Education Limited. Available at: https://mrce.in/ebooks/Circuits%20(Electric)%2011th%20Ed.pdf

18 Thomas R.E., Rosa A.J., Toussaint J.G. (2016) The Analysis and Design of Linear Circuits. John Wiley & Sons, United Kingdom. Available at: https://picture.iczhiku.com/resource/eetop/sYITSqrrPjHwGvMN.pdf

19 Huijsing J. (2017) Operational Amplifiers: Theory and Design. 3rd ed., Springer, Cham. https://doi.org/10.1007/978-3-319-28127-8

20 Ron M. (n.d.) Op-amps for Everyone: Texas Instruments. Available at: http://www.alldatasheets.com .

21 Bugg D.V. (2021) Electronics: Circuits, Amplifiers and Gates. CRC Press. https://doi.org/10.1201/9780367807894

22 Lee B. (2018) Solid-State Electronics: Theory and Methods. Intelliz Press, New York. Available at: https://books.google.com/books/about/Solid_state_Electronics_Theory_and_Metho.html?id=KMv8zgEACAAJ

23 Fiore J.M. (2021) Operational Amplifiers and Linear Integrated Circuits: Theory and Application. Available at: https://eng.libretexts.org [Accessed: 18-Jul-2022].

24 Theraja B.L., Theraja A.K. (2010) A Textbook of Electrical Technology. S. Chand & Co., New Delhi, India. https://dl.ojocv.gov.et/admin_/book/a-textbook-of-electrical-technology-volume-i-basic-electrical-engineering-b-l-theraj

25 Usibe B.E., Adiakpan E.S., Obu J.A. (2013) Design, construction and testing of a vibrometer. *Lat. Am. J. Phys. Educ*., 7(2). https://www.researchgate.net/publication/308355287_Design_construction_and_testing_of_a_vibrometer

26 Irwin J.D., Nelms R.M. (2020) Basic Engineering Circuit Analysis. John Wiley & Sons, United Kingdom. https://www.wiley.com/en-us/Basic+Engineering+Circuit+Analysis%2C+12th+Edition-p-9781119502012

27 PCB Design World. (n.d.) Home Made PCBs – A Step by Step Guide to Build PCBs in Your Home. Available at: https://pcbdesignworld.com [Accessed: 5-Oct-2023].

28 Sassanelli C., Rosa P., Terzi S. (2021) Supporting disassembly processes through simulation tools: A systematic literature review with a focus on printed circuit boards. *J. Manuf. Syst.,* 60, 429–448. https://doi.org/10.1016/j.jmsy.2021.07.009

29 Awasthi A.K., Zeng X. (2019) Recycling printed circuit boards. *Waste Electrical and Electronic Equipment (WEEE)*, Handbook, Woodhead Publ. Series, 311–325. https://primo.aalto.fi/discovery/fulldisplay?docid=cdi_elsevier_sciencedirect_doi_10_1533_9780857096333_3_287&contex

30 Kularatna N. (2019) Electronic Circuit Design: From Concept to Implementation. CRC Press, Boca Raton, FL. https://www.routledge.com/Electronic-Circuit-Design-From-Concept-to-Implementation

31 Pandiev I.M. (2021) Development of PSPICE Macromodel for Monolithic Single-Supply Power Amplifiers. 28th Int. Conf. Mixed Design of Integrated Circuits and System (MIXDES), Lodz, Poland, 178–183. https://doi.org/10.23919/MIXDES52406.2021.9497565

32 Al-Hashimi B. (2019) The Art of Simulation Using PSPICE: Analog and Digital. CRC Press. https://doi.org/10.1201/9780367812188

33 Yang W.Y., Kim J., Park K.W., Baek D., Lim S., Young J., Park S., Lee H.L., Choi W.J., Im T. (2020) Electronic Circuits with MATLAB, PSPICE and Smith Chart. John Wiley & Sons, Hoboken, NJ. https://doi.org/10.1002/978111959896

AUTHORS' INFORMATION

Usibe, Brian Elom – Ph.D.(Eng.), Registered Engineer, Lecturer, Department of Physics, University of Calabar, Calabar, Nigeria; Member: Nigerian Society of Engineers, Institution of Engineering and Technology, UK; Honorary Fellow: Institute of Policy Management Development; Scopus Author ID: 58528585100; https://orcid.org/0000-0003-4388-2480; beusibe@unical.edu.ng.

Iserom, Benjamin F. – Master (Sci.), Researcher, Department of Physics, University of Calabar, Calabar, Nigeria; https://orcid.org/0009-0004-1886-4808; iserombenjamin@gmail.com

Iwuji, Prince Chigozie - Ph.D.(Sci.), Lecturer and Leading Researcher, Department of Physics, University of Calabar, Calabar, Nigeria; Scopus Author ID: 57739427700; https://orcid.org/0000-0001-5715-9336; pciwuji@unical.edu.ng

Aigberemhon, Moses E. – Master (Eng.), Lecture and Researcher, Department of Electrical and Electronics Engineering, University of Cross River State, Calabar, Nigeria; https://orcid.org/0009-0007-3856-1312; moscomag2k2@yahoo.com

Iwuanyanwu, **Iheoma O.** – Ph.D. (Sci.), Lecturer and Leading researcher, Department of Geography and Environmental Science, Faculty of Environmental Sciences, University of Calabar, Calabar, Nigeria. https://orcid.org/0009-0006-1946-435X; omaiwuanyanwu@gmail.com

Ushie, Abel Idagu – Ph.D. (Sci.), Lecturer II, Department of Philosophy, University of Calabar, Calabar; Member of the Philosophical Association of Nigeria, Academic Staff Union of Universities, Nigeria; Scopus ID: 59380460700; https://orcid.org/0000-0002-6524-217X; *abelushie@unical.edu.ng*

Etta, **Emmanuel E.** – Ph.D. (Sci.), Lecturer, Department of Philosophy, University of Calabar, Calabar, Nigeria; https://orcid.org/0000-0001-5713-0373; emmanuelettah@unical.edu.ng

EURASIAN PHYSICAL TECHNICAL JOURNAL

2025, Volume 22, No.3 (53)

https://doi.org/10.31489/2025N3/138-147

Received: 11/04/20254 Revised: 27/05/2025 Accepted: 25/09/2025 Published online: 30/09/2025

Original Research Article

Open Access under the CC BY -NC-ND 4.0 license

UDC: 523.44

SPECTROPHOTOMETRIC STUDIES OF ASTEROIDS II: TAXONOMIC TYPE

Aimanova[1*] G.K., Serebryanskiy[1] A.V., Shcherbina[2,3] M. P., Krugov[1] M.A.

[1] Fesenkov Astrophysical Institute. Almaty, Kazakhstan.

[2] Institute of Astronomy of the Russian Academy of Sciences, Russia;

[3] Sternberg Astronomical Institute, Moscow State University, Russia

*Corresponding author: gauhar@fai.kz

Abstract. *Analysis of spectral observations of a number of Main Belt asteroids, the Apollo family asteroid (NEO) 30825 (1990 TG1), and the rare asteroid 1951 Lick was used to determine their taxonomic types. The observations were carried out in 2023-2024 at the Assy-Turgen Observatory on the AZT-20 telescope equipped with a spectrograph using a volume-phase holographic dispersive element with 360 lines per millimeter in low-resolution mode (R=600). We use the "template" method proposed in (Savelova A.A. et al., 2022) and the visual albedo values. An analysis was carried out for S-type asteroids (107) Arachne and (482) Petrina and the Apollo family asteroid (NEO) 30825 (1990 TG1), which have minerals formed under high-temperature conditions, as well as asteroid (97) Klotho, belonging to the M class, which includes asteroids with an increased metal content. Class A asteroids are characterized by high albedo and a marked increase in reflectance at longer wavelengths. These features indicate the presence of high-temperature olivine or mixtures of olivine with metals, mainly iron and nickel. The presented results show that asteroids (366) Vincentina and (1951) Lick belong to this class. The analysis showed that the normalized reflectance spectrum of (47) Aglaja corresponds to asteroids of spectral class B, the main components of the surface of which are probably anhydrous silicates, hydrated clay minerals, organic polymers, magnetite, and sulfides. According to the authors' results, the normalized reflectance spectrum of asteroid (718) Erida corresponds to the spectral corridor for the T-class template with an albedo ranging from 0.04 to 0.042.*

Keywords: spectrophotometry, asteroids; taxonomic type; reflective spectroscopy;

1. Introduction

Asteroids, as the closest bodies to the Earth, can be considered as possible sources of extraterrestrial natural resources (Board et al., 2010; Lewis, 1996) [1-2], and as relevant technologies are developing, the classification of the asteroids according to certain features of the presence of various minerals for their mining is becoming increasingly in demand). The taxonomic classification of asteroids is a crucial tool in planetology, Earth protection, resource exploration, and understanding the evolution of the Solar System. It is employed in both global space security initiatives and fundamental scientific research, particularly as numerous missions target small celestial bodies. The relevance of asteroid taxonomic classification encompasses scientific, applied, and strategic dimensions. From a scientific perspective, it enhances our comprehension of the Solar System's origin and evolution. In applied contexts, accurate determination of taxonomic type is essential for selecting targets for space missions (e.g., OSIRIS-REx, Hayabusa2, DESTINY+), given that different types exhibit distinct compositions, densities, surface structures, and volatile content.

The observation-based classification of small Solar System bodies has been continuously developed and updated over the last 40 years. While previous iterations of methodology development followed either the availability of large observational campaigns or new instrumental capabilities opening up new dimensions of observation, we see an opportunity to improve, first and foremost, the established methodology.

Taxonomy is the classification of asteroids into categories (classes, taxa) using certain parameters without any a priori rules. The main goal is to identify groups of asteroids that share similar characteristics of their surface composition. Classification into taxa is the first step for further studies in comparative planetology. In the case of asteroids, a precise taxonomic system makes it possible to approach the specific mineralogy for each of the defined classes. Taxonomic systems of asteroids were originally based on broadband colors (Chapman et al. 1971), which made it possible to distinguish two separate types of objects - "S" (rocky) and "C" (carbonaceous). With the increasing amount of information from different types of observations, new taxonomic classes were identified. Historically, the most widely used taxonomies are Tholen (1984) [3] and Barucci et al. (1987) [4], which used data from the Eight-Color Asteroid Survey (Zellner et al. 1985) [5]; Bus & Binzel (2002a) [6], which used SMASSII data, and DeMeo et al. (2009) [7], which is an extension of the previous taxonomy scheme into the near infrared range of the spectrum.

The Tholen classification (Tholen, 1984) [3] is based on photometric studies and offers a method for approximating average reflectance spectra for different classes of asteroids, and also determines their generalized chemical and mineralogical composition. The use of albedo data helped to identify individual classes in this system, which includes 14 spectral classes. In 2002, S. Bus and R. Binzel proposed an expanded version of the classification based on data from the SMASS project, which studied the reflectance spectra of small Main Belt asteroids in the 0.4-1.0 μm wavelength range (Bus and Binzel, 2002) [6]. Unlike the Tholen method, this approach has a much higher spectral resolution and allows for additional details to be considered, which led to the development of a new classification. This system, inheriting the principles of the Tholen classification, expands the number of classes to 24, without taking into account the albedo of asteroids. The Bus-DeMeo classification, proposed later, expanded the methodology for features detected in reflectance spectra up to 2.45 μm wavelength (DeMeo et al., 2009) [7].

Another recent classification of asteroids is based on studies using visible and near-infrared spectrophotometry, as well as on the study of the albedo of these objects (Mahlke et al., 2022) [8]. This classification seems to be quite complete and justified, while maintaining continuity with respect to the two previous ones. The paper presents the transition from one classification to another. Dimensionality reduction and clustering revealed three main complexes: the well-established C- and S-complexes and the restructured M-complex. Spectral classes for all three classifications (Tholen, Bus-DeMeo, Malkhe) [8] are given on the internet resource.

In general, three large complexes can be distinguished: asteroids with low-temperature mineralogy, i.e., not subjected to significant heating during their evolution, the so-called primitive types, or C-complex (C-class); high-temperature asteroids - S-complex asteroids (S-class); and the M(X) complex, which includes asteroids with an increased metal content. The evolution of the X-complex between taxonomies is unclear, since the visual albedo is unknown. In our opinion, the introduction of visual albedo into the analysis of the taxonomic type of asteroid is a justified step, since this characteristic indicates the chemical and mineralogical features of the asteroid's surface.

The obtained results hold both theoretical and practical significance for solar system astrophysics. Determining the taxonomic type of asteroids is crucial for understanding the evolution of the Solar System, the composition of celestial bodies, and assessing potential threats from near-Earth objects. This is particularly relevant for Main Belt asteroids and the Apollo family (Apollo NEOs), especially 30825 (1990 TG1) and the rare asteroid (1951) Lick, which cross Earth's orbit and are of interest for both scientific research and planetary defense. Apollo asteroids constitute the largest subclass of potentially hazardous objects by number, and their taxonomy is vital due to their proximity to Earth and the associated collision risk.

2. Observations

Observations were conducted at the AZT-20 telescope of the Assy-Turgen Observatory using a long-slit spectrograph. A low-resolution mode (R=600) was employed, achieving a dispersion of 4.25 Å per pixel. An EMCCD operating with a gain factor of 5 was used as the detector. The exposure time was 10 seconds, and the spectrograph slit width was 9 arcseconds. To calibrate the wavelengths, the spectra of a standard source -

.

a He-Ne-Ar lamp - were taken. The spectrum of the asteroids was measured using the differential method by comparing the fluxes from the object and a standard star. Stars analogous to the Sun (spectral class G) were used as standards. Analysis is based on reflectivity spectra obtained on 2024-02-22, 2023-11-03, 2023-11-04, and 2023-11-21 at the Assy-Turgen Observatory and comparison with reflective spectra of these asteroids based on INASAN observations performed in 2013–2017 and model spectra obtained from Gaia DR observations. Taxonomic classes were estimated according to the Tholen classification, without taking into account the albedo of the asteroids.

3. Method of analysis

To analyze the reflectance spectra of asteroids, the “template” method proposed in (Savelova et al., 2022) [9] was utilized. The authors propose using templates that are the general spectral boundaries of a taxonomic class, calculated using all normalized reflectance spectra of asteroids of a particular taxonomic class from the SMASSII database (Bus and Binzel, 2020) [10], including visual albedo in the analysis, since this characteristic indicates the chemical and mineralogical features of the surface of asteroids. The template is an area within which the reflectance spectrum of an asteroid belonging to a given taxonomic class is likely to be located.

Template selection was based on asteroid albedos categorized by class, as established in Tholen's seminal work (Tholen, 1984) [3]. Asteroids with numbers up to 2000 from the SMASSII database were selected to compile the database. Based on the SMASS II data, the highest and lowest values of the normalized intensity were determined depending on the wavelength. (The "spectral corridor" of the template). For asteroids of class A, 4 spectra were selected, for class B - 5 spectra, for class C - 74 spectra, for class D - 5 spectra, for class E - 8 spectra, for class F - 7 spectra, for class G - 7 spectra, for class M - 23 spectra, for class P - 11 spectra, for class S - 112 spectra, and for class T - 5 spectra. In this way, data were selected for 11 taxonomic classes, taking into account the albedo. The correspondence between the reflectance spectra of the asteroids considered in this work and the templates was checked at wavelengths in the range of 0.44-0.75 μm.

Table 1-7 presents the designation of the asteroid, date and time of observation, exposure time, and air mass. Data format: 1 - Date and time in YYMMDD, 2 - Universal Time in hhmmss, 3 and 4 - right ascension and declination at the time of observation in the J2000, 5 - distance from the observer to the object (in AU), 6 - distance from the Sun to the object (in AU), 7 - solar elongation (in °), 8 - phase angle of the object (in °), 9 - predicted stellar magnitude, 10 - air mass, 11 - exposure time. Columns 3-9 are given according to the Minor Planet Center at the time of observations. The last row of the table contains information on the EMCCD mode used during observations.

4. Results and discussion

Reflectance spectra analysis for each asteroid was performed. In the figures below, the area of the corresponding template of the taxonomic class under consideration to which the asteroid belongs is highlighted in green, and the reflectance spectra of the asteroid itself, obtained by the authors of this work, are shown in colored lines. *(97) Klotho* is a Main Belt asteroid. Its orbital period is 1592.5213 days, and its rotation period is 35.15 hours. Its geometric albedo is 0.128, its diameter is 100.717 km, and its SMASSII spectral type is class M (Small-Body Database Lookup - NASA) [11]. Data on the observation conditions are given in Table 1, and the normalized reflectance spectrum is shown in Figure 1.)

Table 1. Information on observations of (97) Klotho

Date (y m d)	UT (hms)	R.A. (h m)	Decl. (° ‘)	Delta (AU)	R (AU)	Elong (°)	Ph (°)	$V^{(m)}$	Airmass	Exp Time (s)
1	2	3	4	5	6	7	8	9	10	11
97 Klotho										
2023 11 03	182443	23 33 56.5	-12 48 14	1.437	2.188	127.6	21.0	11.4	2.637	120
2023 11 03	182646	23 33 56.5	-12 48 14	1.437	2.188	127.6	21.0	11.4	2.667	120

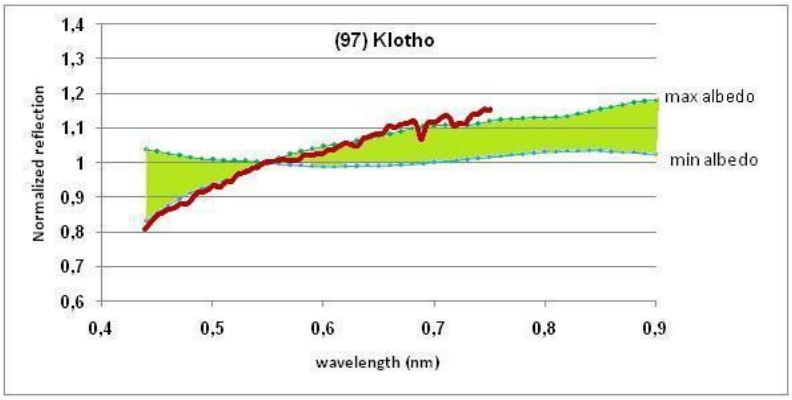

Fig.1. Normalized reflectance spectrum of asteroid (97) Klotho based on FAI observations, green area - spectral corridor corresponding to the taxonomic class M template in the albedo range from 0.072 to 0.203

The results obtained, taking into account the visual albedo, allow classifying (97) Klotho as an M-class asteroid, the third most numerous class of asteroids, the composition of which has been studied rather poorly. It is only known that asteroids of this class have a moderately high albedo (0.1 - 0.2) and contain metals. Some, but not all of them, consist of nickel and iron, with a small admixture of rocks. These asteroids are probably the remains of the metal cores of larger planetesimal asteroids, which were destroyed as a result of mutual collisions in the early stages of the formation of the Solar System. They may be the main source of metal meteorites. *(107) Arachne and (482) Petrina* asteroids, according to our results, can be classified as class S. The information about observations is presented in Table 2, and the normalized reflectance spectra are shown in Figure 2.

Table 2. The information about observations of (107) Arachne and (482) Petrina

Date (y m d)	UT (hms)	R.A. (h m)	Decl. (° ‘)	Delta (AU)	R (AU)	Elong (°)	Ph (°)	$V^{(m)}$	Airmass	Exp Time (s)
1	2	3	4	5	6	7	8	9	10	11
407 Arachne										
2023 11 21	162505	05 54 52.6	+30 29 09	1.627	2.526	149.1	11.6	13.0	1.640	240
2023 11 21	162913	05 54 52.4	+30 29 09	1.627	2.526	149.1	11.6	13.0	1.613	240
482 Petrina										
2023 11 03	144726	21 57 53.3	-08 33 51	2.458	2.921	108.0	18.9	14.2	1.652	120
2023 11 03	144931	21 57 53.3	-08 33 51	2.458	2.921	108.0	18.9	14.2	1.656	

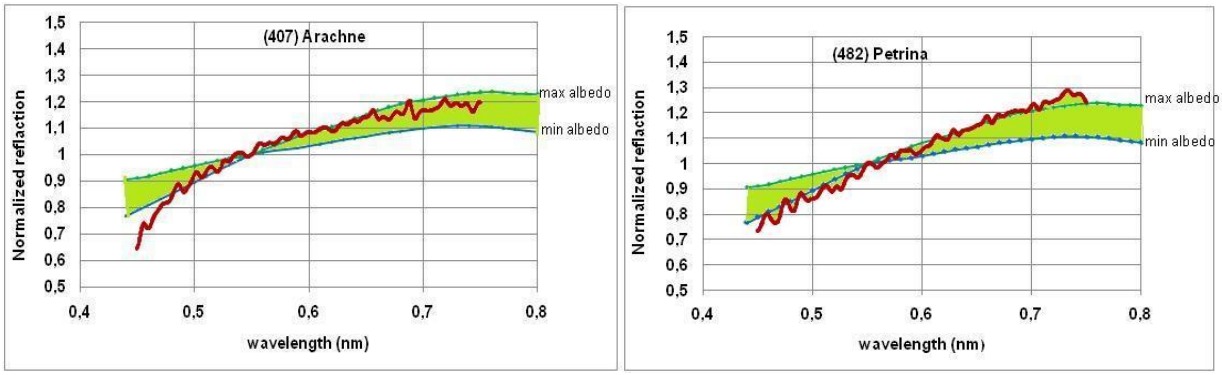

Fig.2. Normalized reflectance spectra of asteroids (407) Arachne and (482) Petrina based on FAI observations, green area - spectral corridor corresponding to the taxonomic class S template in the albedo range from 0.082 to 0.244

(407) Arachne is a Main Belt asteroid. Its orbital period is 1552.6650 days, and the rotation period is 22.627 hours. The geometric albedo is 0.0548, the diameter is 95.07 km, the spectral type according to Tholen is class C, and according to SMASSII its class is Ch (Small-Body Database Lookup NASA) [11].

(482) Petrina is a Main Belt asteroid. Its orbital period is 1897.5417 days, and its rotation period is 11.7922 hours. Its geometric albedo is 0.246, its diameter is 45.751 km (Small-Body Database Lookup - NASA) [11]. Similar to INASAN observations, the reflectance spectrum has an increase in the long-wavelength region and, according to (Shcherbina et al., 2019) [12], corresponds to high-temperature silicate assemblages and belongs to the Tholen class S. The spectral class S indicates a siliceous (rocky) mineralogy. They have a relatively high density. About 17% of asteroids belong to this class, making it the second most common after the carbonaceous C-type.

(718) Erida is a Main Belt asteroid. Its orbital period is 1954.9347 days, and its rotation period is 17.447 hours. Its geometric albedo is 0.042, its diameter is 70.911 km, and its SMASSII spectral type is class X (Small-Body Database Lookup - NASA) [11]. The information about the observations is given in Table 3, and the normalized reflectance spectrum is shown in Figure 3.

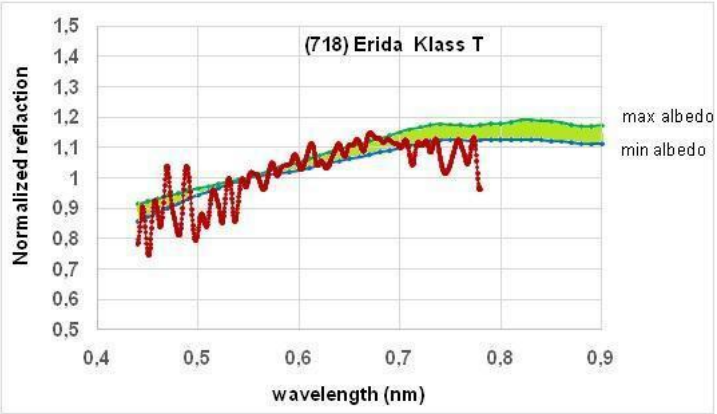

Fig.3. Normalized reflectance spectrum of asteroid (718) Erida based on FAI observations, green area - spectral corridor corresponding to the taxonomic class T template in the albedo range from 0.04 to 0.042

Table 3. The information about observations of (718) Erida

Date (y m d)	UT (hms)	R.A. (h m)	Decl. (° ‘)	Delta (AU)	R (AU)	Elong (°)	Ph (°)	$V^{(m)}$	Airmass	Exp Time (s)
1	2	3	4	5	6	7	8	9	10	11
718 Erida										
2023 11 03	171341	23 24 44.0	-09 30 56	2.837	3.527	127.3	12.9	15.5	1.885	240
2023 11 03	171747	23 24 44.0	-09 30 56	2.837	3.527	127.3	12.9	15.5	1.906	240

According to the Bus-Binzel (SMASS) classification, (718) Erida is an X-type asteroid with featureless spectra and a wide range of albedo, suggesting a variety of surface compositions. X-type spectra typically show low curvature or nearly flat spectral regions. According to Tholen, these are asteroids of unknown composition with dark and moderately red spectra and moderate absorption bands below 0.85 μm.

According to our results, the normalized reflectance spectrum of asteroid (718) Erida falls within a spectral corridor corresponding to the T-type template with an albedo in the range from 0.04 to 0.042. T-type asteroids are rare asteroids of the inner Main Belt. They may be related to P- or D-type asteroids, or possibly highly modified C-type objects. Asteroids of this class were originally thought to be anhydrous, but new spectroscopic data indicate the presence of hydration features. (Hiroi & Hasegawa, 2003) [13] found that asteroid 308 Polyxo has spectral characteristics similar to the Tagish Lake meteorite, which contains signs of hydration. In addition, new spectroscopic observations of T-type asteroids such as (96) Aegle and (570) Kythera also revealed hydration signatures, confirming the presence of water or hydrated minerals on their surfaces (Kwon et al., 2022) [14]. Future study of asteroid (718) Erida will be important to study this rare spectral class and detect signs of hydration.

(47) Aglaja is a Main Belt asteroid with an orbital period of 1787.1149 days, and the rotation period of 13.178 hours. Its geometric albedo is 0.082, the diameter is 168.174 km, the spectral type according to SMASSII is class B, and according to Tholen it is class C. The information regarding the observations is given in Table 4, and the normalized reflectance spectrum is shown in Figure 4.

Table 4. The information about observations of (47) Aglaja

Date (y m d)	UT (hms)	R.A. (h m)	Decl. (° ‘)	Delta (AU)	R (AU)	Elong (°)	Ph (°)	$V^{(m)}$	Airmass	Exp Time (s)
1	2	3	4	5	6	7	8	9	10	11
47 Aglaja										
2023 11 03	151112	22 03 42.0	-13 22 29	2.067	2.549	107.7	21.8	12.9	1.907	120
2023 11 03	151316	22 03 42.0	-13 22 28	2.067	2.549	107.7	21.8	12.9	1.903	120

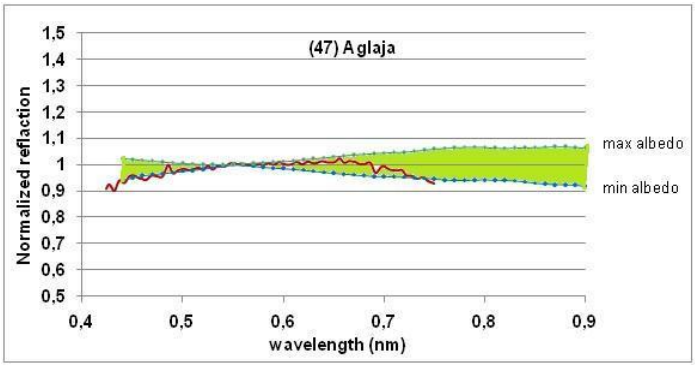

Fig.4. Normalized reflectance spectrum of asteroid (47) Aglaja based on FAI observations, green area - spectral corridor corresponding to the taxonomic class B template in the albedo range from 0.066 to 0.129

Results presented in this study indicate that this asteroid is of class B in accordance with SMASSII classification. Asteroids of this class have a nearly linear spectrum and are distinguished only by spectral tilt. The main constituents of the surface are probably anhydrous silicates, hydrated clay minerals, organic polymers, magnetite, and sulfides. *(366) Vincentina* is a Main Belt asteroid. Its orbital period is 2037.5442 days, and its rotation period is 12.7365 hours. Its geometric albedo is 0.091, its diameter is 86.368 km, and its SMASSII spectral type is of class A (Small-Body Database Lookup - NASA) [11]. The information regarding the observations is given in Table 5, and the normalized reflectance spectrum is shown in Figure 5

Table 5. The information about observations of (366) Vincentina

Date (y m d)	UT (hms)	R.A. (h m)	Decl. (° ‘)	Delta (AU)	R (AU)	Elong (°)	Ph (°)	$V^{(m)}$	Airmass	Exp Time (s)
1	2	3	4	5	6	7	8	9	10	11
366 Vincentina										
2023 11 03	155150	22 33 43.9	-07 04 42	2.411	2.992	116.8	17.2	13.9	1.661	120
2023 11 03	155356	22 33 43.9	-07 04 42	2.411	2.992	116.8	17.2	13.9	1.667	120

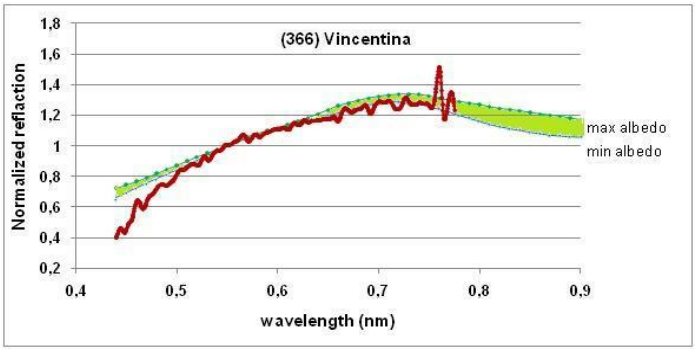

Fig.5. Normalized reflectance spectrum of asteroid (366) Vincentina based on FAI observations, green area - spectral corridor corresponding to the taxonomic class A template in the albedo range from 0.122 to 0.29

The obtained results indicate that this asteroid corresponds to the spectral class A according to the SMASSII classification. This is a rare class of asteroids (since 2005, only 17 asteroids of this class have been discovered), which are characterized by a fairly high albedo (between 0.17 and 0.35) and a reddish color in the visible part of the spectrum, which is determined by a significant increase in the reflectivity of asteroids of this class towards long wavelengths.

Asteroids of this class show strong absorption in the UV region of the spectrum, as well as at wavelengths of 0.7 and 1.05 μm in the IR region, while there are no absorption bands at a wavelength of 2 μm, which indicates the presence of high-temperature olivine or a mixture of olivine with metals, mainly iron and nickel. The discovery of olivine in asteroids is significant, as olivine is typically formed only under high temperatures, ranging from 1100 °C to 1900 °C. This, in turn, suggests that asteroids of this class are fragments of intermediate silicate shells from larger asteroids, which, at an early stage in their history, were in a partially or completely molten state and underwent stratification (differentiation) of magma. Asteroids of class A predominate mainly in the inner part of the Main Asteroid Belt.

(1951) Lick is a rare type of Mars-crossing asteroid with a diameter of approximately 5.6 kilometers. In the SMASS taxonomic classification, Lick's spectral corresponds to a rare A-type asteroid (Small-Body Database Lookup - NASA) [11] with a surface consisting of almost pure olivine (J. de León et al., 2004) [15]. Its orbital period is 598.8541 days. The most recent observation by Michael Lucas in February 2011 yielded a rotation period of 5.317 hours with an amplitude of 0.33 magnitudes (Lucas et al., 2001) [16]

According to three observations made by the infrared astronomical satellite IRAS, the diameter of the asteroid is 5.57 kilometers and its albedo is 0.09 (Tedesco et al., 2004) [17]. The information regarding the observations is given in Table 6, and the normalized reflectance spectrum is shown in Figure 6.

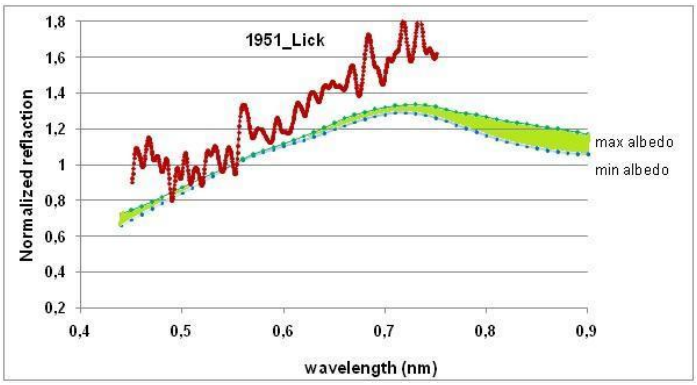

Fig.6. Normalized reflectance spectrum of asteroid (1951) Lick based on FAI observations, green area - spectral corridor corresponding to the taxonomic class A template in the albedo range from 0.122 to 0.29

Table 6.The information about observations of (1951) Lick

Date (y m d)	UT (hms)	R.A. (h m)	Decl. (° ‘)	Delta (AU)	R (AU)	Elong (°)	Ph (°)	$V^{(m)}$	Airmass	Exp Time (s)
1	2	3	4	5	6	7	8	9	10	11
1951 (Lick)										
2024 02 22	142710	04 51 11,4	+02 42 01	0.958	1.471	98.1	41.7	16.5	1.34	60
2024 02 22	142824	04 51 11,5	+02 42 03	0,958	1,471	98,1	41,7	16,5	1.34	60
2024 02 22	142958	04 51 11,5	+02 42 05	0,958	1,471	98,1	41,7	16,5	1.35	120
2024 02 22	143230	04 51 11,6	+02 42 06	0,958	1,471	98,1	41,7	16,5	1.35	240

It was not possible to figure out a taxonomic class taking into account the albedo using the “template” method, using observations presented in this study. Based on the visual albedo (1951) Lick fits into the spectral corridors of classes M (in the albedo range from 0.072 to 0.203) and S (in the albedo range from 0.081 to 0.244), but does not fit into the spectral corridor of templates for these classes at all and has a significant increase in reflectivity in the visible spectrum, similar to class A asteroids

This increase in reflectivity, the “reddening” of the reflectance spectrum, according to [Brunetto, R., de León, J., & Licandro, J. (2007) [18] was caused by space weathering. The researchers compared the spectrum of (1951) Lick with laser ablation experiments on silicate olivine to determine the effect of space

weathering on its surface. The results showed that the asteroid's surface is heavily weathered, and the saturation level of weathering is similar to laboratory experiments, indicating an age of the surface of the order of 10^7-10^8 years Figure 7. Observations obtained in this work confirm the large value of the spectral slope at the level of 1.9 μm^{-1}.

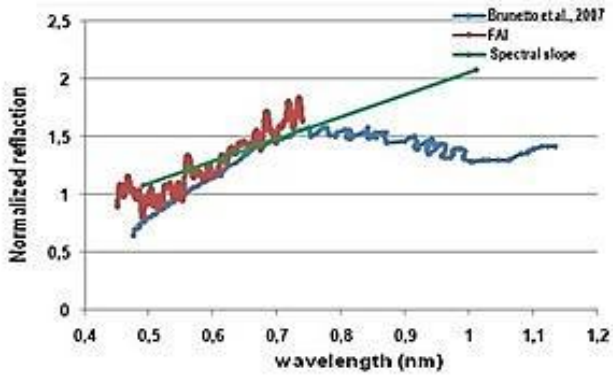

Fig.7. The FAI spectrum of Lick (red) compared with the spectra of San Carlos olivine (blue line) scaled at 0.55 µm, and the line represents the spectral slope

Apollo 30825 (1990 TG1) is an Apollo-family (NEO) Earth-crossing asteroid with an orbital semi-major axis greater than Earth's (> 1 AU), but a perihelion distance less than Earth's aphelion (q < 1.017 AU), and a minimum distance from Earth of 0.06912 AU. The orbital period is 1388 days; the rotation period of the asteroid is 2.62428 hours. The geometric albedo is 0.262, the diameter is 5.6 ± 2.1 km [11]. Its spectral class S [2] indicates that this is a "rocky" asteroid composed mainly of silicates, iron, and magnesium. The information regarding the observations is given in Table 7, and the normalized reflectance spectrum is shown in Figure 8.

Table 7. The information about observations of 30825 (1990 TG1)

Date (y m d)	UT (hms)	R.A. (h m)	Decl. (° ')	Delta (AU)	R (AU)	Elong (°)	Ph (°)	$V^{(m)}$	Airmass	Exp Time (s)
1	2	3	4	5	6	7	8	9	10	11
30825 (1990 TG1)										
2024 02 22	150513	07 50 47,2	-01 57 22	0,494	1,407	140,8	26,4	15,2	1.54	60
2024 02 22	150621	07 50 47,1	-01 57 22	0,494	1,407	140,8	26,4	15,2	1.54	60
2024 02 22	150812	07 50 46,9	-01 57 21	0,494	1,407	140,8	26,4	15,2	1.53	120
2024 02 22	151032	07 50 46,7	-01 57 20	0,494	1,407	140,8	26,4	15,2	0.52	240

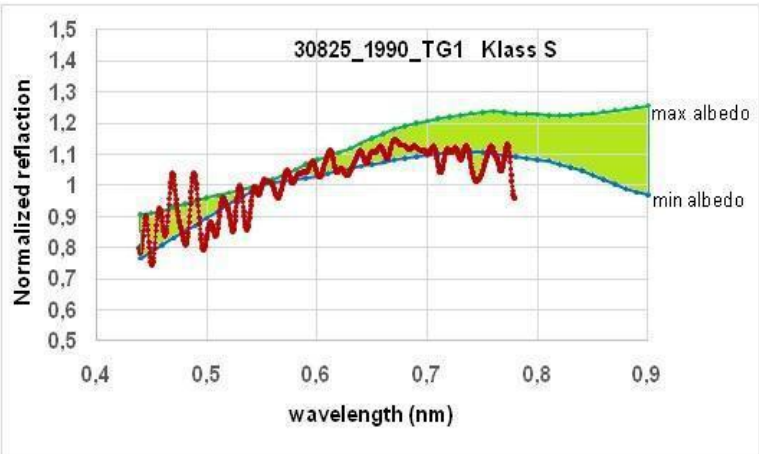

Fig.8. Normalized reflectance spectrum of asteroid 30825 (1990 TG1) based on FAI observations, green area - spectral corridor corresponding to the taxonomic class S template in the albedo range from 0.081 to 0.244

The template analysis shows that the albedo of asteroid 1990 TG1 fits into the spectral class A, which has an albedo range from 0.081 to 0.29. However, its spectrum is more consistent with the S class (Figure 7). The asteroids are of the silicate type, quite bright (albedo from 0.10 to 0.22). They are rich in metals: iron, nickel, and magnesium. Their spectrum is enhanced at long wavelengths, similar to the spectrum of iron meteorites. According to (Benner et al., 2008) [2], asteroid 30825 (1990 TG1) has a circular polarization ratio (SC/OC) of 0.27 ± 0.03, indicating a moderately rough surface on centimeter-to-decimeter scales. The moderate roughness may be the result of micrometeorite bombardment and other processes, such as space weathering, that have altered the asteroid's surface over time. These processes include surface color change (reddening), decreased albedo, and weakening of spectral lines.

5. Conclusion

In this paper, spectral observations of several Main Belt asteroids, the Apollo family asteroid (NEO) 30825 (1990 TG1), and the rare asteroid 1951 Lick were analyzed to determine their taxonomic classes. In general, the results obtained correspond to the generally accepted large taxonomic classes. Asteroids (107) Arachne and (482) Petrina can be classified as S-class asteroids with minerals formed under high-temperature conditions. The Apollo family asteroid (NEO) 30825 (1990 TG1) was also included in this class. (97) Klotho belongs to the M-class asteroids, which include asteroids with an increased metal content. Asteroids with a fairly high albedo and a significant increase in reflectivity in the long-wavelength part of the spectrum of class A include asteroids (366) Vincentina and (1951) Lick, which indicates the presence of high-temperature olivine or a mixture of olivine with metals, mainly iron and nickel, in their composition. The normalized reflectance spectrum of (47) Aglaja corresponds to asteroids of the spectral class B, the main components of the surface of which are possibly anhydrous silicates, hydrated clay minerals, organic polymers, magnetite, and sulfides. According to results presented in this study, the normalized reflectance spectrum of asteroid (718) Erida corresponds to the spectral corridor of the template for class T asteroids, with an albedo range from 0.04 to 0.042. Class T are rare asteroids of the inner part of the Main Belt. According to the SMASSII classification, without taking into account the albedo, asteroid (718) Erida belongs to class X.

It should be noted that the "template" method used is empirical: spectral "corridors" are derived statistically, without direct physical modeling of mineralogy. Its reliability is limited by the relatively low spectral resolution of the data (R ≈ 600) and the uncertainty of albedo measurements, which can reach 20–30%. Thus, the method is suitable for first-order taxonomic classification but cannot provide an unambiguous mineralogical interpretation, especially for rare classes such as A and T. These limitations and the quality of the observational material obtained prevented a definitive conclusion regarding their classification and taxonomic type. Further observations of the corresponding asteroids with higher resolution or in the near-infrared range are necessary.

Conflict of interest statement.
The authors declare that they have no conflict of interest in relation to this research, whether financial, personal, authorship or otherwise, that could affect the research and its results presented in this paper.

CRediTauthor statement
Aimanova G.K. and Serebryanskiy A.V.: Conceptualization, Methodology, Investigation, Data Curation, Writing Original Draft; **Shcherbina M.P.:** Methodology, Resources, Validation; **Krugov M.A**.: Resources.
The final manuscript was read and approved by all authors.

Funding
This research has been funded by Program No. BR20381077 of the Aerospace Committee of the Ministry of Digital Development, Innovations and Aerospace Industry of the Republic of Kazakhstan.

The observations at the "Peak Terskol" Observatory were conducted as part of the state assignment of the Institute of Astronomy of the Russian Academy of Sciences, code FFWN-2024-0010, approved by the Ministry of Education and Science of Russia, using the Large-Scale Research Facility "Zeiss-2000 Telescope" of the Core Shared Research Facilities "Terskol Observatory" of INASAN.

References

1 Board S.S. (2010) Defending Planet Earth: Near-Earth Object Surveys and Hazard Mitigation Strategies. National Academies Press, 152. https://doi.org/10.17226/12842

2 Benner L. A. M., Ostro S. J., Magri C., Nolan M.C., Howell E. S., Giorgini J. D., Jurgens R. F., Margot J.-L., Taylor P.A., Busch M.W., Shepard M.K. (2008) Near-Earth asteroid surface roughness depends on compositional class. *Icarus*, *198(2),* 294-304. https://doi.org/10.1016/j.icarus.2008.06.010

3 Tholen D.J. (1984) Asteroid taxonomy from cluster analysis of photometry. The University of Arizona, 1984. Available at: https://repository.arizona.edu/handle/10150/187738

4 Barucci M.A., Capria M.T., Coradini A., Fulchignoni M. (1987) Classification of asteroids using G-mode analysis. *Icarus, 72(2),* 304-324. https://doi.org/10.1016/0019-1035(87)90177-1

5 Zellner B., Tholen D.J., Tedesco E.F. (1985) The eight-color asteroid survey: Results for 589 minor planets. *Icarus,* 61(3), 355-416. https://doi.org/10.1016/0019-1035(85)90133-2

6 Bus S.J.,Binzel R.P. (2002) Phase II of the Small Main-Belt Asteroid Spectroscopic Survey: The Observations. *Icarus, 158(1),* 106-145. https://doi.org/10.1006/icar.2002.6857

7 DeMeo F.E. Binzel R.P., Slivan S.M., Bus S.J. (2009) An extension of the Bus asteroid taxonomy into the near-infrared. *Icarus,* 202(1), 160-180. https://doi.org/10.1016/j.icarus.2009.02.005

8 Mahlke M., Carry B., Mattei P.A. (2022) Asteroid taxonomy from cluster analysis of spectrometry and albedo. *Astronomy & Astrophysics,* 665. A26. https://doi.org/10.1051/0004-6361/202243587

9 Savelova A.A., Busarev, V.V., Shcherbina, M.P., Barabanov, S.I. (2022) Using "templates" of spectral types of asteroids to enhance the mineralogy of these bodies and detect the signs of sublimation-pyretic and solar activity. *INASAN Science Reports*, 7, 143-148. [in Russian] http://dx.doi.org/10.51194/INASAN.2022.7.2.008

10 Bus S., Binzel R.P. (2020) Small Main-belt Asteroid Spectroscopic Survey, Phase II V1.0. urn:nasa:pds:gbo.ast.smass2.spectra:1.0. NASA Planetary Data System; https://doi.org/10.26033/fj1d-vb37

11 Solar System Dynamics. Electronic resource. 20.08.2024. Available at: Small-Body Database Lookup - NASA

12 Shcherbina M.P., Busarev V.V., Barabanov S.I. (2019) Spectrophotometric Studies of Near-Earth and Main-Belt Asteroids. *Moscow University Physics Bulletin, 74(6).* 675–678. Available at: https://link.springer.com/article/10.3103/S0027134919060237

13 Hiroi T., Hasegawa S. (2003) Probing the surface environment of large T-type asteroids (96) Aegle and (570) Kythera. *Monthly Notices of the Royal Astronomical Society,* 475(3), 3419-3430. https://doi10.1051/0004-6361/202243816

14 Kwon Y.G., Hasegawa S., Fornasier S., Ishiguro M., Agarwal J. (2022) Probing the surface environment of large T-type asteroids. *Astronomy & Astrophysics,* 666, A173. https://doi.org/10.1051/0004-6361/202243816

15 de León J., Duffard R., Licandro J., Lazzaro D. (2004) Mineralogical characterization of A-type asteroid (1951) Lick. *A&A, 422(3),* 59–62. https://doi.org/10.1051/0004-6361:20048009

16 Lucas Michael P., Ryan, Jeffrey G., Fauerbach, Michael, Grasso, Salvatore (2011) Light curve Analysis of Five Taxonomic A-class Asteroids. *The Minor Planet Bulletin, 38(4).* 218–220. Available at: https://mpbulletin.org/issues/MPB_38-4.pdf

17 Tedesco E.F., Noah P.V., Noah M., Price S.D. (2004) IRAS Minor Planet Survey. IRAS-A-FPA-3-RDR-IMPS-V6.0. NASA Planetary Data System, 2004. https://doi.org/10.26033/pf3k-m168

18 Brunetto R., de León, J., Licandro J. (2007) Testing space weathering models on A-type asteroid (1951) Lick. *Astronomy & Astrophysics,* 472(3), 653-656. https://doi.org/10.1051/0004-6361:20077722

AUTHORS' INFORMATION

Serebryanskiy, A.V. — PhD, Head of the observational astrophysics department Fesenkov Astrophysical Institute. Almaty, Kazakhstan; https://orcid.org/0000-0002-4313-7416; serebryanskiy@fai.kz

Aimanova G.K. — Candidate of Physical and Mathematical Sciences in Astrophysics, Chief Researcher, Fesenkov Astrophysical Institute. Almaty, Kazakhstan; https://orcid.org/0000-0002-3869-8913; gauhar@fai.kz

Shcherbina M. P. — Candidate of Physical and Mathematical Sciences in Astrophysics, Researcher. Institute of Astronomy of the Russian Academy of Sciences, Russia; Sternberg Astronomical Institute, Moscow State University, Russia; https://orcid.org/0000-0002-8455-2034; mpshcherbina@inasan.ru

Krugov M.A. — Engineer, Fesenkov Astrophysical Institute. Almaty, Kazakhstan; https://orcid.org/0000-0002-2788-2176; krugov@fai.kz

EURASIAN PHYSICAL TECHNICAL JOURNAL

2025, Volume 22, No.3 (53)

https://doi.org/10.31489/2025N3/148-155

Received: 28/07/2025 Revised: 09/09/2025 Accepted: 25/09/2025 Published online: 30/09/2025

Original Research Article

Open Access under the CC BY -NC-ND 4.0 license

UDC: 537.533.34

A NOVEL DESIGN OF AN ENERGY ANALYZER FOR CHARGED PARTICLES BASED ON A NON-UNIFORM ELECTROSTATIC FIELD

Kambarova Zh.T.[1*], Saulebekov A.O.[1,2], Kassymov S.S.[1]

[1] Karaganda Buketov University, Karaganda, Kazakhstan
[2] Kazakhstan branch of Lomonosov Moscow State University, Astana, Kazakhstan
*Corresponding author email: kambarovazht@gmail.com

Abstract. *A new design for an energy analyzer based on an axial symmetric non-uniform field has been proposed. Using the superposition method of a cylindrical field and second-type axially dodecapole, the electron-optical scheme for the energy analyzer has been developed. Numerical modeling of the electron-optical scheme of the device was performed, and its analytical characteristics were obtained. It is shown that the proposed design combines high resolution and effective luminosity. The results confirm the feasibility of using the developed device for studying charged particle beams in outer space.*

Keywords: energy analyzer, non-uniform field, multipole, modeling, charged particle beams.

1. Introduction

Satellites and spacecraft often encounter systematic effects caused by increased charged particle beams. These adverse radiation effects include single event upsets, anomalous background, increased radiation exposure to astronauts, and premature aging of spacecraft components (computers, detectors, etc.). Current strategies to mitigate these risks include a variety of engineering solutions to address these problems. This also includes a deep understanding of the physical processes that occur during flight and the impact of the environment on the entire spacecraft. Therefore, measurements of the ionizing radiation environment in near-Earth orbit are critical to reducing risks to satellite systems and crewed space missions. Spectrometers began to be used as the main instrument for space research more than half a century ago. The main analytical element of a spectrometer is an analyzer. The operation of all analytical devices is based on the use of the characteristics of charged particle motion in fields created by corresponding electrode systems. One of the main problems and areas of development in energy and mass spectrometry is related to the improvement of electrode systems.

Cylindrical mirror type analyzers are widely used in the study of resonance phenomena in gases, in spectroscopy for chemical analysis, for obtaining spectra of secondary electrons, photoelectrons, and Auger electrons, as well as in space research. The cylindrical mirror analyzer has become a basic element of various electron spectrometers manufactured in countries near and far abroad by leading instrument-making companies [1,2]. Electrostatic analyzers of charged particles, tuned to specific potentials, are classified according to their geometry: cylindrical, spherical, toroidal, and others. They are used to analyze the energy, mass, and angular characteristics of charged particle beams in space plasma. There is a relationship between the geometry of the electrodes that create the electrostatic field and the electron-optical characteristics of the

analyzers. These regularities must be taken into account when designing electrostatic analyzers for space experiments.

Modern developments demonstrate a wide range of solutions. In particular, [3] describes a low-energy particle electron instrument built on board the Arase spacecraft (Exploration of energization and Radiation in Geospace). The instrument is designed to measure the three-dimensional electron distribution function in the energy range from 19 eV to 19 keV. The instrument is based on a toroidal top-hat electrostatic energy analyzer. Results show that the instrument works well in space, and the measurement results are good for scientific purposes. In [4], an analyser for deep space and interplanetary missions was developed, capable of registering the flux, composition, and direction of highly penetrating particles in deep space. It is noted that the analyzer can fill a gap in the observation of galactic cosmic rays in the GeV region and provide accurate information on the spectrum, composition and timing of energetic particle emission from the Sun. The authors note its importance for space weather research and radiation safety. In [5], a brief review of three new instruments designed to measure ion composition in the magnetosphere is presented. The authors emphasize that monitoring of ion composition in geosynchronous orbit is not currently performed, and it is an important component for understanding the dynamic space environment in near-Earth space. The focus is on unique methods of measuring ion composition in detector sections located after the electrostatic analyzer. The work [6] presents the results of numerical calculations of a high-resolution analyzer based on a confined cylindrical field designed to study the fluxes of charged particles in outer space. The combination of high energy resolution with high transmittance, simplicity of construction and compactness make this device very promising for space technologies.

The miniaturized device developed in [7] is an electrostatic analyzer with improved geometry. The use of a spiral shape allows to obtain an instrument that is 2.7 times smaller in volume than a conventional cylindrical electrostatic energy analyzer with a comparable input cross section, while improving the energy resolution by 10%. The size reduction is the first step towards miniaturization of such instruments for in situ measurements of space plasma properties. In [8], an instrument was proposed for space plasma physics research capable of measuring the total ion velocity distribution function as well as the velocity distribution function for individual particles with mass per charge (m/q). The device consists of a deflecting system, a toroidal energy per charge (E/q) analyzer, and a hemispherical condenser that serves either as a second stage E/q analyzer or as a controllable time-of-flight velocity filter. The deflector system maintains a full 360 degrees azimuth tilt angle and allows selection of ions for analysis in the toroidal section. Current research is focused on improving electrostatic analyzers, including methods for resolving space plasma components [9], developing a top-hat design with a time gate for measuring low-energy ions 10[], and analytical approaches to modeling new mass spectrometer designs [11].

In works [12,13], a new approach to solving Laplace's equation for the analytical representation of circular multipoles is proposed. This new class of axial symmetric Laplace fields is based on the superposition of a cylindrical field and components of new harmonic functions - circular multipoles. Although a wide range of potential fields has been developed within the multipole approach, research into the effect of these fields on charged particle beams remains of practical interest. To date, the most attention has been paid to analyzers based on hexapole-cylindrical, octupole-cylindrical, and decapole-cylindrical fields [14-16]. Further research should be aimed at identifying optimal combinations of multipole fields that reduce aberrations and increase the efficiency of the devices.

Given the growing demands of modern technologies for the study of charged particle beams, the further development of the theory of energy analyzer focusing is becoming a relevant problem. Of particular importance is the search for electron-optical systems based on new electrostatic fields or combinations of known mirror configurations. In particular, it is necessary to investigate the possibilities of correcting geometric aberrations in deflector energy analyzers by using axial symmetric multipoles. The aim of this work is to develop and study the design of a charged particle energy analyzer based on the superposition of a cylindrical field and a circular dodecapole in order to improve its electron-optical characteristics and energy resolution.

2 Structure of electrostatic multipoles with rotational symmetry

According to [12], the energy analyzer field can be constructed as a superposition of the base field and a set of circular multipoles coaxial with the base field. In the case of an electrostatic deflection field, this construction looks as follows:

.

$$g(R,\xi) = \ln R + qU_q(R,\xi) + sU_S(R,\xi) + \omega U_{oct}(R,\xi) + dU_{dec}(R,\xi) + ..., \quad (1)$$

where $\ln R$ is basic cylindrical field, $U_q, U_S, U_{oct}, U_{dec}$ are circular multipoles (quadrupole, hexapole, octupole, decapole, etc., $q, s, \omega, d, ...$ are weight coefficients of multipoles, R, ξ are relative radial and axial coordinates.

The first-type axially dodecapole is described by the following harmonic function:

$$u_{dd}(\rho,\xi) = R^6 - 18R^4\xi^2 + 24R^2\xi^4 - \frac{16}{5}\xi^6, \quad (2)$$

The nodal point (2) is located on the symmetry axis ξ. Figure 1 shows the family of equipotential lines of the first-type axially dodecapole. The dotted lines in this and subsequent figures denote zero equipotential lines.

The second-type axially dodecapole is described by the following function:

$$\tilde{u}_{dd}(R,\xi) = R^6 \ln R - 18\left(\ln R + \frac{1}{3}\right)R^4\xi^2 + 24\left(\ln R + \frac{5}{6}\right)R^2\xi^4 - \frac{16}{5}\left(\ln R + \frac{11}{6}\right)\xi^6, \quad (3)$$

Fig. 2 shows the family of equipotentials of the second-type axially dodecapole. A characteristic feature of this function is the presence of a node point located on the symmetry axis (R=ξ=0). The construction of the family of equipotential lines were carried out using Python package. The zero potential lines converging at the nodes separate regions of opposite sign. As can be seen from Figure 2, unlike the the first-type axially dodecapole, the structure of the second-type function is much more complex. First, there is an additional region (shaded in the figure) isolated from the main zero potential line. Second, there is a saddle point *S* with coordinate R_s in the plane of symmetry. For function (3), this coordinate is R_s = 0.84648, and the potential at this point is -0.06131.

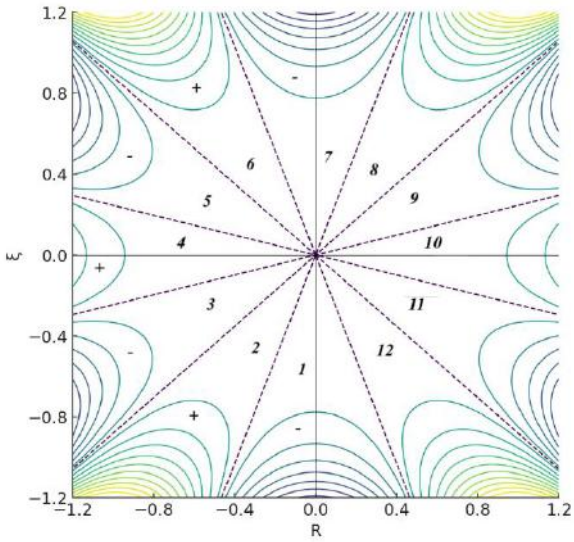

Fig.1. Family of equipotentials of the first-type axially dodecapole

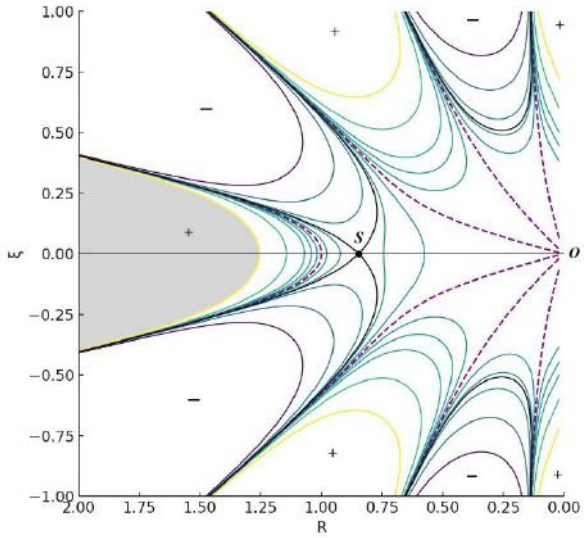

Fig.2. Family of equipotentials of the second-type axially dodecapole

The potential distribution under consideration is defined as a superposition of a logarithmic cylindrical field and the second-type axially dodecapole. It is described by the following expression:

$$U(\rho,\xi) = \omega\,\tilde{u}_{dd}(R,\xi) + \mu \ln R \quad (4)$$

where $\mu \ln R$ is potential of an axial symmetric cylindrical field, μ is coefficient specifying the weight contribution of the cylindrical field, $\tilde{u}_{dd}(\rho,\xi)$ is potential of the second type axially dodecapole, ω is weight contribution of the dodecapole.

Series of Figures 3 and 4 demonstrate families of equipotentials of the total field (4), formed by the superposition of the second type axially dodecapole and a logarithmic cylindrical field. In the series of Fig. 3, the families of equipotentials of the total field are presented for various positive values of the coefficient μ (μ>0) with a constant weighting factor ω=1. At small values of μ, the characteristic sectoral structure of the dodecapole with a pronounced "petal-like" shape of the equipotentials is preserved. The figures illustrate how, with increasing μ, the composite field gradually transforms from the dodecapole case (μ=0, Fig. 2) into a distribution approaching the cylindrical configuration.

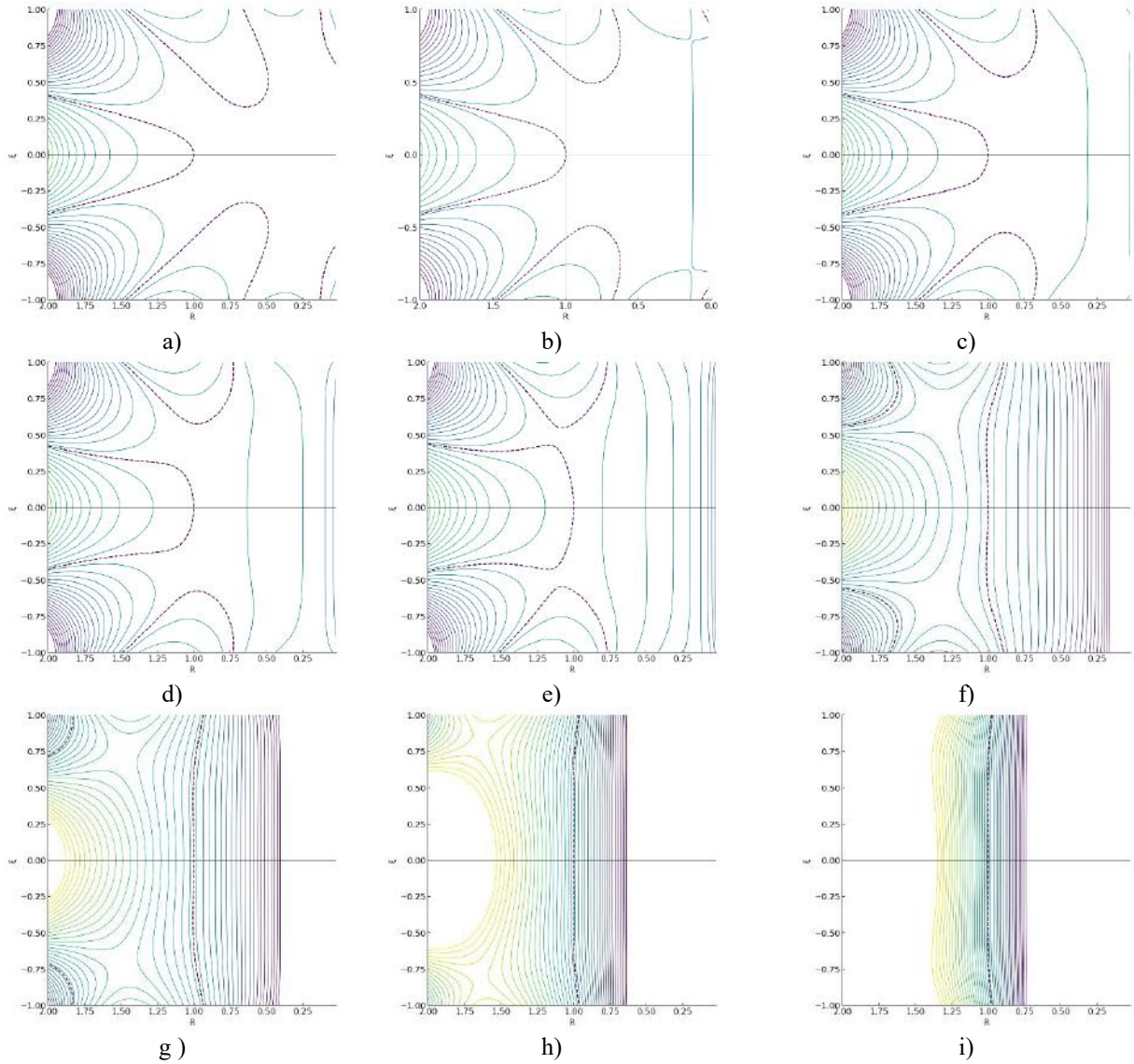

Fig. 3. Family of equipotentials of the total field $U(\rho,\xi)=\omega u_{dd}(R,\xi)+\mu\ln R$ for various values of the coefficient μ (μ>0), a constant weighting factor ω=1:
a) μ=0.1; b) μ=1; c) μ=2, d) μ=5, e) μ= 10; f) μ= 50; g) μ= 100; h) μ= 200; i) μ= 300.

In the series of Figures 4, the families of equipotentials of the total field are presented for various negative values of the coefficient μ (μ<0) with a constant weighting factor of the dodecapole field ω=1. For negative values of μ, the transformation of the composite field occurs in a "mirror-like" manner relative to the case of positive μ. At small absolute values of μ, the characteristic dodecapole structure with a clearly defined "petal-like" form of the equipotentials is preserved. As |μ| increases, the cylindrical component becomes fully dominant, and the configuration of the equipotentials of the composite field approaches that of a cylindrical distribution.

.

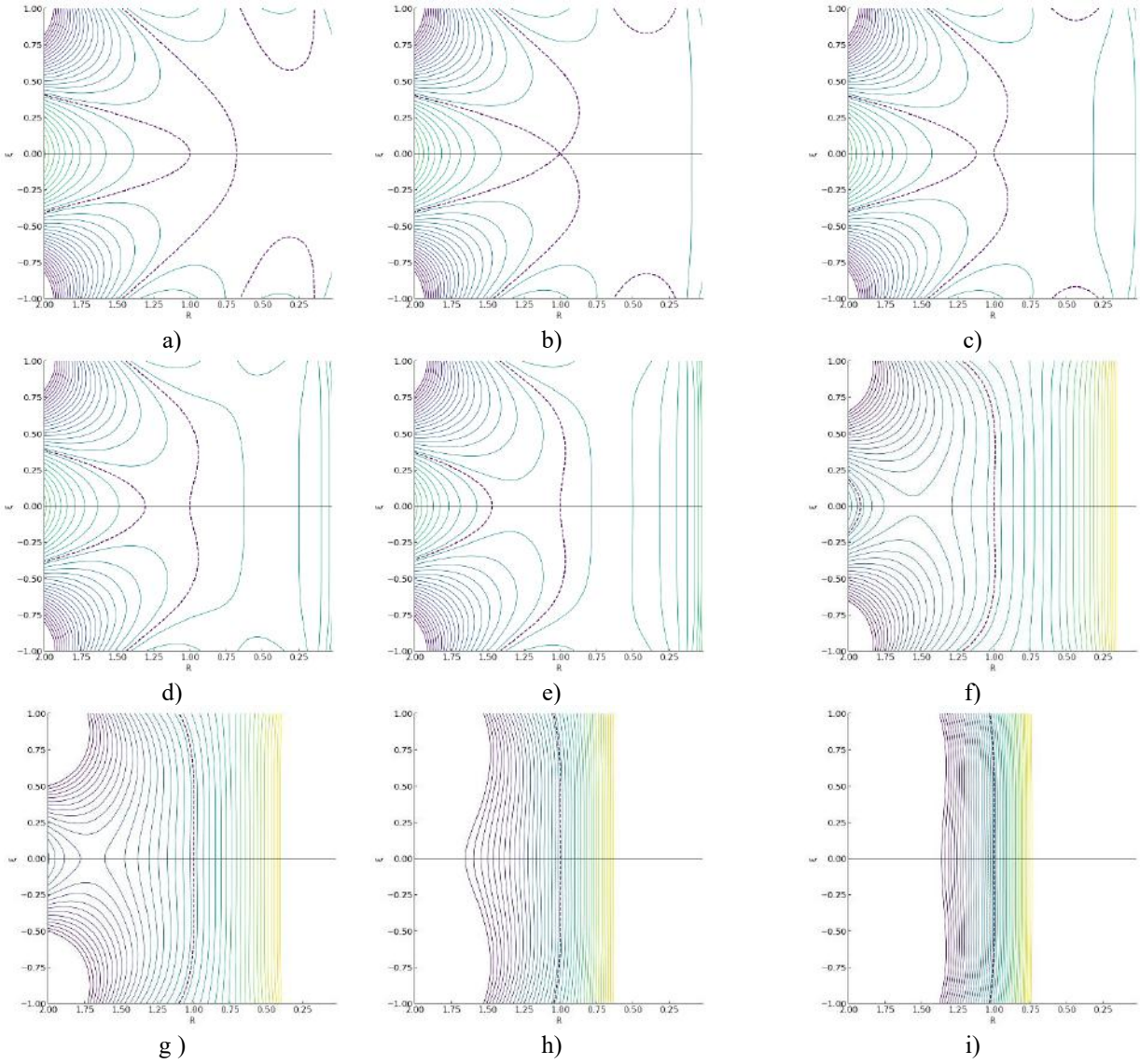

Fig. 4. Family of equipotentials of the composite field $U(\rho,\xi)=\omega u_{dd}(R,\xi)+\mu\ln R$ for various values of the coefficient μ (μ<0), a constant weighting factor ω=1:
a) μ=-0.1; b) μ=-1; c) μ=-2, d) μ=-5, e) μ=- 10; f) μ= -50; g) μ=- 100; h) μ=- 200; i) μ= -300.

Thus, at small values of the coefficient μ, which determines the contribution of the cylindrical field, the total field retains the equipotential structure characteristic of the dodecapole. At larger values of μ, the multipole component is almost completely suppressed, and the structure of the field becomes purely cylindrical. Therefore, the analysis of the families of equipotentials of the total field demonstrates that varying the parameter μ makes it possible to effectively control the spatial structure of the field.

3. Modeling of the energy analyzer scheme based on an non-uniform electrostatic field

The electrostatic multipole-cylindrical field is formed in the space between two axially symmetric coaxial electrodes. The inner electrode has a cylindrical shape with radius r_0 and is kept at zero potential, while a deflecting potential U_0 is applied to the outer curvilinear electrode, whose profile follows one of the equipotential lines of the total field. In this study, the primary interest is focused on determining the shape of the outer deflecting electrode. As a result of analyzing the calculated equipotentials, a configuration was selected that can be implemented in the form of an outer deflection electrode.

The results of numerical modeling of the particle energy analyzer, which was designed using the selected shape of the outer deflection electrode, are presented below. The electron-optical scheme modelled using the numerical program “Focus”, which is designed for modelling corpuscular optics systems [17].

Figure 5 shows the electron-optical scheme of an energy analyzer based on the superposition of a cylindrical field and the second type axially dodecapole. The image is shown in the radial *r* and axial *z* planes. The scheme is symmetrical about the central *z*-axis. The profile of the outer deflecting electrode (2) coincides with the equipotential of the total field at the selected parameters μ = -50, ω= 1.

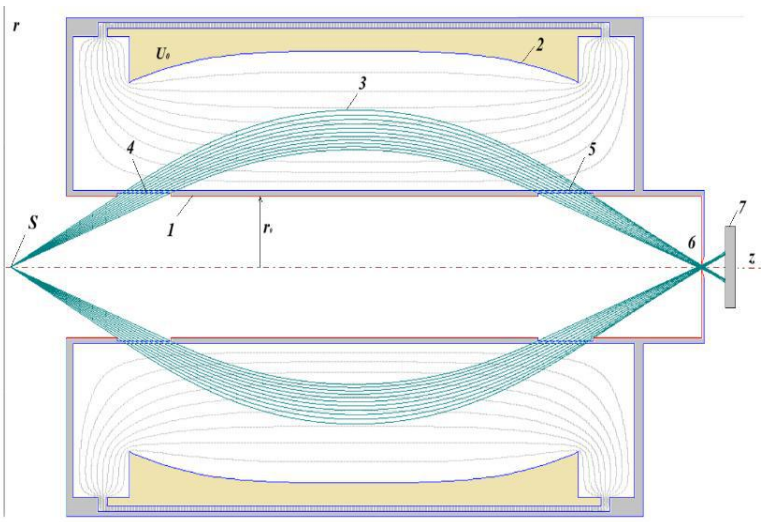

1 – inner cylinder, 2 – outer deflecting electrode, 3 – charged particles, 4 – entrance window, 5 – exit window, 6 – exit diaphragm, 7 – collector, *S* – source of charged particles

Fig. 5. Electron-optical scheme of the dodecapole - cylindrical mirror energy analyzer

From source S, located at a distance Δ=2.5 from the analyzer, charged particle beams (3) are emitted, which enter the field through the entrance window (4) on the inner cylinder (1). Under the action of the electrostatic field, the charged particle beams are deflected towards the axis. Particles that pass through the exit window (5) in the inner cylindrical electrode (1) and the limiting exit diaphragm (6) reach the collector (7), where they are registered. In the “axis-axis” angular focusing regime, the ratio of the analyzer's tuning energy E_0 to the potential V is $E_0/V = 1.175$ eV/V. It follows that by changing the potential V of the outer deflection electrode, the energy spectrum E_0 of charged particles can be scanned sequentially. Table 1 shows the corpuscular-optical parameters of the particle energy analyzer.

Table 1. Corpuscular-optical parameters of the dodecapole - cylindrical energy analyzer

Parameters	Values
Focusing type «axis- axis»	
Focusing order	2
Focusing angle	39°
X focusing coordinate	33.4737
Y focusing coordinate	-0.816079
Reflection parameter, *P*	0.99
Energy dispersion, *D*	6.9

Fig. 6 shows the instrumental function of a mirror energy analyzer, which, as noted above, provides second-order angular “axis-axis” focusing. The exit diaphragm with a radius of R_d=0.027r_0 was placed at the focal point, where r_0 is the radius of the inner cylindrical electrode. The optimal angle range was 39°±5°. The luminosity of the energy analyzer was 11% of 2π, and the relative energy resolution was R=ΔE/E=0.7%.

.

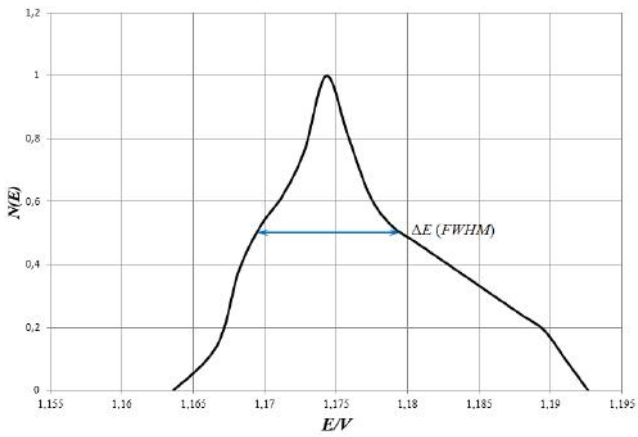

Fig. 6. The instrumental function of a mirror energy analyzer

In comparison with the decapole–cylindrical energy analyzer operating in the "axis–ring" focusing regime [16] (R = 0.74% at a luminosity of 8.2% of 2π), the proposed mirror analyzer ("axis–axis" focusing) provides a comparable energy resolution of R = 0.7% while achieving a higher luminosity of 11% of 2π.

4. Conclusion

The structure of axial symmetric multipole fields, in particular, the axially dodecapole and its superposition with a logarithmic cylindrical field, has been investigated. The equipotential series of the investigated field showed that changing the parameter μ, which determines the contribution of the cylindrical field, allows controlling the spatial structure of total field. The selection of the optimal configuration of equipotentials opens up the possibility of practical implementation of the outer deflecting electrode of the analyzer. Numerical modeling showed that the proposed design provides the second-order "axis-axis" type angular focusing. The corpuscular-optical characteristics of the device indicate the high efficiency of the proposed scheme: the relative energy resolution of about R≈0.7% makes it possible to use the device for high-precision energy analysis, and the luminosity of about 11% of 2π, is a significant indicator for compact mirror systems.

Thus, the use of a superposition of a cylindrical field and a second type axially dodecapole allows the creation of an energy analyzer with strong focusing capability, high energy resolution, and sufficient luminosity. The results obtained confirm the promise of the developed design for studying charged particle beams in outer space.

Conflict of interest statement

The authors declare that they have no conflict of interest in relation to this research, whether financial, personal, authorship or otherwise, that could affect the research and its results presented in this paper.

CRediT author statement

Kambarova Zh.T.: Writing - Review & Editing; Investigation, **Saulebekov A.O.:** Conceptualization, Writing - Original Draft, Methodology; **Kassymov, S.S.–** Methodology, Editing. The final manuscript was read and approved by all authors.

Acknowledgments

The research was supported by Ministry of Science and Higher Education of the Republic of Kazakhstan, Grant number AP26101393

References

1 Zashkvara V.V., Ashimbaeva B.U. (1998) Cylindrical mirror analyzer with adjustable angular focusing. *Journal of Electron Spectroscopy and Rel. Phen.*, 94, 89 – 96.

2 Shugayeva T.Zh., Spivak-Lavrov I.F., Amantaeva A.Sh. (2025) Gridless Cylindrical Mirror Energy Analyzer for Electron Spectroscopy. *J. Phys.: Conf. Ser.,* 2984, 012030, https://doi.org/10.1088/1742-6596/2984/1/012030

3 Kazama Y., Wang B.J., Wang S.Y., et al. (2017) Low-energy particle experiments-electron analyzer (LEPe) onboard the Arase spacecraft. *Earth Planets Space*, 69, 165. https://doi.org/10.1186/s40623-017-0748-6

4 Ambrosi G., et al. (2019) The Penetrating particle ANalyzer (PAN) instrument for measurements of low energy cosmic rays. *IEEE Nuclear Science Symposium and Medical Imaging Conference (NSS/MIC)*, 1-8. https://doi.org/10.1109/NSS/MIC42101.2019.9059946

5 MacDonald E.A., Funsten H.O., Dors E.E., Thomsen M.F., et al. (2009) New Magnetospheric Ion Composition Measurement Techniques. *AIP Conf. Proc.,* 16, 1144 (1): 168–172. https://doi.org/10.1063/1.3169283

6 Ilyin A.M., Ilyina I.A. (2014) High-resolving electrostatic charged particles energy analyzer with fine tuning for space investigations. *Journal of Instrumentation*, 9, P08005. https://doi.org/10.1088/1748-0221/9/08/P08005

7 Amerl P.V., Yau A.W. (2005) Towards the miniaturization of a space-borne electrostatic energy analyzer: the miniature enhanced geometry electrostatic analyzer (MEGEA). I*nternational Conference on MEMS, NANO and Smart Systems,* 139-142. https://doi.org/10.1109/ICMENS.2005.128

8 Keller J.W., Chornay D.J., Hunsaker F.H., et al. (1999) Gated time-of-flight plasma composition analyzer for space physics research. *Rev. Sci. Instrum*., 70 (7), 3167–3172. https://doi.org/10.1063/1.1149881

9 Nicolaou G., Haythornthwaite R.P., Coates A.J. **(2022)** Resolving Space Plasma Species with Electrostatic Analyzers. *Front. Astron. Space Sci.*, ***9***, 861433. https://doi.org/10.3389/fspas.2022.861433

10 Gershman D.J., Avanov L.A., Collinson G., Tucker C.J., Barrie A., Chornay D.J., Paschalidis N.P., Rowland D., Moore T.E. **(**2023**)** A Gated Time-of-Flight Top-Hat Electrostatic Analyzer for Low Energy Ion Measurements. *Rev. Sci. Instrum***.,** **94***,* 083304. https://doi.org/10.1063/5.0139022

11 Spivak-Lavrov I.F. (2016) Analytical methods for the calculation and simulation of new schemes of static and time-of-flight mass spectrometers. *Adv. Imaging Electron Phys.*, 193, 45–128. https://doi.org/10.1016/bs.aiep.2015.10.001

12 Zashkvara V.V., Tyndyk N.N. (1992) Axially symmetric multipole in magnetic analyzers. *Nuclear Instruments & Methods in Physics Research. Section A*, A321, 439-446.

13 Zashkvara V.V., Ashimbaeva B.U., Chokin K.Sh. (2002) Calculation of trajectories in a multipole cylindrical field. *Journal of Electron Spectroscopy and Rel.Phen.*, 122, 195-202.

14 Kambarova Zh.T., Saulebekov A.O., Trubitsyn A.A. (2022) The All-sky Spectrometer of Hot Cosmic Plasma. *The Astronomical Journal*, 164 (2), 47 (1-10). https://doi.org/10.3847/1538-3881/ac7561

15 Kambarova Zh.T., Saulebekov A.O., Kopbalina K.B., Tussupbekova A.K., Saulebekova D.A. (2021) About the possibility of creating an efficient energy analyzer of charged particle beams based on axially-symmetric octupole-cylindrical field. *Eurasian Physical Technical Journal*, 18(2), 96–102. https://doi.org/10.31489/2021No2/96-102

16 Kambarova Zh.T., Trubitsyn A.A., Saulebekov A.O. (2018) Axially symmetric energy analyzer based on the electrostatic decapole-cylindrical field. *Technical Physics*, 63, 11, 1667–1671. https://doi.org/10.1134/S1063784218110142

17 Sautbekova, Z.S., Trubitsyn, A.A. (2022) FOCUS CPM Software for trajectory analysis of real axially symmetric electrostatic mirrors: Methods and Algorithms. *Eurasian Physical Technical Journal*, 19(3), 91–96. https://doi.org/10.31489/2022No3/91-96

AUTHORS' INFORMATION

Saulebekov, A.O. - Doctor of phys.-math. sciences, Professor, Kazakhstan branch of Lomonosov Moscow state University, Astana, Kazakhstan, Scopus Author ID: 6505502480, WoS Researcher ID:ABA-6235-2020, ORCID iD: 0000-0002-6842-9263, saulebekovarman@gmail.com

Kambarova, Zh.T. - PhD, Associate Professor, Physical and Technical Faculty, Karaganda Buketov University, Karaganda, Kazakhstan, ORCID ID: 0000-0001-9808-5484, Scopus ID: 55543382800, WoS Researcher ID: AAV-8669-2020, kambarovazht@gmail.com

Kassymov, S.S. - Candidate of phys.-math. Sciences, Head of the Science Department, Karaganda Buketov University, Karaganda, Kazakhstan, Scopus Author ID: 57191039180, WoS Researcher ID: U-5081-2018, ORCID ID: 0000-0003-4979-9127, skasymov@mail.ru

.

EURASIAN PHYSICAL TECHNICAL JOURNAL

2025, Volume 22, No.3 (53)

https://doi.org/10.31489/2025N3/156-162

Received: 25/03/2025 Revised: 02/06/2025 Accepted: 25/09/2025 Published online: 30/09/2025

Original Research Article

Open Access under the CC BY -NC-ND 4.0 license

UDC 530.1; 519.6; 517.938; 004.42

NUMERICAL ANALYSIS AND CHAOS CONTROL: A STUDY OF LORENTZ SYSTEMS WITH VISUAL BASIC FOR APPLICATION IMPLEMENTATION

Shugayeva T.*, Amantaeva A., Spivak-Lavrov I.

K. Zhubanov Aktobe Regional University, Aktobe, Kazakhstan

*Corresponding author: tlektes.tleubaeva@gmail.com

Abstract. *The study focuses on the numerical analysis and chaos control of Lorenz systems, leveraging Visual Basic for Application in Microsoft Excel for modeling and visualization. Chaotic systems, including the Lorenz attractor, represent a fundamental concept in nonlinear dynamics and chaos theory, characterized by sensitivity to initial conditions, nonlinearity, and fractal dimensionality. These properties make such systems valuable for analyzing complex processes in physics, biology, engineering, and economics. The research extends traditional exploration of the Lorenz attractor by introducing numerical methods such as the four-point Adams method with adaptive step selection. Classical parameter sets and non-classical modifications are examined. Additionally, a modified Lorenz system incorporating a supplementary term is analyzed, demonstrating distinct dynamic behaviors and trajectories. This work highlights the applicability of the developed Visual Basic for Application-based tools for solving nonlinear differential equations and visualizing complex attractors. The integration of Adams and Krylov methods enhances computational efficiency and precision. The outcomes align with previous studies and suggest that the software can address a wide range of applied mathematical and engineering challenges, including chaos management in dynamic systems. The findings underline the potential of the Lorenz attractor as a testbed for chaos control methods and numerical analysis techniques, with broader implications for scientific and practical applications across various disciplines.*

Keywords: Lorenz attractor, chaos theory, nonlinear dynamics, numerical analysis, Visual Basic for Application, Adams method, Krylov method, chaos control, dynamic systems.

1. Introduction

Chaos theory has become an important branch of modern science, bridging mathematics, physics, climatology and other disciplines. One of the key concepts is the Lorentz strange attractor, first described by Edward Lorentz in 1963. His work [1] became the basis for the study of dynamical systems where deterministic equations lead to complex and seemingly random behavior. This theory is of great importance, from understanding weather changes, to creating complex models in engineering and economics [2]. A strange Lorenz attractor is a mathematical set characterized by fractional dimensionality, aperiodicity, and sensitivity to initial conditions [3]. Studies have shown that the systems described by these equations are predictable in the short term and chaotic over large time intervals. This became the basis for new methods of numerical modeling, including the use of modern tools such as Visual Basic for Application (VBA) in Microsoft Excel [4]. In modern science, the use of the term “chaos” is associated with the need to describe systems that are characterized by outwardly completely random behavior and at the same time have a hidden order. The extremely urgent scientific problem of chaos management has not been solved yet. The study of

various methods and laws of suppression of irregular oscillations in nonlinear systems with chaotic dynamics can be mentioned as the most important among the many existing aspects of its solution [5, 6]. The problem of controlling nonlinear objects and processes with chaotic dynamics is of great applied importance. This paper extends the traditional overview of the Lorentz attractor through numerical analysis, application of VBA for modeling, and discussion of possible approaches to chaos control.

2. Chaos Theory and Nonlinear Dynamics

Chaos theory studies deterministic dynamical systems whose behavior is sensitive to initial conditions, resulting in phenomena that appear random despite the strict determinism of the system. Key properties of chaos include:

– Sensitivity to initial conditions: even minimal changes in the starting data can significantly alter the evolution of the system [1].

– Nonlinearity: in chaotic systems there is a nonlinear dependence between variables, which leads to complex interactions [7].

– Fractional dimensionality: chaotic attractors tend to have a fractal structure [8].

These properties make chaos theory a fundamental tool for analyzing complex systems in various fields such as physics, biology, economics and engineering. Nonlinear dynamics, being the foundation of chaos theory, focuses on the study of the behavior of systems described by nonlinear differential equations, including phenomena such as bifurcations, aperiodic oscillations and fractal structures. Scientific developments in this field have contributed to the understanding of chaos mechanisms and the development of methods for its suppression in engineering and applied problems.

3. Lorenz Model

In 1963, a paper was published in the journal [1] that set the foundations of chaos theory. In this paper, a nonlinear autonomous system of ordinary differential equations of the first order (dynamical system) describing the motion of air flows in a flat fluid layer of constant thickness was first obtained from the system of Navier Stokes equations by decomposing the flow velocity and temperature into Fourier series with subsequent truncation to the first and second harmonics:

$$\begin{aligned} \dot{x} &= s(y - x), \\ \dot{y} &= rx - y - xz, \\ \dot{z} &= xy - bz, \end{aligned} \tag{1}$$

Where s, r and b – are some positive numbers, the parameters of the system.

Usually, studies of the Lorentz system are carried out at s =10, r =28 and b = 8/3 (classical values of the parameters). In general, chaos theory is a section of mathematics that studies the behavior of deterministic dynamical systems, where the solutions have a rather complex structure, so it seems that they behave randomly in time [9]. The dynamical system of differential equations (1) can also arise in the description of other processes [10-11]. For any solution of the Lorentz system, there exists a moment of time when the corresponding phase trajectory is immersed in a sphere of fixed radius. Therefore, there exists a limit set - Lorentz attractors - to which all trajectories of the dynamical system are attracted at $t \to \infty$ [12]. Thus, an attractor determines the behavior of solutions to the system of equations (1) over large time intervals. Due to the lack of exact methods for solving nonlinear dynamical systems of differential equations of general form, numerical methods such as, for example, the improved Euler scheme or the Runge-Kutta method are usually used to analyze the attractor structure.

4. Modeling the Dynamics of the Lorentz System in VBA Microsoft Excel

In our study, numerical integration of the differential equations describing the Lorenz attractor was performed using a program implementing the four-point Adams method with automatic step selection. The results of numerical integration are presented in Figs. 1-3. Figures 1-3 show the projections of the trajectories describing the strange Lorentz attractor on the yx, zx, yz planes, respectively.

.

Figures 1-3 demonstrate graphs obtained as a result of numerical integration of the equations describing the Lorentz attractor with classical parameters. Figures 1–3 demonstrate phase trajectories of the classical Lorenz system with parameters s=10, r=28, b=8/3. All projections clearly show the characteristic two-petal structure of the attractor, reflecting the chaotic behavior of the system. The trajectories demonstrate strong sensitivity to the initial conditions: with a slight change in the initial coordinates, significantly different paths are formed in the phase space. This confirms the presence of a strange attractor and a complex topology of the phase region.

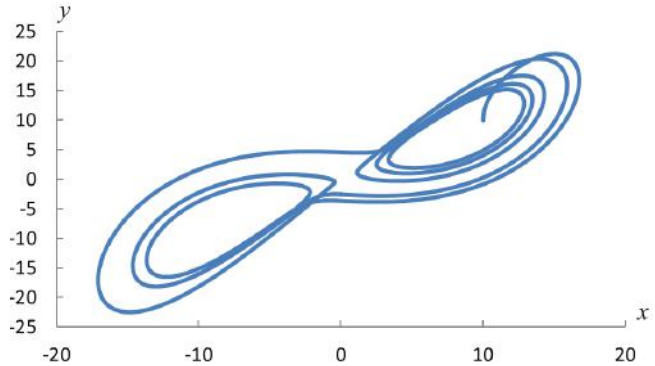

Fig. 1. Graph of the projection of the Lorentz attractor trajectories on the *yx* plane.

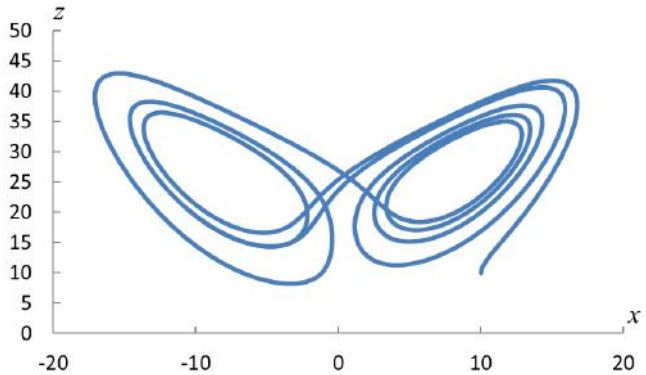

Fig. 2. Graph of the projection of the Lorentz attractor trajectories on the *zx* plane.

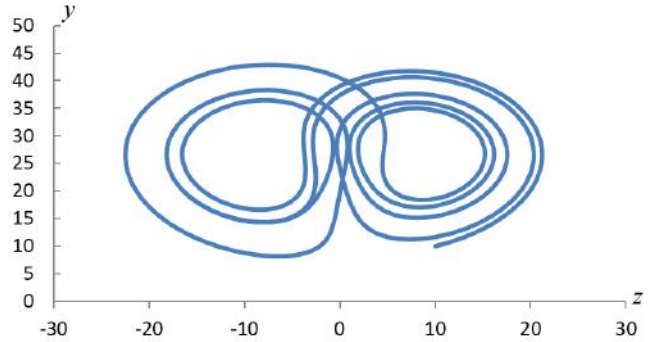

Fig. 3. Graph of the projection of the Lorentz attractor trajectories on the *yz* plane.

Figures 4–6 are phase projections of the trajectories of the Lorenz dynamic system with parameters s=15, r=35, b=10/3 which differ from the classical values and demonstrate an increased intensity of chaotic modes. The numerical experiment is based on the Adams method with automatic step selection, which ensures adequate integration accuracy while maintaining computational stability even under conditions of pronounced sensitivity to the initial conditions. Figure 4 (projection onto the yx plane) demonstrates a more pronounced stratification of the phase trajectories compared to the classical configuration. The attractor structure retains its characteristic two-petal shape, but asymmetry and an increase in the oscillation amplitude are observed. This indicates a shift towards more pronounced nonlinear effects, accompanied by an increase in the fractal dimension and an increase in the effect of sensitivity to the initial state of the system.

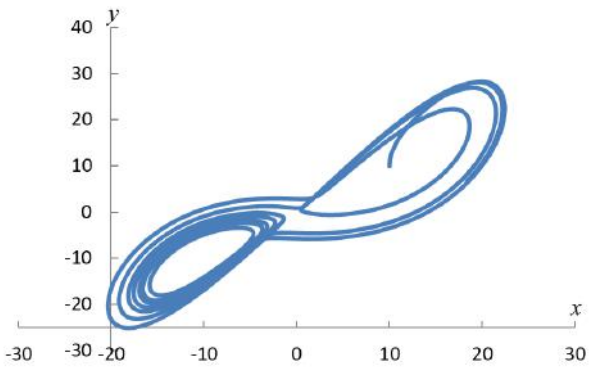

Fig. 4. Graph of the projection of the Lorentz attractor trajectories on the *yx* plane when s =15, r =35 and b =10/3.

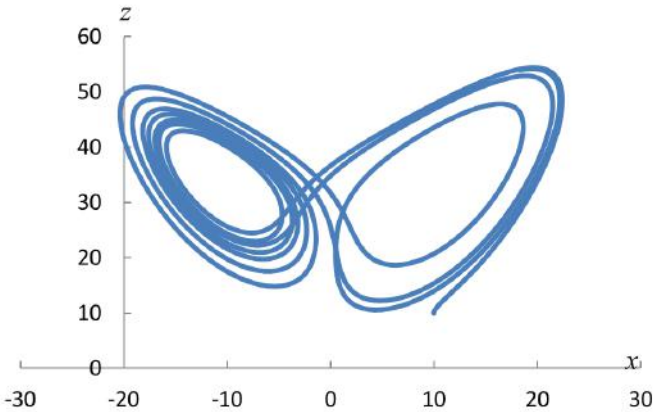

Fig. 5. Graph of the projection of the Lorentz attractor trajectories on the *zx* plane when s =15, r =35 and b =10/3.

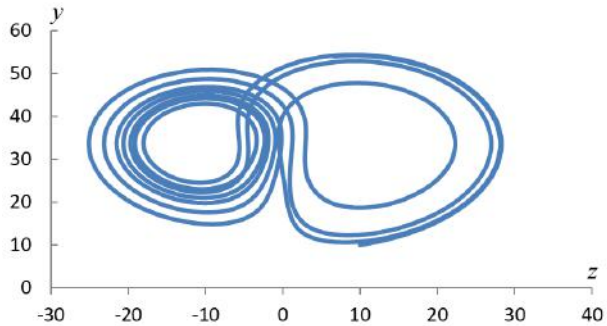

Fig. 6. Graph of the projection of the Lorentz attractor trajectories on the *yz* plane when s =15, r =35 and b =10/3

Figure 5 (projection onto the zx plane) clearly illustrates the spatial decomposition of the phase volume with the dominance of axially oriented spiral formations. It should be noted that there is a shortcoming in the notation: the z and x axes are not labeled, which requires correction for an accurate interpretation of the phase dynamics. Nevertheless, a qualitative analysis of the shape of the trajectories allows us to conclude that there is a pronounced spatial correlation between the variables for the specified set of parameters.

Figure 6 (projection onto the yz plane) emphasizes the presence of dynamic anisotropy in the system: the density of trajectories varies depending on the coordinates, which indicates the existence of quasi-stable regions of the phase space. The shape of the attractor acquires a more elongated structure, characteristic of systems with enhanced nonlinearity and a variable energy level.

Comparison with previously published studies, particularly [13] and [14], demonstrates that even when utilizing a non-standard computational environment-namely, VBA within Microsoft Excel-and operating under non-classical parameter regimes, our numerical approach maintains a high degree of agreement with established results. This consistency not only affirms the correctness of our implementation but also

.

highlights the robustness and applicability of the method for investigating complex nonlinear dynamical systems.

While prior studies [13, 14] introduced modified forms of the Lorenz system and analyzed their chaotic behavior, fixed points, and stability characteristics using conventional high-level computational platforms such as MAPLE and MATLAB, the present work extends this line of research along a novel trajectory. Specifically, we propose a new modification of the Lorenz equations by introducing an additional nonlinear term into the first equation, which leads to previously undocumented dynamical regimes.

In our formulation, the modified Lorenz system is defined as follows:

$$\begin{aligned} \dot{x} &= s(y - x) + yz, \\ \dot{y} &= rx - y - xz, \\ \dot{z} &= xy - bz, \end{aligned} \tag{2}$$

where s,r and b are positive parameters, and the term yz introduced an additional nonlinear coupling into the evolution of x.

The results of numerical integration for this modified system are presented in Figure 7-9. These figures illustrate the significant changes in the topology of the phase space: the attractors become more elongated, asymmetric, and exhibit increased structural complexity. These qualitative transformations indicate the emergence of new dynamic modes and validate the sensitivity of the system to structural perturbations. The transition to these new behaviors is clearly visible across all phase projections, thereby confirming both the effectiveness of the proposed numerical method and the adequacy of the visualization framework implemented within the VBA environment.

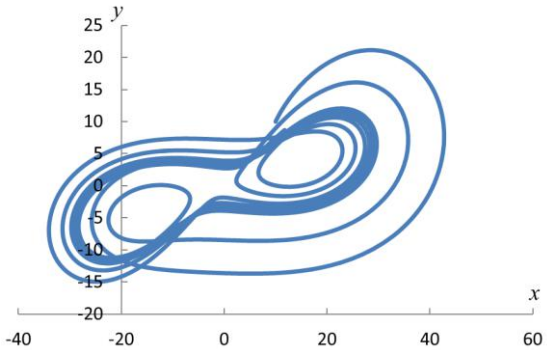

Fig. 7. Graph of the projection of the trajectories of the modified Lorentz attractor on the *yx* planes.

Based on the classical Lorenz model, the study demonstrates that the proposed methods and approaches lead to results similar to those presented in [13]. Numerical integration of the system of Lorentz differential equations was performed using a computer program written in VBA language and implementing the four-point Adams method with automatic selection of the integration step. The Krylov method of successive convergences was used to find the acceleration points for the Adams method. A VBA program implements both the Adams method and the Krylov method, ensuring that they work together.

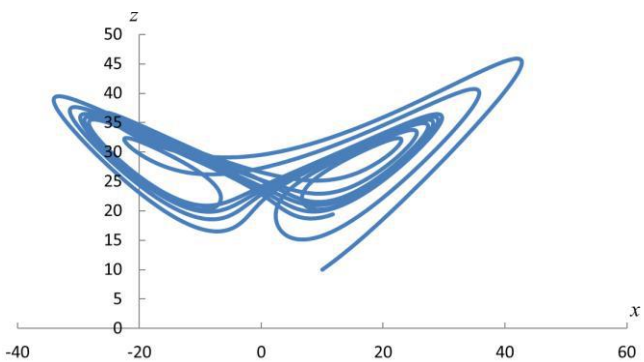

Fig. 8. Graph of the projection of the trajectories of the modified Lorentz attractor on the *zx* planes.

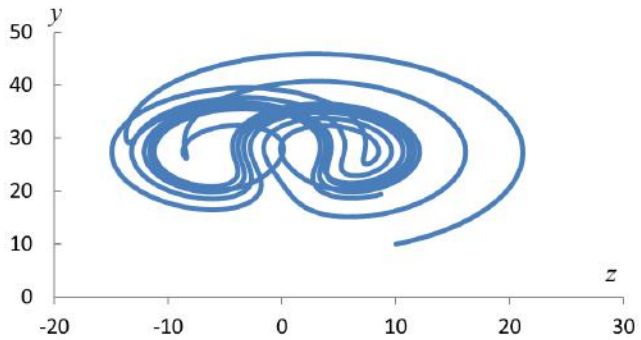

Fig. 9. Graph of the projection of the trajectories of the modified Lorentz attractor on the *yz* planes.

Typically, acceleration points are defined in regions where the field is weak and trajectories are nearly straight. These points are calculated using the Krylov method and are subsequently used to implement the Adams method. When numerically integrating a system of differential equations by the Adams method, the integration step is automatically selected so as to ensure a given accuracy of calculations [15-17].

5. Conclusion

In this study, a numerical model for analyzing the chaotic dynamics of the Lorenz system was implemented and tested using the Adams and Krylov methods integrated into a VBA implementation in Microsoft Excel. The stated goal — studying the behavior of the Lorenz system and developing tools for controlling its chaotic dynamics — was achieved through numerical modeling and comparative analysis of various system parameters, including both classical and modified configurations. The Adams method with automatic step selection allowed us to obtain stable numerical solutions with high accuracy, and the implementation of the Krylov method contributed to the acceleration of convergence in areas of the phase space with low dynamics. This is especially important in long-term modeling of complex nonlinear systems, where the accumulation of numerical errors can significantly affect the result. The phase trajectory graphs obtained for various sets of parameters demonstrated characteristic signs of chaotic behavior and confirmed the high sensitivity of the model to the initial conditions, which corresponds to theoretical expectations.

Comparison of the results with published works, where Maple and MATLAB were used, showed the coincidence of phase portraits, which confirms the correctness of the selected numerical methods and their implementation in the VBA environment. Despite the use of relatively simple tools, the developed model demonstrated efficiency and can be used both for educational purposes and for applied research of nonlinear dynamic systems. Thus, the work contributes to the practical implementation of methods of numerical analysis and visualization of chaos, and also demonstrates the possibilities of controlling complex dynamics through the selection of parameters and the use of computational algorithms. A promising direction for further research is the introduction of additional mechanisms for controlling chaos, including feedback, as well as expanding the model to other types of nonlinear systems.

Conflict of interest statement

The authors declare that they have no conflict of interest in relation to this research, whether financial, personal, authorship or otherwise, that could affect the research and its results presented in this paper.

CRediT author statement

Shugayeva T.: Investigation, Formal Analysis, Writing-Reviewing and Editing; **Spivak-Lavrov I.:** Conceptualization, Methodology, Supervision; **Amantaeva A.:** Software and Analysis. The final manuscript was read and approved by all authors.

Funding

The work was carried out within the framework of a project with grant funding from the Ministry of Science and Higher Education of the Republic of Kazakhstan (AR22685992)

.

References

1. Shen B.-W., Pielke R.A. Sr., Zeng X., Zeng X. (2024) Exploring the Origin of the Two-Week Predictability Limit: A Revisit of Lorenz's Predictability Studies in the 1960s. *Atmosphere*, 15, 7, 837. https://doi.org/10.3390/atmos15070837
2. Pikovsky A., Rosenblum M., Kurths J. (2001) *Synchronization: A universal concept in nonlinear sciences*. New York, Cambridge University Press, 411 p. https://doi.org/10.1017/CBO9780511755743
3. Chen G., Yu X. (2003) *Chaos Control: Theory and Applications.* Berlin, Springer-Verlag, 292, 347. https://doi.org/10.1007/b79666
4. Press W.H., Teukolsky S.A., Vetterling W.T., Flannery B.P. (2007) *Numerical recipes: The art of scientific computing (3rd ed.).* Cambridge University Press, 1256. Available at: https://numerical.recipes/book.html
5. Tchoumtcha D.B., Dagang C.T.S., Kenne G. (2024) Synergetic control for stand-alone permanent magnet synchronous generator driven by variable wind turbine. *International Journal of Dynamics and Control*, 12(7), 2888–2902. https://doi.org/10.1007/s40435-024-01384-w
6. Peng X., Zhou S. (2023) Finite-time stochastic control for complex dynamical systems: The estimate for control time and energy consumption. *Systems & Control Letters*, 181, 105711. https://doi.org/10.1016/j.syscon.2023.105711
7. Strogatz S.H. (2024) *Nonlinear dynamics and chaos: With applications to physics, biology, chemistry, and engineering (3rd ed.)*. Chapman and Hall/CRC. 616 p. https://doi.org/10.1201/9780429398490
8. Hargittai I. (2024) Remembering Benoit Mandelbrot on his centennial – His fractal geometry changed our view of nature. *Structural Chemistry*, 35(1), 11–24. https://doi.org/10.1007/s11224-024-02290-9
9. Petrzela J. (2024) Chaotic systems based on higher-order oscillatory equations. *Scientific Reports, 14*, 21075. https://doi.org/10.1038/s41598-024-72034-6
10. Ovsyannikov I., Rademacher J.D.M., Welter R., Lu B. (2023) Time averages and periodic attractors at high Rayleigh number for Lorenz-like models. *Journal of Nonlinear Science*, 33(5), 99. https://doi.org/10.1007/s00332-023-09933-x
11. Neimark Y.I., Landa P.S. (2009) *Stochastic and chaotic oscillations.* Librocom, 500. https://doi.org/10.1007/978-94-011-2596-3
12. Nemytsky V.V., Stepanov V.V. (2004) *Qualitative theory of differential equations*. Editorial URSS. 523. https://doi.org/10.1016/j.physleta.2008.07.032 [in Russian]
13. Tee L.S., Salleh Z. (2013) Dynamical analysis of a modified Lorenz system. *Journal of Mathematics*, 820946. http://dx.doi.org/10.1155/2013/820946
14. Zhou W., Xu Y., Lu H., Pan L. (2008) On dynamics analysis of a new chaotic attractor. *Physics Letters A,* 372(36), 5773–5777. https://doi.org/10.1016/j.physleta.2008.07.032
15. Spivak-Lavrov I.F., Shugaeva T.Zh., Kalimatov T.S. (2019) Prismatic mass analyzer with the conical achromatic prism and transaxial lenses. *International Journal of Mass Spectrometry*, 444, 116180. https://doi.org/10.1016/j.ijms.2019.116180
16. Spivak-Lavrov I.F. (1995) Mass spectrometer based on cone-shaped achromatic prism. *Nuclear Instruments and Methods in Physics Research Section A: Accelerators, Spectrometers, Detectors and Associated Equipment*, 636(1), 485–490. https://doi.org/10.1016/0168-9002(95)00267-7
17. Spivak-Lavrov I. F., Baisanov O. A., Shugayeva T.Zh., Urinbaeva G. T. (2021) Time-of-flight mass analyzer based on transaxial mirrors. *Acta Physica Polonica B. Proceedings Supplement*, 14(4), 857–864. https://doi.org/10.5506/APHYSPOLBSUPP.14.857

AUTHORS' INFORMATION

Shugayeva, Tilektes Zh. – PhD, K. Zhubanov Aktobe Regional University, Aktobe, Kazakhstan; ORCID iD:0000-0002-4797-4529; tlektes.tleubaeva@gmail.com

Spivak-Lavrov, Igor F. – Doctor of Physical and Mathematical Sciences, Professor, K. Zhubanov Aktobe Regional University, Aktobe, Kazakhstan; ORCID iD: 0000-0001-6235-3897; spivakif@rambler.ru

Amantaeva, Amangul Sh. – PhD student, K. Zhubanov Aktobe Regional University, Aktobe, Kazakhstan; ORCID iD: 0000-0002-1693-9085; aamantaeva@zhubanov.edu.kz

SUMMARIES	ТҮСІНІКТЕМЕЛЕР	АННОТАЦИИ

Исматов А.А., Romanitan C., Ашуров Х.Б. Адилов М.М., Рахимов А.А.

Темір нанокатализаторларының аннелдеу арқылы морфологиялық эволюциясы және көміртекті нанотүтікшелердің өсуі

Электронды-сәулелік физикалық бу тұндыру әдісі арқылы кремний субстраттарында темір нанокатализаторларын синтездеу олардың каталитикалық қолданылуына байланысты елеулі назарға ие болып отыр. Бұл зерттеуде қыздырып босаңдату температурасының (500°C, 550°C және 600°C) Fe нанокатализаторларының құрылымдық және морфологиялық сипаттамаларына әсері және оларды химиялық бу фазасында тұндыру әдісімен көміртекті нанотүтікшелерді өсіру үшін қолданылуы қарастырылған. Атомдық-күштік микроскопия және сканерлеуші электронды микроскопия әдістерімен өлшеу қыздырып босаңдату температурасының артуы орташа нанокластер өлшемін кішірейтетінін көрсетті, ал 600°C-та қыздырып босаңдату кезінде шамамен 30 нм орташа өлшемді нанокластерлер алынды; сондықтан олар катализатор ретінде анағұрлым тиімді болып табылады. Раман спектроскопиясы көміртекті нанотүтікшелердің өсуі тек 600°C-та қыздырып босаңдатылған субстратта байқалғанын растады және жоғары кристалдылықты әрі төмен ақау концентрациясын білдіретін ID/IG қатынасының (<1) жоғары мәнін көрсетті. Радиалды тыныс алу режимі шыңдарының болмауы синтезделген көміртекті нанотүтікшелердің көпқабатты екенін дәлелдейтін қосымша айғақ болып табылады. Бұл нәтижелер көміртекті нанотүтікшелердің өсуін барынша тиімді ету үшін темір нанокатализаторларының нанокластер өлшемдері мен таралуын электронды-сәулелік физикалық бу тұндыру әдісі және жылулық өңдеу арқылы жоғары дәлдікпен бақылау қажет екенін көрсетеді.

Кілт сөздері: темір нанокатализаторлары, көміртекті нанотүтікшелері, физикалық бу тұндыру, химиялық бу тұндыру, Раман спектроскопиясы, атомдық-күштік микроскопия, сканерлеуші электронды микроскопия.

Исматов А.А., Romanitan C., Ашуров Х.Б. Адилов М.М., Рахимов А.А.

Аннелировочно-индецированная морфологическая эволюция железных нанокатализаторов, вызванная отжигом для роста углеродных нанотрубок.

Синтез железных нанокатализаторов на кремниевых подложках методом электронно-лучевого физического осаждения из паровой фазы привлекает значительное внимание благодаря своим каталитическим свойствам. В данной работе исследуется влияние температуры отжига (500 °C, 550 °C и 600 °C) на структурные и морфологические характеристики нанокатализаторов Fe и их использование при росте углеродных нанотрубок методом химического осаждения из паровой фазы. Измерения методом атомно-силовой микроскопии и сканирующей электронной микроскопии показали, что повышение температуры отжига приводит к уменьшению среднего размера нанокластеров, и при 600 °C формируются нанокластеры со средним размером около ~30 нм, что делает их более эффективными в качестве катализаторов. Раман-спектроскопия показала, что ростуглеродных нанотрубок наблюдается только на подложке, отожжённой при 600 °C, и характеризуется высоким отношением ID/IG (<1), что указывает на высокую кристалличность и низкую концентрацию дефектов. Отсутствие пиков радиального дыхательного режима служит дополнительным доказательством того, что синтезированные углеродных нанотрубок являются многостенными. Полученные результаты указывают на необходимость точного контроля размеров и распределения нанокластеров с использованием электронно-лучевого физического осаждения из паровой фазы и термической обработки для максимизации эффективности нанокатализаторов Fe при росте углеродных нанотрубок.

Ключевые слова: Железные нанокатализаторы, углеродные нанотрубки, физическое осаждение из паровой фазы, химическое осаждение из паровой фазы, рамановская спектроскопия, атомно-силовая микроскопия, сканирующая электронная микроскопия.

Середа Д.Б., Кругляк И.В., Середа Б.П.

Функционалды-белсенді шихталарды пайдалану арқылы көпкомпонентті хромды жабындыларды алу.

Бұл зерттеулердің мақсаты – көміртекті болаттарда тұрақсыз температуралық жағдайда тозуға төзімді хромды жабындар алу. Ол үшін функционалды-активті ұнтақ қоспалары қолданылып, химия-термиялық өңдеу уақытын 6–8 сағаттан 1 сағатқа дейін қысқартуға мүмкіндік береді. Жұмыстың ғылыми жаңалығы – функционалды-белсенді шихталармен жүргізілетін химия-термиялық өңдеу кезінде түзілетін газ фазасының құрамын анықтау үшін термодинамикалық талдауды қолдануда. Бұл әдіс аммоний қосылыстарының концентрациясын бор арқылы легирленген хромды жабындарда оңтайландыруға және олардың физика-механикалық қасиеттерін болжауға мүмкіндік берді. Дайындалған технологияның практикалық маңызы – феррит-перлитті құрылымды болаттарда хромды жабындардың тозуға төзімділігін арттыру. Бұл оларды динамикалық және соққылы жүктемелер жағдайында тиімді пайдалануды қамтамасыз етеді. Ұсынылған әдіс өнеркәсіптік қолдануға арналған аса тиімді қорғаныш жабындыларын жасауға жаңа мүмкіндіктер ашады. Жабындылардың микроқұрылымы мен фазалық құрамын зерттеу үшін оптикалық микроскопия (Neophot-32) және сканерлеуші

электронды микроскопия (REM-106i) қолданылды. Триботехникалық сынақтар СМТ-1 және МТ-5 үйкеліс қондырғыларында жүргізілді. Химия-термиялық өңдеу барысында түзілетін газ ортасының құрамы термодинамикалық модельдеу арқылы анықталды, ал дайын материалдардың құрамын оңтайландыру тозуға төзімділік критерийі бойынша математикалық эксперименттерді жоспарлау әдістерімен іске асырылды. Нәтижесінде, ұнтақ шихта құрамына борқұрамды компоненттер мен аммонийлі газтранспорттық реагенттерді енгізу газ тәрізді қосылыстар мен конденсацияланған фазалардың түзілуіне ықпал ететіні анықталды. Ұсынылған функционалды-белсенді қоспалар 15–60 минут ішінде қалыңдығы 150 мкм-ге дейінгі қорғаныш хромды қабаттардың түзілуін қамтамасыз етеді.
Кілт сөздері: көміртекті болат, хромдау, легирлеу, бор, қорғаныш жабынды, шихта, термодинамика, тозуға төзімділік.

Середа Д.Б., Кругляк И.В., Середа Б.П.

Получение многокомпонентных хромовых покрытий с использованием функционально активных шихт.

Целью данных исследований является получение износостойких хромистых покрытий на углеродистых сталях в нестационарных температурных условиях с использованием функционально-активных порошковых смесей, что позволяет сократить время химико-термической обработки с 6-8 часов до 1 часа. Научная новизна работы заключается в использовании термодинамического анализа для определения состава газовой фазы, образующейся при химико-термической обработке с функционально активными шихтами, что позволило оптимизировать концентрацию аммониевых соединений при легировании бором, хромовых покрытий и предсказать их физико-механические характеристики. Практическое значение разработанной технологии заключается в повышении износостойкости хромистых покрытий на сталях с феррит-перлитным строением, что обеспечивает их эффективное использование при динамических и ударных нагрузках. Предложенный метод открывает новые возможности для создания высокоэффективных защитных покрытий для промышленного применения. Для исследования микроструктуры и фазового состава покрытий использовались оптическая микроскопия (Neophot-32) и сканирующая электронная микроскопия (REM-106i). Триботехнические испытания проводились на трениях установках СМТ-1 и МТ-5. Состав газовой среды, образующейся при химической термообработке, был определен с помощью термодинамического моделирования, а оптимизация состава компонентов заготовочных материалов была проведена с помощью методов математического планирования экспериментов с критерием оптимизации в виде износостойкости хромовых покрытий, легированных бором. В результате было установлено, что добавление в состав порошковой шихты борсодержащих компонентов и аммониевых газотранспортных реагентов способствует образованию газообразных соединений и конденсированных фаз. Предложенные функционально-активные смеси обеспечивают образование защитных хромовых слоев толщиной до 150 мкм в течение 15-60 минут.
Ключевые слова: углеродистая сталь, хромирование, легирование, бор, защитное покрытие, шихта, термодинамика, износостойкость.

Козловский А.Л., Боргеков Д.Б., Тлеулесова И.К., Жумажанова А.Т., Молдабаева Г.Ж., Бурханов Б.Ж., Хаметова А.А.

Көп компонентті керамиканы қорғаныш экрандау және термотосқауыл материалдар ретінде қолдану тиімділігін бағалау.

Жұмыста TeO_2, CeO_2, WO_3, ZnO, Bi_2O_3, ZrO_2 оксидтерін әртүрлі молярлық қатынастарда араластыру арқылы алынған көп компонентті керамиканың экрандау сипаттамаларын салыстырмалы талдау нәтижелері келтірілген, олардың вариациясы вариативті фазалық құрамына ие керамиканы алуға мүмкіндік берді. Рентгендік фазалық талдау нәтижелеріне сәйкес композиттік керамиканың құрамына цирконий диоксидін қосу $ZrCeO_2$ моноклинді алмастыру фазасының қалыптасуына әкеледі, оның үлесінің артуы керамика құрамындағы фаза-аралық шекаралардың концентрациясының өзгеруі арқылы беріктік қасиеттерінің жоғарылауына әкеледі. Кристалдық құрылымның тұрақсыздығына әкелуі мүмкін термиялық әсерлерге төзімділікке жүргізілген тестілік сынақтар барысында керамика құрамындағы ZrO_2 үлесінің ұлғаюы термиялық индукцияланған босаңсу процестеріне төзімділіктің артуына, сондай - ақ термошок әсерін сынау кезінде керамиканың стресске төзімділігінің артуына әкелетіні анықталды. Зерттелетін керамиканың экрандау сипаттамаларын анықтау кезінде, $ZrCeO_2$ тұрақтандырушы фазасының көп компонентті керамикаларының құрамындағы түзілу экрандау тиімділігінің артуына, сондай-ақ ұзақ мерзімді термиялық әсерлер мен термошок сынақтары нәтижесінде экрандау сипаттамалардың сақталу тұрақтылығына әкелетіні анықталды. Бұл ретте өлшенетін параметрлердің тиімділігінің ең үлкен өсуі, $ZrCeO_2$ фазасы түрінде қосындылары жоқ тұрақтандырылған керамикалармен салыстырғанда өсімі 2.5 еседен астам болатын жылу оқшаулау сипаттамаларын бағалау жағдайында байқалады.
Кілт сөздері: композиттік көп компонентті керамика, экрандаушы материалдар, термошок әсері, тұрақтандыру, допирлеу.

Козловский А.Л., Боргеков Д.Б., Тлеулесова И.К., Жумажанова А.Т., Молдабаева Г.Ж., Бурханов Б.Ж., Хаметова А.А.

Оценка эффективности применения многокомпонентных керамик в качестве защитных экранирующих и термобарьерных материалов.

В работе представлены результаты сравнительного анализа экранирующих характеристик многокомпонентных керамик, полученных путем смешивания оксидов TeO_2, CeO_2, WO_3, ZnO, Bi_2O_3, ZrO_2 в различных молярных соотношениях, варьирование которых позволило получить керамики с вариативным фазовым составом. Согласно результатам рентгенофазового анализа, добавление в состав композитных керамик диоксида циркония приводит к формированию моноклинной фазы замещения $ZrCeO_2$, увеличение вклада которой приводит к повышению прочностных свойств за счет изменения концентрации межфазных границ в составе керамик. В ходе проведенных тестовых испытаний на устойчивость к термическим воздействиям, способным привести к дестабилизации кристаллической структуры было установлено, что увеличение вклада ZrO_2 в составе керамик приводит к увеличению сопротивляемости к термически – индуцированным процессам разупрочнения, а также повышению стрессоустойчивости керамик при испытаниях на термошоковое воздействие. При определении экранирующих характеристик исследуемых керамик было установлено, что формирование в составе многокомпонентных керамик стабилизирующей фазы $ZrCeO_2$ приводит к увеличению эффективности экранирования, а также стабильности сохранения экранирующих характеристик в результате длительных термических воздействий и термошоковых испытаний. При этом наибольший рост эффективности измеряемых параметров наблюдается в случае оценки теплоизоляционных характеристик, рост которых составляет более чем в 2.5 раза по сравнению с нестабилизированными керамиками, в составе которых отсутствуют включения в виде фазы $ZrCeO_2$.

Ключевые слова: композитные многокомпонентные керамики, экранирующие материалы, термошоковое воздействие, стабилизация, допирование.

Турдиев М.Т., Касенов Б.К., Нухулы А., Бектурганов Ж.С., Касенова Ш.Б., Сагинтаева Ж.И., Куанышбеков Э.Э.

Сирекжер және ауыспалы металдардың оксидтері негізіндегі жаңа жартылай өткізгіштің термодинамикалық және электрфизикалық қасиеттері

Зерттеу жұмысы манганиттер мен цирконаттардың қасиеттерін біріктіретін жаңа қосылысты зерттеуге арналған, бұл жоғары тиімді функционалды материалдарды жасауға жол ашады. Қосылыс лантан оксиді, цирконий оксиді, марганец оксиді және натрий карбонатының 800–1200 °C температура аралығындағы әрекеттесуі арқылы синтезделіп, рентгенқұрылымдық талдау әдістерімен, соның ішінде кубтық тор параметрлерін анықтау арқылы зерттелді. Жылусыйымдылықтың температураға тәуелділігін талдау екінші ретті фазалық ауысуларды көрсетті және оның өзгерісін сипаттайтын теңдеулер шығарылды. Энтропия мен энтальпия сияқты термодинамикалық сипаттамалар есептелді. Электрофизикалық өлшеулер белгілі бір температура диапазонында материалдың жартылай өткізгіштік табиғатын растады және эталондық материалдардан асып түсетін диэлектрлік өтімділіктің жоғары мәндерін көрсетті.

Кілт сөздері: манганит, лантан, цирконий, натрий, жылусыйымдылық, термодинамикалық функциялар, электрофизика.

Турдиев М.Т., Касенов Б.К., Нухулы А., Бектурганов Ж.С., Касенова Ш.Б., Сагинтаева Ж.И., Куанышбеков Э.Э.

Термодинамические и электрофизические свойства нового полупроводника на основе оксидов редкоземельных и переходных металлов.

Исследование посвящено изучению нового соединения, сочетающего свойства манганитов и цирконатов, что открывает путь к созданию высокоэффективных функциональных материалов. Соединение синтезировано взаимодействием оксида лантана, оксида циркония, оксида марганца и карбоната натрия при температурах от 800 до 1200 °C и исследовано методами рентгеноструктурного анализа, включая определение параметров кубической решетки. Анализ температурной зависимости теплоёмкости выявил фазовые переходы второго рода, на основе которых выведены уравнения, описывающие её изменение. Рассчитаны термодинамические характеристики, такие как энтропия и энтальпия. Электрофизические измерения подтвердили полупроводниковую природу материала в определённом диапазоне температур и выявили высокие значения диэлектрической проницаемости, превосходящие значения эталонных материалов.

Ключевые слова: манганит, лантан, цирконий, натрий, теплоёмкость, термодинамические функции, электрофизика.

Юсупова Ж.Б.

Күміс наноболшектерінің синтезі және олардың антраценнің флуоресценциясы мен сіңіруіне әсері.

Жұмыста ерітіндінің pH мәнінің арал тәрізді күміс қабықшаларының түзілу процесіне әсері қарастырылды. Зерттеу нәтижелері бойынша тиімді синтез жүргізу үшін оңтайлы pH мәні 8 екені анықталды. ImageJ

бағдарламасы көмегімен Ферет диаметрі бойынша бөлшектердің таралуы талданды. Алынған гистограмма химиялық жолмен тұндырылған қабықшаның сапасының жоғары екенін растады. Ұсынылған синтез әдісі берілген қасиеттері бар күміс нанобөлшектерінің қабықшаларын алуға мүмкіндік береді. Синтезделген күміс қабықшаларының антраценнің люминесценттік қасиеттеріне әсері зерттеліп, олардың фотоника мен сенсорлық технологияларда қолдану мүмкіндігі көрсетілді.
Түйінді сөздер:: күміс аралша қабықшалары, антрацен, pH, ImageJ.

Юсупова Ж.Б.

Синтез наночастиц серебра и их влияние на флуоресценцию и поглощение антрацена.

В работе исследован процесс синтеза островковых серебряных плёнок с акцентом на влияние pH раствора как ключевого параметра успешного формирования плёнки. Установлено, что оптимальным значением pH для эффективного синтеза является 8. Также представлены результаты анализа распределения частиц по диаметру Ферета, выполненного с использованием программного обеспечения ImageJ. Гистограмма распределения подтвердила высокое качество химически осаждённой плёнки. Разработанный метод синтеза позволяет изготавливать плёнки наночастиц серебра с заданными свойствами. Изучено влияние синтезированных серебряных плёнок на люминесцентные свойства антрацена, что подчёркивает их перспективность для применения в фотонике и сенсорных технологиях.
Ключевые слова: островковые плёнки, наночастицы серебра, антрацен, pH, ImageJ.

Генбач А.А., Бондарцев Д.Ю.

Минералды жабындылары бар салқындату жүйесі үшін жылуалмасуды жалпылау зерттеуі.

Табиғи материалдардан жасалған жабындылары бар салқындату жүйелеріндегі жылуалмасу процестері термоқұралдың детонациялық жалынының параметрлеріне және табиғи материалдардың жылуфизикалық қасиеттеріне байланысты зерттелді. Тотығуыш артық коэффициенті бірден кем болғанда жалынның спиндік детонациясы байқалды, бұл жағдайда бүрку процесі 2–6 есеге дейін қарқынданды. Жабындылар басқа күшейту жүйелерімен салыстырғанда жоғары сенімділік көрсетті. Жабындыдағы меншікті жылу ағындарының ең жоғары мәндері (2–20×10⁶ Вт/м²) аралығында, ал тербеліс жиілігі 200 Гц-ке дейін жетті. Жабындының артық қызу диапазоны (20÷75) К құрады. Модельде және тәжірибелік түрде термоқұралдардың термодинамикалық сипаттамалары анықталды, материалдардың гранулометриялық құрамы алынды, жанарғылардың гидродинамикалық жұмыс режимдері (отынды жағу тәсілі, ағын ұзындығы, ағын бұрышы) таңдалды. Термоқұралдың осьтік симметриялық аса-дыбыстық детонациялық газ ағынының жабындыға нормаль бағытта әсер ету моделі құрылды. Эксперименттік мәліметтері бойынша жылуалмасу коэффициенттері ламинарлық теориямен алынғаннан (5...6) есе жоғары және турбулентті жылуалмасу заңымен салыстырғанда бірнеше есе төмен екені көрсетілді. Бөлшектердің ұшу уақыты, жабындының оңтайлы қалыңдығы, ұнтақтың диаметрі, жабындының сығылу және созылу кезіндегі шекті кернеулері анықталды.
Түйінді сөздер: жылу- және массалмасу, жабындылар, термиялық құралдар, жану камерасы, шүмектер, детонациялық шырақ.

Генбач А.А., Бондарцев Д.Ю.

Исследование обобщения теплопередачи для системы охлаждения с минеральными покрытиями.

Проведены исследования теплообмена в системах охлаждения с покрытиями из природных материалов в зависимости от параметров детонационного пламени термоинструмента и теплофизических свойств природных материалов. Зафиксировано явление спиновой детонации пламени при коэффициенте избытка окислителя менее единицы, при этом процесс напыления интенсифицировался от 2 до 6 раз. Покрытия показали высокую надежность по сравнению с другими системами наддува. Максимальные удельные тепловые потоки на покрытии составляют (от 2 до 20×10^6 Вт/м^2), частота колебаний - до 200 Гц. Диапазон перегрева покрытия составил (20÷75) К. На модели и экспериментально установлены термодинамические характеристики тепловых инструментов, получен гранулометрический состав материалов, подобраны гидродинамические режимы работы горелок (способ сжигания топлива, длина струи, угол наклона струи). Построена модель взаимодействия осесимметричной сверхзвуковой детонационной струи газов термоинструмента по нормали к покрытию, причем коэффициенты теплоотдачи по данным эксперимента в (5...6) раз выше, чем дает ламинарная теория, и в несколько раз ниже, чем для закона турбулентного теплообмена. Определены время полета частиц, оптимальная толщина покрытий, диаметр порошка, предельные напряжения сжатия и растяжения покрытия.
Ключевые слова: тепло- и массообмен, покрытия, термические инструменты, камера сгорания, сопла, детонационный факел.

Байтелесов С. А., Таджибоев Д. П., Фаизиев Т.Б., Кунгуров Ф. Р., Аликулов Ш.А.

ВВР-СМ реакторындағы басқару және қорғау жүйесі арналарының конфигурациясын өзгерткен жағдайда ИРТ-4М ядролық отынында энергия бөлінуі мен температураның таралуын анықтау.

Бұл жұмыстың мақсаты – ВВР-СМ реакторының белсенді аймағында 235U бойынша 19,75% байытылған отыны бар ИРТ-4М типті жылу бөлетін жинақтағы (ЖБЖ) температураның таралуын екі жағдайда анықтау: ортасында дөңгелек тесігі бар, қырлары дөңгелектенген төртбұрышты түтікпен және дөңгелек түтікпен. Қырлары дөңгелектенген төртбұрышты және ортасында дөңгелек тесігі бар түтіктің орнына ЖБЖ ішіне дөңгелек түтік орнатылған жағдайда осы аймақтағы су көлемі артады. Бір жағынан, бұл жылу берілісті жақсартады, өйткені салқындатқыш су көлемі көбейеді; екінші жағынан, судың көлемінің ұлғаюы жанындағы жылу бөлетін элемент (ЖБЭЛ) аймағына жылулық нейтрондар ағынының артуына әкеледі, бұл өз кезегінде энергия бөлінудің артуына себеп болады. Бұл өзгерістерді анықтау үшін төртбұрышты түтігі бар арна мен дөңгелек түтігі бар арнаға нейтрон-физикалық және жылу-гидравликалық есептеулер жүргізілді. Нәтижесінде, ортасында дөңгелек тесігі бар қырлары дөңгелектенген төртбұрышты түтікті реттеуіш компенсатор аспабын орнатуға арналған бағыттаушы ретінде қолданылатын дөңгелек түтікке ауыстыру ВВР-СМ реакторының ядролық қауіпсіздігіне әсер етпейтіні анықталды.

Кілт сөздері: жылу бөлетін жинақ (ЖБЖ), нейтрон-физикалық және жылу-гидравликалық есептеу, көлденең және тік арналары, реактордың белсенді аймағы, жану.

Байтелесов С. А., Таджибоев Д. П., Фаизиев Т.Б., Кунгуров Ф. Р., Аликулов Ш. А.

Определение распределения энерговыделения и температуры в ядерном топливе ИРТ-4М при изменении конфигурации каналов системы управления и защиты в реакторе ВВР-СМ.

Целью данной работы является определение распределения температуры в тепловыделяющей сборке (ТВС) типа ИРТ-4М с топливом обогащением 19,75% по 235U в активной зоне реактора ВВР-СМ для двух случаев: с квадратной трубкой со скругленными краями и круглым отверстием в центре и с круглой трубкой. В случае установки круглой трубки внутри ТВС вместо квадратной со скругленными краями и круглым отверстием объем воды в этом пространстве увеличивается. С одной стороны, это приводит к улучшению теплоотвода, поскольку объем охлаждающей воды возрастает, а с другой стороны, увеличение объема воды приводит к увеличению потока тепловых нейтронов в прилегающей области тепловыделяющего элемента (ТВЭЛ), что, в свою очередь, ведет к росту энерговыделения. Для определения этих изменений были выполнены нейтронно-физические и тепло-гидравлические расчеты для канала с квадратной трубкой и для канала с круглой трубкой. Установлено, что замена квадратной трубки со скругленными краями и круглым отверстием в центре на круглую трубку, используемую в качестве направляющей для установки компенсирующего органа регулирования, не повлияет на ядерную безопасность эксплуатации реактора ВВР-СМ.

Ключевые слова: тепловыделяющая сборка (ТВС), нейтронно-физический и тепло-гидравлический расчет, горизонтальные и вертикальные каналы, активная зона реактора, выгорание.

Джавад, М.Х., Абдуламир, М.Р.

Zn-Al қорытпа плазмасының электрондық температурасы мен тығыздығын оптикалық спектроскопиялық диагностикалау: лазер энергиясының плазма параметрлеріне әсері

Бұл зерттеуде мырыш пен алюминий қорытпасынан алынған плазманың қасиеттері лазерлік спектроскопия әдістерімен зерттелді. Қорытпа жергілікті өндірісте дайындалған және оның құрамы сәйкесінше 20–80% мырыш пен алюминийден тұрды. Лазер энергиясы 500-ден 900 мДж-ге дейін бапталатын режимде қолданылған, негізгі толқын ұзындығы 1064 нм болатын иттрий-алюминий гранатына (YAG) негізіндегі неодим-легирленген лазер пайдаланылды. Бұл плазманың тәртібін зерттеу және оның жалпы қасиеттерін, соның ішінде электрон тығыздығы мен температурасын анықтау үшін жүргізілді. Электрондардың температурасын анықтау үшін Больцман диаграммасы әдісі қолданылды, ал электрон тығыздығын есептеу үшін Штарк жіктеу әдісі пайдаланылды. Осы екі негізгі параметр негізінде плазманың қосымша сипаттамалары есептеліп, анықталды. Зерттеу нәтижелері лазер энергиясының плазма параметрлеріне айқын әсерін көрсетті: лазер энергиясы артқан сайын электрон температурасы мен тығыздығы едәуір артты. Электрон температурасының ең жоғары мәні 900 мДж кезінде 0,918 эВ-қа жетті, ал 500 мДж кезінде ол 0,537 эВ болды. Екінші жағынан, нәтижелер жоғары лазер энергияларында Дебай саны мен плазмалық жиіліктің артқанын, ал жоғары қуат жағдайында Дебай ұзындығының айқын азайғанын көрсетті.Бұл зерттеудің басты мақсаты – плазманың қасиеттерін тереңірек түсінуге және лазер қуатының осы қасиеттерге әсерін айқындауға үлес қосу. Мұндай нәтижелер металдарды гравюралау мен таңбалау сияқты көптеген өнеркәсіптік және технологиялық қолданыстарға жол ашады.

Кілт сөздері: Zn-Al қорытпасы, плазманың оптикалық спектроскопиясы, плазма қасиеттері мен параметрлері.

Джавад М.Х., Абдуламир М.Р.

Оптическая спектроскопическая диагностика температуры и плотности электронов в плазме сплава Zn-Al: влияние энергии лазера на параметры плазмы.

В данном исследовании свойства плазмы, полученной из цинкового и алюминиевого сплавов, исследовались с помощью методов лазерной спектроскопии. Сплав местного производства и состоял из 20–80 процентов цинка и алюминия соответственно. Для изучения поведения плазмы и определения ее общих свойств, таких как плотность электронов и температура, использовался лазер на иттрий-алюминиевом гранате, легированном неодимом, с основной длиной волны 1064 нм и регулируемой энергией лазера от 500 до 900 мДж. Для определения температуры электронов использовался метод построения диаграмм Больцмана, а для расчета плотности электронов использовался метод разложения Штарка. На основе этих двух основных параметров были рассчитаны и определены остальные дополнительные параметры плазмы. Результаты, полученные в ходе данного исследования, показали выраженное влияние энергии лазера на параметры плазмы, поскольку температура и плотность электронов значительно возрастали с ростом энергии лазера, причем эти параметры постепенно увеличивались с ростом энергии лазера. Максимальное значение электронной температуры составило 0,918 эВ при 900 МДж, а при 500 мДж – 0,537 эВ. С другой стороны, результаты показали увеличение как числа Дебая, так и плазменной частоты при высоких энергиях лазера, в то время как длина Дебая явно уменьшалась при высокой мощности. Основная цель данного исследования – способствовать более глубокому пониманию свойств плазмы и влияния мощности лазера на эти свойства, что открывает возможности для множества приложений, включая гравировку и маркировку на металлах, а также для многих промышленных и технологических применений.

Ключевые слова: сплав Zn-Al, оптическая спектроскопия плазмы, свойства и параметры плазмы.

Шарипов М.З., Мажитов Ж.А., Эргашев Ш.Х., Шодиев Э.Б., Нарзуллаева З.М.

Шағын биогаз қондырғысының жылутехникалық және геометриялық параметрлерін алмастыру.

Бұл мақала шағын биогаз қондырғыларының жылутехникалық және геометриялық параметрлерін негіздеу мәселелеріне арналған. Тұрақты және жаңартылатын энергетикалық ресурстарға деген өсіп келе жатқан сұраныс биогаз технологияларының маңыздылығын, әсіресе ауылдық және аграрлық қолданбалар үшін шағын масштабта арттырады. Алайда, биогаз өндірісінің тиімділігі мен тұрақтылығы көбінесе реактордың жылутехникалық жұмыс жағдайларына және оның геометриялық параметрлерін оңтайландырумен байланысты. Бұл зерттеудің мақсаты – жылутехникалық және геометриялық параметрлерді алмастырудың шағын биогаз қондырғысының жұмысына әсерін талдау. Зерттеу нысаны – конструктивтік сипаттамалары реттелетін зертханалық биогаз реакторы. Жұмыстың әдіснамалық негізін математикалық модельдеу, есептеу талдауы және реактор ішіндегі жылуалмасу мен материалдық баланс процестерін тәжірибелік тексеру құрайды. Зерттеу нәтижелері бойынша биореактор құрылымының оңтайлы геометриялық өлшемдерін (диаметрі мен ұзындығын) анықтау және жылулық шығындарды азайту әдістері қарастырылды. Математикалық модельдеу әдістері арқылы әртүрлі жылуоқшаулау қалыңдығы мен биомасса дозалары кезінде реактордың оңтайлы өлшемдері есептелді. Көлемі 30 м³ болатын биореактор үшін оңтайлы диаметрі 2800 мм, ал ұзындығы – 4900 мм құрайды, бұл ретте реактор көлеміндегі биомасса үлесі орталық сектор бұрышы арқылы өрнектеледі.

Кілт сөздері: биогаз қондырғысы, жылулық параметрлер, реактордың жылуоқшаулауы, ашыту процесі, биомасса, анаэробты жағдайлар, энергия тиімділігі.

Шарипов М.З., Мажитов Ж.А., Эргашев Ш.Х., Шодиев Э.Б., Нарзуллаева З.М.

Замещение теплотехнических и геометрических параметров малогабаритной биогазовой установки.

Данная статья посвящена вопросам обоснования теплотехнических и геометрических параметров малогабаритных биогазовых установок. Растущий спрос на устойчивые и возобновляемые энергетические ресурсы повышает значимость биогазовых технологий, особенно на маломасштабном уровне для сельских и аграрных приложений. Однако эффективность и стабильность биогазового производства во многом зависят от теплотехнических условий работы реактора и оптимизации его геометрических параметров. Цель данного исследования заключается в анализе влияния замещения теплотехнических и геометрических параметров на работу малогабаритной биогазовой установки. Объектом исследования является лабораторный биогазовый реактор с регулируемыми конструктивными характеристиками. Методологической основой работы являются математическое моделирование, вычислительный анализ и экспериментальная проверка процессов теплообмена и материального баланса внутри реактора. По результатам исследования показано, что были проанализированы методы определения оптимальных геометрических размеров (диаметра и длины) конструкции биореактора и снижения тепловых потерь. С помощью методов математического моделирования рассчитаны оптимальные размеры реактора при различных толщинах теплоизоляции и дозировках биомассы. Оптимальный диаметр для биореактора объёмом 30 м³ составляет 2800 мм, а длина — 4900 мм, при этом доля биомассы в объёме реактора выражается через угол центрального сектора.

Ключевые слова: биогазовая установка, тепловые параметры, теплоизоляция реактора, процесс брожения, биомасса, анаэробные условия, энергоэффективность.

Асқарұлы Р., Файзулла Т., Абылканов М., Сыздыков А.Б., Саханов К.

Қатал климаттық жағдайларда композиттік материалдар мен аддитивті өндіріс арқылы роботтық қолдың беріктігін арттыру.

Қатты желдер, радиация әсері және жиі болатын орман өрттері сияқты қатал қоршаған орта жағдайлары роботтандырылған жүйелердің сенімді жұмысына елеулі қиындықтар туғызады. Апат салдарын жою және қауіпті ортада жұмыс істеуге арналған робототехникаға қызығушылық артып келе жатқанына қарамастан, аддитивті өндіріс арқылы жасалған компоненттердің мұндай жағдайларда төзімділігі жеткілікті зерттелмеген. Бұл зерттеу роботты манипуляторлардың экстремалды жағдайларда жұмыс өнімділігін арттыру үшін композиттік материалдар мен аддитивті өндіріс технологияларын қолдануды қарастырады. Композиттік элементтерден толық жасалған робот қолымен жабдықталған модульдік ровер әзірленіп, сыналды. Зерттеу PETG пластигі мен көміртекті талшықтың термиялық әсерге, статикалық жүктемеге және радиацияға төзімділігі тұрғысынан құрылымдық сенімділігін бағалауға бағытталды. Сонымен қатар, қашықтан басқаруға арналған ым арқылы басқару интерфейсі ұсынылып, функционалды прототип жасалды. Зерттеу нәтижелері материалдарды таңдау мен тұрақты роботтық жүйелерді жобалау стратегиялары туралы жаңа түсініктер береді және қатал қоршаған орта жағдайларында жұмыс істей алатын тұрақты робототехниканы дамытуға үлес қосады.

Кілт сөздері: Автоматтандырылған жобалау жүйелері, баспа платасы, автоматтандырылған өндіріс жүйелері, автоматтандырылған инженерлік талдау жүйелері, телекоммуникациялық ретрансляция қызметі, қабаттап балқыту әдісі.

Аскарулы Р., Файзулла Т., Абылканов М., Сыздыков А.Б., Саханов К.

Повышение долговечности роботизированнруки с использованием композитных материалов и аддитивного производства в суровых климатических условиях.

Несмотря на суровые условия окружающей среды, такие как сильные ветра, радиационное воздействие и частые лесные пожары, которые создают серьёзные трудности для надёжной работы роботизированных систем, устойчивость аддитивно изготовленных компонентов в таких условиях остаётся недостаточно изученной. В данной работе исследуется использование композитных материалов и технологий аддитивного производства для повышения эффективности роботизированных манипуляторов в экстремальных условиях. Был разработан и испытан модульный ровер, оснащённый роботизированной рукой, полностью изготовленной из композитных элементов. Исследование сосредоточено на оценке структурной надёжности пластика PETG и углеродного волокна с точки зрения термического воздействия, статической нагрузки и радиационной стойкости. Также была представлена система управления жестами для дистанционного управления и создан функциональный прототип. Результаты исследования дают новые представления о выборе материалов и стратегиях проектирования устойчивых роботизированных систем, способствуя развитию робототехники, предназначенной для работы в суровых условиях окружающей среды.

Ключевые слова: автоматизированное проектирование, печатная плата, автоматизированное производство, автоматизированное проектирование, телекоммуникационные релейные службы, моделирование методом наплавления.

Сарсенбаев Е., Острецов К., Бақтыбеков Қ., Мусина А., Ысқақ Ә.

Нанокласс ғарыш аппараттарына арналған OBCARM G2 NANO әмбебап модульдік борттық басқару кешені.

OBCARM G2 NANO әмбебап модульдік борттық басқару жүйесі 3U–12U нанокласты ғарыш аппараттарына арналған. Жүйе байланыс, Жерді қашықтықтан зондтау және Заттар интернеті (IoT) миссияларында қолдануға бейімделген. Архитектурасы интерфейс және процессор модульдерінен құралады. Процессор модулі Zynq Ultrascale+ SoC негізінде орындалған және ARM TMS470 контроллерінің телеметриясын басқаруды қолдайды. Ол орталық процессор үшін 500 МБ DDR4 жедел жадымен, бағдарламаланатын логикалық матрица үшін 125 МБ жедел жадымен, ұшу бағдарламалық жасақтамасын сақтауға арналған 125 МБ QSPI Flash және 128 ГБ eMMC Flash жадымен жабдықталған. Интерфейс модулі борттық басқару жүйесінің қуат тарату желілерін, ішкі жүйелер интерфейстерін, пайдалы жүктеменің деректерін қабылдау және беру арналары мен оларды түрлендіру және буферлеу драйверлерін қамтиды. Бағдарламалық басқару нақты уақыттағы QNX операциялық жүйесі негізінде іске асырылады, ал процессор мен бағдарламаланатын логикалық матрица арасындағы өзара әрекеттестік жоғары өнімді AXI шинасы арқылы қамтамасыз етіледі. Ғарыш аппаратының ішкі жүйелерін интеграциялау үшін бірыңғай CAN шинасы қолданылады. Механикалық құрамдастар 95 × 95 × 35 мм өлшемінде орындалған, температура сенсорлары және артық жылуды ыстық нүктелерден шығаратын жылу көпірімен толықтырылған.

Кілт сөздері: борттық басқару жүйесі, бағдарламаланатын логикалық матрица, процессор, интерфейс модулі, CubeSat.

Сарсенбаев Е., Острецов К., Бактыбеков К., Мусина А., Ыскак А.

Универсальный модульный бортовой комплекс управления OBCARM G2 NANO для космических аппаратов нанокласса

Разработана универсальная модульная бортовая система управления OBCARM G2 NANO для космических аппаратов нанокласса 3U-12U, предназначенных для связи, дистанционного зондирования Земли и Интернета вещей. OBCARM G2 NANO состоит из интерфейсного и процессорного модулей на отдельных печатных платах. Процессорный модуль на базе Zynq Ultrascale+ SoC обеспечивает поддержку управления телеметрией модуля на базе ARM TMS470 и необходимую периферию, включая 500 МБ оперативной памяти DDR4 для центрального процессора, 125 МБ оперативной памяти для программируемой логической матрицы, 125 МБ QSPI Flash для хранения полетного программного обеспечения и 128 ГБ eMMC Flash в качестве постоянного запоминающего устройства. Интерфейсный модуль содержит линии питания модулей OBC, интерфейсы системы управления и передатчика/приемника данных полезной нагрузки, а также драйверы, обеспечивающие преобразование и буферизацию данных полезной нагрузки. В OBCARM G2 NANO используется операционная система реального времени QNX для выполнения программных операций и высокопроизводительная шина AXI для взаимодействия процессорной системы с программируемой логической интегральной схемой. Для обеспечения работы подсистем космического аппарата в единой сети используется шина CAN. Габариты механического оборудования OBCARM G2 NANO, включая набор датчиков температуры и тепловой мост для отвода избыточного тепла от горячих точек, составляют 95 мм x 95 мм x 35 мм.

Ключевые слова: бортовой комплекс управления, программируемая логическая матрица, процессор, интерфейсный модуль, CubeSat.

Жумажанов Б.Р., Жетписбаева А., Кулакаева А., Маханов К., Жумажанов Б.С.

Қатаң шектеулері бар наноспутниктерге арналған оптикалық жүктемені әзірлеу және оңтайландыру.

Бұл мақалада Жерді қашықтан зондтау наносеріктері үшін ықшамды, жоғары өнімді оптикалық пайдалы жүктемені жобалау және оңтайландыру қарастырылады. Пайдалы жүктеме түзеткіш линзаларға ие Ричи-Кретьен телескопына негізделген және 600 км орбитадан 6 метрлік кеңістіктік ажыратымдылықты (GSD) қамтамасыз етеді, сонымен қатар масса, габариттер, энергия тұтыну және ғарыш ортасындағы жұмыс жағдайларына қатаң шектеулерге сәйкес келеді. Zemax 2024 бағдарламалық жасақтамасын пайдалана отырып жүзеге асырылған жобалау процесі 12U CubeSat платформасының шектеулері аясында жоғары сапалы кескіндерді алуға бағытталған. Нәтижелер жобаның орындалатындығын растайды және Найквист жиілігінде модуляция беру функциясының 0,26-дан жоғары мәнін қамтамасыз етеді. Бірнеше негізгі өнімділік көрсеткіштері, соның ішінде жүйелік модуляцияның беріліс функциясы бағаланды. Қажетті параметрлерге жеткеннен кейін линза түзеткіш жүйесі қосылып, өріс бұрыштары оңтайландырылды. Линзалардың материалдары ретінде BK7 және Fused Silica таңдалды. Модельдеу нәтижелері әзірленген оптикалық пайдалы жүктеме ғарыш жағдайында пайдалану талаптарына, соның ішінде зымыран тасығышты ұшырған кезде діріл жүктемелеріне төзімділікке сәйкес келетінін растайды.

Кілт сөздері: Жерді қашықтықтан зондтау, модуляция тасымалдану функциясы (MTF), пайдалы жүктеме, нано-жерсерік, ғарыш аппараты.

Жумажанов Б.Р., Жетписбаева А., Кулакаева А., Маханов К., Жумажанов Б.С.

Разработка и оптимизация оптической полезной нагрузки для наноспутников при строгих ограничениях.

В данной статье представлены проектирование и оптимизация компактной высокопроизводительной оптической полезной нагрузки для наноспутников дистанционного зондирования Земли. Полезная нагрузка основана на телескопе Ричи-Кретьена с корректирующими линзами, обеспечивает пространственное разрешение 6 метров на пиксель (GSD) с орбиты на высоте 600 км, соответствуя жестким ограничениям по массе, габаритам, энергопотреблению и условиям эксплуатации в космической среде. Процесс проектирования, выполненный с использованием программного обеспечения Zemax 2024, ориентирован на достижение высокого качества изображений в рамках ограничений, характерных для CubeSat 12U. Результаты подтверждают осуществимость проекта, обеспечивая значение функции модуляции переноса более 0,26 на частоте Найквиста. Оценивались несколько ключевых показателей производительности, включая системную функцию передачи модуляции. После достижения требуемых параметров была добавлена система линзовых корректоров и оптимизированы углы поля. В качестве материалов линз были выбраны BK7 и Fused Silica. Результаты симуляций подтверждают, что разработанная оптическая полезная нагрузка соответствует требованиям для использования в условиях космоса, включая устойчивость к вибрационным нагрузкам при запуске ракеты-носителя.

Ключевые слова. Дистанционного зондирования Земли, функции модуляции переноса (MTF), полезная нагрузка, наноспутник, космический аппарат.

Байболатов Е.Ж., Налибаев Е.Д., Кожагулов Е.Т.

Күрделі желілерді тілдік бейімділік эволюциясын динамикалық жүйелер арқылы зерттеу.

Бұл жұмыста құрылымдалған агенттер популяциясында тіл үшін бәсекелестік пен тілдік бейімділіктің эволюциясын зерттеуге арналған динамикалық жүйелер моделі ұсынылған. Әр агент тілге қатысты ұстанымын сипаттайтын үзіліссіз бейімділік айнымалысы арқылы сипатталады және бұл айнымалы агенттердің өзара әрекеттесуі, тілді сақтау және сыртқы әлеуметтік бедел күштерінің бірлескен ықпалымен дамиды. Модельде агенттің бейімділігін минус бір мен бір аралығында шектеп тұратын бейсызық демпфирлеу механизмі қарастырылған, сондай-ақ қабылдағыштық пен тілді сақтау параметрлерінің әртүрлілігі, гетерогенділігі ескеріледі. Модельдің сызықты режимі талданып, симметриялы және асимметриялы желілік топологиялар жағдайында орнықты нүктелердің тұрақтылығы зерттеледі. Толық байланысқан және «шағын әлем» типті желілердегі модельдеу нәтижелері әртүрлі динамикалық сценарийлерді көрсетеді: тілдің жойылуы, қостілділіктің сақталуы және популяцияның қарама-қарсы тілдік топтарға өздігінен бөлінуі. Бұл нәтижелер тіл динамикасын қалыптастыруда әлеуметтік құрылым, тұлғалық сәйкестік және сыртқы ықпалдардың өзара байланысын түсінуге мүмкіндік береді.

Кілт сөздері: бейсызық динамика, күрделі жүйелер, желілер.

Байболатов Е.Ж., Налибаев Е.Д., Кожагулов Е.Т.

Изучение эволюции языковой адаптации в сложных сетях с использованием динамических сетей.

В данной работе предлагается модель динамических систем для изучения языковой конкуренции и эволюции языкового смещения в структурированных популяциях агентов. Каждый агент характеризуется непрерывной переменной смещения, отражающей его языковую предпочтительность, которая эволюционирует под совместным влиянием взаимодействий с окружением, сохранения родного языка и внешних факторов. Модель включает нелинейный механизм демпфирования, ограничивающий смещение агента в фиксированном диапазоне от минус единицы до единицы, и допускает гетерогенные параметры восприимчивости и сохранения. Мы анализируем модель в линейном режиме и проводим анализ устойчивости неподвижных точек при симметричных и асимметричных топологиях сетей. Моделирование на полностью связанных и "маломировых" сетях демонстрирует разнообразные динамические сценарии, включая исчезновение языка, сохранение билингвизма и спонтанное расщепление популяции на противоположные языковые группы. Полученные результаты позволяют глубже понять взаимодействие социальной структуры, идентичности и внешнего влияния в формировании языковой динамики.

Ключевые слова: нелинейная динамика, сложные системы, сети.

Usibe B.E., Iserom B.F., Iwuji P.C., Aigberemhon M.E., Iwuanyanwu I.O., Ushie A.I., Ettah E.E.

Вин көпірі бар генератор конструкциясын талдау: прототиптен температуралық сипаттамаларға дейін.

Вин көпіріндегі генератордың прототипі бір операциялық күшейткіш негізінде диодты көпірмен құрастырылды, ол кері байланыс тізбегіне қосылып, шығыс тербелістер амплитудасын тұрақтандыру үшін азғындалған кері байланыспен қамтамасыз етілді. Сұлбаны модельдеу үшін PSPICE 10.0P нұсқасындағы сұлбалық симулятор қолданылды. Модельдеу нәтижелері дәлдігін растау үшін осциллографпен алынған өлшеу нәтижелерімен салыстырылды; дәлдігі 90% құрады. Жұмыс температурасымен генератордың орнығу уақыты арасындағы, сондай-ақ резонанстық жиілік арасындағы тәуелділіктер зерттелді және қорытып шығарылды. Жобаланған генератордың резонанстық жиілігі 142,86 Гц-тен 16,67 кГц-ке дейінгі диапазонда реттеледі. Осы жиіліктер диапазонын өлшеуге арналған сұлба прототипі сәтті талданды, ал температуралық тербелістердің шығыс сигналдарына әсері зерттеу нәтижелері ұсынылған. Сондай-ақ, шығыс ығысу кернеуінің, көз токтарының және сұлбаның жалпы ыдырайтын қуатының температуралық тәуелділігі көрсетілген. Жалпы нәтижелер көрсеткендей, генератордың жұмыс температурасы (температуралық диапазон шегінде) оның шығыс сигналына болжанбайтын әсер етеді, бұл дәлдігі жоғары маңызға ие жағдайларда генератордың сипаттамаларына теріс ықпал етуі мүмкін.

Кілт сөздері: вин көпірі бар генератор, температуралық тұрақтылық, резонанстық жиілік, ауыспалы сипаттама, сұлбаны модельдеу, PSPICE.

Usibe B.E., Iserom B.F., Iwuji P.C., Aigberemhon M.E., Iwuanyanwu I.O., Ushie A.I., Ettah E.E.

Анализ конструкции генератора с мостом Вина: от прототипа до температурных характеристик.

Прототип генератора на мосту Вина был спроектирован и собран на одном операционном усилителе с диодным мостом, включенным в цепь обратной связи с вырожденной обратной связью для обеспечения стабилизации амплитуды выходных колебаний. Для моделирования схемы также использовался симулятор схем PSPICE версии 10.0P. Результаты моделирования сравнивались с результатами измерений, полученными с помощью осциллографа, для подтверждения достоверности результатов; точность составила 90%. Были исследованы и выведены зависимости между рабочей температурой и временем установления генератора, а также резонансной частотой. Резонансная частота разработанного генератора регулируется в

диапазоне от 142,86 Гц до 16,67 кГц. Прототип схемы, используемый в данной работе для измерения этого диапазона частот, был успешно проанализирован, представлены результаты исследования влияния колебаний температуры на выходные сигналы. Также представлены результаты температурной зависимости выходного напряжения смещения, токов источника и общей рассеиваемой мощности схемы. Общие результаты представленных параметров показывают, что рабочая температура генератора (в пределах температурного диапазона) оказывает непредсказуемое влияние на его выходной сигнал, что может негативно сказаться на характеристиках генератора, где точность имеет большое значение.
Ключевые слова: генератор с мостом вина, температурная стабильность, резонансная частота, переходная характеристика, стимулирование схемы, PSPICE.

Айманова Г.К., Серебрянский А.В., Щербина М.П., Кругов М.А.

Астероидтардың спектрофотометриялық зерттеуі II: таксономиялық типтер.

Бас белдеудегі астероидтардың қатарындағы, Аполлон тобындағы (АСЗ) 30825 (1990 TG1) және сирек типтегі (1951) Lick астероидтардың таксономиялық типтерін анықтау мақсатында спектрлік бақылауларына талдау жүргізілді. Бақылаулар 2023-2024 жылдары Ассы-Түрген обсерваториясында АЗТ-20 телескопының көлемдік-фазалық голографиялық дисперсті элементті, миллиметрге 360 сызықты тор, пикселі 4.25 Å дисперсиялы, бірінші биннингте EMCCD жұмыс режимінде, күшейту коэффициенті 5 және экспозиция уақыты 10 секунд, саңылау ені 9 бұрыштық секундта спектрографында төменгі ажыратымдылық режимінде (R=600) жүргізілді. Астероидтардың таксономиялық типтері олардың шағылысу спектрлері бойынша анықтау кезінде (Савелова және басқалар, 2022) еңбегінде ұсынылған "үлгілер" әдісі және астероидтардың беткі затының химиялық-минералогиялық ерекшеліктерін көрсететін сипаттайтын визуалды альбедо мәндері қолданылды. Жоғары температуралы минералогиясы бар S-типті (107) Arachne және (482) Petrina астероидтарына және Аполлон (NEO) 30825 (1990 TG1) астероидтарына талдау жүргізілді. (97) Klotho оғары металды астероидтарды қамтитын M типті астероидтарға жатады. Жоғары жеткілікті альбедомен және спектрдің ұзын толқындық бөлігінде шағылысу қабілетінің айтарлықтай өсуі бар A класындағы астероидтарға олардың құрамында жоғары температуралы оливиндердің немесе оливиннің металдармен, негізінен темірмен және никельмен қоспасы бар астероидтарға (366) Vincentina және (1951) Lick жатады. (47) AGLAJA жүргізілген талдау нормаланған шағылысу спектрі астероидтардың B спектрлік класына сәйкес келетіндігін көрсетті, олардың беттерінің негізгі құраушылары сусыз силикаттар, гидратталған саз минералдары, органикалық полимерлер, магнетиттер және сульфидтер болуы мүмкін. Авторлардың нәтижелері бойынша (718) Erida астероидының нормаланған шағылысу спектрі альбедо диапазоны 0,04-тен 0,042-ге дейінгі T класының үлгісіне сәйкес келетін спектрлік аймаққа сәйкес келеді.
Кілт сөздері: спектрофотометрия, астероидтар; таксономиялық түрі, шағылу спектрі.

Айманова Г.К., Серебрянский А.В., Щербина М.П., Кругов М.А

Спектрофотометрические исследования астероидов II: таксономические типы

Проведен анализ спектральных наблюдений ряда астероидов Главного пояса, астероида семейства Аполлон (АСЗ) 30825 (1990 TG1) и астероида редкого типа (1951) Lick с целью определения их таксономических типов. Наблюдения проводились в 2023-2024 годы в обсерватории Ассы-Тургень на спектрографе телескопа АЗТ-20 в режиме низкого разрешения (R=600) с использованием объемно-фазового голографического диспергирующего элемента с 360 линиями на мм, дисперсией 4.25Å на пиксель, в первом биннинге с использованием режима работы EMCCD с коэффициентом усиления 5 и временем экспозиции 10 секунд, ширина щели 9 угловых секунд. При определении таксономического типа астероидов по их спектрам отражения использовался метод “шаблонов”, предложенный в работе (Савелова и др., 2022) и значения визуального альбедо - характеристика, указывающая на химико-минералогические особенности поверхностного вещества астероидов. Проведен анализ астероидов S-типа (107) Arachne и (482) Petrina и астероида семейства Аполлон (NEO) 30825 (1990 TG1), обладающим высокотемпературной минералогией. К астероидам M типа, включающим в себя астероиды с повышенным содержанием металлов, относится (97) Klotho. К астероидам класса A с достаточно высоким альбедо и значительным ростом отражательной способности в длинноволновой части спектра, что свидетельствует о присутствии в их составе из высокотемпературных оливинов или смеси оливина с металлами, в основном с железом и никелем, отнесены астероиды (366) Vincentina и (1951) Lick. Проведенный анализ показал, что нормированный отражательный спектр (47) Aglaja соответствует спектральному классу астероидов B, основными составляющими поверхности, которых, возможно, являются безводные силикаты, гидратированные глинистые минералы, органические полимеры, магнетиты и сульфиды. По результатам авторов нормированный спектр отражения астероида (718) Erida соответствует спектральному коридору, соответствующему шаблону класса T с диапазоном альбедо от 0,04 до 0,042.
Ключевые слова: спектрофотометрия, астероиды; таксономический тип, спектр отражения.

Камбарова Ж.Т., Саулебеков А.О., Касымов С.С.

Электрстатикалық біртексіз өріс негізіндегі энергия талдағыштың жаңа конструкциясы

Осьтік симметриялы біртекті емес өріс негізінде құрылған энергия талдағышының жаңа конструкциясы ұсынылды. Цилиндрлік өріс пен екінші типті дөңгелектік додекапольдің суперпозициясы әдісін қолдануымен аспаптың электронды-оптикалық сұлбасы есептелген. Электронды-оптикалық сұлбаның сандық модельдеуі жүргізіліп, аспаптың аналитикалық сипаттамалары есептелген. Ұсынылған конструкция жоғары ажырату қабілеттілікпен қатар тиімді жарық күшін қамтамасыз етеді. Нәтижелер ұсынылған аспаптың ғарыштық кеңістіктегі зарядталған бөлшектер ағындарын зерттеу үшін перспективті екенін көрсетті.

Кілт сөздері: энергия талдағыш, біртексіз өріс, мультиполь, модельдеу, зарядталған бөлшектер ағындары.

Камбарова Ж.Т., Саулебеков А.О., Касымов С.С.

Новая конструкция энергоанализатора с электростатическими неоднородным полем

Предложена новая конструкция энергоанализатора, построенного на основе осесимметричного неоднородного поля. С использованием метода суперпозиции цилиндрического поля и кругового додекаполя второго типа разработана электронно-оптическая схема прибора. Проведено численное моделирование электронно-оптической схемы прибора и получены его аналитические характеристики. Показано, что предложенная конструкция сочетает высокую разрешающую способность и эффективную светосилу. Результаты подтверждают целесообразность применения разработанного прибора для исследований потоков заряженных частиц в космическом пространстве.

Ключевые слова: энергоанализатор, неоднородное поле, мультиполь, моделирование, потоки заряженных частиц.

Шугаева Т.Ж., Амантаева А., Спивак-Лавров И.Ф.

Сандық талдау және хаосты басқару: «Visual Basic for Applications» қолдану арқылы Лоренц жүйелерін зерттеу.

Бұл жұмыста Лоренц жүйелерінің хаостық динамикасын сандық талдау және басқару қарастырылған. Модельдеу және визуализация үшін Microsoft Excel ортасындағы Visual Basic for Applications тілі пайдаланылды. Лоренц аттракторы сияқты хаостық жүйелер бейсызық динамика мен хаос теориясының негізгі ұғымдары болып табылады. Олар бастапқы шарттарға сезгіштігімен, бейсызықтылығымен және фракталдық өлшемділігімен сипатталады. Зерттеуде сандық әдістер қолданылды: адаптивті қадам таңдауымен төрт нүктелі Адамс әдісі классикалық параметрлерде (“s=10, r=28, b=8/3”) және модификацияланған мәндерде (“s=15, r=35, b=10/3”) зерттелді. Сонымен қатар, қосымша мүше енгізілген модификацияланған Лоренц жүйесі қарастырылып, жаңа динамикалық режимдер көрсетілді. Жұмыста VBA негізіндегі құралдардың бейсызық дифференциалдық теңдеулерді шешудегі және күрделі аттракторларды визуализациялаудағы тиімділігі көрсетілді. Адамс және Крылов әдістерінің интеграциясы есептердің дәлдігі мен орнықтылығын арттыратыны дәлелденді. Нәтижелер хаосты басқару мен қолданбалы есептерде пайдалану үшін перспективалар ашатынын көрсетеді.

Кілт сөздер: Лоренц аттракторы, хаос теориясы, бейсызық динамика, сандық талдау, Visual Basic for Applications, Адамс әдісі, Крылов әдісі, хаосты басқару, динамикалық жүйелер.

Шугаева Т.Ж., Амантаева А., Спивак-Лавров И.Ф.

Численный анализ и управление хаосом: исследование систем Лоренца с применением «Visual Basic for Applications».

В работе рассматриваются численный анализ и управление хаотической динамикой систем Лоренца с использованием Visual Basic for Applications в среде Microsoft Excel для моделирования и визуализации. Хаотические системы, включая аттрактор Лоренца, представляют собой фундаментальную концепцию нелинейной динамики и теории хаоса, характеризующуюся чувствительностью к начальным условиям, нелинейностью и фрактальной размерностью. В исследовании применены численные методы, включая четырехточечный метод Адамса с адаптивным выбором шага, для анализа классических параметров (“s=10, r=28, b=8/3”) и модифицированных значений (“s=15, r=35, b=10/3”). Кроме того, рассмотрена модифицированная система Лоренца с дополнительным членом, демонстрирующая новые режимы динамики. Работа подчеркивает практическую применимость VBA-инструментов для решения нелинейных дифференциальных уравнений и визуализации сложных аттракторов. Результаты показывают эффективность интеграции методов Адамса и Крылова для повышения точности и устойчивости вычислений, что открывает перспективы для использования в прикладных задачах управления хаосом.

Ключевые слова: аттрактор Лоренца, теория хаоса, нелинейная динамика, численный анализ, Visual Basic for Applications, метод Адамса, метод Крылова, управление хаосом, динамические системы.